Noise assisted effects in physics and biophysics studied by the optical trapping technique

Ignacio A. Martínez

Supervisor: Professor Dmitry Petrov

ICFO-The Institute of Photonic Sciences and Universitat Politècnica de Catalunya

Barcelona, February 7, 2014

A Guadalupe y Pepe

Acknowledgements

First of all, I want to acknowledge to my Thesis supervisor Prof. Dmitry Petrov the opportunity he gave me four years ago. He had the patience to teach me for the very beginning all I know. If I could choose again, I would repeat the choice. I expect to have just half of his passion in work, that will be enough. Thanks you D.

I also want to express my gratitude to Prof. Lluis Torner, for his success developing the perfect environment to do research at the highest international level. I would also to acknowledge the economic support of the Spanish Ministry of Science and Innovation.

Within Optical tweezers group, thanks specially to Filip, who has the patience to work with me the first months, and to Raúl, who has read carefully, comma by comma, this Thesis.

I must also remember all my PhD student colleges, Mónica, Saurabh, Stefan, Pau, Antonio, Silvie, Ali, the different postdocs who have shared time with me, Claudia Nieva, Satish Rao, Michal Wojdyla. To my *biology* collaborators, Denis Spricigo and Meritxell Tort, so many hours watching the movement in the screen! I cannot forget Édgar Roldán, and his face at the end of the working nights. Luis Dinis enter in the collaboration between ICFO and UCM at the end, but his work become esential to understand our results.

Thanks to all my *slaves*: Mario, Erwan, Frederic, Simon, Stephen, Xavi. I learnt with you much more that you think.

Prof. Susana Campoy shared her knowledge to make posible both biology chapters. Thanks Susana!

Thanks also to Prof. Karen Volke-Sepulveda, although not included here, I expect to go on our colaboration. Thanks Karen!

I would like to remember Prof. Parrondo, whose ideas motivated the bulk of the statistical physics part of this Thesis. Without his help I could not be here. Thanks JM!

Along these four years I have met many people, without them, life would be imposible: Carlés, Belén, Igor, Zsuzsi, Laura, Mireia, Ricardo, Pelayo, Silvia, Juan, Sybille, Chris, Marta, Sebas, Pablo, Rodri, Maria and a very long etcetera that will not fit here. Thanks to all of them.

¿Y qué puedo decir de mi familia? Sin ellos nunca hubiera sido posible llegar. Tengo que agradecer especialmente a mis padres, la libertad que siempre me han dado, a mis hermanos Ana y Cristóbal, especialmente a ella, que tuvo la mala

suerte de lidiar con mi último año en Madrid. No me puedo olvidar de mis tíos y primos, de mis abuelos, especialmente Lola: ella empezó todo en aquellas tardes con esas cartillas, de mi tía Elia. Acordarme ahora de todos los que me han acompañado hasta aquí, ya en Madrid, Héctor, Ryu, Ana,..., o antes, Alicia, Miguel, Christian, Paco,... Gracias a todos.

Abstract

Almost two centuries after the first observations of Robert Brown, the study of systems ruled by noise has become a significant part of modern physics and other so diverse situations, such as the stock market, personal networks, ecosystems, etc. In particular, we focus on the so-called *small systems*, where the thermal fluctuations determine the dynamics and energetics of the system. Examples of this scale are biopolymers, such as DNA or RNA, molecular motors, living cells or colloidal particles in suspension. As the energy exchanges between a small system and its environment are of the order of magnitude of thermal fluctuations, apparent violations of the classical laws of thermodynamics appear.

We have studied the role of noise in biological and physical systems. As the main experimental tool we have used the optical tweezers technique, which allows one to exert forces in the pN range, as well as to spatially confine the studied objects improving the accuracy of the experiments. A highly focused laser beam creates a time and space controllable optical potential profile. This permitted to investigate noise assisted effects in different scenarios.

Two biological systems were considered, namely, single DNA molecule and single bacterium. We showed that the motion of the stretched DNA molecule in the entropic regime (forces below 5 pN) includes an additional noisy component whose spectral power is proportional to $1/f^{\alpha}$. The presence of this noise may be related with changes of the probability of folding and unfolding events when the DNA strand is extended. On the other hand, we studied the trajectory of single bacteria, whose motion includes inherently noisy components. Using a novel technique with only one optical trap we measured the dynamics of a trapped single bacterium *S. enterica.* We found that the trajectory within a single trap can reveal the different behavior of the samples. In addition to the validation of our technique, we have characterized the phenotype of mutant cheV in anaerobic conditions.

In the second part of the thesis, we studied stochastic thermodynamic using a micron-sized dielectric sphere.The control of the temperature in such experiments has a key importance to understand the energetics of the small systems. We suggested a novel technique to control the kinetic temperature of a sphere by applying of an external force with the same power spectral density (PSD) as one of the thermal noise. We experimentally tested our hypothesis in equilibrium, measuring the position histogram and PSD of the microsphere, and out of equilibrium, implementing a protocole to test Crooks theorem. We conclude that our technique allows one to control the kinetic temperature of a Brownian particle over a wide range of values, from room temperature to several thousand Kelvin with high temporal accuracy.

The most obvious application of this technique is the realization of non-isothermal processes. Among them, an adiabatic process is essential although controversial in small systems. We study its meaning in a colloidal particle experiment, paying attention to the consequences of the overdamped approximation. Finally, we could realize for the first time the Carnot cycle, using a colloidal particle in a liquid as a working substance.

The effect of the thermal bath is also present in the thermodynamics of information. In the last chapter, we considered the derivation of an universal equivalence between the energetics of a process and the probability of a system to choose it among other options. The obtained expression can be considered a generalization of the Landauer limit. We tested our theory in an experiment where a continuous transition from a single well to a double well potential produces a symmetry breaking affecting a Brownian particle. Moreover, combining two of the process, we were able to achieve the first realization of a Szilard engine based on symmetry breaking and symmetry restoration.

Resumen

Casi dos siglos después de la observación de Robert Brown, el estudio de sistemas gobernados por ruido se ha convertido en una parte significativa de la física moderna. Con el objetivo de obtener información, y de tratar de predecir, sistemas complejos, se han trazado analogías en situaciones muy diversas, tales como el mercado de valores, las relaciones interpersonales, los ecosistemas, etc. En particular, si nos detenemos en los denominados como *sistemas pequeños*, podemos observar como las fluctuaciones térmicas determinan su dinámica y su energética. Al tratarse de sistemas cuyos intercambios de energía con el entorno son del orden de magnitud de las fluctuaciones, podemos observar aparentes violaciones de las leyes clásicas de la termodinámica. Ejemplos de esta escala son las diversas biomoléculas como el ADN o el ARN, los diversos motores moleculares o una célula en su conjunto, pasando por partículas coloidales en suspensión.

Para el estudio de los sistemas mesoscópicos, hemos usado la técnica de la pinza óptica, la cual nos permite ejercer fuerzas del orden de picoNewtons con resolución nanométrica. Por medio de un haz fuertemente enfocado, podemos crear un potencial óptico donde objetos con índice de refracción mayor que el del medio son atrapados.

En esta tesis hemos estudiado el rol del ruido en sistemas biológicos y en sistemas físicos. En primer lugar, observamos que la dinámica estacionaria de una molécula individual de ADN en el régimen entrópico (fuerzas por debajo de 5 pN) muestra una componente espectral que sigue una ley de potencias $1/f^{\alpha}$. Por otra parte, también estudiamos la trayectoria de bacterias bajo una única trampa óptica. La bacteria elegida fue la *Salmonella enterica*, en diversas mutaciones para poder fijar su fenotipo. En particular, además de validar la técnica, caracterizamos el fenotipo del mutante cheV en condiciones anaeróbicas.

El control de la temperatura en experimentos de partículas coloidales es de una importancia clave para completar la energética de los sistemas pequeños. A pesar de que existen métodos para variar la temperatura del fluido, estos cambios están siempre acotados por límites físicos, como evaporación, y sufren de inconvenientes, como convección y cambios de la viscosidad del fluido, que impiden un estudio *cómodo* de los procesos no isotermos. Enunciamos una hipótesis muy sencilla: *nuestra partícula coloidal es incapaz de diferenciar entre el ruido térmico y un fuerza externa de la misma naturaleza.* Comprobamos que nuestra hipótesis es correcta en equilibrio y no equilibrio, por medio del estudio del histograma de posiciones, del PSD e implementando un protocolo donde poder estudiar el teorema de Crooks.

La aplicación más obvia de esta técnica es la realización de procesos no-isotermos. Dentro de ellos, es imprescindible la aproximación al concepto de adiabaticidad, tan presentes en la termodinámica clásica. Siendo imposible rodear de paredes adibáticas nuestro sistema, desarrollamos los diversos protocolos sugeridos durante los últimos 10 años en la literatura. Como colofón, desarrollamos el primer ciclo de Carnot experimental con partículas coloidales.

El efecto del baño térmico también se encuentra presente en la termodinámica de la información. En el último capítulo de la tesis, desarrollamos una expresión analítica que relaciona la probabilidad de llevar a cabo un proceso con la energía que se puede extraer del baño térmico durante el mismo. Esta expresión puede considerarse una generalización del principio de Landauer. Gracias a la flexibilidad que nos presta el AOD para generar potenciales ópticos, comprobamos la relación con un experimento con partículas coloidales. Para terminar, presentamos un motor de Szilard con partículas coloidales, el cual permite obtener trabajo del baño térmico a través de la información disponible sobre el sistema.

Contents

Acknowledgements

Abstract

1

Introduction

1.1 Why noise? Why optical tweezers?

Noise can be thought of as a random disturbance added to a principal signal. Although it is an unwanted contribution in communications [1] or image processing [2, 3], it has great importance in Nature. Noisy behavior appears in many different scenarios, such as city traffic, heart rhythms, the stock market, molecular motor motion, colloidal physics, etc. [4–6].

Recently, considerable attention has been focused on the constructive role of noise in Nature. A great deal of experimental evidence in various fields of science has corroborated the viewpoint that the influence of noise, which always accompanies all actual systems, is not restricted to destructive and thermodynamic effects. One of the shining examples of such behavior is stochastic resonance. Stochastic resonance describes processes whereby the addition of a random function (*noise*) to a weak information carrying signal can enhance the signal's detectability by a nonlinear system or intensify the information content of the system's output. The best system performance is achieved with an optimum noise intensity.

Recent ground breaking technological developments have made possible the exploration with high accuracy of the so-called mesoscopic world [7–9]. The mesoscopic world is defined as the size range between the macroworld, ruled by classical physics, and the microworld, ruled by quantum mechanics. Within this range, one can find systems with sizes from a few nanometers composed of just a few atoms, such as proteins, up to several microns, such as biomolecules or cells. One remarkable fact in this range is that the energy exchanges between the system and its environment are of the order of kT, the thermal energy. Here, k is Boltzmann's constant and T is the absolute temperature. These energy values allow the systems to break the classical laws of thermodynamics [10]. This fact, in itself amazing, can be linked to some open questions such as *how can living cells obtain such a high efficiency when they are ruled by noisy signals?* A good example is kinesin, which apparently works at 60% efficiency during the conversion to mechanical work of the chemical energy obtained by hydrolyzing ATP when moves along the cellular microtubules [11]. Such efficiency is twice the efficiency presented by Curzon in his analysis of power plants [12]. The high efficiency observed in the motion of kinesin leads to other questions, *can small systems convert thermal energy into useful work?* For instance, the possibility of transforming correlated electrical noise into free energy in the case of specific enzymes was discussed in [13].

Most theoretical investigations on noise-driven effects have been devoted to studying systems with a single, usually white, noise source. This formulation is physically natural and fruitful because every actual system involves an internal thermal noise whose intensity is determined by its temperature. In many situations, the time scale of the random perturbations is much shorter than that of the characteristic time scale of the system. It is then a good assumption to consider uncorrelated random signals. This assumption considerably simplifies the problem. However, in the physical world, this idealization is not completely valid [14]. In order to understand the importance of corrections to white noise and more generally, in order to investigate the role of noise correlations of arbitrary strength, it is thus necessary to study also nonwhite noise, i.e., colored noise of small to moderate-to-large correlation strength.

The term *colored noise* usually refers to noise sources with a frequency-dependent power spectrum, in analogy to the spectrum of light. In the case of white noise, the power spectrum does not depend on the frequency and its Fourier transform, which corresponds to the correlation function of the noise, is the Dirac delta function. On the other hand, the term *correlated noise* refers to spatial dependence. The term used to refer to both the colored noise and correlated noise is *non-Markovian.* The presence of non-Markovian noise also means that the system possesses a hidden memory. When the dependence on the frequency is characterized by a power law, f^{α}, we can classified the signal into different *colors*. If $\alpha = -2$ we talk about *brown noise*, present in the trajectory of a Brownian particle; if $\alpha = -1$, we talk about *pink noise*, etc.

Experimental data indicate that noise in biological processes is non-Markovian. Examples include currents through voltage-sensitive ion channels in cell membranes, signals from the sensory system of rat skin [15, 16], and noise sources in different biological systems [17]. It has also been observed that biological transport works in the presence of white thermal noise and an internal, generally correlated, random noise of biological origin, such as the hydrolysis mechanism of ATP [18]. A Brownian motor can work not only when time correlations exist in a periodic but asymmetric potential landscape, but also when out-of-equilibrium, correlated noise participates in the transitions between two internal states of the system. Colored noise is again necessary and the average flux depends strongly on the amplitude of the noise and its spectrum [19]. The understanding of the exact mechanism of protein motion in the cytoskeleton has led physicists to study several stochastic ratchet models. The simplest of these models involves an overdamped particle, representing, for instance, the motor protein kinesin, in a periodic but not symmetric force field, driven by noise. The periodic forces are exerted by the asymmetric dimmers on the kinesin while the noise term represents the fluctuating environment. This model leads to a macroscopic particle current in a specific direction. In the additive correlated noise, the finite correlation time corresponds to a kinesin binding event and subsequent energy release through hydrolysis.

DNA is the basis of life as we know it. Inside the cell nucleus, different fundamental processes, such as transcription, replication, and translation, need the loss of the quaternary structure of the biomolecule. During these processes, the DNA strand undergoes numerous mechanical entropic unfolding and extension events that are primarily supported by the polymer-like phosphate backbone, thus making it critical to have a full understanding of how the DNA structure responds to forces. On the other hand, as a polymer, DNA tries, in the absence of external forces, to maximize the number of accesible microstates: it tries to maximize its entropy [20]. If we apply a low external load to stretch it, we will exert some work against the so called *entropic force*. As a small system, the entropy associated to a single DNA is a stochastic quantity, being able to fluctuate over different trajectories. Even in equilibrium, its value is a changing quantity. From this hypothesis, the spontaneous changes of entropy can be turned into fluctuations in the position of the molecule.

Although biomolecules have been studied for the last twenty years with force spectroscopy [20], the dynamics of DNA is still not completely understood.

Questions still remain about the force spectrum of conformational fluctuations of the chemical structure of DNA in the low force regime, where entropy is a driving factor. It has been shown that the internal modes of a DNA extended up to 80% are related by a power law, decreasing in intensity with the mode number [21,22]. Internal hydrodynamic effects should raise the polymer friction coefficient as the molecule extends, causing a sequential increase in the polymer relaxation time [23, 24]. Extended DNA molecules are characterized by two different sets of relaxation times and spring constants (longitudinal and transversal), and the dynamics at high extensions points to yet unexplained nonlinear behavior [25]. In particular, the correlation functions have super-exponential relaxation, something that may indicate the presence of new physical effects.

Moreover, the development of nanotechnology is deeply connected with the understanding of the biological system acting in the mesoscale. Several authors have pointed out the need to profit from the natural designs of engines to develop artificial nanodevices, and thus we speak about *biology inspired nanotechnology* [26, 27]. One of the most studied examples of engines in nature is the flagellar motor, which allows bacteria to move in liquid media. We can say that a molecular motor is efficient if the displacement due to the flagellar movement is greater than the diffusion itself [27]. This natural engine is composed of several elements acting together in order to produce a helical rotation. If we observe the motility of a single bacterium using a microscope, the bacterium will show a combination of straight line trajectories in, apparently, a noisy combination. Actually, this motility can be considered as the combination of two different behaviors: running, i.e., motion along a straight line, and tumbling, a random motion that changes the orientation of the cell. This combination allows the bacterium to explore its environment by a kind of *trial and error* mechanism where the cell determines *a posteriori* whether the chosen direction improved the environmental conditions or not [28]. Both behaviors underlie the process of chemotaxis: bacteria have transmembrane receptors which can detect the concentration of chemical products. This mechanism allows the bacterium to move towards attractants (or escape from repellents).

Since 1993 [10], the study of the thermodynamics of small systems has grown considerably. As was mentioned before, it is characteristical that the energy of the system be of the same order of magnitude as the thermal fluctuations, and so the postulates of classical thermodynamics are no longer completely correct [1]. In order to properly analyze these effects, fluctuation theorems (FTs) have been developed. FTs are specific tools for studying the probability of

---

[1] In fact, Thermodynamics is valid only in the thermodynamic limit

the system's reducing or increasing its entropy along a process. Some of the different FTs have been experimentally tested in colloidal particles [29] and biological samples [30]. Fluctuations and *rare events* scale with the thermal energy. Thus, the management of the temperature of FT experiments is of the utmost importance for testing and understanding the thermodynamics of small systems. Although there are techniques that allow this control [31], those changes are always restricted between physical bounds, such as evaporation or convection, limiting the possible range of action. This small range is enough to appreciate changes in the behavior of biomolecules or cells [31], although it would be desirable to have a broader range to study the FTs along non-isothermal processes.

The realization of thermodynamic processes follows immediately from this technique. The problem of a very dilute classical gas has been theoretically studied for years, with special attention to the so-called adiabatic processes [32]. The importance of these processes lies in their connection with the idea of irreversibility, and hence, with the efficiency of thermal engines. In our experimental scenario, we can find analogies with this kind of study. However, we can identify one main difference: we can not place *adiabatic walls* which would avoid any heat transfer between the system and the bath. This *problem* is shared with the thermodynamic processes carried out in biological systems, such as cells. The total control of the thermal bath may be the key to completing the experimental work in stochastic thermodynamics, opening up the possibility to generate adiabatic processes, not achieved as yet, and it can also be applied to the development of microsized engines, in analogy with those studied recently in [33].

The effect of a thermal bath is also present in the thermodynamics of information. This science was developed to find the physical limits in computing, analogously to thermodynamics which tried to optimize steam engines. In 1961, Landauer gave an illustrative example to explain the explicit dissipation of heat when a bit is erased [34]. The erasure process deletes the state of the *bit* without using its information content. The bit was modelled as a double well potential with a tunable well height, it being possible to apply an external force to *reboot* the *bit*. Landauer's principle is the solution of the Maxwell demon problem [35]. There is no physical limitation to knowing the state of each molecule or for managing the door, but each time the demon erases the previous state of the memory, an amount of heat $kT \log 2$ will be released to the thermal bath. An example of a *gedankenexperiment* in which this demon appears is the so-called *Szilard engine* [36].

The original vision of Szilard [36], although there are other versions [37],

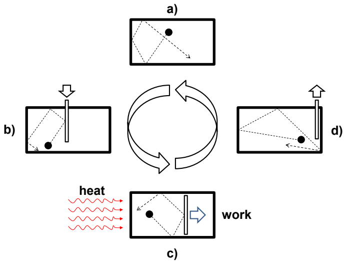

Figure 1.1: Description of Leo Szilard's idea for obtaining useful work from a thermal bath. a) A cylinder has a gas consisting of a single molecule inside. Its walls are diathermal, so the unimolecular gas is in thermal equilibrium with the environment. b) An extra wall is included in the middle of the cylinder. The extra wall can act as a piston which is subject to the pressure of the molecule. c) The available volume for the molecule grows in an isothermal process. As the heat can pass through the wall, the energy from the thermal bath is converted into useful work against the piston. d) The piston reaches the end of the cylinder, where it can be extracted to restore the original scheme.

consists in a single molecule gas inside a cylinder made with diathermal walls in contact with a thermal bath (T). The cylinder can be separated into two subvolumes by the addition of an extra wall (if the addition is slow enough, no work will be needed to perform it). The extra wall can act as a piston which will be allowed to move to the empty subvolume: the process will be the same as an isothermal expansion of a unimolecular gas in a cylinder: the gas will exert work on the piston, which can be put to use. This extra energy will come from the thermal bath that is equilibrating the molecule with the environment via the passage of heat from the molecule through the diathermal walls. Finally, when the piston reaches the end of the cylinder, it is extracted and the initial configuration is restored. The extra work is $kT\log 2$ when the piston is placed at the middle of the cylinder. If we position the piston elsewhere, the possible extracted work will be:

$$W = \int_{\alpha V}^{V} \frac{kT}{V} dV = -kT\log\alpha, \tag{1.1}$$

where α is the percentage of the cylinder which remains empty, in the previous stage $\alpha = 1/2$. We see how the useful work is a function of the probability of finding the molecule in one of the subvolumes.

Throughout the last decade, different experiments have been made in the field of the thermodynamics of information. For example, Toyabe *et al.* designed a microscopic Maxwell's demon [38]. There, a particle was placed on a spiral-staircase like potential where the bead could jump between steps using thermal energy. On the other hand, an experimental demostration of Landauer's principle can be found in [39]. They use an optical landscape to model a bit, and therefore, to study the released heat from an erasure. We asked ourselves if this principle could have a higher implication, *does the process of choosing have a thermodynamical implication?*. This is not just an academic problem, as it is analogous to one of the challenges of modern molecular biology, i.e., the understanding of protein folding, a situation where the system can choose between different conformations. In fact, there are studies that have shown that the features of symmetry breaking may be used to understand those systems [40].

In order to manage and interact with objects in the mesoscale, several techniques have been developed [41]. In this thesis, the experimental work was done with the optical tweezers technique. Briefly, the light has energy and momentum. Although the momentum tranfer due to a light source is quite small, the laser allows to power its effects. The first evidence of forces applied to small object were reported by Ashkin in the 1970s [42]. Using a highly focused laser beam, we are able to micromanipulate objects ranging from cells to dielectric beads, implementing small forces (∼pN) with nanometric resolution. This technique is based on the creation of potential well(s) in order to confine small objects in the range from the Rayleigh regime up to the Mie regime [43–45]. For big particles, the basic principle of the optical trap is based on the conservation of the momentum of the light by propagation through the particle. For a small particle, another physical phenomena is implied when the incident beam excites the dipole moment in the particle inducing its attracion to the maximum of the optical beam intensity. In any case, the applied force can be assumed to be linear $F_{\text{trap}} = -\kappa \Delta x$, where κ is the constant of the trap and Δx is the distance between the probe and the equilibrium position. Although the ease of the spring analogy is very useful in a great number of experiments, there are cases where one must increase the complexity of our system. There are several methods of generating an optical potential landscape with a dependence on time and space and with the desired shape. There are different methods of designing any optical potential landscape in real time [43, 46].

1.2 Aims and workplan. Description of the chapters

Here, we propose the experimental study of noise-assisted effects both in multi- and mono-stable systems. We mainly concentrate on experiments that may be used to explain the physical effects observed in bio-systems and the thermodynamics of small systems. As experimental samples for these studies, we used single DNA molecules, single bacterium, and colloidal suspensions, i.e., micron-sized spherical particles suspended in liquids, which provide ideal model systems suitable for addressing many problems in statistical physics.

Using the optical trapping technique, we generated a potential landscape with an appropriate time and space evolution. The bead can move both deterministically (due to the gradients of the potential energy) and randomly (due to the inherent Brownian fluctuations). In specific parts of this thesis, it was necessary to interact with the sample, in other words, to apply an external force. The polystyrene beads have an intrinsic superficial charge that can be used to exert an electric force. Using a couple of electrodes, a difference of voltage was applied, transforming our custom made chamber into a capacitor [47]. The combination of optical trapping with electrophoresis permits us to model practically any noise-assisted effect. In Chapter 2 an overview of the optical tweezers technique and all the different experimental tools used in the thesis will be presented. An important issue to be described is the collection of experimental methods used to calibrate the system. At the end of the chapter, two original contributions to the field are presented, namely, a technique to measure the whole force map of a trap with a single laser beam and an acousto-optic deflector and a method to extend the linear detection range of the position of the bead by the forward scattered light up to several microns.

Schematically, this thesis can be divided into two main parts: biophysics (Chapters 3 and 4) and stochastic thermodynamics (Chapters 6, 7 and 8). In the first part of this thesis, we study biological systems such as single biomolecules, double-strand DNA, and a single bacterium, *S. enterica.*

The random conformations that a DNA molecule forms in solutions occur in the presence of the thermal noise, with a white spectrum, of the forces, but also an important role is played by out-of-equilibrium mechanical activity. These mechanical effects are directly related to biochemical reactions in the long polymer chain. The power spectrum of such force fluctuations is defined by processes that are different from the thermal noise and therefore may depend on the frequency of the fluctuations (*colored noise*). Recent detailed studies of the sources of fluctuations in some biological systems, in particular in bio-molecular motors [48], offer strong experimental indications that the noise signals in these systems include also a non-white component with a frequency-dependent power spectrum. The effect of colored noise is not restricted to destructive and thermodynamic effects [49], but also may change mechanical processes in biochemistry [50]. Force studies of single DNA molecules using single molecule force spectroscopy brought new insight in into various DNA biological functions [20, 21, 51, 52].

Classical experiments have been developed with strong tweezers, with stiffness of the order of hundreds of picoNewton per micron. Our premise is to go in the opposite direction, trying to maintain one of the beads slightly trapped, with a low stiffness. Therefore, the fluctuations of the biomolecules can be correlated with the fluctuations of the trapped bead and the experimental noise will not hide the possible effects. By this simple experiment, we noticed the presence of a colored noise ($1/f^\alpha$) when the molecule is stretched within the entropic regime. Experiments showed that the fluctuations of the DNA molecule extended up to 80% by a force of 3 pN include the colored noise contribution with spectral dependence $1/f^\alpha$ with $\alpha \sim 0.75$.

The swimming pattern of the bacteria is a key point in the virulence of these pathogens, the study of a single bacterium being fundamental to understand its mechanism. This movement is not deterministic, but presents a stochastic behavior that can be divided into two main phenotypes, namely, *running* and *tumbling*. The term *running* refers to the straightforward movement of the cell, while *tumbling* is the *reorientation* of the bacterium to another direction. Berg points out in [28] that the changes in the cell's swimming are random and the cell chooses after the change whether the new direction improves its enviromental conditions. Although the study of a single bacterium with optical tweezers has been developed in depth [53–60], it is still quite complex in its optical part compared to the usual biology laboratories. Here, we propose the most simple configuration of the optical tweezers, whose combination with a robust data processing based on a previous study by our group [61] allows obtaining quantitative data from the single bacterium within the optical potential. We used this method to study the importance of the cheV protein in the swimming profile, and hence, in the chemotaxis pathway.

In the second part of the thesis, we study noise-assisted effects in simpler experiments. By the use of colloidal particles within optical landscapes, we are able to study the energetics of thermodynamical processes in the mesoscale. Chapter 5 presents a summary of stochastic thermodynamics. This is a key tool for analyzing and understanding the experimental data. The study of the mesoscopic world carries out the fluctuations due to the system's energy having the same order of magnitude as the thermal energy. These fluctuations arise from the stochastic behavior of the thermodynamic quantities such as work, heat, and entropy, and it is necessary to redefine the thermodynamic laws as *fluctuation theorems*. Thanks to this framework, it is possible to calculate the energy exchanges, work, and heat, from the observables of our system, the position of the sample and the exerted forces [62].

As we mentioned above, temperature is of key importance in the mesoscale: the fluctuations scale with the temperature. Therefore, controlling the temperature is of great importance. The Langevin equation models the temperature as a white noise term. From this starting point we have proposed a novel method to mimic the temperature in colloidal particle experiments. We add an extra source of noise with a white spectrum to the trapped microsphere, which can not distinguish the extra force from an increase in the fluid's temperature. We demonstrate experimentally how the temperature increase affects the histogram of the position of the Brownian particle, its power spectral density, its response to an external perturbation, and the statistics of the Kramers transitions in a double-well potential. Effects related to the nonideal character of the white noise generated experimentally are also analyzed. This experimental technique allows tuning and controlling the kinetic temperature of the sphere with millisecond resolution over a wide range and along a single spatial direction. We checked this equivalence by analyzing the behavior of the bead under stationary conditions and testing the Crook's fluctuation theorem.

The realization of thermodynamical processes follows immediately from the previous technique. Drawing on an analogy between the classical scheme of an ideal gas within a cylinder with a piston and an optically trapped particle, we can develop the energetics of the different processes. We define the *volume* of our system as a function of the stiffness of the trap κ. The different thermodynamic parameters, such as entropy, Helmholtz free energy, etc., are derived from the thermodynamic relations [63]. Recently, some authors have pointed out the non-triviality of using the overdamped approximation, especialy in non-isothermal processes [64]. We can study the different processes with a large range of temperature differences. On the other hand, the possibility of synchronizing the temperature with the stiffness allows us to build different processes that can be candidates for the concept of *adiabatic*. The final combination of the processes would lead to the construction of stochastical engines [33], especially the celebrated Carnot cycle [65, 66]. The results are described in Chapter 7.

Chapter 8 presents a universal relation of the energetics of symmetry breaking (SB). SB involves an abrupt change in the set of microstates that a system can explore. This change has unavoidable thermodynamic implications. According to Boltzmann's microscopic interpretation of entropy, a shrinkage of the set of compatible states implies a decrease of entropy, which eventually needs to be compensated by a dissipation of heat and consequently requires work. On the other hand, in spontaneous SB, the available phase space volume changes without the need for work, yielding an apparent decrease of entropy. Here we show that this decrease of entropy is a key ingredient in the Szilard engine and Landauer's principle and report a direct measurement of the entropy change along SB transitions in a Brownian particle. The SB is induced by a bistable potential created with two optical traps. The experiment confirms the theoretical results based on fluctuation theorems, allows us to reproduce the Szilard engine's extracting energy from a single thermal bath, and shows that the signature of a SB in the energetics is measurable, providing new methods of detecting the coexistence of metastable states in macromolecules.

1.3 Main contributions

Briefly the main achievements of the thesis are:

- Development of two techniques within the optical trapping framework that permit improving the accuracy of stochastical measurements.
- Observation of a correlated noise source in a single DNA extended within the entropic regime.
- Determination of the phenotype of a single bacterium using a single optical tweezer by a novel approach. Characterization of the role of the protein CheV in the chemotaxis pathway of the *Salmonella enterica serovar Typhimurium* under anaerobic conditions.
- Use of an external source of noise to mimic temperatures in colloids up to 3000K.
- Study of non-isothermal thermodynamical processes in the mesoscale. Design and construction of a mesoscopic Carnot cycle.
- Analytical study of the universal features of symmetry breaking and restoring. Experimental test of the relation between energetics and probabilities by optical tweezers experiments. Study of the differential Landauer extended principle. We build a Szilard engine with optical tweezers.

2

Optical trapping

The study of systems at the mesoscale represents one of the most beautiful landscapes in physics. In this scale, the thermal energy is comparable to the energies involved in many processes occurring at this level, giving to the system the opportunity to fluctuate along different possibilities, allowing transitions forbidden in the macroscale. One of the best tools to study this branch of the modern physics is the optical trapping technique. Laser tweezers can apply forces in the range of piconewtons to systems with characteristic sizes in the nanometric scale. Light has energy and momentum, what was observed long time ago in the comets, whose tails always points in the opposite sense to the Sun. Thanks to the development of the laser [67], it is possible to use a powerful source of coherent light. In the 70s, Arthur Ashkin proved that laser beams could be used to apply forces to a small object [42]. More than forty years later, the optical tweezers technique has been developed to study from atoms [68], to eukaryotic cells [55], passing through small dielectric spheres [7], viruses [56], biomolecules [21, 69, 70] , and a long etcetera. The use of optical tweezers is clear and successful due a main reason: the easiness of the defined force, the analogy with a perfect spring is a great advantage in order to study different problems using the classic Hooke's law:

$$F = -\kappa \Delta x \tag{2.1}$$

where κ represents the **stiffness** of our trap under this conditions. Obviously, we have several restriction to this regime: What is the range of linearity of the force? Is the force profile the same to any particle? What does the stiffness depend on? In this chapter, we present an overview of the general properties and the technical aspects of the optical trapping technique, and we then present two ways to improve its performance.

2.1 Theory: gradient forces, radiation pressures

Light carries energy and momentum. However, while the simple action of placing the hand under the sunlight, we can feel the heating due to the energy, we can not feel the pressure of the light in our hand as its momentum is several order of magnitude lower.In spite of the low amount of carried momentum, it was appreciate centuries ago by the observation of the comet's tail: the huge distances and intensities in astronomy makes its detection possible.

The laser made available high power sources of coherent light, thus increasing the intensity of radiation pressure effects [67]. By highly focusing a laser, Ashkin demonstrated the possibility of exerting forces to dielectric objects thanks to the radiation pressure [42]. Although his first experiments only allowed him to apply forces, he could later design the confinement of small objects (smaller than the laser wavelength) due to the presence of gradient forces [7].

What is beyond the radiation pressure? There are two contributions to the total force exerted by the light to the trapped object: the gradient force and the radiation pressure. The gradient force is proportional to the spatial gradient of light intesity and therefore, assuming for example a Gaussian shape, acts in the three axis *(x,y,z)* while the radiation pressure acts in the optical axis *(z)*, Fig 2.4. The gradient force is the responsible of the confinement and the stability of the trap will be related to the ratio between both kind of forces.

Although Ashkin's first idea was the atom trapping, the optical trapping technique splashed different branches of Physics. While Steven Chu and colleagues were focused in the atom trapping, several groups designed biophysical experiments with the optical tweezers. From the bacteria to the virus, the combination of low forces and highly accurate optical trapping gave a strong impulse to the single molecule (bacteria) studies.

The quantification of the optical forces responsible for the optical trapping is not an easy task. Although such a quantification is not in the core of this thesis,

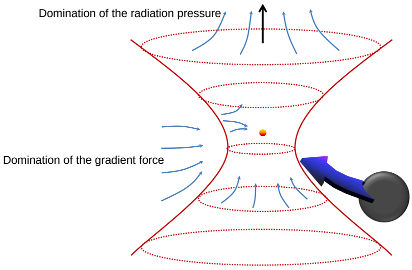

Figure 2.1: Schematic description of the forces acting in an optical trap. The colloidal particle feels the gradient and the radiation forces, this one having to be compensated by the former to achieve stability. From a certain value of the bead position in the axial plane, the radiation pressure will always dominate, pushing the microsphere above. Adaptation from David Grier webpage.

which is rather aimed at the aplication of OT as a tool to study noise assisted effects, it is important to give a brief overview of the physics underlying.

First of all, it is important to realize that the trap profile is not defined by a part of the system, as the trapped object or the trapping laser, but it is determined by the whole system. From the polarization of the light to the geometry of the trapped object, all the different parameters (refractive index, wavelength, NA of the objective, etc...) must be present in an analitic depiction of the force map. Depending on the ratio between the object size and the trapping laser wavelength, it is identified two limits: i) The *Rayleigh limit* when the radius of the microsphere is several times smaller than the laser wavelength $(\lambda >> r)$. ii) If the object is large compared with the laser wavelength $(r >> \lambda)$, the problem can be faced in the *geometric optics* (GO) limit. In any case, if the laser wavelength is comparable with the probe size the problem must be solved by the Mie's scattering.

Ashkin derives in 1992 the equation

$$\vec{Q} = \frac{\vec{F}}{n_m P/c} \tag{2.2}$$

where n_m is the refractive index of the media, P is the laser power, $\vec{F}$ the total force and c the light speed. By this derivation, it is probed that the force map is independent of the trapping laser power, without taking account the non-linear effects. This equation will be very useful for us along this thesis, see section 2.6, because allows the experimental characterization of our system for any laser power.

$\vec{Q}$ is called the *vector efficiency factor* and defines how efficiently the momentum is transferred to the microsphere. $\vec{Q}$ can be interpreted as the force map of the tweezers, it doesn't depend in the optical power, but the shape will remain constant.

Let be an arbitrary object (defined by its volume V, enclosed inside a surface S, with a distribution of charges $q(\vec{r},t)$ and currents $\vec{j}(\vec{r},t)$) in interaction with an electromagnetic wave ($\vec{E}(\vec{r},t)$, $\vec{B}(\vec{r},t)$). The *Lorentz law* ((2.3)) connects the mechanical forces acting on the object with the present em field [71].

$$\vec{F}_L(\vec{r},t) = \int_V \left[q(\vec{r},t)\vec{E}(\vec{r},t) + \vec{j}(\vec{r},t) \wedge \vec{B}(\vec{r},t)\right] dV \tag{2.3}$$

Both, the electric and the magnetic fields are the superposition of the incident and the scattered field. Then, the total change of the momenta is the sum of the change of the e-m and the mechanical momenta, $\vec{P} = \vec{P}_M + \vec{P}_{em}$.

$$\frac{d}{dt}\vec{P} = \underbrace{\vec{F}_L(\vec{r},t)}_{MECHANIC} + \underbrace{\frac{d}{dt}\int_V \epsilon_0 \vec{E}(\vec{r},t) \wedge \vec{B}(\vec{r},t) dV}_{ELECTROMAGNETIC} \tag{2.4}$$

Next step is the use of the Maxwell equations in (2.4). The Maxwell stress tensor is defined as $T_{\alpha\beta} \equiv \epsilon_0 \left[E_\alpha E_\beta + c^2 B_\alpha B_\beta - \frac{1}{2}\left(\vec{E}\vec{E} + c^2\vec{B}\vec{B}\right)\delta_{\alpha\beta}\right]$. Therefore, the change in total momenta reads as follows:

$$\frac{d}{dt}\left(\vec{P}\right)_\alpha = \int_V \sum_\beta \frac{\partial}{\partial x_\beta} T_{\alpha\beta} dV = \oint_S \sum_\beta T_{\alpha\beta} s_\beta dS \tag{2.5}$$

where $\hat{s}$ defines the normal vector to the surface. In summary, the problem is reduced to solve (2.5) under the given boundary conditions. Obviously, the study of this scheme when is particularized to an optical tweezers case is non-trivial. The characterization of the electromagnetic fields of a highly focused laser beam is a great problem to measure. One solution was proposed by Mazolli *et al* in [72], where they derived an explicit partial wave representation for the force exerted to a sphere of arbitrary radius. In figure 2.2 is shown the dependence of the stiffness with the sphere radius. κ is maximum when the radius is similar to the wavelenght.

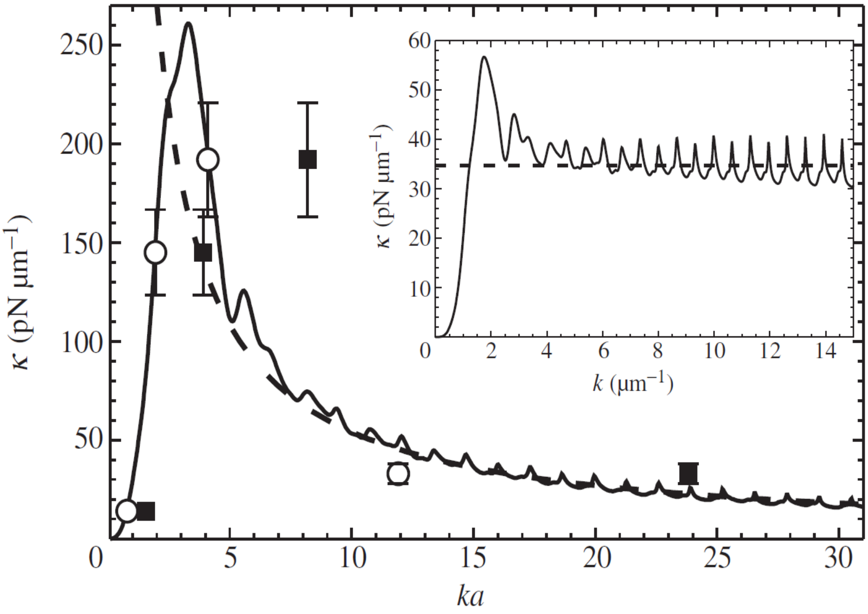

Figure 2.2: Value of the stiffness as function of the ratio between the bead's radius and the the wavelenght, by Mazolli *et al* solution. κ has a maximum value when the radius is close to the wavelength, where is not valid any aproximation. Inset figure represents κ as exclusive function of the wavelength. Notice how κ tends to a constant value in the *GO* limit. Oscillation are due to intereference effects [72]. Figure taken from [72]

As we previously commented, the OT characterization can be easily solved in two determined limits, see Fig. 2.3, the *geometrical optics* limit and the *Rayleigh limit.*

2.1.1 Optical force in the Rayleigh limit ($r \ll \lambda$)

When the probe is much smaller than the light wavelength, the electromagnetic field ($\vec{E}$) is felt uniformly by the object. Then, the particle can be consider as

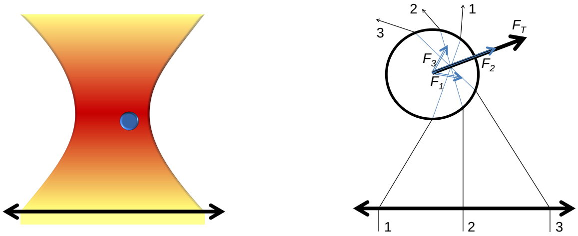

Figure 2.3: Schematic vision of the two limits. On the left we have a sphere much smaller than the wavelenght, hence, much smaller than the focus width and the Rayleigh limit is valid. On the left, the sphere is trapped under the geometrical optics interpretation.

a dipole [73]. As the electric field can be considered uniform, the problem is simplified to the interaction of a dipole with an electromagnetic wave. Under this hypothesis, the forces exerted on the sphere by the light can be decomposed in two parts. First, the radiation pressure will produce a force in propagation axis of the light. This scattering term is written as:

$$\vec{F}_{rad} = \frac{n_m \sigma}{c} \langle \vec{S} \rangle \tag{2.6}$$

where $\langle \vec{S} \rangle$ is the average of the Poynting vector and σ is the scattering cross-section of a Rayleigh sphere of radius r:

$$\sigma = \frac{8}{3}\pi (kr)^4 r^2 \left(\frac{m^2 - 1}{m^2 + 2} \right)^2 \tag{2.7}$$

where $\vec{k}$ is the wavenumber of the light ($k = 2\pi n_m/\lambda$), $m \equiv n_s/n_m$ is the ratio between the refractive index of the sample (n_s) with the refractive index of the media (n_m). On the other hand we have the force due to the gradient of electric field: the so-called *gradient force*. This effect corresponds to the Lorentz force acting on a dipole induce by ligth.

$$\vec{F}_{grad} = \frac{\alpha}{2} \vec{\nabla} \langle \vec{E}^2 \rangle \tag{2.8}$$

where α is the polarizability of the particle:

$$\alpha \equiv n_m^2 r^3 \left(\frac{m^2 - 1}{m^2 + 2} \right) \tag{2.9}$$

While the radiation force will only act in the sense of light propagation, the gradient force acts along the three axis, always in the sense defined by the light intensity gradient. Therefore, the more NA used to focus the light, the larger the gradient force will be, making possible to obtain a situation where the gradient force dominates over the radiation pressure, creating a stable equilibrium position.

2.1.2 Optical force in the geometrical optics limit ($r \gg \lambda$)

If the size of the object is much larger than the wavelength, the geometric optics is a suitable tool to study the problem. By definition, the diffraction effects are negligible. When the light changes from a medium defined by a refractive index n_m to another defined by n_s, the light will change its direction according to the Snell's law. This change in direction is due to the change in momenta between the light and the medium. In the particular case of a suspended particle, the ray will exit again, producing another momentum change.

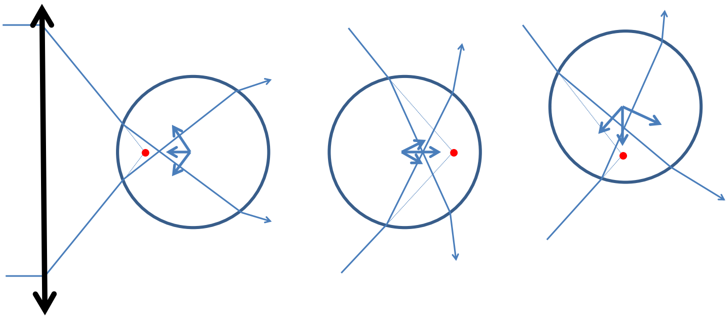

Figure 2.4: Adapted from [74]: Paths followed by two rays of the laser beam through a dielectric sphere in the *GO* limit. Each figure represents a relative position of the sphere from the focus (red point). Changes in the direction are compensated by a momentum transfer which points to the focus of the beam.

In this scenario, the beam can be interpreted as a collection of rays with different intensities. Then, the problem is reduced to a transmission-reflection scheme through a sphere. Let us suppose a single ray with power P hitting the sphere at an angle θ. The ray's associated momentum is n_mP/c. Once the ray

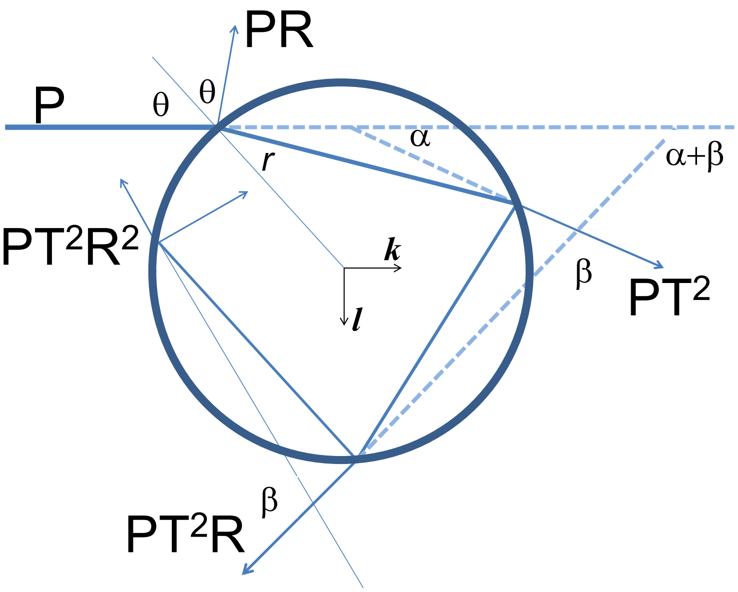

Figure 2.5: Path of a single ray across a dielectric bead in the *GO* limit. R and T represents the Fresnel coefficients for reflexion and transmition. Adapted from [74].

hits the sphere, the ray will be transmitted and reflected endlessly, see fig 2.5, and each ray will have the different Fresnel coefficients associated to its power PT^2, PT^2R, PT^2R^2, ... The associated $\vec{Q}$ factor to this particular ray will be defined as follows:

$$\begin{aligned}\vec{Q} = &\left\{1 + R\cos 2\theta - \frac{T^2\left[\sin(2\theta - 2r) + R\cos 2\theta\right]}{1 + R^2 + 2R\cos 2r}\right\}\hat{k} \\ &+ \left\{R\sin 2\theta - \frac{T^2\left[\sin(2\theta - 2r) + R\sin 2\theta\right]}{1 + R^2 + 2R\cos 2r}\right\}\hat{l}\end{aligned} \tag{2.10}$$

where r is the angle of refraction, $\hat{k}$ and $\hat{l}$ are the unitary vector parallel and perpendicular to the direction of the incident ray, and R and T are the Fresnel reflection and refraction coefficients. Both R and T depend on the polarization, thereby spreading the polarization dependence to the trapping forces. Therefore, the total force is the summation over all the rays that compose the beam. It is necessary to remark two main results in the range of validity of this limit. First, the trapping forces are independent on the size of the sphere, see Fig. 2.2 inset. Secondly, there are some ranges of NA where the trapping force decreases with the increasing NA [73].

2.2 Nanodetection

The quatification of the observation in an experiment is a key point in science. In our experiments two main variables must be known: the exerted force and the position of the sample. The search for quantitative measurements has developed several techniques to know where is our sample with an accuracy close to nanometers, in a range of time shorter than microseconds. Below, we give an overview of different tracking techniques. In this thesis, the study of the scattered ligth was the chosen option to detect the probe position [75, 76].

2.2.1 Video tracking

By the analysis of the microscope image of the particle by a commercial camera is possible to track the position of the object by different algorithms [77]. The image can be registered as a circle in the case of the microspheres whose center is tracked along time. The intensity of the pixels can be fitted to Gaussian profiles in order to increase the sensitibity of the method (up to 5 nm).

Although in this case the detection range would not be a problem and the need of a conversion between volts and nanometers is avoided, the video tracking lacks a high acquisition frequency compared as with forward scattering method. The increase of this acquisition frequency would carry on an increase in the cost of the camera.

2.2.2 Forward scattering: QPD

An auxiliar laser in the visible range is focused at the same point that the trapping laser [1]. The trapped object produces an interference pattern which is collected by a condenser objective. This interference pattern is recorded by a quadrant photodetector (QPD). A QPD is an electronic device composed by four individual cells (i) that transform the light intensity (I_i) in a value of

---

[1] A visible wavelength is chosen due to the ease of the alignement.

voltage (V_i). These four values of voltage can be directly linked to analogous values in each axis (V_x, V_y, V_z) as follows:

$$\begin{aligned} V_x &= (V_2 + V_4) - (V_1 + V_3) \\ V_y &= (V_1 + V_2) - (V_3 + V_4) \\ V_z &= V_1 + V_2 + V_3 + V_4 \end{aligned} \tag{2.11}$$

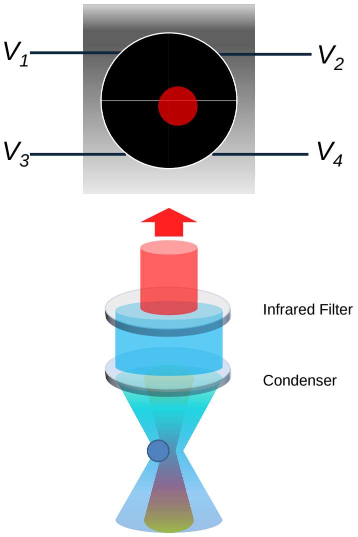

Figure 2.6: The laser peaked in the visible range is scattered by the trapped dielectric microsphere. This light is collected and collimated by a condenser objective to be projected in a *QPD*. The trapping infrared light is removed by an additional filter placed before the *QPD*. This device is divided in four independent cells which transform the incident light in four voltage signals.

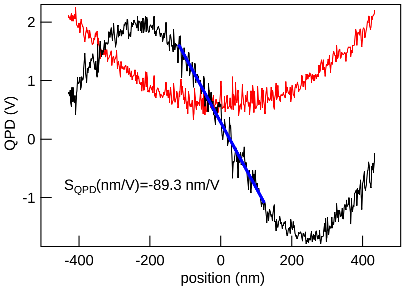

Figure 2.7: Response of the QPD to the scattered light by a 1μm diameter bead moving along the x-axis. Black line corresponds to the V_x signal, red curve to the y-axis, normal to x and to the optical axis. Notice how the linear range of V_x is some nanometers broader than the non-cross-talking range. The linear range of V_x is fitted to a straight line whose slope corresponds to the calibration factor S_{QPD}.

Within a certain range, the light intensity is proportional to the displacement, see Fig. 2.6 and Fig. 2.7, making posible to have position detection at high frequency (in our setup up to 200 kHz). A mathematical demosntration of this method is given in [78], based in Mie scattering.

Once the voltage is recorded the calibration requires the determination of two unknown quantities: the conversion factor between volts and nanometers, S_{QPD}(nm/V), and the stiffness of the system, κ.

2.3 Calibration

When the QPD method is chosen to detect the motion of our system there are two unknown quantities: the stiffness of the trap and the conversion between voltage in the QPD and nanometers. The Langevin equation (LE) is written as follow:

$$\gamma \dot{x}(t) = -\kappa x(t) + \xi(t) + F_{ext}(t) \tag{2.12}$$

where $\gamma \equiv 6\pi r\eta$ corresponds to the dissipative term (in Stoke's regime, with r the radius of the bead and η the dynamic friction coefficient of the medium) and ξ is the white force associated to the Brownian motion, defined by $\langle\xi(t)\rangle = 0$ and $\langle\xi(t)\xi(t')\rangle = \sqrt{2kT\gamma}\delta(t-t')$.

From this starting point we can use different ways to find the value of the stiffness. Below are detailed several techniques to address this determination.

2.3.1 Viscous drag method

If the external force in the LE is induced by a well known flux, within the Stoke's regime, then it can be written $F_{ext} = \gamma v$. In this situation, the trapped bead will be displaced from its initial equilibrium position a distance Δx. Neglecting the brownian effects, the force balance just depends in one unknown parameter κ:

$$\kappa = \gamma \frac{v}{\Delta x} \tag{2.13}$$

Notice that S_{QPD} has to be known *a priori*, and hence, it is an useful method when it is applied to the video tracking but not to the QPD method.

2.3.2 Time of flight method

Imagine two traps of different intensities close each other, the bead is trapped in the stiffer trap. If the stronger one is switched off, the bead will fly from one equilibrium position to the other. The Langevin equation of this system can be considered as a strongly overdamped oscillator, neglecting the brownian motion.

$$\gamma \dot{x}(t) + \kappa x(t) = 0 \tag{2.14}$$

being κ the stiffness of the weak trap. The solution of (2.14) is:

$$x(t) = x_0 \exp\left(-\frac{t}{\tau_C}\right) \tag{2.15}$$

where $\tau_C \equiv \frac{\gamma}{\kappa}$ is the correlation time. Although this method will give us immediately the value of the stiffness, we will not be able to get the conversion factor S_{QPD}.

2.3.3 Power Spectrum Density

The analysis of the Brownian motion of the trapped microsphere allows the determination of the trap stiffness. The LE evaluated in the Fourier space provides to compute the Power spectra density (PSD), which can be interpretated as the energy density along frequencies. In this particular scenario, PSD takes the shape of a Lorentzian curve:

$$PSD(f)[m^2/Hz] = \frac{kT}{2\pi^2\gamma\,(f^2+f_c^2)} \tag{2.16}$$

where the corner frequency, $f_c \equiv \frac{\kappa}{2\pi\gamma}$, can be directly fitted to obtain the value of the stiffness. The physical meaning of the Lorentzian refers to the time scale of the probe. For frequencies above the corner frequency, the microsphere does not feel the trap, behaving as a diffusing particle. The characteristic time of our system will be the correlation time $\tau_c \equiv \gamma/\kappa \equiv 2\pi/f_c$.

The PSD given by the experimental data is evaluated in V^2/Hz, if the value of A ($A \equiv kT/2\pi^2\gamma$) from the experiment (A_{exp} (V^2/Hz)) is compared with the theoretical value, whose values are well defined, it is possible to obtain a value for the conversion factor, $S_{QPD}(m/V) = \sqrt{\frac{A_{theo}}{A_{exp}}}$

$$PSD_{exp}(f)[V^2/Hz] = \frac{A_{exp}}{(f^2+f_c^2)} \tag{2.17}$$

$$f_c \equiv \frac{\kappa}{2\pi\gamma} \tag{2.18}$$

In the section 2.3.5 is given an example of calibration at three different optical power. The value of the stiffness must be proportional to this power, while the value of S_{QPD} remains constant.

2.3.4 Equipartition theorem. Boltzmann statistics

Equipartition theorem is a balance between the kinetic energy of a system and its potential energy. In the case of an overdamped system in the presence of a thermal bath, our bead's kinetic energy can be approximated as a perfect gas, having $kT/2$ energy units per degree of freedom. As the three axis are decorrelated, only one degree of freedom is considered. On the other hand, the average potential energy is assumed to behave as a perfect spring, only determined by its stiffness, κ:

$$\frac{1}{2}\kappa\left\langle x^2\right\rangle = \frac{1}{2}kT \tag{2.19}$$

where the brackets of $\langle x^2\rangle$ refers to an ensemble average. In order to measure κ accurately, a good statistics is needed, which is obtained by a long enough measurement time [2]. Another path is to solve the Fokker-Planck equation in stationary state. In this situation, the solution is the Boltzmann distribution, where the probability is related to the potential landscape and the thermal energy. As a Gaussian is expected, the shape of the distribution is only determined by its mean (null) and its dispersion, $\langle x^2 \rangle$, exactly as the equipartition theorem result.

$$\rho(x) = \frac{\exp \frac{-U(x)}{kT}}{\mathcal{Z}} \tag{2.20}$$

where Z is the partition function, $\mathcal{Z} = \int_{\Re} \exp \frac{U(x)}{kT} dx$. This is very useful tool due to the posibility of obtaining the potencial, $U(x)$, from the analysis of the trajectories. In the case of more complicated potentials, as seen in Chapter 8, we will be able to recover the potential from the trajectories, becoming of great importance. On the other hand, once the potential is known, it is posible to recover the value of the kinetic temperature, see Chapter 6.

2.3.5 Calibration example

A single microsphere (R= 0.5 μm) is optically trapped with the setup described in 2.4.3. The interference pattern is recorded by a QPD at a sampling frequency of 5kHz. Fig. 2.8 a) and b) show the trajectory for different optical powers (P_{red}=7.1 mW, P_{blue}=23.2 mW, P_{black}=81.8 mW) and their pdf, ρ(x), respectively. The different ρ(x) are fitted to Gaussian distributions as corresponds to quadratic potentials.

If the optical power is decreased, the particle will be able to explore further distances, what is reflected in a broader pdf. The PSD is also shown in the 2.8c. The stiffness can be directly extracted from the Lorenzian fits and used to obtein values of the QPD conversion factor (S_{QPD}(V/nm)). The conversion factor is obtain by two independent methods: the equipartition theorem and the PSD. Both values are compared in the next table:

Power (mW)	κ (pN/μm)	S_{PSD}(nm/V)	S_{ET}(nm/V)
7.1±0.1	11.3±0.2	98.3	99.4
23.2±0.1	29.7±0.5	95.6	97.6
81.8±0.1	139.6±0.9	89.3	99.1

---

[2] Notice how *long* or *short* is refered to the characteristic time of the system, $\tau_c = \gamma/\kappa$.

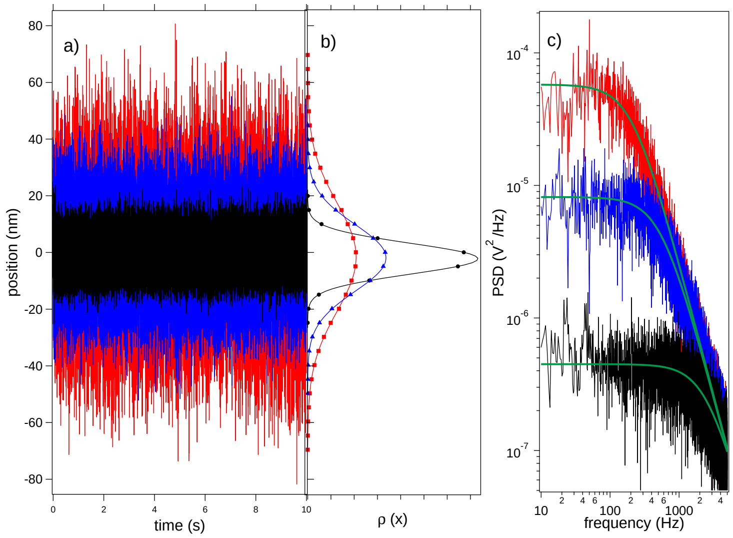

Figure 2.8: a) Trajectory, b) histogram and c) PSD of an optically trapped bead of 1μm diameter. When the optical power is increased, the corner frequency is shifted to higher values. All the PSD converge to the same curve at high frequencies, the bead will behave as a free particle for frequencies higher than f_c.

The value of the conversion factor must be conserved for any optical power as it does not depend on the trap stiffness but on the properties of the QPD and the detection laser. In this particular example, the values have a dispersion smaller than 7%.

2.4 Material and methods

2.4.1 Building potential landscapes: Acousto-optic deflector

Although the use of parabolic potential has a wide spectra of applications, there are cases where it is needed to build more complicated force scenarios. For example, the use of an optical beam with angular momentum makes possible to generate torques in the samples [61], holographic tweezers allow the use of light interference to produce the desired distribution of optical power, in order to produce, for instance, ratchet potentials [79]. In this thesis, we focus on the management of a laser beam through an acousto-optic deflector (AOD), a device that allows to displace accurately the focal plane at high velocity.

An AOD is an optical device composed by a crystal managed by an acoustic wave that can change the direction of the light that pass through the crystal. Based on the acousto-optic effect, a particular case of photoelasticity, the trapping laser can be managed by this device to move the equilibrium position of the trap with high accuracy in space (nanometric resolution) and with a fast time response (μs). In order to be able to displace the equilibrium position of the trap without changing its shape, the AOD must be placed in a plane optically conjugated to the objective.

One of the multiple options is to create multiple traps in a *time-sharing regime*. The *time-sharing regime* is based on the change of the position of the laser trap at least one order of magnitude faster than the time response of the system. In a typical experiment, a dielectric 1μm bead is trapped in water. In this situation, the relaxation time is of the order of milliseconds. Therefore, the trap can be switched on-off at 10kHz and the bead will only notice the decrease of the optical power, but the absence of trap in the *off* steps will not affect its dynamic, in other words, the $\vec{Q}$-factor will not change. At the same time, we can use the *off* steps to place this pulse in other position, where another trap will be created. In summary, by the *time sharing* technique, we can create potential landscapes as sum of different Gaussian wells with the same shape (same $\vec{Q}$) and different associated power (different stiffness). Time-sharing techniques using AODs have been described previously in [80, 81]). By a suitable ratio between the time the laser is in each position, it is possible to build traps with the desire ratio between stiffnesses. If the time spent by the laser visiting the trap A is five times longer than that in position B, the trap A will be five times stiffer than trap B. This feature will be exploted in next section, see epigraph 2.6.

This technique has been broadly explored in the field of optical tweezers [39, 46]. In this thesis, this tool has been implemented to map the optical trapping force, see section 2.6, and in the study of the energetics of the symmetry breaking, see Chapter 8.

2.4.2 Implementing external forces: Electric fields in the chamber

The application of external forces to trapped beads is a key point in this thesis. On the other hand, the experiments must be done in an enviroment where the ex-

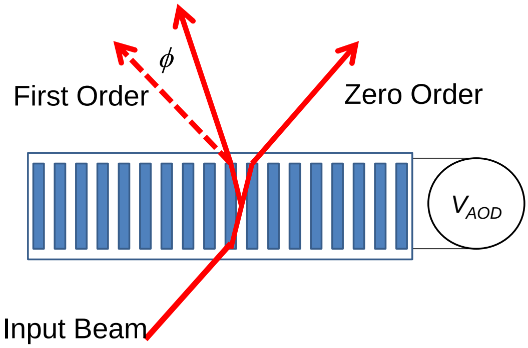

Figure 2.9: The laser beam passing through the crystal can be modulated in its direction by the aplication of an acousto-optic wave, to change the angle ϕ. The AOD wmust be in a plane conjugated to the objective to do not change the shape of the trap when the angle is changed.

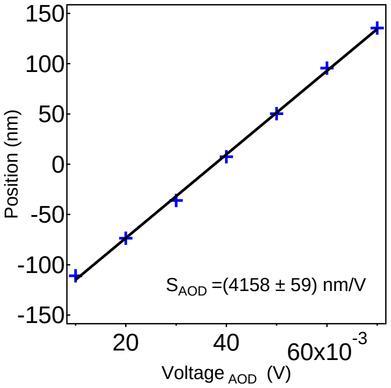

Figure 2.10: Calibration of the position of the trap as a function of the input voltage of the acousto-optic deflector. The response is linear and allows the correspondence between the position of the beam, the center of the trap, and the voltage.

ternal noise is minimized and the possible hidrodynamical flows are neglectibles. The polystyrene beads acquire surface charge when they are suspended in a polar liquid like water. Thanks to this charge, we can use an electric field to apply the desired force [82]. The chamber must be built with a desing that maximizes the force with the voltage, to obtain the higher forces with a minimal applied voltage. The chamber depiction is represented in Fig.2.11 where the working zone is the central channel, where the width is minimum. The representation is analogous to a resistance circuit where the broader zones correspond to low resistance and the central thin part has a higher resistance where most of the voltage drops. Although the electrical field is inversional proportional to the lenght of the channel, in order to obtain a higher homogenity of the field lines, the length of the channel is fixed to 5mm.

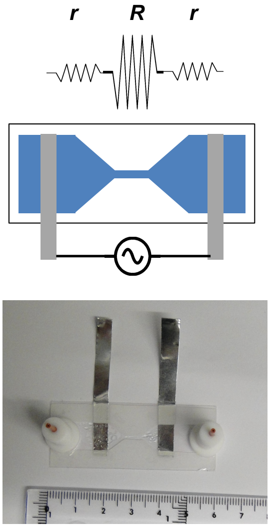

Figure 2.11: Top: Simplified representation of the electric circuit in analogy with resistances. The width of the channel is related to the resistance. Middle: Depiction of the custom-made chamber. Bottom: Photograph of the system.

The custom made fluid chamber is built by two coverslips (Deckglässer, 24×60mm). In one of them, two aluminium electrodes (CIFEC Ref. 1630 30 μm) were glued. A parafilm layer (Parafilm®P7793-1EA) was sandwiched between the two coverslips. The desired channels were drawn in the parafilm by a laser printer and melt at 85^{o}C.

It is crucial to warranty the stability of the signals along time. An easy experiment is carried out to have this certainty: A 0.5 μm radius polystyrene bead is optically trapped. A sinusoidal signal is applied to the electrodes and the position of the bead is tracked for two hours. The amplitude of the particle's oscillations is analyzed, see Fig. 2.13, and we observe that the force remains constant along the whole experiment. This fact must be enough to warranty the validity of our hipothesis.

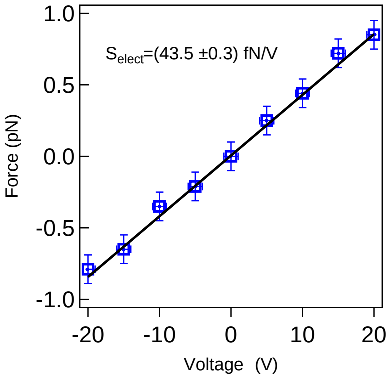

Figure 2.12: Example of electric force calibration. The force exherted in a 1 micron of diameter polystyrene bead when an external voltage is applied. The force is not only function of the voltage, but of the chamber construction. Calibration must be done for each experiment.

2.4.3 Optical setups

Along this thesis, depending on the project, different characteristics were required. Therefore, three setups were built, each one with different properties. All of them have several common points as the trapping laser, always in the infrared, or the nanodetection system is always based in the scattered light projected in a QPD, but the experiments were carried out with some differences. In the following epigraphs, we show the different optical configurations used in this thesis, detailing in which chapter they were used. Setups are exposed at increasing order of complexity.

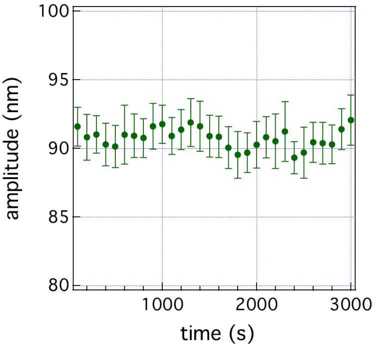

Figure 2.13: A sinusoidal signal of low frequency, 1Hz, is applied for two hours. The amplitude of the microsized sphere is recorded and analized in function of time. As the force remained constant, it is tested the validity to considerthe system as independent of time, allowing to perform experiments of long duration.

Single bacteria setup

The study of single bacteria in pure biology laboratories by the use of optical trapping is not fully implemented. Along 4, we will present a study of the motility of the Salmonella *enterica* when different proteins of its chemotaxis pathway are modified. To carry out this study, we build the simplest possible setup of optical trapping, a single laser which is used to trap the bacteria and to take quantitative measurements of its position. This setup is a perfect device to be implemented in a clasical biological lab, being able to be managed with a basic knowledgement about optics. Optical trapping was carried out using a 1064 nm (ManLight, ML10-CW-P-OEM/TKS-OTS, maximal power 3 W) optical beam from a laser coupled to a single-mode fiber (Avanex) expanded up to 10 mm and then focused by a 100× NA=1.3 objective (Nikon, CFI PL FL 100X AN 1.30 WD 0.16 mm), as shown in Fig. 2.14. The forward scattered light of the trapping beam was collected by a 40 × objective, and analyzed using a quadrant-position detector (QPD) (NewFocus 2911). The resulting signals were then transferred to a computer software via an analog to digital conversion card (National Instruments PCI-6120).

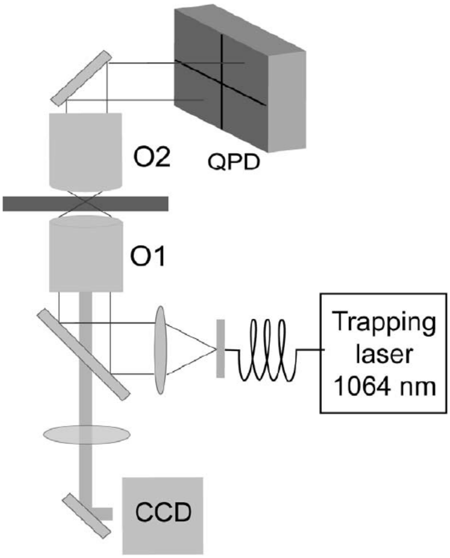

Figure 2.14: Simplest optical tweezers setup. Single laser used to trap the bacteria. Its scattered light is projected to a QPD and analyzed

Noise setup

The previously described application of external force by electric fields is implemented in this setup. To manage the optical potential, the beam is managed by an AOD, see epigraph 2.4.1.The AOD(ISOMET LS55 NIR) steers a 1060 nm optical beam from a laser coupled into a single-mode fiber (ManLight, ML10-CW-P-OEM/TKS-OTS, maximal power 3 W). The AOD modulation voltage is obtained from an arbitrary waveform generator (TaborElectronics WW1071) controlled by a LabView program. The beam deflected by the AOD, is expanded and inserted through a oil-immersed objective $O1$ (Nikon, CFI PL FL 100× NA 1.30) into a custom-made fluid chamber. An additional 532 nm optical beam from a laser coupled to a single-mode fiber (OZOptics) is collimated by a (×10, NA=0.10) microscope objective and passes through the trapping objective. The forward scattered detection beam is collected by a (×10, NA=0.10) microscope objective $O2$, and its back focal-plane field distribution is analyzed by a quadrant position detector (QPD) (New Focus 2911) at an acquisition rate of 20 kHz.

A 532 nm band pass filter in front of the QPD blocks beams with wavelengths different from the detection beam wavelength. The AOD permits the control of the position of the beam focus. AOD is also used to map the force distribution, as described in epigraph 2.4.1. The custom-made fluid chamber, see epigraph 2.4.2, was placed on a piezoelectric-controlled calibrated stage (Piezosystem-Jena, Tritor 102) allowing the 3D translation. The electrodes of the chamber were fed by a signal created in a commertial signal generator (TaborElectronics WW1071). In the particular cases where we would need a higher voltage than the given by the generator (±10V), the signal was amplified 100 times by a DC amplifier (TREK 610E).

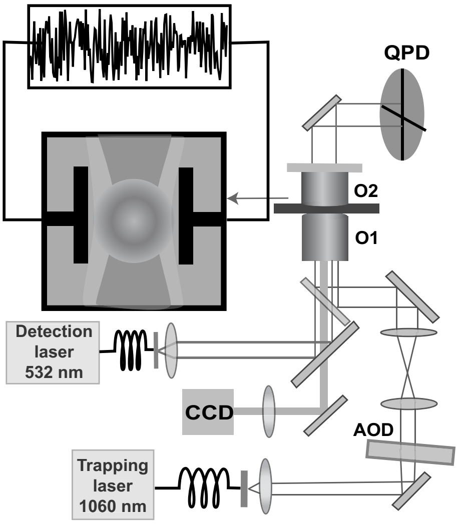

Figure 2.15: Setup with noise generator

This setup is used in Chapters 6, 7 and 8

Dual trap setup

The stretching of DNA has been studied for the last 20 years [20]. The different experiments carried out in biomolecules need high intensities of the trapping laser due to the need to achieve high forces (up to 100pN). Then, it is important to do not waste optical power to generate a dual trap, like, unfortunately in the time-sharing regime. For this purpose, in this setup we used two independent lasers which generate an individual trap each. The position of the trapped object in each trap is individually recorded. As it is described in Fig. 2.16, a 980 nm optical beam from a laser coupled in a single-mode fiber (Avanex, 1998PLM 3CN00472AG HIGH POWER 980nm), expanded up to 10 mm and then focused by a 100 × NA=1.3 objective (Nikon, CFI PL FL 100X AN 1.30 WD 0.16 mm) permitted the optical trapping. The additional trap is generated by an expanded 1060 nm optical beam from a laser coupled in a single-mode fiber (ManLight, ML10-CW-P-OEM/TKS-OTS, RMS noise less than 0.2, maximal power 3W). The position of this trap can be changed by a computer-controlled mirror. This mirror was optically conjugated with the input pupil of the trapping objective using two lenses (L_1=10cm, L_2=40cm), also responsible for the magnification of the beam.

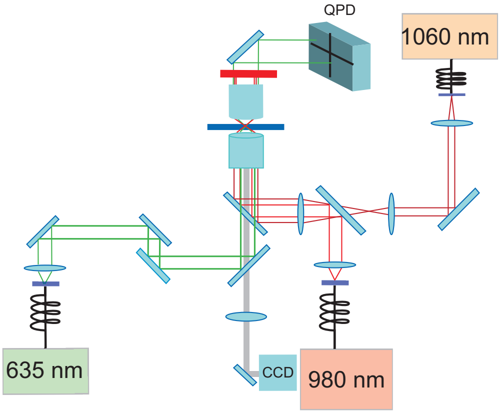

Figure 2.16: Dual trap setup

An additional 635 nm optical beam from a low-noise laser (Coherent, ultra-low noise diode laser LabLaser635, RMS noise less than 0.06 for bandwidths of 10 Hz to 10 MHz) was coaxial to the propagation direction of the trapping beam and was used as the position detection beam. The forward scattered light of the detection beam was collected by a 40 × objective, and analyzed by a position detector (Newport, 2931 position-sensitive detector). The forward scattered light of the trapping beams were blocked by a short-pass filter (Thorlabs FES0700). The resulting signals were then transferred through an analog-to-digital conversion card (National Instruments PCI-6120) to computer software. This setup is used in Chapter 3.

2.5 Breaking the limits of detection: Back-focal-plane position revisited

2.5.1 Introduction

The main problem of the nanodetection of the position with the scattered light is the limited range of linearity. In the previously presented scheme in section 2.3.3, the linear range is limited to a region 500 nm width. But there are several classes of experiments where the probe may be displaced by external forces at a distance of several micrometers from the probes initial position. Examples are an extension of a single DNA molecule [21,69,70] or amyloid fibrils [83] produced by a dual trap optical system. Other experiments make use of optical tweezers in statistical physics studying thermodynamical parameters of a colloidal particle pulled by a moving optical trap [84–86], Kramers transitions in a double-well optical potential [87–89], optical binding [90], non equilibrium steady states generated by means of a rotating laser beam [91], and artificial Brownian motors [27].

In all those cases the absolute position of the probe is a relevant measure together with the relative probe position in the trap focus. At a fixed position of the QPD the displacement of the probe by moving of the trap or by an external force produces a unique and linear QPD response only in a restricted region of the probe displacement, usually several hundreds nanometers. However, for example, in experiments with a colloidal particle pulled by a moving trap, the displacement of the probe must occur for distances of several micrometers, and the traditional back focal plane (BFP) scheme cannot provide the absolute value of the probe position. Hence, other techniques have to be used in such experiments, such as methods of digital video microscopy [92]. An automated optical force clamp [93] in which both the trap position (via acousto-optic deflectors) and the sample position (using a three-dimensional piezo stage) are controlled by a computer program is a fruitful approach for single molecule studies when high temporal resolution is not required. During motor-driven movement, both the trap and the stage are moved dynamically to apply a constant force while keeping the trapped probe within the calibrated (and linear) range of the detector.

Along this section, we will show how to change the traditional BFP detection system with QPD to extend the linear range of the QPD response; that is, to measure with the same high speed detection system both the probe absolute position and the probe relative position in the trap for probe displacements up to several micrometers. Multi-pixel detectors (i.e. CMOS or CCD sensors) to monitor particle positions are equally precise as quadrant diodes in position resolution, and they are linear up to much larger displacements. However, the proposed scheme with quadrant diodes is a more simple solution capable to provide a high frequency data acquisition rate, which is important specially for statistical physics applications of PFM.

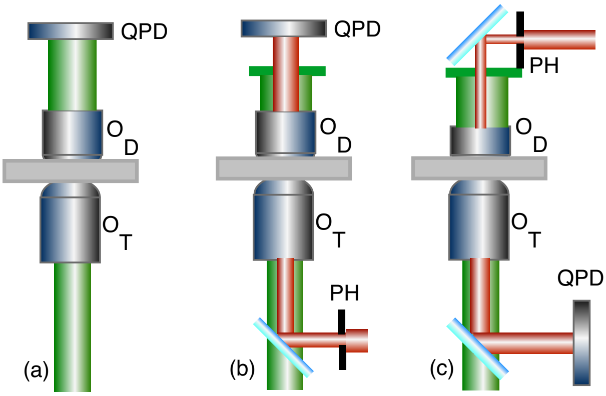

Figure 2.17: Schematic of the back-focal-plane position detection system: (a) the trapping beam introduced by a trapping objective O_T is also used to detect the probe position, (b) an additional beam of other wavelength (or polarization) introduced through the trapping objective O_T is the detection beam. In both schemes the condenser objective O_D collimates the detection beam before sending it to the QPD. In (c) the detection beam is introduced by the objective O_D. By choosing the NA of O_D and the size of a pinhole PH one may tune the size of the detection spot in the focal plane of O_T.

2.5.2 Methods

The two critical parameters of the position detection system are the displacement sensitivity and the linear response range. Both are functions of the intensity distribution that reaches the detector and therefore depend on the sizes of the focal beam and the probe, as well as the numerical apertures of the trapping and collimating objectives.

According to the models of one-dimensional displacement of a spherical scatterer in the objective's focal plane developed in [75, 76, 94–96] for both Rayleigh scatterers and Mie scatterers, an expansion of the detection spot extends the linear range of detection but reduces the position sensitivity.

We consider the restrictions imposed on the BFP position detection system when it is explored in a specific experiment as optical tweezers. In the detection scheme usually used for optical tweezers (Fig.2.17a), the parameters of the beam waist in the focal plane are set to provide the gradient optical force in the axial direction sufficient to overcome the scattering force [80]. As it is well known this condition is achieved by using high numerical aperture objectives.

We estimate the beam waist w_0 by the strong focusing condition required for the optical trapping. The field distribution near the focal plane of a linearly polarized Gaussian beam focused by an aplanatic lens with numerical aperture NA and focal distance f is described by an integral representation for the electromagnetic fields [97]. In Fig.2.18a and Fig.2.18b we illustrate the intensity distribution in the focal plane of the lenses with different apertures NA and sizes of circular aperture R on the objective's input pupil. Let us consider the usual configurations shown in Fig.2.17a. As we mentioned above, the trapping objectives have high NA (NA>1.0) by definition. The maximal focal beam waist is $0.18\,\mu m$ obtained without the aperture (Fig. 2.18a. Following [75, 76, 96] it gives the linear range of the position detection about several hundreds nanometers. The incident beam clipping cannot be useful in this case because it reduces the axial gradient trapping force and therefore the optical trapping becomes impossible.

A possible solution may be the configuration shown in Fig.2.17b. An additional weak beam of a different wavelength or polarization is used for the position detection and the optical systems for the trapping and detection beams are uncoupled. The expansion of the detection focal spot by reducing the incident beam width by the pinhole (compare the curves (1) and (2) in Fig.2.18a may increase the linear range without affecting the trapping force. In this configuration the detection beam must also propagate through the high NA trapping objective. Small focal distances of such objectives do not allow for considerable expansion of the linear range even with the input detection beam clipping. The apertures smaller than $500\,\mu m$ can theoretically expand the focal spot of the detection beam. However in experiments configured according to Fig.2.17b there is always a distance of several centimeters between the aperture and the input objective pupil. Diffraction effects at small apertures do not allow the beam width at the objective input to remain the same as the aperture size.

We suggest to change the role of the condenser objective O_D: in all previous

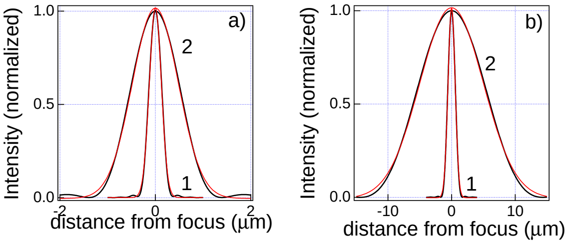

Figure 2.18: Normalized electric field intensity in the focal plane vs. distance from the focus calculated for the objectives with $NA = 1.3$ (focal distance $f = 2.7\,mm$ (a) and $NA = 0.1$ (focal distance $f = 28.9\,mm$) (b). In both cases the input Gaussian beam has the waist $0.5\,cm$. The results are shown for two radius of the aperture $0.5\,cm$ (1) and $0.05\,cm$ (2). The Gaussian fitting of the numerically obtained results gives $w_0 = 0.18\,\mu m$ (curve 1) and $w_0 = 0.68\,\mu m$ (curve 2) for the objective with $NA = 1.3$ and $w_0 = 0.78\,\mu m$ (curve 1) and $w_0 = 7.05\,\mu m$ (curve 2) for the objective with $NA = 0.1$. The values of the focal distances are taken from www.edmundsoptics.com. The wavelength in vacuum is $0.63\,\mu m$.

experimental setups this objective has been used only to collimate the detection beam. In our scheme (Fig.2.17c) we introduce the detection beam through the objective O_D. Unlike the conventional detection schemes (Fig. 2.17a and Fig. 2.17b), NA of O_D may be chosen at will since it does not affect the trapping force. Then the combination of such a low NA objective together with a tunable pinhole permits us to create in the trapping objective's focal plane the detection spot of a variable size defined by the full width of the incident detection beam and NA of O_D. As shown in Fig. 2.18b the beam waist w_0=7 μ m may be achieved with the aperture of 0.05 cm. An additional experimental advantage of this configuration is that the aperture may be located in the vicinity of the input pupil of O_D.

2.5.3 Experimental setup

The experimental setup includes the following principal parts (Fig.2.19). A 1060 nm optical beam from a laser coupled into a single-mode fiber (ManLight, ML10-CW-P-OEM/TKS-OTS, maximal power 3 W) is steerable by an acousto-optical deflector/modulator (AOM/D) (ISOMET LS55 NIR). The AOM/D input voltage is controlled by an arbitrary waveform generator (Tabor Electronics, WW 5062). After the AOM/D the beam is extended and inserted through a ×100 NA=1.3 objective (Nikon, CFI PL FL 100X NA 1.30) into a home-made fluid chamber permitting the steerable optical trapping of polystyrene spheres of various sizes. The output plane of AOM/D is optically conjugated to the objective input pupil. An additional 635 nm optical beam from a low-noise laser (Coherent, ultra-low noise diode laser LabLaser635, RMS noise less than 0.06 for bandwidths of 10 Hz to 10 MHz) is coupled first into a mono mode fiber to improve its spatial distribution. Then the output beam of the fiber is collimated by a ×10 NA=0.10 microscope objective (EdmundsOptics) and passes through an iris pinhole. A NA=0.1 objective (EdmundsOptics) focuses the beam at the trapping objective«s focal plane. The forward scattered detection beam is collected by the trapping objective, and the BFP field distribution is analyzed by a QPD (New Focus 2911). A 635 nm band pass filter in the front of the QPD blocks beams with wavelengths different from the detection beam wavelength. The QPD output signals are being transferred through an analog-to-digital conversion card (National Instruments PCI-6120) to computer software. A CCD camera permits to observe images of the probe in the focal plane of the trapping objective.

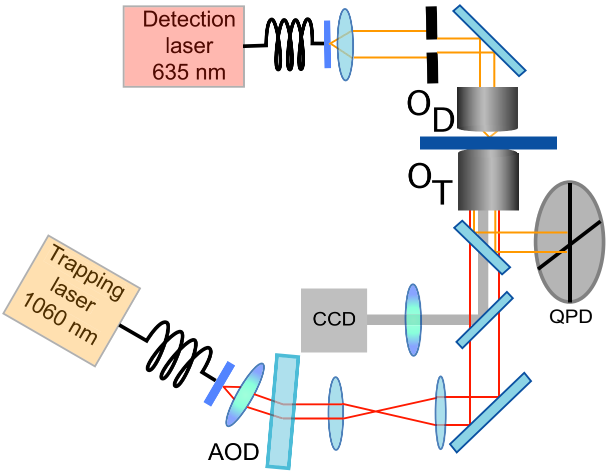

Figure 2.19: Experimental setup.

2.5.4 Results

To calibrate the position detector, i.e., to obtain a conversion factor between the probe displacements and QPD output signals we used a standard optical tweezers calibration technique based on the probe position fluctuation spectrum [98]. At a given position of the trapped probe (polystyrene spheres of 1 and 2 μm in diameter) inside the detection spot the probe«s Brownian fluctuations were acquired and their power spectral density are being fitted to the Lorentzian curve [80]. The fitting parameters gave the stiffness of the trap and the conversion factor mentioned above.

Afterwards, we calibrated the deflector. We trapped the probe and steered it applying triangle signals of different amplitudes with a frequency of 0.7 Hz to the acousto-optical deflector. For small amplitudes (less than $0.02\,V$ for our AOD/M) of the triangle signal such that the probe displacements do not exceed 100 nm we measured a ratio between the amplitude of the modulation signal and the probe displacement using the calibration factor obtained from the Brownian fluctuations analysis. We then confirmed with an image analysis that the same ratio remains for the modulation amplitudes ±2 V corresponding to probe displacements ± 3μm. To do this, with the CCD camera we captured images of the trapped probe for different amplitudes of the modulation signal. Then knowing the size of the probe we calculated the displacement of the probe in nm for a given value of the modulation signal.

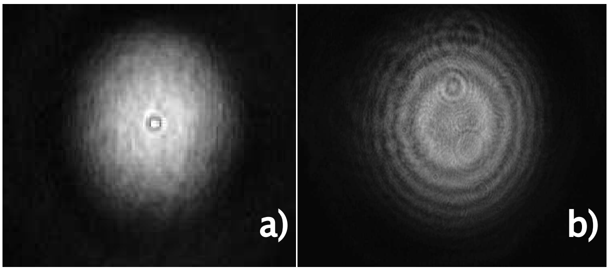

Figure 2.20: (a) 2 μ m sphere trapped inside the spot of the detection beam in the focal plane of the trapping objective. (b) Interference rings observed at the plane of the QPD.

Figure 2.20a demonstrates that the trapped sphere size is much smaller than the detection beam diameter. When the sphere is displaced, the interference rings at the trapping objective BFP (Fig. 2.20b) shift within the detection

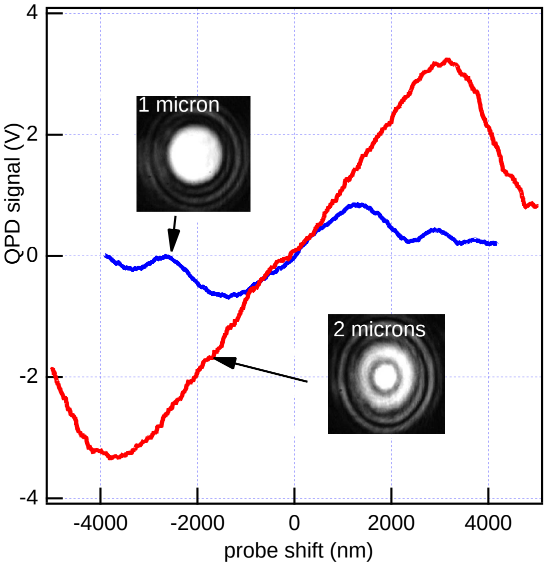

Figure 2.21: Position detectors output signal (the probe diameter is 1 μm, blue line, and 2μm, red line) as a function of probe displacement shows a nonlinear character when the probe displacement exceeds the size of the detection spot 8 μm. However, at probe shifts less than ±1500nm (the 1μm probe diameter) there is a linear dependence between the QPD output and the probe position. The minor deviations from the linear dependence in the linear part of the QPD response are due to the non uniformity in the detection beam intensity as well as Brownian fluctuations of the probe position. For the probe with diameter 2μm the linear range is ±3500 nm. The insets show the images of the interference rings of the detection beam observed at the plane of the QPD for the 1μm and 2μm probes.

beam; however no shift of the whole detection beam is observed.

Figure 2.21 shows the position detector response vs. absolute position of the probe for a 1μm probe. As seen the linear detection range was achieved within ±1500 nm displacement. The nonlinear behavior of the output signal at higher displacements is due to at least two reasons. First, the probe moves out of the detection spot. Second, the interference fringes of the forward scattering detection spot are limited by the trapping objective pupil. Notice also that at low modulation frequency of the experiment the Brownian fluctuations of the probe position are observed on the output signal traces.

Figure 2.21 demonstrates results obtained with a 2 μm probe when the diameter of the detection spot is extended even more than in 1μm case shown in the same figure. As seen, the linear range is in this case ±3500 nm.

When the probe shifts achieve the nonlinear range of the position detector signals an unavoidable cross-talk between QPD output signals occurs. In [99] this cross-talk was used to extend the linear range of the position detection system in the conventional geometry Fig.2.17a) up to one micrometer. Unlike our technique, this method requires calculations of a special calibration curve that makes the data processing more computationally expensive and slow. Moreover it does not in principle achieve the linear range extension up to several micrometers since the calibration curve can not be calculated for such large shifts. Our technique yields the probe position directly without any additional processing of the QPD data. Also at each given position of the probe its Brownian fluctuations may be acquired with the acquisition rate, which is defined only by the QPD electronic properties.

2.5.5 Conclusions

The proposed technique is simple, but has several shortcomings. The displacement sensitivity is less than the one in the traditional scheme. In fact, in the model of Rayleigh scattering, for example, the sensitivity decreases with the detection beam size as w_0^{-3} [75,76]. We noticed also that the instrumental noise of the optical setup affects the electronic output signals strongly than in the conventional scheme.

2.6 What is beyond the parabolic regime? Mapping the force of the whole trap

2.6.1 Introduction

One of the greatest characteristics of the optical trapping technique is the analogy of its restoring force with a perfect spring. The force can be considered to linear depend to the distance to the equilibrium position and it will be characterized by a single parameter, namely its stiffness. However, as previous experiments have demonstrated, the optical restoring force is linear with the probe displacement only within a restricted range, usually several hundreds of nanometers. In other words, the optical trapping potential (OTP) is harmonic only for this range of displacements. There are several experiments where the probe may be displaced by external forces at a distance of several micrometers from the probe's initial position. The probe exhibits larger excursions away from the trap center and the harmonic approximation for OTP is no longer valid. An example is an extension of a single DNA molecule [69] produced by a dual trap optical system. Other experiments make use of optical tweezers in statistical physics by studying thermodynamical parameters of a colloidal particle pulled by a moving optical trap [84, 85], Kramers transitions in a double-well optical potential [88], optical binding [90] or non equilibrium steady states generated by means of a rotating optical beam [91]. The map of the trap stiffness is a required part of the calculations of thermodynamic parameters as work and entropy when the probe is pulled by the trap [39]. In these cases the restoring force for arbitrary distances of the probe from the trap center should be measured. For a given distribution of the optical beam intensity near the focus, the OTP varies due to the size of the probe, its refractive index or absorption, and in situ OTP mapping methods that are not restricted to harmonic potentials are required.

The OTP is a complex function of the input beam field distribution, power at the objective focus, beam waist, properties of the focusing objective, and the design of a fluid chamber for optical trapping experiments, as it defines the optical system's astigmatism. The absolute calibration of the optical trapping systems can be done [100], but it is individual for each system and not straightforward. Changes of any element in the previously characterized trap system require a new calibration procedure. Calculations of the trapping force using known algorithms are possible. However, the results are affected by many parameters that are difficult to measure with high accuracy. For example, experimental results in [101] had to be linearly scaled by a factor of 4.0 to fit the calculated values due to uncertainties in some of parameters, such as an infrared transmission of the microscope objective and an actual input optical beam profile.

Several methods to characterize qualitatively the OTP on its entire range have been suggested: a time of flight method, where the motion of the probe after a sudden trap displacement is analyzed [102–105]; a drag force technique, where the position of the trapped probe is studied by gradually increased known drag force [106–108].

In [109] a dual-beam optical trapping system was proposed. A strong, stationary, and previously calibrated trap holds the probe (see Fig.2.22). Its OTP is deep enough and external forces can not displace the probe out the range of the harmonic approximation. The intensity of a trap whose OTP has to be analyzed is adjusted such that its optical force acts as a perturbation exerting on the probe a variable force while scanning near the strong trap. Later this technique was modified and improved considerably in [101, 110].

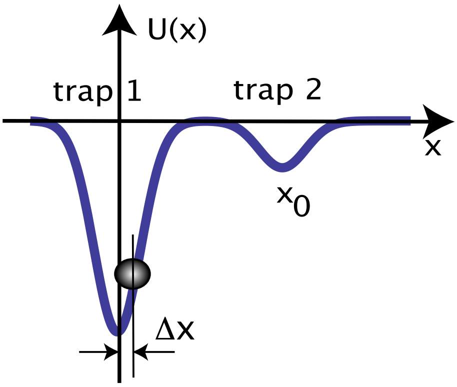

Figure 2.22: A strong trap (1) holds the probe while the trapping force of a weak trap (2) at a distance x_0 shifts the position of the probe to Δx. The stiffness of the trap 1 is strong enough such that Δx does not reach the limit of the harmonic approximation of its OTP. Therefore the force exerted by the trap 1 is equal to the stiffness of the trap 2 multiplied by Δx.

Our approach based on this dual-beam OTP mapping technique. The main goal is to find a simple technical realization of this method based on the belief that up-to-date optical traps both in their laboratory and commercial variants include an acousto-optical deflector (AOD). This procedure can be used in already existing optical trapping systems with its minimal possible changes when only a new control protocol of AOD is required.

2.6.2 Methods

The two traps are created with the same laser, hence, the optical path is identically, also the wavelength and the trapped sphere. The only difference between the two traps would be the power, that as it was detailed in section 2.1 is separable from the $\vec{Q}$-factor of the trap. Then, it is reasonable to start from the hipothesis of any trap created with the given setup will have the same setup varying just in a multiply-factor. Once we admit it, the power ratio between one trap and the other can be enough to warranty the bead will always stay inside the parabolic regime of the strongest trap. The strongest trap can be easily calibrated with its stiffness, being possible to know what is the force exerted in each displacement (Δx)

The dual-beam technique requires two optical traps with different stiffness. Acousto-optic deflectors are one of the most frequently used devices for generation of multiple optical traps. The individual traps are not generated simultaneously but a single optical beam is rapidly switched between a number of optical focuses by changing the frequency of acoustic waves propagating in the AOD. Multiple optical traps are possible as long as the focused beam is returned to the same location faster than the time it takes for the probe to diffuse away from that location, typically on the order of tens of milliseconds. The time sharing regime of AOD has the greatest additional flexibility because it allows independent control of both the positions of two optical traps (changing the frequency of acoustic waves) and their stiffnesses. In fact, since the probe observes an average intensity, the trapping force at each location may be changed by a proper choice of the timing ratio between two frequency components at the AOD input.

Figure 2.23 illustrates how a dual trap with controllable distances between the traps and ratios between their stiffnesses may be produced with an AOD, an analogue RF driver, and a generator of modulation signals. The alternation of trap positions is controlled by timing signals generated by a modulation generator adjusted to give a low frequency square wave with a controllable duty ratio. The analogue voltage is transferred to the modulation input of a RF driver. The drivers' RF output is then transferred to the AOD. The relative optical intensity in each trap depends on the duty ratio of the modulation signal, and the distance between the traps is defined by the amplitude of the square wave. In order to provide an additional flexibility to the optical trapping system a DC modulation signal was added to the square modulation wave. It permits to shift the positions of both traps simultaneously. We used this signal by a calibration of the traps as it is described below.

2.6.3 Experimental realization

The optical setup used in this epigraph is the same that was described in section 2.4.3, although, by the definition of the technique, it can be done in any optical tweezers setup whose optical trapping beam is managed by an AOD. Briefly, in this particular case, a 1060 nm optical beam from a laser coupled into a single-mode fiber (ManLight, ML10-CW-P-OEM/TKS-OTS, maximal power 3

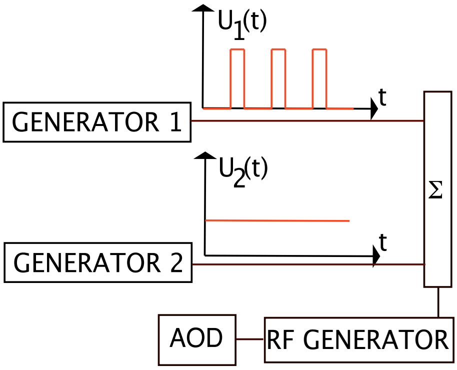

Figure 2.23: Protocol of the time sharing regime. Signals of a modulation generator 1 $U_1(t)$ modulate the frequency of a RF generator in such a way that two traps with a controllable distance between the traps and a ratio of the trap's stiffnesses are created in the focal plane of the trapping objective. When the amplitude of the square signal varies, the position of one of the trap remains fixed while the position of the other trap shifts. As seen, the duty cycle of the square wave provides the higher stiffness of the fixed trap comparing with the stiffness of the movable trap. Signals of a modulation generator 2 $U_2(t)$ change the positions of both traps simultaneously.

W) was steerable by an acousto-optical deflector/modulator (AOM/D ISOMET LS55 NIR). The input modulation voltage (Fig.2.23) that controlled a RF generator of the AOM/D is generated by an arbitrary waveform generator (Tabor Electronics, WW 5062) managed by a custom-made LabView program. Two lenses L_1 and L_2 expanded the trapping beam up to 8 mm in diameter and conjugated the AOD output plane with the input pupil plane of the trapping objective. The extended beam was inserted through a ×100 $NA = 1.3$ objective (Nikon, CFI PL FL 100X NA 1.30) into a home-made fluid chamber permitting the steerable optical trapping of polystyrene spheres of various sizes. The maximal separation between the fixed and the movable traps was 3μm.

A CCD camera provided images of the trapped probe. An additional 532 nm optical beam from a laser coupled to a mono-mode fiber was collimated by a ×10 NA=0.10 microscope objective (EdmundsOptics) and propagated coaxially with the trapping beam through the trapping objective. The forward scattered detection beam was collected by a ×10 NA=0.40 microscope objective (EdmundsOptics), and the back-focal-plane field distribution is analyzed by a quadrant position detector (QPD) (New Focus 2911). A 532 nm band pass filter in front of the QPD blocks beams with wavelengths different from the detection beam wavelength. The QPD output signals are being transferred through an analog-to-digital conversion card (National Instruments PCI-6120) to computer software. These signals provided information of the coordinates of the trapped probe. The data acquisition rate was 20 kHz. The detection beam permits the calibration of the optical traps and the detection system using Brownian fluctuations analysis [80]. The analysis is based on determining the power spectrum of the position of a trapped object. For a particle bound in a harmonic potential the power spectrum for position is a Lorentzian. The trap stiffness and the calibration factor S_{QPD} between the momentary position of the probe (in nm) and the amplitude of the QPD output (in V) may be determined by fitting the spectrum to a Lorentzian. Polystyrene beads of 1μm and 2μm in diameter (Keiser) were used in experiments. The duty ratio used in this work was 5:1. The frequency of the square modulation wave was 20kHz and therefore the focused beam is switched between two locations faster than the time it takes for the probe to diffuse away from the locations (around 8 milliseconds in our experiments).

The system needs two calibration procedures. First at a given whole intensity of the trapping beam measured before the AOD we varied the modulation signal U_2 (Fig.2.23) and moved the position of the fixed trap with a trapped probe to the detection beam spot. Using data on the probe's position obtained from the QPD during 20 s we calculated the stiffness of the fixed trap and the calibration factor S_{QPD} as it was described above 2.3.3. The calibration factor was S_{QPD}= 1050 nm/V_{QPD}.

Secondly, the AOD must be also calibrated. In this case, the calibration is done following the protocole described in 2.4.1. In this particular setup, S_{AOD}=2800 nm/V. We then confirmed by an image analysis that the same ratio remains for the modulation amplitudes up to U_1=±3 V. To do this, we captured images of the trapped probe with the CCD camera for different amplitudes of the modulation signal U_1. Then knowing the size of the probe as a scale we calculated the displacement of the probe in nm for a given value of U_1. The image analysis agrees with the previous calibration.

To chose the ratio of the intensities of two traps we used the following considerations. We knew from previous publications [106, 110] that the trap stiffness has a constant value only in the range of ±200 nm near the trap center. Therefore the excursions of the probe in the strong trap due to the force exerted by the weak trap should not exceed 200 nm in order to use the constant value of the stiffness found from the thermal fluctuations analysis. We found that with the stiffness of the strong trap larger than 20 pN/μm and by the duty cycle of the square modulation signal 5 : 1 this condition is satisfied.

After the calibration procedure we trapped the probe by the strong trap with the movable trap being at the distance of several μm from the fixed trap, and moved the fixed trap to the position of the detection beam spot changing U_2. Then the movable trap was displaced to the direction of the fixed trap and for each position of the movable trap a new position of the trapped probe was measured. Multiplying it by the stiffness of the fixed trap we found the force that the movable trap exerts on the probe at a given distance between the probe and the movable trap centre.

2.6.4 Results

Below we present examples of application of the technique. Fig. 2.24 a) shows the radial force component $F(r)$ exerted on the spheres of two diameters, and the trap stiffness, $\kappa(r) = -dF(r)/dr$ (Fig. 2.24 b)) obtained by numerical differentiation of the force. In both experiments the intensity of the movable trap was equal. As seen a non-monothonic behavior of the trap stiffness near $r = 0$ for 2μm spheres is observed as it was previously demonsrated in [104, 106, 110]. The maximal value force changes slightly with the probe's diameter but the coordinate of the maximal force changes strongly and it corresponds approximately to the probe's diameter.

Figure 2.25 demonstrates the OTP obtained from the experimental dependence $F(r)$ following the formula

$$U(r) = -\int_{-1}^{r} F(r')dr' \tag{2.21}$$

The depth of OTP characterizes experimentally the free energy of the system.

As seen in Fig. 2.24 b), which is, in fact, the second derivative of $U(r)$, for 1 μm sphere the OTP may be considered as a harmonic only at a short range of distances. For 2 μm spheres the harmonic approximation is valid even in a shorter range.

In [111] the depth of the OTP in the axial direction for a 0.216 μm sphere was obtained to be $0.12\,10^{-18}J$ with similar beam power. Keeping in mind that in the axial direction the trapping force is usually several times lower than in the radial direction and that the stiffness grows with the probe size in the range between hundreds of nanometer to micrometer (Figure 5 from [72]), our results

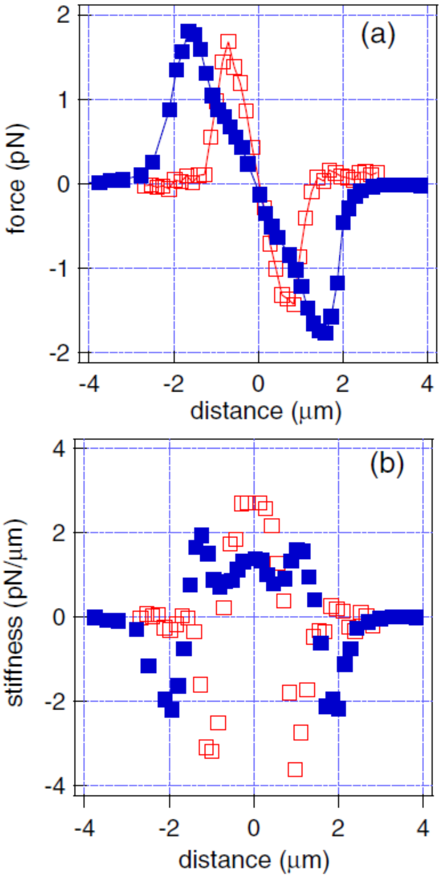

Figure 2.24: (a) Force exerted on 1 μm (red open squares) and 2μm (blue squares) spheres vs. radial distance. (b) trap stiffness vs. radial distance. The optical trap has a beam power of 3 mW. We confirmed that the force map is not affected by further increase of the strong trap stiffness by keeping the same intensity of the weak trap.

are in agreement with previous observations. Also in [105] a similar OTP depth was observed experimentally and supported by numerical simulations. However a comparison with our measurements is difficult due to the absence of data on the

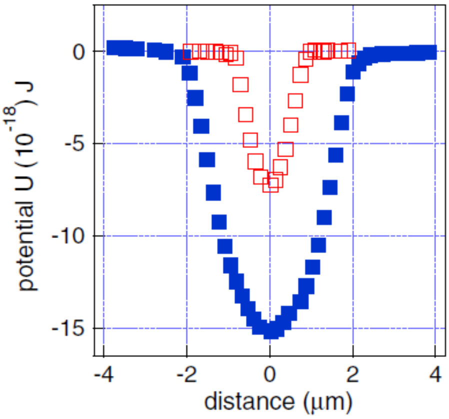

Figure 2.25: Optical trapping potentials for 1μm (red open squares) and 2μm (blue squares) spheres.

optical power. We also compare our measurements with results obtained in [110]. Fitting the force profile shown in Fig. 2 c) in [110] to $F(r) = -are^{-(r/d)^2}$, where a and d are the fitting parameters, and then integrating this force we obtained the potential depth value $(25 \times 10^{-18} J)$ comparable with our results. An indirect evidence of the OTP depth is the escape time from the potential well that in our case was so long that its measurement could not be performed. In an overdamped system, the escape time from a potential well of depth U is given by $\tau = \tau_0 e^{U/k_B T}$ where $\tau_0 = \gamma/\kappa$ [112]. Using parameters of our experiments it is possible to show that the probability for the probe to escape from the trap is very low.

2.6.5 Conclusions

In conclusion, we suggest a simple protocol for the force mapping of the optical trap in an optical tweezers setup that already include an AOD. The application of this protocol does not require new elements in the existing optical system. The same protocol may be applied also if high-speed galvo mirrors are used as the trapping beam deflectors.

3

Colored noise in the fluctuations of a single DNA molecule

3.1 Introduction

Deoxyribonucleic acid (DNA) is the basis of life as we know it. It is a biopolymer that contains all the genetic information needed in the cellular processes, being found in all living cells. One of the most prevalent forms of DNA is a linear double-stranded DNA. The double helix provides both bending and twisting rigidity, making linear DNA a semi-flexible, charged polymer chain. Like any polymer in solution, DNA forms a random conformation that maximizes its entropy. The process of stretching a single DNA molecule reduces the number of accesible microstates that is compensated by the so-called entropic force. The understanding of the response of DNA to external forces is of a key importance because nuclear processes, such as transcription, replication and translation, needs the loss of the quaternary structure. The entropic force, which governs the mechanical flexibility of DNA, plays a key role in all its cellular functions and its experimental characterization is being actively developed [20]. A double strand DNA molecule in solution bends and curves locally. Such fluctuations shorten the molecule's end-to-end distance, even against the applied force. The elastic behavior of DNA is thus, purely entropic in origin. The entropic elasticity has been explored in the range from 0.01 to 10 pN [113]. As the DNA extension reaches its B-form contour length, the force required to stretch it increases rapidly, because the double helix is straightened out and resists further increase in length. This regime is called the enthalpic regime. At extension force of 65 pN, very little additional force is required to increase the DNA length to 1.7 times its contour length. This is so called overstretching regime [114], [69].

The dynamics of extended polymers is not fully understood and is in principle of great interest. The dynamics of a single DNA molecule has been studied earlier for partially extended states. It was shown that the internal modes of a DNA extended up to 80% are related by a power law decreasing its intensity with the mode number [21], [22]. Internal hydrodynamic effects should raise the polymer friction coefficient as the molecule extends, causing the sequential increase of the polymer relaxation time [23], [24]. Extended DNA molecules are characterized by two different sets of relaxation times and spring constants (longitudinal and transverse), and the dynamics at high extensions points to yet unexplained nonlinear behavior [25]. Particularly, the correlation functions have super-exponential relaxation that may indicate the presence of new physical effects.

Random conformations that a DNA molecule form in solutions occur in the presence of the thermal noise with white spectrum of the forces, but also an important role is played by out-of-equilibrium mechanical activity. These mechanical effects are directly related to biochemical reactions in the long polymer chain. The power spectrum of such force fluctuations is defined by processes that are different from the thermal noise and therefore may depend on frequency of the fluctuations (*colored noise*). Recent detailed studies on the sources of fluctuations in some biological systems, in particular in bio-molecular motors [48], offer strong experimental indications that the noise signals in these systems include also the non-white component with frequency-dependent power spectrum. The effect of colored noise is not restricted to destructive and thermodynamic effects [49], but also may affect mechanical processes in biochemistry [50].

Force studies of single DNA molecules using single molecule force spectroscopy brought new insight in to various DNA biological functions [20, 21, 51, 52]. Questions still remain about the force spectrum of conformation fluctuations of DNA chemical structure in the low force regime where entropy is a driving factor. The DNA molecule acts as a platform for a host of critical biological functions such as transcription, replication, and other molecular motor driven processes. During these processes, the DNA strand undergoes numerous mechanical entropic unfolding and extension events that are primarily supported by the polymer-like phosphate backbone, thus making it critical to have a full understanding of how the DNA structure responds to forces.

The aim of this work is to study experimentally the spectra of fluctuations of a single thermally excited DNA molecule in different states of extension in the regime of entropic elasticity. We explore well-known experimental schemes: the molecule is anchored between two optically trapped dielectric beads, or between an optically trapped bead and a surface (cover slip or pipette) [52, 69, 70, 115]. The time traces of the bead position are analyzed under a varied load applied to the molecule. In this work, the power spectral densities (PSD) of the bead fluctuations for different extensions of the molecule were compared with the power spectral density for the same bead without the molecule attached. Finally, we subtracted the spectrum of thermally excited fluctuations of the molecule. To the best of our knowledge we demonstrated experimentally for the first time that in the regime of entropic elasticity the random fluctuations of the extended DNA molecule include also the contribution with frequency-dependent power spectrum.

3.2 Methods

The main parts of the experimental setup are explained in previous section 2.4.3. Briefly, a dielectric bead with a DNA molecule attached to it is chemically connected to the surface of a movable cover slip. Another bead connected to the opposite end of the DNA is trapped by a focused optical beam (980nm). An additional optical beam (635 nm) is coaxial to the propagation direction of the trapping beam. Its forward scattering intensity is characterized with a pinhole and a quadrant position detector in order to measure the bead position and calibrate the optical trap, see section 2.3.3. The PSD of the bead position is calculated for different distances between the center of the optical trap and the center of the bead connected to the cover slip. Unlike previous publications, the optical trap's stiffness is kept similar to the DNA stiffness such that the fluctuations of the molecule became significant and are not hidden by the instrumental noise.

In a second experiment we changed the experimental setup, and we used two optical traps to extend the molecule (see below inset in Fig. 3.7). The goal was to find how an additional isolation of the studied system from the instrumental noise and changes of the detection trap's stiffness (approximately 7 times) affect the spectrum of the measured fluctuations. Here, we introduced in the optical

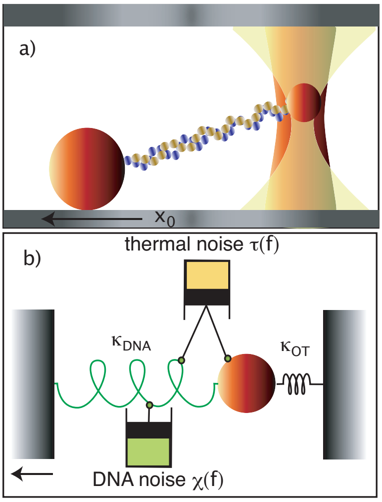

Figure 3.1: a) A single DNA molecule anchored between an optically trapped bead and a bead stucked to the coverslip of the fluid chamber. The optically trapped bead's position is monitored by a position detector via scattering of a detection beam. To stretch the molecule, the cover slip was moved at a distance x_0 by a given position of the trapping beam. b) 1D-mechanical analog of (a): the bead motion is governed by the trapping beam and the molecule, both considered as elastic strings with stiffnesses κ_{OT} and κ_{DNA}, respectively. The thermal noise with known power spectrum density $|\xi(f)|^2 = 2k_B T\gamma$ perturbs the motion of the bead and the molecule. The fluctuations of the DNA with unknown power spectral density $|\chi(f)|^2$ affect also the bead position.

trapping system an expanded 1060 nm optical beam from a laser coupled in a single-mode fiber. The position of this trap can be changed by a computer-controlled mirror. This mirror was optically conjugated with the input pupil of the trapping objective using two lenses.

The studied molecule was a double-stranded λ -DNA from *E. Coli* amplified at 12 kbp using standard polymerase chain reaction (PCR) techniques with sample concentrations of 40 ng/μL. The molecules were tagged with biotin and digoxigenin (DIG) at each end to attach to streptavidin and anti-digoxigenin (anti-DIG) coated polystyrene beads, respectively.

DNA molecules were first incubated with the streptavidin-coated beads (1.87

μm diameter) for 45 minutes in phosphate buffer solution (PBS) at pH 7.4. Then the samples were washed and injected along with the anti-DIG-coated beads (3.15 μm diameter) into a fluid chamber. The final DNA-bead constructs were assembled *in situ* [116]: we trapped the streptavidin-coated bead by the optical trap and then we moved the anti-DIG-coated bead, spontaneously attached to the surface of the fluid chamber, to the streptavidin-coated bead. After some time the binding between the DNA and the stuck bead can occur with a certain probability. This event was verified by moving the anti-DIG coated bead and observing its behavior. The motion of the surface caused the molecule's extension, and the dynamics of the optically trapped bead was measured by the position detection system.

To verify that a single DNA molecule was present between the beads, force-extension curves [70] were measured. Fitting the experimental data shown in Fig. 3.2 to a well established worm-like chain (WLC) model [117] $F_{DNA} = \frac{kT}{4P}(\frac{1}{(1-L/L_0)^2} - 1 - \frac{4L}{L_0})$ allows two basic parameters to be extracted: the contour length (L_0) and persistence length (P). (Here L is the equilibrium extension, k is the Boltzmann constant, and T is the absolute temperature). In all measurements, the measured contour length at 4.1 μm was consistent and verified our amplification protocol for this length as well as the rough length estimate found with electrophoresis and image analysis. (In the experimental data analysis, we neglected the bead's motion in z direction resulting from displacements of the cover slip).

To calibrate the optical trap we acquired the time-traces of the bead position without molecules connected to the bead. The data acquisition rate was $50\, kHz$, the acquisition time was 100 s. The bead was trapped $10\, \mu m$ above the surface. Histograms of the bead position are shown in Fig. 3.2. The PSD for the motion along the load direction (x) and in the perpendicular direction (y) are shown in Fig. 3.3 and 3.4. For calibrating the optical trap we used a well established procedure [118], fitting the experimental PSD of the free bead to a Lorentzian curve:

$$PSD_0(f) = \frac{kT}{2\pi^2\gamma(f_c^2 + f^2)}, \tag{3.1}$$

where $\gamma = 6\pi\eta r$ is the drag coefficient, η is the viscosity, r is the radius of the bead, f is the frequency, and $f_c = \kappa_{OT}/(2\pi\gamma)$ is the corner frequency. The stiffness was found to be κ^x_{OT}=(4.0±0.1)pN/μm and κ^y_{OT}=(4.7±0.1) pN/μm, for the x and y directions, respectively. The difference in stiffnesses is due to the linear polarization of the trapping beam [119]. (In the case of the bead attached to the non-stretched molecule the calibration of the optical trap was

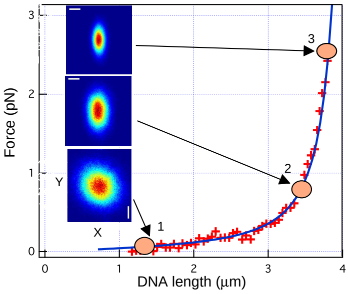

Figure 3.2: An experimental extension curve data (crosses) fitted to the WLC model (blue solid line). The fitting gives the expected contour length (L_0) of 4.1 μm and persistence lengths (P) that vary between 47 - 57 nm for different measurements. Error bars are calculated to be far less than the size of the plotting symbols and are therefore not shown. The PSD measurements were done for the free bead (1) and for two states of molecular extension (2) and (3). The insets show histograms of the bead position in the xy plane, perpendicular to the beam propagation direction, with white lines indicating the scale ($25\,nm$). We studied the histograms of the free bead and then, obtaining the trapping potential we founded, that it is parabolic in the range of ±400 nm.

not possible because the proximity of the stuck bead scattered the detection beam and interfered strongly with the scattering on the optically trapped bead). The values of the stiffnesses were close to those found by using the equipartition theorem: $\kappa_{OT}\langle x^2\rangle = kT$, see below Table 3.1.

Then, we measured the PSD of the bead position with the molecule connected. After confirming the presence of only one molecule between the beads as was described above, we slowly extended the molecule up to the states of extension marked as 2 and 3 in Fig. 3.2. A flexible polymer coils randomly in solution [20]. Therefore, the time traces by a given distance between the stuck bead and the optical trap center presented a stepwise behavior with a step duration usually within 10 seconds. We analyzed the position PSD during the intervals when no steps were observed. Figures 3.3 and 3.4 show the PSD obtained from raw data using this processing.

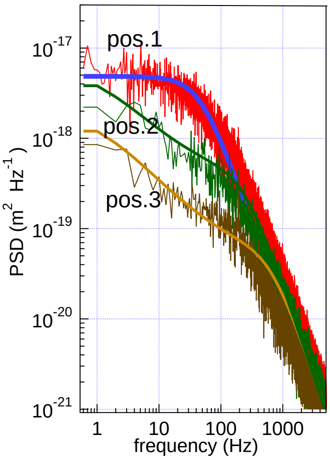

Figure 3.3: PSD of the x-position of the optically trapped bead for the free bead (pos.1) and for the bead connected to the molecule for two positions of the molecule extension (pos.2) and (pos.3) given in Fig.3.2 . The solid lines show the best fit to the Lorentzian function valid when only the random force with white spectrum acts on the free bead (pos.1), and the curves (pos.2) and (pos.3) that fit the experimental spectra of the bead position with the DNA noise included (see below). The experimental data for the free bead are well fitted to the Lorentzian curve even at frequencies below 1 Hz due to small level of instrumental noise.

3.3 Experimental results

When the mechanical load grows, the PSD of the x coordinate demonstrates changes, whereas the PSD of the y coordinate remains almost the same. However, in order to interpret the observed excess noise one has to consider many other sources of excess noise that exist in the optical trapping experiments with single DNA molecules [93], [120]. Special precautions were taken in our experiments to reduce the level of the instrumental noise affecting measurements. In particular, we shielded the optics with a plastic enclosure, in order to minimize the airflow in the instrumental chamber. Also, we used an optical table levitated on pneumatic isolators, and all moving parts (translations stages and mirrors) were operated by motorized actuators controlled outside of the chamber. The

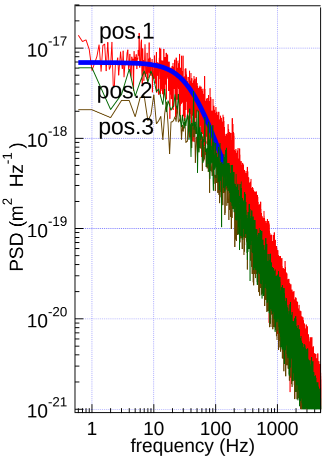

Figure 3.4: PSD of the y-position of the optically trapped bead for the same conditions as in the Fig. 3.3. The labels of the curves have the same meaning as in Fig. 3.3.

detection laser was a stabilized diode laser (less than 0.1% power instability). The trapping beam was obtained from a low-noise (0.17% output power instability during 1 hour) fiber coupled laser. The optically trapped bead's position fluctuations generated due to the laser instability were expected to be the same order of magnitude and therefore the PSD changes due to the trapping beam instability had to be the same order.

In order to evaluate the drift and the low-frequency fluctuations in the microscope stage, we measured the PSD of the streptavidin-coated bead stuck on the cover slip. The stuck-bead spectrum provides an upper bound of the absolute noise detection. The low-frequency spectra of signals from the position detector are shown in Fig. 3.5 for the stuck bead (4) together with the spectra for the free optically trapped bead (1) and the bead connected to the molecule for the values of the molecule extension (3) (Fig. 3.2). As seen, the power of the instrumental noise at 1 Hz is 10^{-4} of that in the spectrum of the free bead. At a frequency of 30 Hz the difference is 5 10^{-6}. When the extended molecule is attached to the probe, the changes of the spectrum in the same frequency range are about 10^{-1}. If we assumed DNA is a pure elastic string that connects the probe with the cover slip surface and transmits 100% of its vibrations to the probe, the magnitude of the PSD changes for the free bead and for the bead with extended DNA would be insignificant in comparison with the changes observed in the experiments. We believe, that the low stiffness of the optical trap (4 pN/μm) is crucial for our measurements with a single optical trapping. Previous results on the extended DNA dynamics were obtained for the trap stiffness of, for example, 100 pN/μm [93], 530 pN/μm [120], 1900 pN/μ m [121]. Such high values of the stiffness permitted to achieve a sub-nanometer resolution, but the isolation from the instrumental noise meets more stringent requirements. In fact, as follows from (3.1), at frequencies lower than the corner frequency, the PSD is inverse proportional to the square of the trap stiffness. Using the optical trap with low stiffness, we increased the contribution of low frequency Brownian components of the trapped probe motion. The extended molecule connects the surface of the cover slip with the probe, but the observed changes in the PSD cannot be explained quantitatively by the instrumental noise keeping in mind its level measured with the stuck bead.

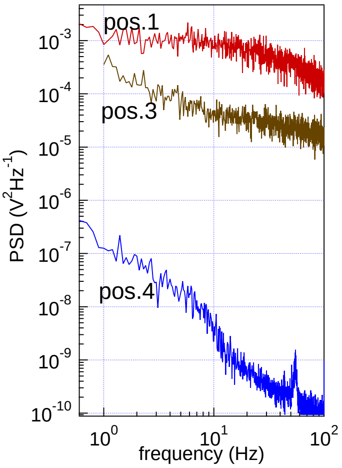

Figure 3.5: PSD of the signals from the x-position detector for the optically trapped free bead (pos.1), for the bead connected to the extended molecule (pos.3)(see Fig. 3.2) , and for the stuck bead (pos.4) within a frequency range of 0.6-100 Hz.

3.4 Discussion

We interpreted the results in terms of the hypothesis of thermally excited fluctuations of the DNA with unknown power spectral density $|\chi(f)|^2$ that also affect the bead position (Fig. 3.1b). Below we present a phenomenological description of the effect that permits us to subtract the spectral dependence of $|\chi(f)|^2$ from the measured spectrum of the probe motion.

As shown in [25] the measured longitudinal 7.6×10^{-9} Ns/m and transverse $17.3\times\ 10^{-9}$ Ns/m friction coefficients of the molecule are independent of extension over the range of extension less than 80 %. Hence, the observed change of the PSD corner frequency is explained by higher effective stiffness of system (the bead and the molecule) rather than changes of the molecule friction coefficients. Then dynamics of the optically trapped bead connected to the DNA molecule is given by

$$\gamma\dot{x} + \kappa_{OT}x(t) + \kappa_{DNA}\left[x(t) - x_0\right] = \xi(t) + \chi(t). \tag{3.2}$$

Solving the equation (3.2) and supposing that $\xi(t)$ and $\chi(t)$ are not correlated, we have the PSD of the bead position when the molecule is connected to the bead as

$$PSD_{DNA}(f) = \frac{|\xi(f)|^2 + |\chi(f)|^2}{4\pi^2\gamma^2(f^2 + f_{cDNA}^2)}, \tag{3.3}$$

where $f_{cDNA} = (\kappa_{OT} + \kappa_{DNA})/(2\pi\gamma)$ is the corner frequency corrected for the elastic properties of the DNA.

The thermal noise spectrum does not depend on frequency $|\xi(\tilde{f})|^2 = 2kT\gamma$. Hence, in order to find a spectrum of the molecule fluctuations using (3.3) we need to know the stiffness of the molecule κ_{DNA}. Experimental data (Fig.3.3 and 3.4) shows that fitting of the PSD to the Lorentzian function cannot be used to find f_{cDNA}. As an approximation, we found the value of the total stiffness coefficient $\kappa_{OT} + \kappa_{DNA}$ by proceeding as follows. Supposing, that the equipartition theorem is still valid even with presence of the additional noise, we obtained the total stiffness using the histograms of the bead positions (insets in Fig. 3.2). Table 3.1 presents the results of calculations. The obtained values of the DNA stiffness agree with those obtained in previous experiments [25, 122].

With these values we used (3.3) to calculate the spectrum of the molecular noise $|\chi(f)|^2$. The results of the calculations are shown in Fig. 3.6.

Fitting the experimental power spectrum density $|\chi(f)|^2|$ to the dependence $1/f^\alpha$ shows that α changes from 0.8 for smaller value of loads to 0.7 for bigger loads, and the intensity of the noise increases with the load. However, the

load	no load ($\kappa_{DNA} = 0$)	2	3
$\kappa^x_{OT} + \kappa^x_{DNA}, pN/\mu m$	4.0 ± 0.1	11.3 ± 0.1	30.5 ± 0.3
$\kappa^y_{OT} + \kappa^y_{DNA}, pN/\mu m$	5.1 ± 0.1	6.5 ± 0.1	10.3 ± 0.1

Table 3.1: The values of the total stiffness $\kappa_{OT} + \kappa_{DNA}$ for two loads and for the free bead.

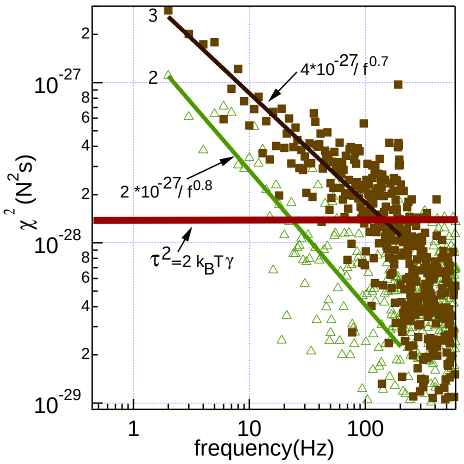

Figure 3.6: The spectrum of the thermally excited noise of the extended DNA molecule for two loads (2) and (3) (see Fig. 3.2).

accuracy of our measurements does not permit us to make conclusions whether this difference is significant. The straight horizontal line in Fig. 3.6 shows the level of the thermal noise $|\xi(f)|^2$ acting on the bead. As seen, the thermal white noise has less intensity than the colored noise of the molecule for frequencies below 30 Hz. For frequencies >30Hz the colored noise interferes strongly with the thermal noise, making its detection difficult.

We also observed changes in the position PSD for the direction perpendicular to the load direction (see Fig. 3.4). These changes are much smaller due to a low transversal stiffness of the DNA molecule [25].

Let us consider now results obtained using two optical traps to extend the molecule (Figure 3.7). Applying the procedure described above to the data presented in Fig. 3.7 we subtracted the additional noise. As Fig. 3.8 shows, the

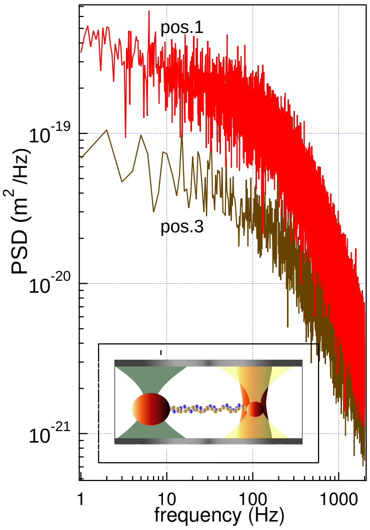

Figure 3.7: PSD of the x-position of the optically trapped bead for the free bead (pos.1) and for the bead connected to the molecule extended with the force of 2 pN (pos.3) (see the extension curve in this case in the inset Fig. 3.8). Inset shows the experimental setup with a DNA molecule between two optically trapped beads. The movable (left) trap that extends the molecule has stiffnesses $\kappa_x = 127pN/\mu m$ and $\kappa_y = 143pN/\mu m$. The unmovable (right) trap has stiffnesses $\kappa_x = 27pN/\mu m$ and $\kappa_y = 30pN/\mu m$. The detection beam is coaxial to this trapping beam.

additional noise signal with the spectrum $1/f^{\alpha}$ with $\alpha \sim 0.75$.

These new measurements confirm that the signal-to-noise ratio is independent of the trap stiffness at low frequencies. The ability to resolve fluctuations of the DNA molecule's length above the Brownian noise of the beads is independent of the trap stiffness. This result was proved previously by several groups [120, 121, 123, 124].

The noise behavior as $|\chi(f)|^2 \sim 1/f^{\alpha}$ with $\alpha < 1$ is characteristic of the system possessing so called $1/f$ noise, which was previously observed in such distinct phenomena as a vacuum tube voltage, a resistance of semiconductors, a traffic flow rate, economic data [125, 126], and in ionic current - voltage measurements of nano pores [127]. This noise is also present in statistics of DNA

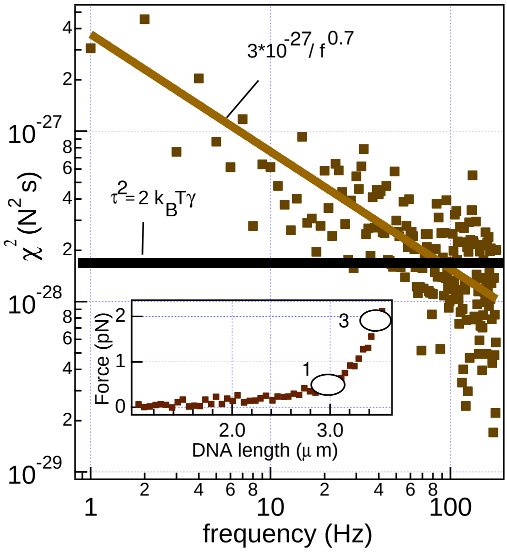

Figure 3.8: The thermally excited noise spectrum of the extended DNA molecule for the load (pos.3) (see Fig. 3.7). Inset shows the extension curve obtained with the dual-trap extended DNA molecule. The two positions labelled (1) and (3) correspond the free bead and the bead connected to the molecule extended with the force of 2 pN.

sequences [128, 129], and in temperature fluctuations during thermal denaturation of the DNA double-helix [130]. The colored noise component is a measure of the memory existing in the system [131].

3.5 Conclusions

Our experiments showed that the fluctuations of the DNA molecule extended up to 80% by a force of 3 pN include the additional colored noise with spectral dependence $1/f^{\alpha}$ with $\alpha \sim 0.75$. Below we give an example that illustrates possible consequences of the presence of the colored noise for the DNA functionality.

The effect of noise, which always accompanies all actual systems, is not restricted to destructive and thermodynamic effects, but also the noise is an integral part of such effects as stochastic resonance and fluctuation driven transport [131]. Being mechanical in nature, many fundamental processes in DNA occur by discrete physical movements. The size of these displacements may be dictated by the inherent periodicity of the molecule. Such processes can be viewed as reactions an energy landscape [50]. The discrete motion in these processes originates from the fact, that the states along these reaction pathways are highly localized minima within this energy landscape. The probability of the discrete mechanical steps depends on the ratio of the minima depth energy and the energy of the fluctuations acting on the molecule from the environment, and is described by the Kramers transition theory [131, 132]. Also, an external deterministic force may change this probability due to the induced redistribution of the energy landscape. For DNA in its natural conditions (in liquid), the Brownian noise stemming from fundamental thermal forces is the main contributor to the noise acting on the molecule. The Kramers transition theory is valid only when the thermal noise with white spectrum exists in the system. As we show here, the component with colored noise spectrum exists in the molecule and therefore these additional fluctuations may be added to the thermal noise, causing changes in the probability of noise-induced events. Recent experiments have shown that, for several proteins, the dependence of folding and unfolding rates on solvent viscosity does not obey Kramers theory [133]. A theoretical attempt to explain the violation of Kramers theory for the dependence of protein folding rates on viscosity showed that the presence of the correlated (colored) noise may be important [134].

One may expect considerable changes in the spectrum of the colored noise of the fluctuations of a DNA extended up to the enthalpic and overstretching regimes, where a force-induced melting of the two strands is achieved. These measurements require more stiffer optical traps and, therefore, the use of optical setups with eliminated stage drift through, for example, a laser-based detection and feedback [120, 135], and/or dual-optical trap designs [123, 136], that circumvent stage drift. The comparison of the noise spectra of single stranded and double stranded molecules is one of our future aims.

4

Study of the dynamics of a single *S. enterica* by a single optical trap.

4.1 Introduction

Bacterial motility is associated to a wide range of biological processes and it plays a key role in the virulence of many pathogens. On efficiency of movement lies the organism's ability to survive, it is possible to say that the movement due to active transport is efficient when its importance is greater that the diffusion of the bacteria itself [27]. The locomotion of unicellular organisms in aqueous media is mediated by several different mechanisms, among which, the bacterial flagellum is the most thoroughly studied [137–140]. This complex structure is composed of several elements that act together to produce helical rotation [141–143]. As a semi-rigid helical filament, the flagellum consists of three substructures analogous to an artificial mechanical system: the basal body, which provides an anchor to the bacterial envelope and contains the motor; the filament, which acts as the propeller; and the hook, which connects the basal body to the filament, and acts as a universal joint [138, 143]. Flagella propelled swimming has been thoroughly studied in enteric bacteria such as *Salmonella enterica* serovar Typhimurium (referred to in the following as *S.* Typhimurium) [141, 143], the bacterium used to develop the method described herein. As other peritrichous bacteria, *S.* Typhimurium have several flagella over its surface. There are between five and ten flagella several micrometers in length but only about 20 nm in diameter that can rotate both clockwise (CW) and counterclockwise (CCW) [144, 145].

If we observe the motion of a single bacterium under microscope, its trajectory will not be completely deterministic. Bacterial motion can be described as a combination of two types of behavior: running and tumbling, Fig. 4.1. During running, the bacterial flagella rotate CCW and form a bundle that pushes the cell in straight line [144, 145]. The bundle collapse when one or more motors of the flagella turn in the CW direction, in which case the bacterium tumbles and reorients itself in another direction [144, 145]. While at the beginning of each run the cell moves in a random direction, the combination of both movements, i.e., straight lines (running) and random changes (tumbling), allows the cell to explore its environment.

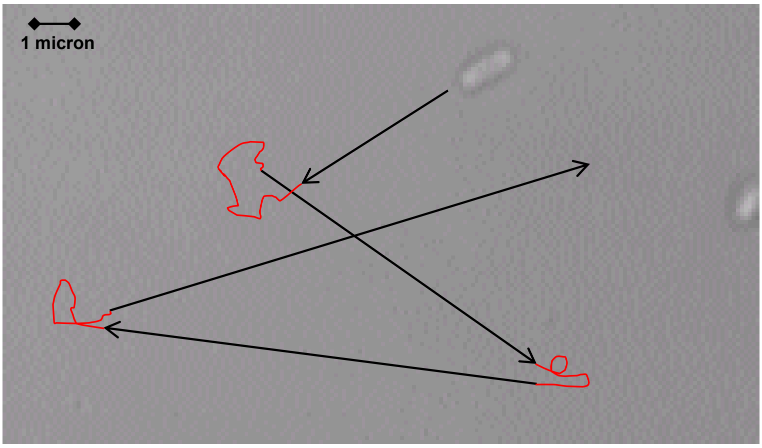

Figure 4.1: Frame of a single bacteria swimming in a liquid environment in our experimental setup. Its motility is composed by two stages, namely running (black straight lines) and tumbling (red curved lines). The combination of both movements allows the cell to explore more efficiently its environment.

Running and tumbling underlie the process of chemotaxis [146] and provide the means by which bacterial cells migrate towards favorable chemicals (attractants) or away from unfavorable ones (repellents). The strategy of the cell to change its direction is stochastic. In other words, the tumbling stage change randomly the swimming direction, and then it decides if the environment is getting worse or better [28].

In *S.* Typhimurium and other bacteria, the presence of chemoattractants/repellents is detected by transmembrane receptors, the methyl-accepting chemotaxis proteins (MCPs) [147], which are associated through the adaptor CheW protein to the CheA kinase [146]. Signal recognition at the chemoreceptor level is determined by degree of MCPs methylation, which in turn reflects the activities of CheR and the methylesterase CheB, and modulates CheA autophosphorylation activity [148]. The phosphorylated kinase (CheA-P) phosphorylates the CheY response regulator, with CheY-P then acting on the flagellar motor. In the absence of CheY-P, the flagella turn CCW and therefore the bacterium runs whereas in the presence of CheY-P the flagella rotate CW and thereby induces tumbling (Fig. 4.2). When a bacterium senses an attractant gradient, its runs become longer as the number of tumbles decreases, such that the cell migrates up the gradient [149]. Consequently, chemotaxis enables the bacterial cell to find better environments for growth.

Chemotaxis and swimming are also key to the virulence of many pathogens [150–152]. In this context, flagellar movement has been intensively studied, mainly via two different strategies: direct visualization of free-moving bacteria and investigations of the rotation of tethered cells. The former typically involves the use of dark-field, differential interface contrast microscopy or, in cells specifically labeled with a fluorescent tag, fluorescence microscopy [145, 153–155]. In addition, the motile behavior of cells has been directly studied using microfluidics assays. [156, 157]. Alternatively, in tethered cells assays, the bacteria are fixed to a surface via their flagella [154]. In this case, there is CW or CCW rotation of the basal body depending on the rotational direction of the flagella. Tethered assays normally rely on high-speed video recorders and image processing software programs that quantify swimming speed, the time between the running and tumbling steps, etc.

Among the other experimental approaches used to characterize chemotaxis and flagellar rotation are those based on optical trapping (for example, [53–60]). This method exploits the fact that the inner refractive index (cytoplasm) of the bacterium is larger than that of its surrounding medium, such that in the presence of a tightly focused optical beam a radiation force directed towards the beam focus is produced. This results in the immobilization of the bacteria, whose trapped position can be examined using several techniques that provide a microsecond time and nanometer spatial resolutions. The most detailed in-

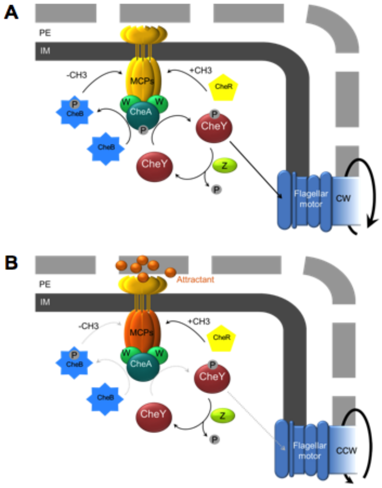

Figure 4.2: The chemotaxis pathway. (a) When the methyl-accepting chemotaxis proteins (MCPs) are highly methylated or unbound (yellow), CheA is activated by phosphorylation. Once activated, it phosphorylates the CheY and CheB response regulators. CheB-P demethylates the MCPs and the high level of CheY-P interacts with the flagellar motor, increasing the frequency of clockwise (CW) rotation, which causes the cell to tumble. (b) MCPs associated with a ligand (attractant) or less methylated (orange), maintain the CheA in a non-phosphorylated, inactive state. Consequently, the CheB methylesterase is not active and does not demethylate the MCPs. CheR methylation of the MCPs, decreases the sensitivity of these receptors. In addition, the CheY-P levels are reduced, leading to an increase in counterclockwise (CCW) flagellar rotation frequency, causing the cell to run. PE, periplasm; IM, inner membrane; Z, CheZ; W, CheW. The grey discontinuous arrows indicate non-occurring reactions (based on [147, 148]).

formation on chemotaxis is obtained when flagellar bundle rotation and the counter-rotation of the cell body are analyzed simultaneously. However, until now, this was possible only by using the dual optical trap system proposed in [59] in which a bacterium is trapped at each end by two optical beams polarized orthogonally. The scattered light of both beams is then analyzed separately by two position-sensitive detectors. The Power Spectral Density (PSD) of the output signals from the detectors yields two peaks corresponding to flagellar rotation and body rotation. An analysis of the phase between the detector signals provides a description of the rotation.

An important step in the simplification of this experimental setup (but without a loss of information) was recently reported by [60] where a single optical trap was used to capture a bacterium with a single polar flagellum rotating either CCW or CW. Using a position sensitive photodetector, the authors were able to detect the characteristic frequencies of the bacterium motion by analyzing the PSD of the cell's position. In addition, they could measure the flagellar motor switching rate under different chemical simulations.

In the following we describe the further refinement of this simple but informative single optical trap technique. We demonstrate that additional information can be obtained if the analysis of the temporal position of the bacterium also includes calculations of the cross-correlation function of the cell trajectory in the plane normal to the optical axis. By applying this approach to a bacterium that uses the run-tumble swimming pattern to navigate within its environment, we were able to study the swimming patterns of different mutant strains across the entire range of bacteria motion within the optical trap. The procedure was validated in dead, running (*cheY*, *cheW*), tumbling (*cheB* mutant) and wild-type strains of *S.* Typhimurium. It was then used, as an example of its potential applications, to identify the role of the CheV protein in the rotation of *S.* Typhimurium flagella.

4.2 Materials and Methods

One of the goals of this chapter is to develope an experimental setup with the lowest possible complexity. Briefly [1], an infrarred laser (1064nm, Avanex) is highly focused by a high NA objective (Nikon, CFI PL FL 100X AN 1.30 WD 0.16 mm). The forward scattered light is collected by a 40× objective (Nikon, CFI PL FL 100X AN 1.30 WD 0.16 mm) and projected to a quadrant-photo diode (NewFocus 2911). The optical trapping is not harmless to the bacteria, even if the optical power is reduced to the minimal able to trap ($\approx$ 20mW), the infrarred light interactuates with the chemical reactions in the aerobic methabolism of the bacteria [59, 158, 159]. To avoid it, we prepare an

---

[1] More details in section 2.4.3

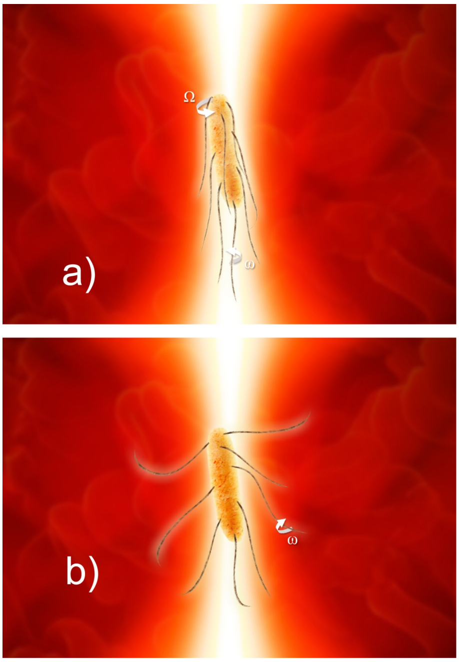

Figure 4.3: A simplified explanation of the two possible flagellar conformations. On a) is a cell with all flagella rotating CCW and consequently forming a bundle that gives a translation velocity to the bacteria, which runs. The motion of a living bacterial cell is characterized by a body roll with frequency Ω, and by flagellar bundle rotation ω. On b) is a tumbling cell with the flagella rotating CW such that no bundle is formed. This process gives extra energy to the cell's dynamics, but does not produce any rotation around the optical axis of the trapping system.

anaerobic media where the experiments were carried out[2]. In order to test our technique, we used different well-known mutants whose phenotype is well defined. The *S*. Typhimurium LT2 *cheB* mutant derivative is a knockout mutant of the CheB methylesterase, which in the bacterial chemotaxis pathway controls the level of MCPs methylation (Fig. 4.2). The *cheB* mutants are characterized by a high frequency of tumbling [160]. The *S*. Typhimurium LT2 *cheY* and

---

[2] Information about bacterial strains, media included in Appendix A

cheW mutants are ideal candidates for exploring running motility, because both present only running pattern of motility (not tumbling), what is also known as the smooth swimming profile [161]. We also study the behavior of dead cells within the trap and cells coming from a wild strain. On the other hand, we use our method to characterize the phenotype of the *cheV* mutant.

4.2.1 Processing of the experimental data

The different motility phenotypes are classified based on the study of the trajectory, $\{x(t), y(t)\}$, of a single cell optically trapped by the optical tweezers. The starting point of this analysis is the model of the rotation of a solid sphere [61]. Consider a sphere suspended in a liquid medium and confined within a harmonic potential well, where it moves randomly due to thermal excitation. An external torque is exerted on the sphere such that in the absence of any trapping potential the sphere rotates around the z-axis with a constant angular velocity due to friction. The angular velocity is determined by the balance between the torque applied to the sphere and the drag torque. The Langevin equations in the overdamped conditions describe the trajectory $(x(t), y(t))$ of the sphere as:

$$\gamma\dot{x}(t) + \kappa x(t) + Hy(t) = \sqrt{2kT\gamma}\xi_x(t), \tag{4.1}$$

$$\gamma\dot{y}(t) + \kappa y(t) - Hx(t) = \sqrt{2kT\gamma}\xi_y(t), \tag{4.2}$$

where γ is the friction coefficient, κ is the trap stiffness, H is the torque parameter for an arbitrary rotation, k is the Boltzmann constant, T is the temperature, and $\xi(t)$ is the white gaussian noise term. The autocorrelation functions (ACF) and the cross-correlation functions (CCF) are calculated from (4.1) and (4.2):

$$ACF(\tau) = \int_{-\infty}^{\infty} x(t)x(t+\tau)dt = \int_{-\infty}^{\infty} y(t)y(t+\tau)dt = \frac{kT}{\kappa}e^{-\kappa\tau/\gamma}\cos\frac{H}{\gamma}\tau, \tag{4.3}$$

$$CCF(\tau) = \int_{-\infty}^{\infty} x(t)y(t+\tau)dt = \frac{kT}{\kappa}e^{-\kappa\tau/\gamma}\sin\frac{H}{\gamma}\tau. \tag{4.4}$$

The $ACF(\tau)$ and Power Spectral Density (PSD) form a Fourier pair and both functions can be calculated from the experimental traces of an optically trapped object.

As seen from (4.3) and (4.4), in the absence of rotational motions of the trapped object $H = 0$, then $CCF(\tau) = 0$ and $ACF(\tau)$ is an exponential function proportional to the viscous force acting on the object.

To apply this model to trapped cells able to rotate in the optical trap, the possible types of rotations must be specified. A flagellated bacterial cell has two main sources of movement: the flagellar rotation and the thermal energy of the bath. Based on the PSD and the traces, two discrete frequencies can appear in the motion of living cells [59, 162]: the body roll characterized by the frequency Ω (around 1-10 Hz), and the flagellar bundle rotation with the frequency ω (between 70 and 140 Hz) (see Fig. 4.3). From the study of the PSD we can infer that the dynamics of a flagellated bacterium are governed more by rotations with frequency Ω than by those with frequency ω, due to a two orders of magnitude difference in the values of the corresponding peaks in the PSD. Therefore, in the equations describing bacterial movement (4.1) and (4.2) rotations with the frequency ω, can be neglected, while in the equations (4.1), (4.2), (4.3) and (4.4) H is replaced by Ω.

The CCF is studied for a short correlation time of $\tau = \pm 50$ms, when the entire expression (4.4) can be approximated by the Taylor series, $\langle x(t)y(t+\tau)\rangle_{Norm} = e^{-\kappa\tau/\gamma}\sin\frac{\Omega}{\gamma}\tau \rightarrow \frac{\Omega}{\gamma}\tau \equiv \Theta\tau$, where the physical meaning of Θ is the angular velocity of the cell around the optical axis.

Accordingly, bacterial cell dynamics can be classified in terms of three different scenarios: dead, running, or tumbling: In a dead cell, the mean value of Θ ($\langle\Theta\rangle$) is zero since there is no flagellar movement, but only broadening ($\Delta\Theta$) due to thermal fluctuations of the cell. In a running cell, $\langle\Theta\rangle$ has a non-zero value due to rotation of the cell body as a whole. This value can be positive or negative depending on the orientation of the cell inside the trap. As the number of flagella is small, from 5 to 10, the individual behavior of a single flagellum can affect the statistical distribution of $\langle\Theta\rangle$, resulting in a $\Delta\Theta$ that is larger than in the case of a dead cell. In a tumbling cell, flagella do not form a bundle, thus, while the rotation frequency around the z-axis has a zero average, $\langle\Theta\rangle = 0$, the rotation motion with frequency ω is still present (see 4.5), causing a larger broadening of the histogram Θ than in occurs with a dead cell.

Data for each bacterial strain were obtained from ten different randomly chosen cells of four distinct biological replicates, and thus a total of 40 cells per strain. The position of each trapped cell was acquired for 1000 s. The entire set of acquired data was then divided into 1-s-blocks (i.e., 2×10^4 points in each block). For each block of data the CCF was calculated and the dependence of the CCF near $\tau = 0$ was linearly fit, thereby yielding the value of Θ. By repeating the protocol for all blocks a histogram of Θ was produced for each measured cell. Then the next cell was trapped and its corresponding histogram was obtained. About 80% of the histograms were found to behave in a very similar manner. All plots shown below for the wild-type, mutant strains, and dead bacteria, present the x and y traces, PSD, CCF and Θ histogram of one trapped cell either from the corresponding bacterial strain or from a dead cell control. In all cases, the selected histograms were within the above-mentioned 80%.

4.3 Results

In the following, the results obtained using dead bacteria, live wild-type cells, and the three *S*. Typhimurium mutant derivatives (*cheB*, *cheY*, and *cheW*, whose behavior has been well-characterized [160, 161, 163]) are shown. The motion profiles obtained with the proposed technique consist of the ACF and CCF of the trajectories resulting from the different bacterial motility patterns and they provide a reference for further studies.

4.3.1 Dead bacteria pattern

Figure 4.4 shows the $x-$ and $y-$ trajectories of the dead bacteria, with their corresponding PSD, ACF, and CCF. For these cells, the PSDs lack the characteristic discrete frequencies seen with live motile bacteria, and they are very similar to the PSDs of the motion of an optically trapped solid sphere thus, the Lorentzian curve is that expected from the experimental conditions. A cross-correlation is also absent from the trajectory since a dead cell does not have any rotational motion. Therefore, as for an optically trapped bead, the ACF depends only on the viscous drag coefficient and the trap stiffness and therefore decays exponentially.

4.3.2 Tumbling pattern: The *cheB* mutant

The statistical characteristics of the trajectory of this mutant in the optical trap are presented in Fig. 4.5. Rotations with angular frequencies in a band near $\omega = 100$ Hz are seen in the PSD, ACF, and CCF, but their presence is also evident even in the trajectories, see Fig. 4.5 a). As flagella normally rotate CW, there is no bundle formation. The CCF is not a stable function but instead gives a fluctuating value of Θ. This behavior is related to the continuous chaotic movement of the cell inside the trap.

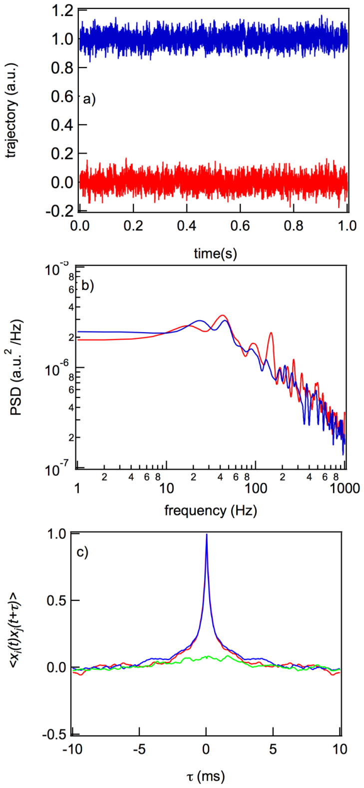

Figure 4.4: Dynamic characteristics of the motion of a dead bacterium: time-traces of the x and y positions during 1 s (a) and their corresponding PSD (b), ACF, and CCF (c). In (a), the $y(t)$ trajectory is shifted in order to improve its visibility. In (c) the red and blue curves are the ACFs of the x and y positions, and the green curve is the CCF

4.3.3 Running pattern: The *cheY* and *cheW* mutants

In Fig. 4.6, *cheY* mutant rotations with ω around 100 Hz, and Ω from 5 to 15 Hz are clearly seen, both in the trajectories (Fig. 4.6a) and in the ACF and CCF (Fig. 4.6c). The differences in the Ω values of the different cells are due to the size differences, which can vary by as much as 30% of the length of

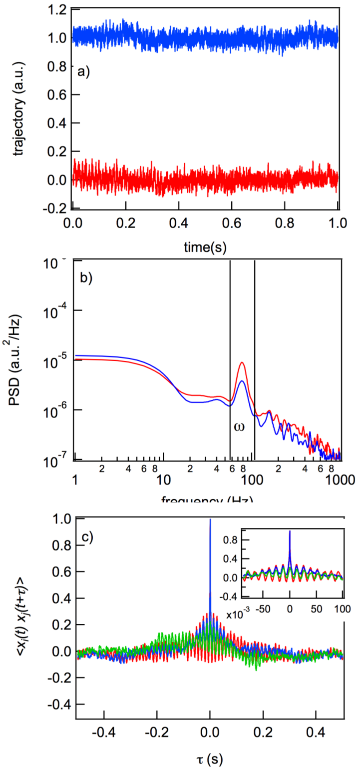

Figure 4.5: Dynamic characteristics of the *cheB* mutant: the trajectories of the x and y positions during 1 s (a) and their corresponding PSD (b), ACF and CCF (c). The red and blue curves are the trajectories, PSD, and ACF of the x and y positions, and the green curve is the CCF.

a typical cell. The same results are observed for the *cheW* mutants. In both mutants, the dynamics of the bacterial cells inside the trap, with most of the flagella rotating CCW, reflect the rearrangement of all the individual flagellum as a collective bundle positioned at one end of the bacterium. This collective process generates a forward velocity (without the trap it is represented by a quasi-straight line [164]) that is responsible for the global bacterial rotation Ω. The PSD has two peaks, one centered at 5-15 Hz, corresponding to the cell body roll (Ω) around the trapping point, and the flagella bundle roll around 100 Hz, indicative of rolling by the flagellar bundle (Fig. 4.6, and data not shown). Accordingly, in these running mutants the histogram of the slope of the CCF for short correlation times clearly points to a different type of dynamic profile from that of tumbling or dead bacteria (Fig. 4.8).

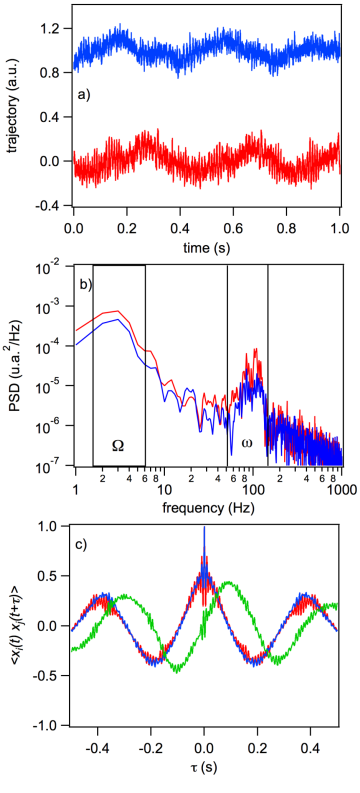

Figure 4.6: Dynamic characteristics of the *cheY* mutant: the trajectories of the x and y positions during 1 s (a) and their corresponding PSD (b), ACF, and CCF (c). The red and blue curves are the trajectories, PSD, and ACFs of the x and y positions, and the green curve is the CCF.

4.3.4 Wild-type swimming pattern

As described above, the swimming pattern of the wild-type strain combines both tumbling and running. In this case, the pattern observed in the representation of the CCF slope for short correlation times is composite of those of the two dynamic types, the tumbling mutant and the running mutant.

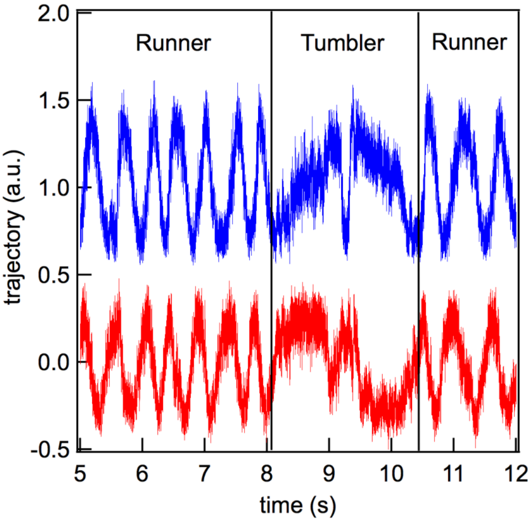

Figure 4.7: Dynamic characteristics of the *S.* Typhimurium wild-type strain: the x (bottom) and y (upper) coordinates of the wild-type bacteria during a 7 s time interval. The switch of the flagellar motor from the running to the tumbling state is shown. The trace of the y coordinate is shifted in order to avoid overlap with that of the x coordinate.

Figure 4.7 illustrates the traces of the wild-type bacterium, showing the switch from a tumbling to a running state. The traces also allow measurement of the characteristic switching rate of the bacterial motor.

4.3.5 Histograms of Θ

The results obtained for each bacterial strain with known dynamic properties can now be summarized using the parameter Θ, i.e., the slope of the CCF for short correlation times. A comparison of the Θ histograms of the four motility patterns (dead cell, tumbling, running, and wild-type cells), distinguishes four types of dynamics (Fig. 4.8). The widths of the histograms indicate contributions beyond Brownian motion. Accordingly, the histograms from the live cells are different from those of dead bacteria (Fig. 4.8). In the former, the flagellar frequency does not remain constant, which implies changes in the translational direction [59].

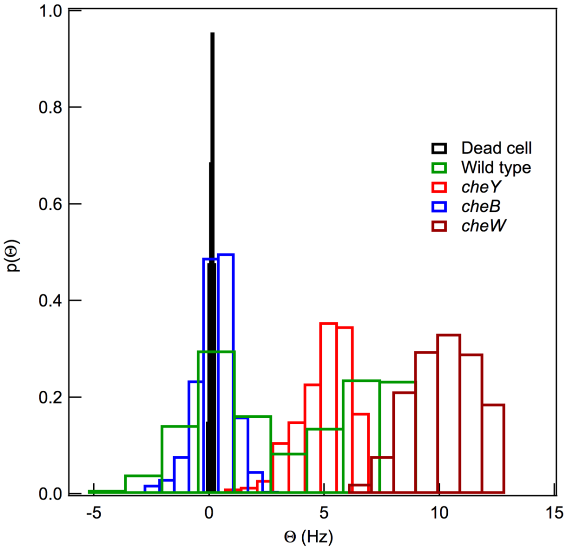

Figure 4.8: The slope, Θ, of the CCF near $\tau = 0$ obtained from the trajectories of single optically trapped dead (black), running (red and brown, corresponding to *cheY* and *cheW* mutants, respectively), *cheB* mutant tumbling (blue), and wild-type (green) bacteria. The histograms of the distributions can be classified into three main groups: (1) The histograms with a single maximum centered at zero that corresponds to tumbling bacteria (*cheB* mutant); (2) those with a single maximum not centered at zero correspond to a deterministic rotation associated with the rotation of a solid sphere, as is the case for running bacteria (*cheY* and *cheW* mutants); and (3) a combination of both profiles, as occurs in the wild-type strain.

The Θ histogram for the wild-type strain is shown in Fig. 4.8. The correlation functions of this cell should change with time. In dead cells, just the

Brownian motion contributes to the width of the histogram, whereas in live cells the contribution of the thermal energy is smaller than that of flagellar motion, resulting in greater broadening of the histograms. Moreover, considering that *S*. Typhimurium has only five to ten flagella per cell, the histograms also reflect the differential dynamics of a single flagellum since changes therein would affect overall cell movement.

4.3.6 Identification of the *cheV* mutant swimming pattern

The function of the CheV protein in the chemotaxis pathway is still not well understood. Although the swimming profile of *S*. Typhimurium *cheV* mutants has been characterized [165], the description contradicts earlier published results [160,163,166]. For this reason, we chose to apply our newly developed, validated technique to study flagellar rotation in the *S*. Typhimurium *cheV* mutant.

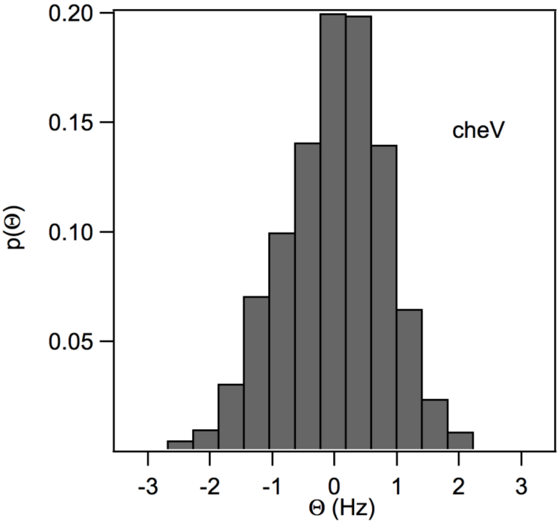

Figure 4.9: The slope, Θ, of the CCF near $\tau = 0$, obtained from the trajectories of the optically trapped *cheV* mutants.

A video analysis as well as examination of the ACF and the slope of the CCF for short correlation times (Fig. 4.9) showed that the *cheV* knockout mutant has a tumbling pattern. The absence of the CheV protein modifies the

Θ distribution, centering it around zero, with an additional contribution to the Θ histogram from the random rotations.

4.4 Discussion

The simple single optical trap used in this study to analyze the swimming pattern of *S.* Typhimurium and several mutants can be broadly applied to measure the full range of bacterial motility and alterations thereof. The core of the method is based on our previous study [61], which described the movement of a sub-micron object confined in an optical trap in the presence of a torque exerted on or produced by the object. The single optical trap assay can detect differences in the dynamic properties of cells of the same culture, seen as a change in the mean value of Θ, expressed as Ω, from one cell to another. Our study of ten independent cells from four independent cultures showed that the distribution of the histograms remained very similar, such that the individual phenotype of a single bacterium could be distinguished. The importance of the different parameters is more readily appreciated in the case of the running mutants. For some bacteria, Θ can achieve values close to 100 Hz. It is important to note that in these cases, the widths of the histogram are similar to those obtained for running mutants with only 10 Hz.

Photodamage to the trapped bacterium has been considered [167] given that infrared light in the presence of oxygen produces free radicals inside the cell, which induce death within a short period of time. In our optical trap system, this problem is avoided by including an oxygen scavenging system in the sample preparation medium, which guarantees a constant low level of oxygen and, hence, cell survival during the measurements. The obtained results validate the utility of this optical trap setup to characterize bacterial motility. The analysis of dead cells as well as running, tumbling and wild-type strains of *S.* Typhimurium demostrated the possibility to correlate the motility characteristics widely described for these cells with specific Θ distribution profiles. Thus, the trajectory of the running mutants is characterized by a mean value of Θ different from zero and that of tumbling mutants by a mean value of Θ near zero with a certain standard deviation in the latter case due to the random disposition of the flagella and the absence of an equilibrium position.

Changes in bundle formation, from the tail to the head and vice-versa, must also be considered [168]. This effect is unlikely to be stable because the bacteria should work against the radiation pressure in the optical trap, it not being possible to define a stable equilibrium position.

In studying the slope of the CCF for the tumbling bacteria, near $\tau = 0$, we found that the flagella of these cells rotate in the CW direction and that, like wild-type and running strains, the bacterial dynamics differ from those of dead bacteria (Fig. 4.4). A dead bacterium behaves as a solid body, therefore, when an extra force is applied, the entire sphere revolves around the trapping point. The sum of these torques will be uniform when averaged over a long time. For a tumbling cell, while the mean value of Θ is close to zero, the histogram will be wider than those obtained from a dead bacterium, since the motion detected in the latter case is Brownian motion (Fig. 4.8).

In addition, for a dead bacterium, there is no flagellar rotation, and therefore neither the ACF nor the CCFs will have a discrete spectrum. The histogram of Θ for a dead bacterium has a width much smaller than for a live one, due to the bacterium's Brownian motion.

Some bacterial species utilize CheV instead of the CheW, whereas in others, including *S.* Typhimurium, both proteins are present. In the latter case, the role of CheV is unknown [167]. Most hypotheses regarding CheV function have focused on the two different protein domains: a CheW-like domain and a phosphorylated receiver domain similar to that of CheY. Accordingly, it has been suggested that CheV plays a role in receptor coupling and in the adaptation of the chemotactic response [165, 169, 170]. Furthermore, a *cheV* knockout mutant was shown to exhibit the same swimming and chemotactic phenotypes as the wild-type strain [171]. Nevertheless, our single optical trap analysis clearly demonstrated the tumbling phenotype of the *cheV* knockout mutant. It should be noted, however, that single optical trap experiments are performed under anaerobic conditions, to avoid cell damage, while in the previously mentioned work the experimental conditions included the presence of oxygen. This is an important consideration because expression of the *cheV* gene is controlled by the global regulators Fnr and ArcA, both of which are involved in O_2 sensing and adaptation [172, 173]. Thus, when the O_2 concentration decreases, ArcA and Fnr directly activate *cheV* expression, greatly increasing the concentration of CheV inside the cell. Therefore, under anaerobic conditions, such as used in the single optical trap, CheV protein are greatly magnified. In addition, the fact that the *cheV* and *cheB* mutants share the tumbling phenotype suggests that the role of CheV in *S.* Typhimurium is more closely associated with adaptation more than with receptor coupling. However, further work is needed to elucidate the role of *S.* Typhimurium *cheV* expression in the chemotactic pathway and its relation to the anaerobic metabolism.

4.5 Conclusions

By analyzing the statistical functions derived from following the trajectories $\{x(t), y(t)\}$ of a bacterium trapped by a single optical beam the different dynamic properties of different bacteria can be distinguished. The approach described herein is based on a model of the rotation of a solid optically trapped sphere. The optical trap technique can be easily implemented in a biological laboratory, since it requires only a small number of optical and electronic parts to convert a simple biological microscope into the required analyzer. In a demonstration of the utility of this method, we determined the motility profile of the *S.* Typhimurium *cheV* mutant derivative under anaerobic conditions, which case it exhibits tumbling behavior. This observation will contribute to elucidating the role of the CheV protein in the bacterial chemotaxis pathway.

4.6 Acknowledgments

This chapter was developed in colaboration with Prof. Llagostera group (Microbiology, Facultat de ciencies. Universitat Autonoma de Barcelona). We wish to acknowledge the assistance of Denis Spricigo in optimizing the bacterial culture preparations for the experiments.

5

Stochastic energetics

The true physical picture includes the possibility that even a regularly going clock should all at once invert its motion and, working backward, rewind its own spring at the expense of the heat of the environment. The event is just 'still a little less likely' than a 'Brownian fit' of a clock without driving mechanism
Erwin Schrödinger, **What is life?** 1944

The energetics of the stochastic processes and its link to its dynamics is a key point in the study of the mesoscopic world. The thermodynamics of small systems is a field with increasing interest and huge advances since the end of the last century [11]. Nevertheless, it is quite contradictory to study the thermodynamics of non-macroscopic systems. Thermodynamics was the science that favored the Industrial Revolution, during the 19^{th} century. Engineers studied how to extract useful work from heat baths to build steam engines and improve their power and efficiency. Indeed, engines are frequently found in nature, and some of them are strikingly similar to those designed by humans. In the size range we want to focus, spanning from tens of nanometers to several microns, we can study the behavior of proteins as kinesin or even more complicated protein systems as the flagellar motors, trying to answer different questions: what its efficiency is or how much heat do they dissipate to the environment. In the case of kinesin, the average of motion is 8 nm every 10 to 15 ms [174], being this movement highly linked to the chemical energy conversion: one ATP molecule is hydrolyzed per each step [11]. This coupling gives an efficiency of about 60 % of chemical energy converted into useful work. If this efficiency is compared to the efficiency of the heat engines cited by Curzon and Ahlborn [12], we see that nature seems to be as twice as efficient. *Can this system be studied in the context of standar thermodynamics? Do the same laws hold here?* In fact, the answer to these questions is not straightforward, and, when dealing with sych small systems is possible to find violations of the classical thermodynamic laws. For example, Carberry *et al* demonstrated that there are individual events where the second law of thermodynamics is violated [29]. The reason why we can not observe these violations in the macroworld is the huge number of particles present in these systems ($N \sim 10^{23}$). If we decrease the size of the system of our interest, thermal fluctuations become important, and it is when this *noisy* behavior arises.

Since 1993, experimental and theoretical tools suitable to study small systems have been developed, thus expanding the validity of classical laws. Indeed, nowadays, classical thermodynamics is undestood as a generalization of the fluctuating systems when $N \to N_A$. Throughout this chapter, a brief overview of this theoretical framework is presented.

5.1 Classical Thermodynamics

Thermodynamics is the study of the restrictions on the possible properties of matter that follow from the symmetry properties of the fundamental laws of physics [175]. The so-called thermodynamic processes are carried out under the four laws of thermodynamics, that read as follows:

Zero law If two systems are both in thermal equilibrium with a third one, both have the same temperature.

First law Energy can be transferred between systems under the form of work (W) or heat (Q). The total energy is conserved, but the internal energy of a closed system changes as: $\Delta U = Q + W$.

Second law Any non-equilibrium system will evolve to a state which maximizes its entropy $\Delta S \geq 0$. An equivalent formulation of this law is the impossibility to apply less work than the difference of free energy between the initial and the final state of a process, $W \geq \Delta F$. The excess of work is released in the form of heat to the thermal bath.

Third law When a the temperature of a system goes to zero, the associated entropy will approach to a constant value. In the particular case of crystals, the constant value of entropy will be specifically null.

Thanks to these laws, we can predict the evolution of a system when any parameter is changed[1]. One of the aims of the classical thermodynamic is the understanding of the energy transfer between systems in contact. The internal energy of a macroscopic system is defined as the sum of kinetic and potential energy over all its components. The energy transfer can be done in two ways: Heat, transfer from the system to its environment($Q < 0$) or to the system from its environment($Q > 0$); and work done by the system to its environment ($W < 0$) or to the system from its environment($W > 0$).

On the other hand, the kinetic theory of gases was supported by the success of the Newtonian mechanics. Along the 19th century, the kinetic theory was developed by Krönig, Clausius and others. It was James Maxwell, who after reading the manuscripts of Clausius, formulated the first statistical physics law, stating his well-known distribution of the molecular velocities in a gas:

$$\rho(v) = \sqrt{\frac{m}{2\pi kT}} \exp\left\{-\frac{mv^2}{2kT}\right\} \tag{5.1}$$

This law has implicit the variance of the velocities, the so-called equipartition theorem:

$$\langle v^2 \rangle = \frac{kT}{m} \tag{5.2}$$

The conexion between the kinetic theory and Thermodynamics had to wait until 1872, when Ludwig Boltzmann derived his H-theorem, whose importance lies in its conexion between the irreversible world of thermodynamics and the reversible laws of micromechanics. Recently, Ken Sekimoto proposed a scheme that clarifies the state of the art [62], see Fig. 5.1. He presented his *stochastic energetics* as the connection between the stochastic dynamics, i.e., Langevin equation, and Thermodynamics [176]. This framework is of great importance in the study of the mesoscopic world, particularly in optical trapping experiments, thanks to its ability to compute the energy transfers, the heat and the work associated to different processes, as a function of the observables of our system, for instance, the position of the particle, the applied force, etc. Afterwards,

---

[1] Thermodynamics is the science of equilibrium states. Therefore, a change in any parameter must be slow enough to define its *quasistaticity*.

Udo Seifert proposed the name *stochastic thermodynamics* to the framework built from the junction of stochastic energetics and the idea that entropy can be assigned along a fluctuating trajectory [177].

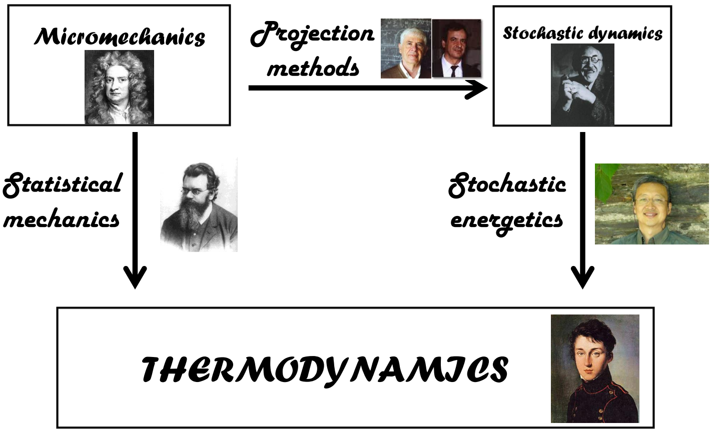

Figure 5.1: Scheme of the *energetics* framework [62]

5.2 Entropy

For centuries, one of the dreams of the engineers has been the perpetual motion, i.e., a machine with 100% efficiency. In fact, the first law does not forbid the extraction of useful work from two thermal baths at the same temperature. Moreover, we could be able to connect a *dream machine* to an ordinary stone from the street and extract energy from it: the only effect predicted by the first law would be that this stone will become cooler. On the other hand, there are empirical evidences that must be taken in account; for instance, when we introduce ice in a glass of water, the ice will melt and the water will become colder, but the reverse process will not take place spontaneusly, the formation of ice in a glass of water. Another example can be the mixing of gases. If we had a volume divided in two parts by a wall, each one filled with a different kind of molecules, and then the wall was removed, we would see how the molecules fill the whole volume and we would never see the molecules splitting and coming back to the previous state. To explain these evidences, it is necessary to introduce a new thermodynamic quantity called *entropy*, and therefore enunciate the second law of Thermodynamics.

The entropy is an extensive thermodynamic quantity that points the direction where processes occur. In other words, the entropy is a physical magnitude that points out the sense of the arrow of time. This fact is non trivial, as the definition of entropy itself, and it is linked with the second law of Thermodynamics, which sets a view of entropy as irreversibility. However, the entropy is not only a parameter that gives us the idea of irreversibility, but it is linked to the degree of disorder of a system and, moreover, with the quantification of our ignorance and information about a system. In the next epigraphs, a brief overview of each meaning is presented.

5.2.1 Entropy as irreversibility: The arrow of time

At the beginning of the 18th century, steam engines started to be one of the key points in the research community. One of the first questions that engineers had to answer was its optimization: *How can we obtain the maximum useful work from two thermal baths?* This question was not trivial, taking into account the fact that the first and the second laws of the thermodynamics were not known. Nevertheless, Sadi Carnot realized that the key point was to avoid irreversibility along cycles [178]. An irreversible process is defined as a process after which it is impossible to return to the initial state without applying external work. Therefore, considering a process from A to B, the associated entropy will always obey:

$$\Delta S \equiv S_B - S_A \geq \int_A^B \frac{\delta Q}{T} \tag{5.3}$$

where the equality corresponds to the *reversible processes*. In the case of irreversible processes, the extra amount of entropy is called the *entropy production* ΔS_{prod}:

$$\Delta S \equiv \int_A^B \frac{\delta Q}{T} + \Delta S_{\text{prod}} \tag{5.4}$$

As ice melting in our drink, entropy production is also present in steam engines. During the process of transferring energy in the form of heat from the hot body and transforming it into useful work, some of this energy is *wasted* or *dissipated*, and this *waste* of energy increases the entropy of the universe. The second law has a deeper meaning, as it is pointing the natural sense of time. Microscopic laws are time reversible[2], i.e., they are valid with the time running forwards or backwards. Then, one physical way to define the sense of time, what the future is, is using the direction where the entropy is increased. This interpretation of entropy will be considered in Chapter 7, where we experimentally study how energy is exchanged in the mesoscopic world and how the irreversibility affects the efficiency of the cycles.

5.2.2 Entropy as disorder: Maxwell's demon

Let us consider a volume $2V$ divided in two equal parts V. Assume that there are $N/2$ undistinguishable molecules painted in red on one side of the wall, and other $N/2$ undistinguishable molecules painted in blue on the other side. The configurational entropy of the system (neglecting the kinetic part) is:

$$S_{\text{UNMIXED}} = 2k \log \left\{ \frac{V^{N/2}}{(N/2)!} \right\} \tag{5.5}$$

that is twice the entropy of a single part of the system. If we remove the wall, the particles are allowed to mix. It is necessary to remark that this effect is not due to a repulsive force between the molecules, but a simple probability effect. Therefore, the entropy of the system once the wall is removed is written as:

$$S_{\text{MIXED}} = 2k \log \left\{ \frac{(2V)^{N/2}}{(N/2)!} \right\} \tag{5.6}$$

It can be compared with the previous state's entropy, giving us a difference of entropy $\Delta S = kN \log 2$. We can increase the difference of entropy in a *quanta* $k \log 2$ per each molecule we add to the system. The interpretation of this increment is that each extra molecule increase the number of possible microstates of the system.

In 1867, James Maxwell wrote a letter to Peter Guthrie Tait where he proposed an apparent paradox in the second law. He imagined a being, the *demon*, able to control a small door between two containers, allowing to pass the hot molecules to one side and the cold molecules to the other side. The movement

---

[2] More correctly, the nature's laws are invariant under CPT

of the door did not carry any work, but the process would decrease the entropy of the universe and it would be possible to extract useful work from the system [35].

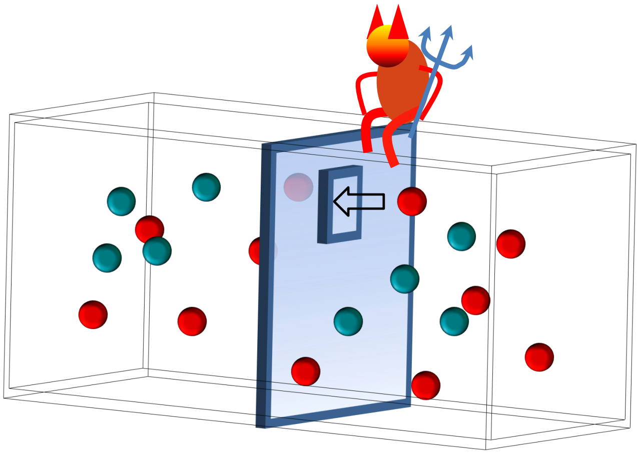

Figure 5.2: The demon controls the door and knows the state of each single molecule. The system evolves, thanks to the demon ability to know the state of each single molecule and to control the micro-door, to a state with a lower entropy. This being stores the information of each system's state.

Although several authors have tried to probe the impossibility of the demon existence, see for example the attempts by Smoluchowski [179] or by Brillouin [180], it is necessary to introduce the next epigraph to understand how the second law is not broken by this being. It is necessary to study the thermodynamics of the information.

5.2.3 Entropy as information: Landauer's principle

The steam engines motivated the study and the understanding of thermodynamics and its limits. A similar situation occurred in the development of computers whose study motivated the exploration of the limits of the information science. The significance of the physical part in the computing science started with Claude Shannon and his studies in the information entropy [181]. The original definition was done in the case of discrete systems, $S \equiv -\sum \rho(x) \log \rho(x)$. Let us consider a simple bit. If we do not know in which configuration it is, the probability is thus equal to 1/2 for both states $p(0,1) = \{1/2, 1/2\}$. Then, the associated entropy will be $S = -0.5 \log 0.5 - 0.5 \log 0.5 = \log 2$. Therefore, if we measure the bit state, and afterwards, we want to erasure its information content[3], the probability space of the system changes to $p(0,1) = \{1, 0\}$, and its associated entropy will change to $S = -0 \log 0 - 1 \log 1 \equiv 0$. The entropy would be reduced in a term $\log 2$ ($k \log 2$ in physical units). This increase of entropy has a thermodynamic implication: by the second law of the thermodynamics, each change of entropy leads to a release of heat, in this case $Q = T\Delta S = kT \log 2$. This result is called the *Landauer limit* and has practical implications in computers design, although nowadays the Landauer limit is still several orders of magnitude below the dissipation of computers. This limit was the key ingredient of the solution that Bennett proposed to solve the demon's paradox [182]. The ability of the demon is not to control the door, but to measure the state of each molecule and hence to compute if it is *hot* ot *cold.* Each measurement carries an erasure of the previous state of the demon's memory, therefore, this reboot liberates heat to the thermal bath compensating the extraction of work done by the demon [35]. This principle was recently experimentally tested by Berut *et al* in a laser-tweezers experiment [39]. Another beautiful experiment was developed by Toyabe *et al* in Japan, where they built a demon's experiment with a spiral-staircase-like potential [38]. The particle jumps by thermal fluctuations between different steps and, by a feedback process, they made the particle climb the potential and thus test the information to energy conversion.

In the case of continuous observables, as in our experiments, the definition of the Shannon entropy reads as follows:

$$S \equiv - \int dx \rho(x) \log \rho(x) \tag{5.7}$$

where the position is considered as a continuous variable x, which follows a pdf $\rho(x)$, always neglecting the kinetic part. This interpretation of entropy will be considered in Chapter 8 where a generalization of the Landauer's principle is analitically derived and experimentally tested.

5.3 Langevin equation

The study of the Brownian motion started in 1827 when the botanist Robert Brown wrote down his observations of the random motion of *Clarkia pulchella*

---

[3] We define *erasure a bit* as reboot it to 0.

pollen grains suspended in water. He observed that a micrometric particle immersed in a fluid had a random movement that never stopped. Experiments carried out by G. L. Gouy showed that there was a correlation between the movement of the bead and its size, the temperature and the viscosity of the fluid. He also observed independence between the trajectory of different particles of the same sample. In 1908, P. Langevin published a novel solution of the problem [183], according to him, much more simple than Einstein's approach [184]. He wanted to study the dynamics of the particle with Newton equation:

$$m\frac{dv(t)}{dt} = F(t) \tag{5.8}$$

where m is the mass of the particle, $v(t)$ is the instantaneous velocity at a given time t and $F(t)$ is the force exerted to the particle[4]. The force $F(t)$ is dominated by the resistance exerted by the fluid to the displacement of the particle, which within the Stoke's regime is written as $F_{dragg} = \gamma\frac{dx}{dt}$. The particle can also be subject to an external potential $U(x)$, such as an optical trap. This term can be expressed as $F_{ext} = -\frac{\partial U}{\partial x}$. The fluctuations due to the constant hitting of the fluid molecules to the Brownian particle are included with in the term $\xi(t)$. Under these assumptions, the equation of motion are:

$$\begin{aligned} \frac{dx(t)}{dt} &= \frac{p(t)}{m} \\ \frac{dp(t)}{dt} = \frac{\partial U(x)}{\partial x} - \frac{\gamma}{m}p(t) &+ \xi(t) \end{aligned} \tag{5.9}$$

The fluctuations are usually understood as occasional impacts of the molecules of the fluid to the sample, with an equal probability of impact in all directions. From this feature, we can set up that the stochastic force has zero mean: $\langle\xi(t)\rangle = 0$. On the other hand, the impacts must be independent of each other, as the thermal bath has no memory. As the frequency of the impacts is large ($\gg$MHz), we can express the autocorrelation as $\langle\xi(t)\xi(t')\rangle = 2kT\gamma\delta(t-t')$, where $\delta(t-t')$ is the Dirac delta. Under these assumptions we have expressed the thermal fluctuations as a Gaussian white noise. Note, however, that this kind of noise does not exist in Nature[5], as a complete whiteness would require an infinite energy [14]. However, this idealization is fundamental for a mathematical approach to many processes. In adittion to likely presence of colored

---

[4] We assume along the whole epigraph that the temperature of the fluid is homogeneous.

[5] For instance, it has been experimentally measured the color of the Brownian motion due to the inertial term [185]

thermal noise, the use of an ideal white noise is not harmless. *LE* was the first example of *stochastic differential equation* (**SDE**), a type of equations with a random term $\xi(t)$ whose possible solutions are random functions [14]. In SDE, the usual rules of calculus such as the Riemann integral or the chain rule are not valid anymore, and it is necessary to use the so-called *Stochastic Calculus*. A brief review is shown in Appendix B.

Another important point of the dynamics of a Brownian particle is the possibility to study it at different time scales. The characteristic time is related with the inertia of the particle, typically defined as $\tau_m \approx m/\gamma$. This time can be interpreted as the typical duration of a straight displacement of the particle. If we consider the samples used in this thesis, polystyrene beads of 1μm of diameter immersed in water, the value of τ_m is of the microseconds order ($\tau_m \approx 10^{-6}$s). In our experiments we have a finite sampling frequency, typically up to 50 kHz, what makes imposible to track the sample at enough time resolution to observe the inertial dynamics. In this case we can neglect the inertia of the particle, using the so-called overdamped approximation. Thanks to it, we can rewrite (5.9) as:

$$\gamma \frac{dx(t)}{dt} + \frac{\partial U(x)}{\partial x} = \xi(t) \tag{5.10}$$

This approximation is not innocuous. If we try to analitically calculate the instantaneous velocity of the particle, we will obtain an unbounded value [62]. Moreover, as we discuss in Chapter 7, the energetics of Brownian particles along non-isothermal process are not complete if we work in the overdamped approximation. Therefore, to enter in thermal induced kinetic studies of the Brownian motion we must always work in the underdamped regime.

5.4 Work and heat in the mesoscopic scale

Work and heat are considered the two ways to interchange energy between a system and its environment. The view at the macroscopic scale is simple: work is done to the system or by the system when a controlable parameter is changed, while the heat is the energy exchanged between the system and its environment to achieve thermal equilibrium. Both parameters are seen as functions of macroscopic quantities as volume, pressure, etc., parameters that are averages of the microscopic parameters. A key question when we want to apply Thermodynamics in the mesoscale is the following: *does it make sense to apply the same scenario in the mesoscale than in the macroscale?*. The main inconvenience is the high influence of the fluctuactions at this scale. In fact, the order of magnitude of the energy is kT, and therefore, the thermal fluctuations play a fundamental role.

In the macroscale, the temperature is a parameter due to the average of the components of the system, e. g., in the case of gases it is due to the average of the velocity of the molecules. Therefore, we can measure the difference of temperature between two states of a macroscopic system to derive the amount of heat transferred, and then we can talk about *calorimetric heat.* Unfortunately, such a direct measurement is not possible in the mesoworld. To start with, the notion of separation between system and environment cannot be done with the classical notion of *wall.* In fact, we cannot measure the tiny differences of temperature around the system in a process with an energy exchange of few kT to derive a value of heat. On the other hand, in the mesoscopic world we must take into account the description of the system. It is not the same to consider all the individual water molecules hitting a Brownian particle than to use the white noise term. Then, we must distinguish between the eliminated degrees of freedom, as the water molecules dynamic in the Langevin equation, from the retained ones. From this point, we can define the work as the energy exchanged due to changes in the retained degrees of freedom, and the heat as the energy exchange due to eliminated ones [62].

5.4.1 Sekimoto approach

The stablishment of the LE (5.10) leads us to ask how is related to the Thermodynamic laws in equilibrium and non-equilibrium processes. First, the framework must include the posibility to describe reversible processes. Nevertheless, the construction of the LE includes a term ($\gamma dx/dt$) that just implies an irreversible processes. As it is explained in [176], the structure of the LE can be rewritten to show the evolution of the internal energy along time:

$$\frac{dU}{dt} = \underbrace{-\gamma \left| \frac{dx}{dt} \right|^2}_{\textbf{energy dissipation}} + \underbrace{\xi(t) \frac{dx}{dt}}_{\textbf{energy fluctuation}} \tag{5.11}$$

The first addend in the rhs part of this equation is only dissipating energy to the bath, being iddentically negative, while the other term is giving and removing energy to the system. The dissipative term is removing the *extra energy* of the system, as the derivative of x will be intimately related with the stochastic force. A good example of the validity of the framework given by

Sekimoto is the mislead of this interpretation, if so, Kramer's description [186] of thermal activation could not be described by Langevin.

Afterwards, in order to link the LE with Thermodynamics, it is possible to regroup the terms, in order to give a better vision of the energy balance. First, let us consider a system where the potential does not depend on time, $U = U(x) \rightarrow dU(x) = \frac{\partial U(x)}{\partial x} dx$. Then LE reads:

$$dU \equiv \frac{\partial U(x)}{\partial x} dx = -\left(-\gamma \frac{dx}{dt} + \xi(t)\right) dx \tag{5.12}$$

Then, as Langevin dynamics conserves the energy of the system with its environment, the only flux of energy to change the internal energy of the system is a **heat** coming from the thermal bath. Combining eq (5.10) with (5.14) we can write down the first definition of heat:

$$dQ \equiv -\left(-\gamma \frac{dx}{dt} + \xi(t)\right) dx \tag{5.13}$$

The heat has a dissipative contribution that is always negative by definition, it is always removing energy from the system. The other term is linked to the thermal fluctuations and it removes and gives energy to the system. Eq. (5.13) can be written in terms of our observables as:

$$dQ = \frac{\partial U(x)}{\partial x} dx \tag{5.14}$$

The next step is to define the relation between LE and **work**. Let the potential be also a function of an extra non-eliminated degree of freedom $a(t)$, $U \equiv U(x, a)$. This free parameter can be the extension of a biopolymer, the stiffness of an optical tweezers, etc. The Langevin equation will read:

$$\gamma \dot{x}(t) - \frac{\partial U(x,a)}{\partial x} = \xi(t) \tag{5.15}$$

and the differential of the internal energy function will be:

$$dU(x,a) = \frac{\partial U(x,a)}{\partial x} dx + \frac{\partial U(x,a)}{\partial a} da \tag{5.16}$$

Comparison of (5.16) with the definition of heat in the mesoscopic systems (5.13) and with the first law of thermodynamics ($dU = dW + dQ$) leads to the following definition of work:

$$dW = \frac{\partial U(x,a)}{\partial a} da \tag{5.17}$$

It is called work the changes of energy coming from a change of the potential due to in a controlable parameter. In summary, the work and the heat in Sekimoto approach are calculated as:

$$Q = \int_{x_0}^{x_t} \frac{\partial U(x,a)}{\partial x} \circ dx \tag{5.18}$$

$$W = \int_{a_0}^{a_t} \frac{\partial U(x,a)}{\partial a} \circ da \tag{5.19}$$

where $\circ$ represents the integral in the Stratonovich sense [6]. Along this thesis, these formulas has played a key role, as the optical potential can be mapped, see section 2.6. As we discuss in Chapters 6, 7 and 8, we have all the possible observables to calculate heat and work along different processes.

In summary, the first idea to keep in mind is that the heat in a mesoscopic system can be interpreted as the disipation by friction and *the work exerted in the system by the particles of the fluid* and *the work exerted to the particles of the fluid by the system.* As it is imposible to characterize the dynamics of the N_A molecules which produce the Brownian motion, the brownian effect is taken into account by an artifitial function, the well studied *white noise.* On the other hand, there are some studies [187] where external noisy forces are applied and the associated work is calculated. Under our point of view, it is possible to interpret this extra energy as a heat flux, as the system is not able to differenciate between the work exerted by such forces and an actual flux of heat. Therefore, these results can be reinterpreted as a double bath systems. We will come back to this point in Chapter 6.

5.5 Entropy along fluctuating trajectories

The idea of entropy assigned to a single fluctuating trajectory may look contradictory, as a classical description defines the entropy as an ensemble quantity. The issue was clarified in a recent paper by Udo Seifert [188], where he adapted the Gavin Crooks definition of stochastic entropy [189]. Let us consider a system which evolves under the time evolution of a control parameter $a(t)$ embedded in a thermal bath. The evolution along the given process is described by a

---

[6] A brief introduction to the stochastic calculus is shown in Appendix B

trajectory $x(t)$. The total change of entropy, $\Delta s^{total}(t)$, can be split into two contributions: on the one hand we have the corresponding entropy associated to the heat dissipation along the process in the environment, $\Delta s^{e}(t)$, and on the other hand, the change of system's entropy, $\Delta s(t)$. The heat along a single trajectory $Q(t)$ can be calculated within the Sekimoto's framework previously described, eq. (B.12). Using the second law of Thermodynamics, the increase in entropy of the medium will be immediately defined as $\Delta s^{e} = Q/T$.

The other contribution is obtained from an analogy with the Gibbs entropy along non equilibrium processes,

$$S(t) \equiv -k \int_{\Re} dx \rho[x(t), a(t)] \log \rho[x(t), a(t)] \tag{5.20}$$

From (5.20) the entropy of the system along a single trajectory can be written as

$$s(t) = -k \log \rho[x(t), a(t)] \tag{5.21}$$

where $\rho[x(t), a(t)]$ is the position pdf obtained from the corresponding Fokker-Planck equation. From this definition we can recover eq. (5.20) as an ensemble over different realizations: $\langle s(t) \rangle = -k \int_{\Re} dx \rho \log \rho = S(t)$. Finally, the total change of entropy can be written as the sum of both changes:

$$\Delta s^{total}(t) = \Delta s^{e} + \Delta s(t) = Q(t)/T - k \log \frac{\rho[x(t), a(t)]}{\rho[x(0), a(0)]} \tag{5.22}$$

Thanks to this formula, if we know the potential $U(x, a(t))$ at any time, we will be able to calculate the production of entropy along single trajectories from experimental data[7].

5.6 Fluctuation theorems.

The well known Loschmidt paradox states that if Thermodynamics is obtained from the micromechanics, then the simmetry in the movement of every molecule should be conserved in the macroworld [190]. As Schrödinger argued, a clock could suddenly start working reverse with no violation of the thermodynamics laws. The effect of reducing the scale, both in time and space, is the posibility of the machine to work *reverse* to our intention. The symmetry effects arise when the number of particles is reduced. When it occurs, thermal fluctuations become

---

[7] See Appendix E

non-negligible and some individual events can break the second law. It follows that the work associated to certain process can be smaller than the difference of Helmholtz free energy between the initial and the final states($W < \Delta F$). These phenomena dissapear when we consider a large number of repetitions of the process, thus taking the mean value of the thermodynamic quantity. Then, the average work must obey the second law: $\langle W \rangle \geq \Delta F$.

These effects are properly studied by the **Fluctuation Theorems** (FTs). They express universal properties of the probability distribution $p(\Omega)$ for functionals $\Omega\left[x(t)\right]$ (like work, heat or entropy change) evaluated along different trajectories with well-known initial distributions $\rho_0(x)$ [177]. In other words, these *strange* behaviors can be quantified and hence, FTs provide the transition between the microscopic reversibility and the macroscopic irreversibility.

In 1993, Evans and Searles [191] derived an expresion to quantify the importance of the thermal fluctuation in the violation of the second law of the thermodynamics and how this effect vanishes exponentially with the increase of the size or the time scale of the system. The probability to disobey the second law was characterized with the entropy consumed or absorbed along a single trajectory:

$$\frac{\rho(\Delta s^{total})}{\rho(-\Delta s^{total})} = \exp(\Delta s^{total}) \tag{5.23}$$

where Δs^{total} represents the total change of entropy along a trajectory of duration t. As the entropy has extensive character, the expansion of the system size or of the trajectory time will vanish the entropy consuming trajectories, coming back to the usual second law. This FT was first experimentally tested by Wang *et al* with optically trapped colloidal particles in 2002, [85].

In order to introduce the existing FTs, let us define a functional Ω (it can be the exerted work, the transferred heat or the entropy difference) that follows a probability density function $\rho(\Omega)$. Following [192], the FTs can be clasified phenomenologically in three groups.

- Integral fluctuation theorems (**IFTs**)

  It is said that Ω is ruled by an IFT when it verifies the following identity:

$$\langle e^{-\Omega} \rangle \equiv \int d\Omega p(\Omega) e^{-\Omega} = 1 \tag{5.24}$$

  From the Jensen inequality[8], we notice that the eq. (5.24) derives into a thermodynamic law form: $\langle \Omega \rangle \geq 0$. To give an example, the total entropy

---

[8] $\langle e^x \rangle \geq e^{\langle x \rangle}$ [193]

change along a process obeys an IFTs. Let us consider the entropy change defined in epigraph 5.5, this functional $\Delta s^{total} = \Delta s^{e} + \Delta s$ will follow the next FT:

$$\langle e^{-\Delta s^{total}} \rangle = 1 \tag{5.25}$$

which implies the inequality $\langle \Delta s_T^{total} \rangle \geq 0$, one expression of the second law of Thermodynamics, i.e., the total entropy can never decrease [188].

- Detailed fluctuation theorems (**DFTs**)

  A stronger relation is found in cases ruled by:

  $$\frac{p(\Omega)}{p(-\Omega)} = e^{\Omega} \tag{5.26}$$

  Under this theorem, the odd moments of Ω can be expressed in terms of the even ones, and vice versa. DFT implies IFT, as the pdf are normalized $\int p(\Omega) d\Omega = 1$ [194].

- Generalized Crooks' fluctuation theorems (**CFTs**)

  Consider a protocole composed by a forward process F and a backward process B. Each process defines a characteristic work pdf: $p_F(\Omega)$ and $p_B(-\Omega)$. The CFT states that:

  $$\frac{p_F(\Omega)}{p_B(-\Omega)} = e^{\Omega} \tag{5.27}$$

  As the probabilities are normalized, a CFT leads to a IFT, but not to a DFT.

5.6.1 Jarzynski's equality

The second law of Thermodynamics can be presented as an inequality relating the Helmholtz free energy between an initial (A) and a final (B) state ΔF_{AB}, and the average work $\langle W_{AB} \rangle$, along the path : $\langle W_{AB} \rangle \geq \Delta F_{AB}$. There, the difference between both parameters is the dissipated work, thus expressing how far we are from the quasiestatic regime. The Jarzynski equality (5.28) establishes an equality between both parameters that **does not depend** on how fast the process $A \rightarrow B$ is befalling [195]:

$$\langle e^{-\beta W_{AB}} \rangle = e^{-\beta \Delta F_{AB}} \tag{5.28}$$

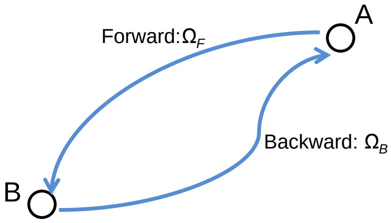

Figure 5.3: Schematic representation of the processes studied by the FTs. We start in a point of the phase space A to arrive to another point B. The protocol allows the measurement of the functional Ω (for instance, the associated work) along the forward and the backward processes. If the system follows a CFT, we can link both to know an associated equilibrium function difference, as the difference of Helmholtz free energy in the case of work.

where the equality the brackets ($\langle\rangle$) represents the average along several realizations of the same process. Therefore, this equality allows the experimental estimation of the Helmholtz free energy difference between two states using non-equilibrium processes. This theoretical results has great importance in the study of the mesoscopic world because: i) it sets an equality in the formulation of the second law of thermodynamics, proving that the classical vision is a consequence of a wider reality. ii) it allows to obtain the parameters which characterize equilibrium states, such as ΔF, from non-equilibrium processes.

5.6.2 Crooks' fluctuation theorem

Gavin Crooks derived a particular case of the fluctuaction theorems for the case of the work [189]. Let a system, characterized by a free parameter $a(t)$, evolve from an initial state A to a final state B. The process of going from A to B is called the *forward* process, while that going from B to A is the *backward* process. If this process is repeated several times, we can build two independent work pdf: $\rho_F(W)$ (forward) and $\rho_B(W)$ (backward). Both distributions are linked by the so-called Crooks' fluctuation theorem:

$$\frac{p_F(W)}{p_B(-W)} = e^{-\beta(W-\Delta F)} \tag{5.29}$$

This theorem has been tested along the past fifteen years with simple examples as colloidal particles or in more complicated systems as biopolymers [196]. A beautiful proof was published in 2005 by Collins *et al*, where they use the FT to obtain the difference of free energies in the case of different RNA mutants by an out-of-equilibrium protocole [30]. Fig. 5.4 shows their results for the work needed to fold and unfold different mutants, where the *forward* and *backward* work pdf cross in the value of the correspond free energy.

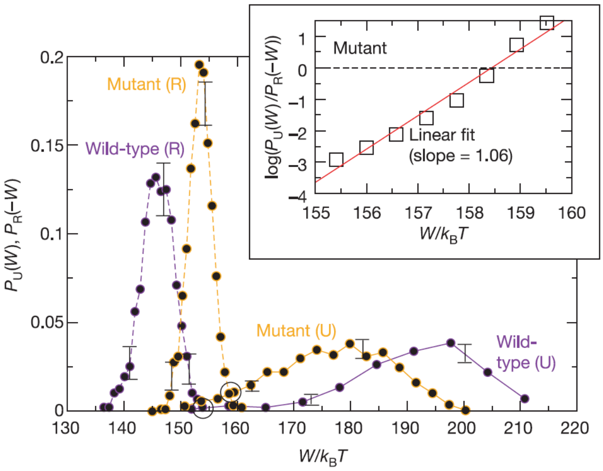

Figure 5.4: Non-Gaussian work distribution in RNA folding (dashed line)-unfolding (solid line) experiment. Results from two different RNA mutants are presented. Crossings between distributions are indicated by black circles. Courtesy of [30].

6

Noise as temperature

6.1 Introduction

The last ten years have seen the dawn of a new branch of physics, the so-called *Stochastic thermodynamics*. From the joint of the Sekimoto's *stochastic energetics* [62] with the proposal that the entropy can be assigned to fluctuating trajectories [188], this new framework should not be considered as such a simple analogy at the mesoscale of the classical thermodynamics, but a new framework with its corresponding laws. One of the key parameters in the mesoworld is the temperature. Due to the small size of the systems, the thermal fluctuations are of the same order of magnitude than the energy that the system exchanges with its environment, allowing *strange* behaviors to appear. Along these years, several experimental techniques have been used to study systems where the thermal fluctuations are relevant [11]. Although several methods to control the temperature have been developed, they are still very limited to a small range of temperatures and sample volume (due to physical bounds as evaporation, convection, etc..). Typically, the temperature has been controlled by heating the Brownian particle or its surroundings. Spherical colloids [197] or nanorods [198] were selectively heated by external sources of light that is not absorbed by the solvent. In [31, 33], the variation of the temperature in the surroundings of a dielectric sphere was achieved by an optical beam whose wavelength matches an absorption peak of the solvent. In all these cases the temperature increase did not exceed several tens of Kelvin. Response time of several tens of milliseconds has been achieved due to small volumes of the studied systems' environments. Although this range of temperature variation is enough to produce changes in the behavior of biological systems, such as cells or biomolecules [199, 200], it is relatively small to test with FTs with large energy exchanges. Besides the viscosity changes due to temperature modification, represents a barrier to experimental testing.

In this chapter, we adress the following questions: *What would happen if another stochastic force were applied to the Brownian particle?*, *Would the particle be able to distinguish it from an increase of the media's temperature?* These questions were mentioned in [62], where a mechanical shaking was proposed with the same white spectrum. If the features of the extra noise were the same than those of the thermal noise, it would mimick thermal fluctuations. This extra noise would be a great tool in order to study the different fluctuation theorems along non isothermal processes, as well as produce different processes not available now, such as adiabatic curves. Let study a microsphere (radius R) immersed in a liquid (temperature T and kinetic viscosity η) inside an optical trapping potential, $U(x, x_0) = \frac{1}{2}\kappa(x - x_0)^2$, where κ is the corresponding stiffness and x_0 is the equilibrium position of the trap. The system can be considered as overdamped, obeying the LE as follows:

$$\gamma\dot{x}(t) = -\kappa[x(t) - x_0] + \xi(t) + \zeta(t), \tag{6.1}$$

Together with the thermal noise represented by $\xi(t)$, we have included an extra noise force by $\zeta(t)$. The properties of the extra force are zero mean, $\langle\zeta(t)\rangle = 0$, and a correlation $\langle\zeta(t)\zeta(t+\tau)\rangle = \sigma^2\Gamma(\tau)$, where σ is the noise's amplitude and $\Gamma(\tau)$ is a normalized function ($\int_{\Re} d\tau\Gamma(\tau) \equiv 1$) peaked at zero. Following the analogy with the thermal noise, the extra noise should have no memory. Therefore, $\Gamma(\tau)$ should be taken as the Dirac function $\delta(\tau)$. Under this assumption, as both noises are uncorrelated, it is possible to define an effective noise function $\xi_{eff}(t) \equiv \xi(t) + \zeta(t)$, whose mean is zero by definition and whose correlation can be written as $\langle\xi_{\text{eff}}(t)\xi_{\text{eff}}(\tau)\rangle = 2kT_{\text{kin}}\gamma\delta(\tau)$, being the effective temperature defined as:

$$T_{\text{kin}} = T + \frac{\sigma^2}{2k\gamma}. \tag{6.2}$$

As the amplitude of the extra noise is a real positive number, the effective temperature felt by the particle will always be higher than the environmental temperature. Notice that the media does not increase its temperature, and therefore, the value of the viscosity term will remain constant, increasing the easiness of the system.

On the other hand, the extra source of noise will be applied in a single axis, from now *x-axis*, then, the temperature will remain constant along the other two directions, *y-axis* and *z-axis*, therefore we can talk about an anisotropic temperature in our system. Unfortunately, due to experimental restrictions, the applied noise cannot be perfectly white, therefore, one of our goals will be to characterize the limitations of the technique. Along this research, we will first study the features of the effective temperature in stationary processes (by the position pdf and the PSD). Later, a double-well potential is implemented to study the thermally activated transitions in the presence of the extra source of noise; and finally, a non-equilibrium process is designed to test the Crooks' fluctuation theorem.

6.2 Experimental details

Various experimental techniques permit exerting controllable forces on an optically trapped sphere, either with magnetic [41] or optical [201–203] fields, or modulating the position of the trap $x_0(t)$ [187]. We have used random electric fields applied to optically trapped dielectric spheres with electric charges that remain constant during a long time, as we demonstrated in 2.4.2. The experimental setup is explained in detail in 2.4.3. In summary, it consists of a 1060nm optical beam (Manlight, ML10-CW-P-OEM/TKS-OTS) which is steered by an AOD (ISOMET LS55 NIR). The beam is highly focused inside a custom-made chamber to create the trap by a high NA oil-immersed objective (Nikon, CFI PL FL 100× NA 1.30). The position of the bead is recorded by an aditional 532nm laser coaxial to the trapping laser. The scattered light is collected by the microscope objective (×10, NA=0.10) and projected to a QPD. A 532 band-pass filter is placed before the QPD to avoid the infrarred scattered light. The studied sample consists of a diluted suspension of polystyrene microspheres (G.Kisker-Products for Biotechnology, polystyrene microparticles PPs-1.0 with a diameter of 1.00± 0.05 μm) in distilled de-ionized water, with a final concentration of a few spheres per ml.

The sample was injected into a custom-made electrophoretic fluid chamber with two electrodes connected to a computer-controlled electric generator and an amplifier 2.4.2. Electrical signals on the electrodes were produced by the generator fed with a noisy sequence close to white Gaussian noise. The sequence was generated using independently distributed random variables $\zeta_{n\delta t}$, with $\langle\zeta_{n\delta t}\rangle = 0$, $\langle\zeta^2_{n\delta t}\rangle = A$, and $\langle\zeta_{n\delta t}\zeta_{m\delta t}\rangle = 0$ for $n \neq m$, A being the variance of the noise. The time interval δt is the clock time of the generator, which is $\delta t = 0.2\,\mathrm{ms}$ in the experiments. Notice that δt is a lower bound to the actual correlation time of the external force, which also depends on the response characteristics of the amplifier.

The kinetic temperature of the optically trapped sphere is obtained from the analysis of the output signals of the position detection system. The system needs two calibration procedures: calibration of the position detection system and calibration of the force exerted by the trap on the sphere. Both calibrations are described in previous sections 2.3.3 2.4.2. Briefly, we will calibrate the detection system in order to be sure that the bead never scapes the linear range of the nanodetection system, S_{QPD}, the chosen method was the study of the PSD over the bead's Brownian fluctuations, see 2.3.3. The other parameteres needed to be known is our trap stiffness. In our experiment, κ=(6.0±0.1 pN/μm and S_{QPD}=1280 nm/V. Secondly, the AOD should be calibrated to know exactly where the equilibrium position of the trap is when the non-equilibrium process is executed, see subsection 2.4.1 S_{AOD}=(4267±40) nm/$\mathrm{V_{AOD}}$. Finally, the electric force must be calibrated S_{elect} and analyze the force over a long space of time to be sure the exerted force is not changing due to Faradaic effects, see subsection 2.4.2. The complete mapping of the force is done following the method described in 2.6. This technique probed that the bead has never gone out of the parabollic regime.

6.3 Experimental results

6.3.1 Brownian sphere in a stationary trap with additional noise

We first analyzed the time traces of the position of the sphere in the optical trap with a given trap stiffness with and without the external force $\zeta(t)$. PSDs of the position of the sphere are shown in Fig.6.1, while Fig.6.2 illustrates the histograms of the sphere position. As seen, the maximal sphere Brownian excursions without the additional noise do not exceed (±50 nm). However with the additional stochastic force the maximal amplitude may be (±250 nm). Even in this case the sphere displacements do not exceed the linear ranges of both the position detection system and the harmonic approximation of the optical trapping potential. At a given value of the noisy voltage at the electrodes (about 200 V in our experiments) the maximal broadening of the position histogram depends strongly on the design of the electrophoretic chamber, which defines the value of the electric field near the optically trapped sphere. For the proof-of-principle experiments described in this report the absolute values of the sphere charge and applied electric field can change results only quantitatively. What is important that 1) the motion of the sphere in the sinusoidal field has the constant amplitude during more than two hours (see 2.4.2) and, 2) the broadening and compressing of the histograms of the sphere position are reversible when we switch on and off the noisy electric field.

The parameters of the computer-controlled generator allowed us to obtained the constant spectrum of the electrical signal for frequencies up to 1 kHz. As can be seen in Fig. 6.1, the PSD in the presence of the additional force is also Lorentzian and the corner frequency f_c does not change, as expected, since it is a function only of κ and γ. On the other hand, the whole PSD increases due to the external force, which can be interpreted as an increase of the effective kinetic temperature. This increase of temperature can also be observed in the stationary probability density $\rho(x)$ of the position of the sphere, depicted in Fig. 6.2. The additional force clearly broadens the histogram.

The following experiment demonstrates how fast one can switch the effective kinetic temperature of a Brownian particle. We studied the temporal response of the amplitude of the random motion of the particle when we changed the amplitude of the additional noise abruptly. Fig. 6.3 shows that the standard deviation of the sphere position (and hence the kinetic temperature) changes with the same rate as the electric field amplitude, so that only the relaxation time of the trap ($\tau_c = \gamma/\kappa =$ 1.4 ms in our experimental conditions) is the limiting factor.

6.3.2 Kramers transitions in the presence of additional white noise

We now consider the motion of the sphere in the presence of the additional stochastic force in an optical trap with more complex structure, namely, in a double-well optical potential. As it is well known, Kramers transitions [186] - thermally activated escape over a potential barrier - may occur in this case. Kramers transitions are important ingredients involved in many chemical, physical, and biological phenomena [131]. To realize Kramers transitions, the optical traps of the dual-well trapping potential must be close to each other, and thermal

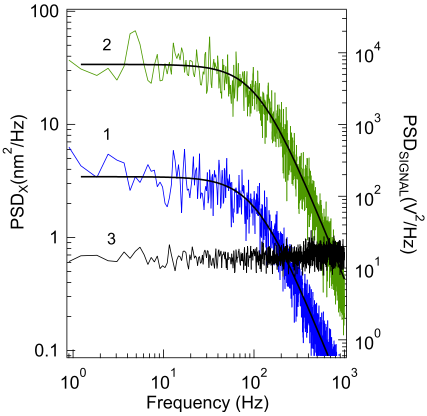

Figure 6.1: PSD of the position of the sphere without (blue curve, 1) and with (green curve, 2) the additional stochastic force. Solid black lines correspond to the Lorentzian fits. The power spectral density of the input noisy signal measured at the electrodes of the fluid cell is also shown (black line, 3).

energy has to be large enough to drive the sphere over the potential barrier between neighboring optical traps. The probability distribution of residence times, i.e., the intervals of time between escape events from trap to trap (the Kramers transition rate) at the overdamping regime depends on the height of the potential barrier and the absolute temperature of the system [186]. Experimental results at room temperature are well described by the Kramers theory [87].

In our experiments, we show that the additional noise decreases the residence time according to a new kinetic temperature. Using a time-sharing protocol 2.4.1, we created a double-well potential where the distance between the two equilibrium positions and their depths could be controlled. Fig. 6.4a) shows a fragment of the time traces of the 1μm diameter sphere moving in the double-well potential. At a given moment of time, the additional noise signal was switched on. The spatial probability density of the sphere $\rho(x)$ is related to the potential energy profile of the trap ,$U(x) = ax^4 + bx^2$, as $\rho(x) = Z^{-1}\exp[U(x)/kT]$, being Z is the partition function. We measured the probability density of the position without additional noise from a time series $x(t)$, and the potential $U(x)$ was found with two wells separated by a barrier whose energy is above the thermal energy kT, as shown in Fig. 6.4b). Fig. 6.4c) shows the residence time probability distribution without and with additional

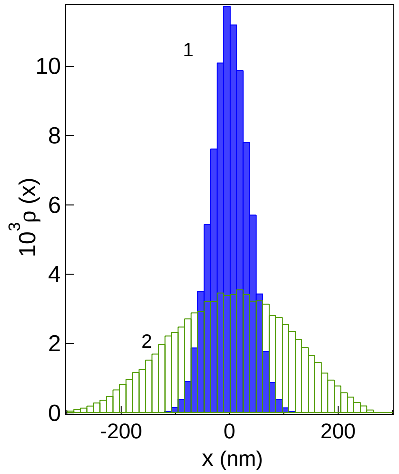

Figure 6.2: Histograms of the sphere position without (1) and with (2) the additional stochastic force corresponding to the PSD curves (1) and (2) shown in Fig. 6.1.

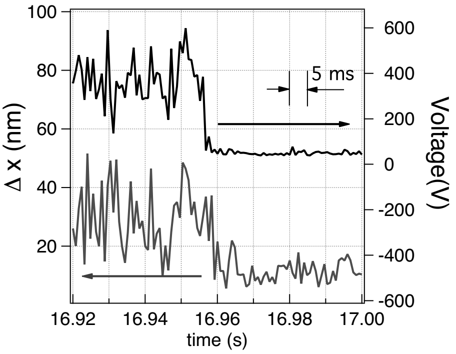

Figure 6.3: Standard deviation of the position of the sphere (left axis) and amplitude of electric signal (right axis) as a function of time at an abrupt change of the electric field.

noise signals. As predicted by Kramers [186], the residence time probability decays exponentially with the residence time. Notice that in the presence of the additional noise, the probability distribution decays faster, which is consistent with an increase of the effective temperature.

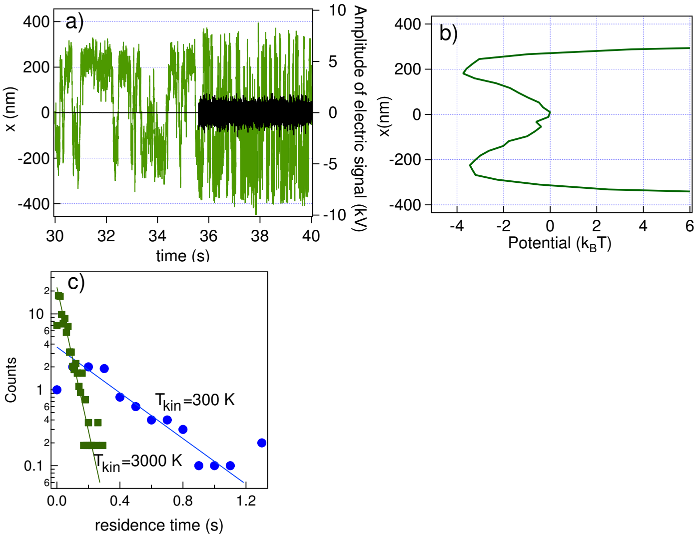

Figure 6.4: a) Position traces (green lines, left axis) of the sphere in the double-well potential. The black lines (right axis) show the voltage on the electrodes. The additional noisy signal was switched on at 35.5 s. As seen the frequency of the Kramers transitions increases. b) Double well trapping potential obtained as $U(x) = -kT \log \rho(x)$. c) Probability of the residence time of the Kramers transitions at room temperature (green squares) and at 3000 K (blue circles).

6.3.3 Non equilibrium process: Testing Crooks' fluctuation theorem

For a complete characterization of the effective thermal bath, we have studied the dynamics of the particle in a non-equilibrium situation. The response of the Brownian particle to an external driving force is related to the temperature. The fluctuation–dissipation relation (FDR) is a mathematical identity relating the temperature, the response close to equilibrium, and the time correlations of the unperturbed system. Crooks fluctuation theorem (CFT) goes further, establishing a relationship between the pdf of the work W along a process arbitrarily far from equilibrium, $\rho_F(W)$, and the pdf of the work in the time-reversed process, $\rho_B(W)$ [189]. Notice that CFT goes beyond the fluctuation-dissipation relationship and it is valid not only in the linear but also in non-linear response limit.

Let the system starts at equilibrium states at temperature T both in the forward and time-reversed processes. If the free energy difference between the final and initial states (of the forward process) is $\Delta F = F_{\text{fin}} - F_{\text{ini}}$, the Crooks theorem states that

$$\log\left[\frac{\rho_F(W)}{\rho_B(-W)}\right] = \frac{W - \Delta F}{kT}, \tag{6.3}$$

This relation has been checked both in simulations and experiments for processes at room temperature [30, 85, 196].

We have implemented the non-equilibrium protocol depicted in Fig.6.5. In the first step, the trap centre is moved from $x_0 = -L$ to $x_0 = +L$ at constant velocity $v = 2L/\tau$, where L=61 nm and τ=6.3 ms. This is the forward process. We then let the sphere relax to the new equilibrium position, keeping the trap centre at $x_0 = +L$ for the same time τ=6.3 ms, which is larger than the relaxation time of the trap, $\tau_c = \gamma/\kappa$=1.4 ms. Then the trap is moved back from $x_0 = +L$ to $x_0 = -L$ with the same velocity $-v$ (reverse process) and it is held fixed at $x_0 = -L$ for the same time τ. This protocol was repeated about 10^4 times. During the protocol the position of the sphere was monitored, and the position traces are shown in Fig.6.5. In each cycle we calculated the work in the forward and backward processes following [62], where the work done by an external agent in a microscopic system during an arbitrarily far from equilibrium process is introduced. If the non equilibrium driving is described by the evolution of a control parameter $\lambda(t)$, then the work done along the process is given by

$$W = \int_{\lambda(0)}^{\lambda(\tau)} \frac{\partial U(x(t), \lambda(t))}{\partial \lambda} \circ d\lambda(t), \tag{6.4}$$

where $\circ$ means that the integral is taken in the Stratonovich sense, and $U(x, \lambda(t))$ is the trapping potential. In our case, the control parameter is the position of the trap centre, $\lambda(t) = x_0(t)$. Notice that the work is a stochastic quantity that depends on the trajectory followed by the particle, $x(t)$.

Fig. 6.6 shows the experimental values of the probability density of the work $\rho_F(W)$ ($\rho_B(-W)$) in the forward (backward) process. We found that they have

Gaussian distributions intersecting approximately at $W = 0$ since in our case $\Delta F = 0$.

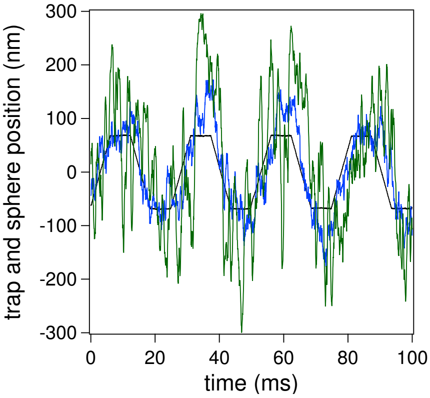

Figure 6.5: The position of the centre of the trap (black line) and the positions of the sphere as a function of time without external electric field (blue curve) and with noisy electric field (green curve).

6.4 Discussion

Consider first the experimental results on the motion of the sphere in a stationary trap with additional noise (Fig. 6.1 and 6.2). We can calculate the effective kinetic temperature either from the data on PSD or on $\rho_{\mathrm{ss}}(x)$. As we show below from the theoretical point of view, the temperatures found using these two sets of data do not equal if the spectrum of the additional noise deviates from the white spectrum.

From the Langevin equation (6.1), we calculated (see details in the appendix I) both the PSD and the stationary probability distribution $\rho_{\mathrm{ss}}(x)$ for an external noise $\zeta(t)$ with arbitrary correlation $\langle \zeta(t)\zeta(t')\rangle = \sigma^2\Gamma(t-t')$, with $\int_{-\infty}^{\infty}\Gamma(t)dt = 1$. The PSD is given by:

$$\mathrm{PSD}(f) = \frac{1}{4\pi^2\gamma^2}\,\frac{2\gamma kT + \sigma^2\tilde{\Gamma}(f)}{f^2 + f_c^2}, \tag{6.5}$$

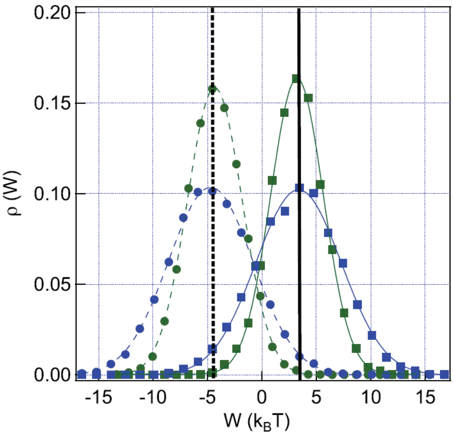

Figure 6.6: The probability density function of the work obtained in around 7000 realizations of the forward process $[\rho_F(W)]$, and the probability density function obtained from the same number of realizations of the reverse process $[\rho_B(-W)]$. The blue (green) solid (dashed) lines represents Gaussian fits to $\rho_F(W)$ and $\rho_B(-W)$ without and with external noisy field. The vertical black lines represent the analytical value of the average work in the forward process calculated using Eq. (6.11) (solid line) and the average of $-W$ in the reverse process (dashed line) which is calculated in an analogous way to Eq. (6.11).

where $\sigma^2\tilde{\Gamma}(f)$ is the Fourier transform of the correlation function of the external noise. However, if $\tilde{\Gamma}(f)$ is constant for frequencies much higher than the corner frequency of the trap f_c, then the PSD (6.5) is indistinguishable from a Lorentzian function with the same corner frequency and the effective kinetic temperature, which we denote as T_{PSD}:

$$T_{\text{PSD}} \equiv \frac{2\pi^2\gamma f_c^2\,\text{PSD}(0)}{k} = T + \frac{\sigma^2}{2k\gamma}. \tag{6.6}$$

On the other hand, the stationary probability density $\rho_{\text{ss}}(x)$ is Gaussian with zero mean and dispersion

$$\langle x^2\rangle_{\text{ss}} = \frac{kT}{\kappa} + \frac{\sigma^2}{\gamma\kappa}\int_0^\infty dt\, e^{-\kappa t/\gamma}\,\Gamma(t), \tag{6.7}$$

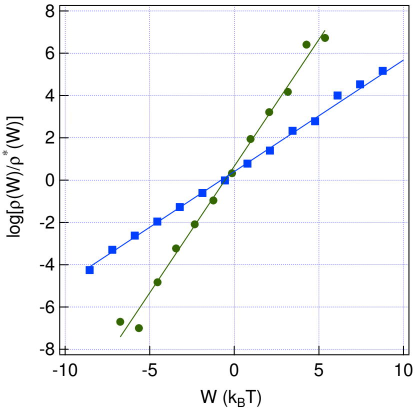

Figure 6.7: $\ln\left[\rho_F(W)/\rho_B(-W)\right]$ as a function of W/kT without (blue squares) and with additional noise (green circles) corresponding respectively to the PSD curves (1) and (2) shown in Fig. 6.1. The solid lines are linear fits of the experimental data.

which yields the effective temperature T_{hist}

$$T_{\mathrm{hist}} \equiv \frac{\kappa\langle x^2\rangle_{\mathrm{ss}}}{k} = T + \frac{\sigma^2}{\gamma k}\int_0^\infty dt'\ \Gamma(t')e^{-t'/\tau_c}, \tag{6.8}$$

being $\tau_c = \gamma/\kappa$ the relaxation time of the particle in the trap. If $\Gamma(t)$ is peaked around $t = 0$ and the correlation time of the noise, given by $\tau_\Gamma \equiv \int_0^\infty dt\, t\, \Gamma(t)$, is small compared to τ_c, T_{hist} is approximatively

$$T_{\mathrm{hist}} \simeq T + \frac{\sigma^2}{2k\gamma}\left(1 - \frac{2\tau_\Gamma}{\tau_c}\right). \tag{6.9}$$

Notice that unlike T_{hist}, T_{PSD} defined as (6.6) does not depend on the correlation time of the noise. The difference between T_{PSD} and T_{hist} is proportional to τ_Γ/τ_c, therefore it vanishes for if the external noise is white. In our experiments, $\tau_c = 1.4$ ms and τ_Γ=0.26 ms, being τ_Γ obtained experimentally from the spectral analysis of the voltage at the electrodes (see below).

In our setup we achieved the constant spectrum of the noise only up to 1kHz (Fig. 6.1). We measured the autocorrelation function of the signal on the electrodes $V(t)$, defined in [204] $\tilde{\Gamma}(t) = \frac{\langle V(t')V(t'+t)\rangle}{\langle V(t')V(t')\rangle}$, which can be fitted to the function $\tilde{\Gamma}(t) = \exp\left[-(t/\tau_\Gamma)^2\right]\cos\left(\frac{t}{\tau_o}\right)$, being τ_Γ=0.26 ms and τ_o= 0.17 ms. The correlation of the noise is related to $\tilde{\Gamma}(t)$ by $\Gamma(t) = N\tilde{\Gamma}(t)$, where N is a normalization constant such that $\int_{-\infty}^{\infty}\Gamma(t)dt = N\int_{-\infty}^{\infty}\hat{\Gamma}(t)dt = 1$. The full expression of the correlation function of the additional noise is

$$\Gamma(t) = \frac{e^{tc^2/4t_o^2}}{\sqrt{\pi}}\frac{e^{-(t/\tau_\Gamma)^2}}{\tau_\Gamma}\cos(t/t_o). \tag{6.10}$$

Figure 6.8 presents a quantitative summary of our measurements performed by different intensities of the additional noise signal. We have increased the intensity of the noisy voltage and from (6.6) we found that $\sigma^2/(2k\gamma)$ is a measure of the noise intensity in Kelvin. We plot the effective temperatures T_{PSD} and T_{hist} as functions of $T_e = \sigma^2/(2k\gamma)$. We observed experimentally that T_{hist} and T_{PSD} coincide within statistical errors.

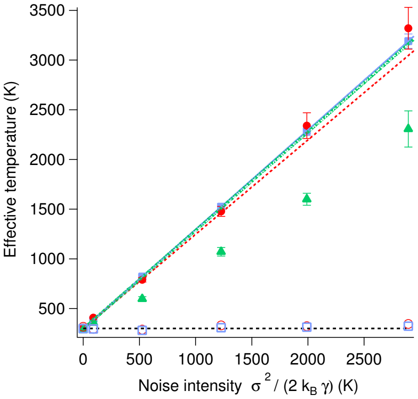

Figure 6.8: Effective kinetic temperatures, T_{PSD} (blue squares), T_{hist} (red circles) and T_C (green triangles) (see the definition of this temperature below) as functions of $T_e = \sigma^2/(2k\gamma)$. Symbols correspond to experimental data, where error bars only take into account the statistical error of the fits with a statistical significance of 90%. Lines represent the analytical values obtained for non-white external noise $\zeta(t)$ with correlation function given by Eq. (6.10) for T_{PSD} (6.6) (blue solid line), T_{hist} (6.8) (red dashed line) and T_C (green dotted line), which was obtained analytically using Eq. (6.12).

Let us consider now experimental results on the out-of-equilibrium process (Figs. 6.5-6.7). As seen in Fig. 6.6, the experimental value of the average work is close to the analytical value of the average of the work done in a time τ over the ensemble of trajectories [205], which for the forward process is obtained by integrating the Langevin equation (6.1) (see Appendix C for details):

$$\langle W \rangle = \gamma v^2 \tau \left[1 + \frac{\tau_c}{\tau} (e^{-\tau/\tau_c} - 1) \right] \tag{6.11}$$

The above result is not affected by the addition of the external noise because the work depends linearly on the additional noise, whose average is zero. Notice also that for slow driving ($\tau/\tau_c \gg 1$) we recover the Stoke's limit $\langle W \rangle \simeq \gamma v^2 \tau$. The analytical value of the work in the forward process without external field is $\langle W \rangle = 14.34$ pN nm whereas the experimental value is $W_{exp} = (15.06 \pm 0.14)$pN nm. Notice that we underestimated the actual error of the work since we only took into account the statistical dispersion of the data but not the experimental error. An error of 0.1 pN in the force and 1 nm in the position would yield approximatively an additional error which might be of the same order of magnitude of the statistical error. We also show in Fig. 6.6 that the PDFs of the work get wider when we increase the amplitude of the external noise, as expected.

We introduce a new effective temperature, the *Crooks Temperature* T_C, to check the consistency of our effective thermal bath for non-equilibrium processes. We define T_C as the inverse of the slope (divided by k) of the linear fit to $\ln \left[\frac{\rho_F(W)}{\rho_B(-W)} \right]$ as a function of W, following Eq. (6.3). The work distributions are Gaussian and in this case Crooks theorem is given by a simple relationship between the average and the variance of the work,

$$T_C = \frac{\sigma_W^2}{2k\langle W \rangle}. \tag{6.12}$$

The expression for σ_W^2 is cumbersome and very sensitive to the specific form of the correlation of the external noise $\Gamma(t)$. T_C can be obtained analytically using (6.12) for a particle described by the Langevin equation (6.1) under an arbitrary external noise with correlation $\Gamma(t)$ and intensity σ^2. Depending on the shape of $\Gamma(t)$, we can get T_C larger or smaller than T_{hist}, for example. The full expression of T_C in terms of the correlation of the additional noise and all the physical parameters of our system can be found in Appendix C.

Figure 6.7 shows that $\ln[\rho_F(W)/\rho_B(-W)]$ depends linearly on W with and without additional noise. We first test the validity of Crooks theorem in the absence of external noise, where $\sigma^2 = 0$ and it is expected that $T_C = T$. The experimental effective temperatures are in this case $T_{\rm hist} = (310\pm\ 3)$K, $T_{\rm PSD} = (297\pm\ 7)$K and T_C=(283±1) K, being the errors purely statistical and therefore a lower bound to the real error. With external noise, the slope of $\ln\left[\rho_F(W)/\rho_B(-W)\right]$ as a function of W decreases when increasing the amplitude of the external noise, indicating an increase of the effective Crooks temperature T_C.

We now try to explain the deviation between T_C (Fig. 6.8) and the temperatures calculated from the position traces in terms of the finite correlation time of the noise. We model the motion of the particle by the Langevin equation (6.1) with the noise correlation that fits the experimental data, given by Eq. (6.10). For $\Gamma(t)$ defined in Eq. (6.10), we obtain using (6.8) $T_{\rm hist} = T + 0.95\ T_e$ which is slightly smaller than $T_{\rm PSD} = T + T_e$ (6.6) and fits the experimental data. However, the analytical value of T_C for different noise intensities (dashed line in Fig. 6.8), given by Eq. (6.12) is significantly above the experimental value of T_C. We notice that our calculations predict that both for slow driving ($t/\tau_c \gg 1$) and in the white-noise limit ($\tau_\Gamma/\tau_c \to 0$) all the temperatures collapse to a single line of slope unity: $T_{\rm PSD} = T_{\rm hist} = T_C = T + T_e$. Both limits were unable to reproduce with our experimental setup because moving the trap slower, the relative error of the work increases and the generator of our setup does not allow to reduce τ_Γ.

Langevin equation is valid for our system since the PSD of the position is Lorentzian. Therefore we discard that the deviation between T_C and both $T_{\rm hist}$ and $T_{\rm PSD}$ observed in our experiment is due to the finite bandwidth of the additional noise. Electrophoretic effects may explain this deviation: in our system, the particle feels a random force which is not exactly the signal recorded from the electrodes due to the reordering of the electric charges of water molecules around the bead. This effect is enhanced when the trap is driven out of equilibrium. Notice that this represents a difference with the experiment introduced in [187] where the trap centre is moved randomly and Crooks temperature tends to the equilibrium temperature when the correlation time of the external noise tends to zero.

6.5 Conclusions

In conclusion, we have presented an experimental technique that allows one to control the kinetic temperature of a Brownian particle over a wide range of values, from room temperature to several thousands Kelvin. The environment created by the noisy external force mimics a high temperature reservoir with the limitations analyzed in this report. Our technique opens the possibility of implementing a variety of non-isothermal processes. For example, the increase of temperature affects only one spatial direction. By coupling the coordinate of the particle along this direction with an orthogonal coordinate, one can effectively couple two thermal baths at different temperature through a Brownian degree of freedom, as in the Feynman ratchet and other Brownian motors and refrigerators. Another possible aplication is the calibration of potential landscapes with energetic walls much higher than the enviromental thermal energy. If the extra source of noise is connected, the system will be able to jump across the barriers to use the Boltzmann equation to map the whole potential. One could also implement adiabatic processes by designing a protocol where $\rho(x)$, and therefore the entropy of the system along a stochastic trajectory [188], $S(t) = -k \log \rho(x,t)$, does not change in time. The density $\rho(x)$ can be kept constant in time with our setup by changing the stiffness of the trap and the intensity of the external random force in a synchronous way. In the next chapter, this possibility is explored to study non-isothermal processes.

6.6 Acknowledgements

This chapter was developed under a colaboration with Prof. J. M. R. Parrondo group, Univ. Complutense de Madrid.

7

Non-isothermal stochastical thermodynamics

7.1 Introduction

The small size of the systems in the mesoscale makes the exchanges of energy be of the same order than the thermal fluctuations. Although the temperature is a key concept and parameter along thermodynamic processes, its control lacks a wide range of variability. Moreover, a temperature change in fluids leads to a change of its viscosity that increases the complexity of the problem. Indeed, there is only a few number of experiments where the temperature is a control parameter [31, 33, 206]. However, one of the goals of stochastic thermodynamics is its application to the nanotechnology [207], drawing an analogy with the macroscopic thermal engines. For this purpose, it is necessary to broaden our knowledge from the deeply studied isothermal processes (both theoretically [10, 208, 209] and experimentally [30, 85, 210]) to the non-isothermal ones. Unfortunately, these troubles reduces the study of system with variable temperature to simpler systems, such as electric circuits [206].

Thanks to the previously explained technique [211], see Chapter 6, we can modify the kinetic temperature of the sample under consideration along different protocoles to study energy exchanges $\{W, Q\}$. Since the first attempts to validy FT [85], optically trapped microspheres have offered a mod el system for experimental studies of stochastical thermodynamics. In this chapter, we do an analogy between an optically trapped bead and a classical piston. First, we try to understand the simplest process, where only one parameter (temperature or stiffness) is changed. Afterwards, we analyzed the effect of heating a sample in its momenta phase space Γ_v, i.e., its kinetic energy. From this empirical observation, we discuss the meaning of adiabatic in our scenario, studying the previously proposed protocoles [64,188]. Finally, an experimental Carnot engine is presented, using a trapped bead as working substance.

The object of study in this chapter is a colloidal particle within a parabollic potential $U(x,\kappa)$ in contact with a thermal bath T_{kin}. The energy of the system can be divided in potential and kinetic energy $E(x,p) = U(x,\kappa) + K(p)$, where the potential is defined as $U = \frac{1}{2}\kappa x^2$and the kinetic energy as $K = \frac{1}{2m}p^2$. Let us consider a process under which the system evolves from A to B defined by a protocole $\lambda(t) = \{\kappa(t), T(t)\}$. The difference of energy can be split as:

$$dE = dU + dK = \underbrace{\frac{1}{2}x^2 d\kappa}_{\delta W} + \underbrace{\frac{\kappa}{2}d(x^2)}_{\delta Q_x} + \underbrace{\frac{1}{2m}d(p^2)}_{\delta Q_v} \tag{7.1}$$

where each term can be associated to work or heat. Throughout a real process, the flux of energy as heat has a kinetic and a potential contribution. The ensemble average of heat and work is defined as:

$$\langle W \rangle = \frac{1}{2}\int_{\lambda(t)} \frac{T}{\kappa} d\kappa \tag{7.2}$$

$$\langle Q_x \rangle = \frac{k}{2}\int_{\lambda(t)} \kappa d\frac{T}{\kappa} \tag{7.3}$$

$$\langle Q_v \rangle = \frac{k}{2}\int_{\lambda(t)} dT \tag{7.4}$$

where both, position and velocity, satisfy equipartition theorem: $\langle x^2 \rangle = kT/\kappa$ and $\langle v^2 \rangle = kT/m$. Next table shows the analitical average values of work and heat of each process. The calculation is done under quasistaticity assumtion over the studied protocoles.

Process	Condition	$\langle W \rangle$	$\langle Q_x \rangle$	$\langle Q_v \rangle$
Isothermal	$dT = 0$	$\frac{kT}{2} \log \frac{\kappa_2}{\kappa_1}$	$-.\frac{kT}{2} \log \frac{\kappa_2}{\kappa_1}$	0
Isochoric	$d\kappa = 0$	0	$\frac{k}{2}\Delta T$	$\frac{k}{2}\Delta T$
Adiabatic overdamped	$T = \Lambda^{\mathrm{OD}}\kappa$	$\frac{k}{2}\Delta T$	0	$\frac{k}{2}\Delta T$
Adiabatic underdamped	$T^2 = \Lambda^{\mathrm{UD}}\kappa$	$k\Delta T$	$-\frac{k}{2}\Delta T$	$\frac{k}{2}\Delta T$

Table 7.1: Average values of thermodynamic quantities over different processes

During an isothermal process, $\langle Q_v \rangle$ will vanish. This fact can be connected to the invariance of $\langle v^2 \rangle$, and then, to the invariance of the velocity phase-space Γ_v. Nonetheless, let us consider the simplest non-isothermal process. The potential landscape remains constant, while the temperature changes from T_1 to T_2. There will not be an exerted work to (by) the system. But two fluxes of heat will increase (decrease) the total energy of the system, both of the same value $\frac{k}{2}\Delta T$. If we study the total phase-space $\Gamma(x, v) = \Gamma_x \Gamma_v$, both components increase scaling with T, see Fig.7.1. The usual strategy to measure the energy exchange in the system is based on the observables of the system, here, the position and the stiffness [62]. However, the measurement of δQ_v requires of the value of the instantaneous velocity, and then, an underdamped description of the system. Unfortunately, those effects appears in much higher frequencies (MHz) than the usual adquisition frequency (kHz). Nevertheless, the mean of the instantaneous velocity in a short enough interval of time shows a variability that can be linked to the instantaneous velocity.

7.1.1 Searching the adiabatic

When a cycle or an engine is designed in the macroscale, the wasted energy must be minimized. The meaning of adiabatic is deeply connected with reversibility, and therefore, with efficiency. There are not reasons to think that this fact is not conserved when we consider the mesoscale. Nevertheless, there is a main inconvenience to translate the concept to small systems, namely, there is not an adiabatic wall to avoid the heat flux between the system and the environment. Therefore, it is needed to search another way to define *adiabaticity* in this scale. Sekimoto seminal work permits measuring heat using the experimental observables [176]. Hence, we can define *a priori* a protocole whose associated mean flux of heat will vanish. For example, Schmiedl and Seifert proposed a coupled jump of the temperature and the trap stiffness that conserves the histogram of position [66]. The overdamped approximation neglects the kinetic energy contribution to the hamiltonian, i.e., $\mathcal{H}_{\mathrm{OD}}(x,\kappa) = U(x,\kappa)$. Therefore, the partition function and the Helmhotz free energy of the system at a given time read:

$$\mathcal{Z} = \frac{1}{h}\int_{\Re} dx e^{-\beta\mathcal{H}} = \sqrt{\frac{2\pi}{h^2\beta\kappa}} \tag{7.5}$$

$$\mathcal{F} = -kT\log\mathcal{Z} = -\frac{kT}{2}\log\frac{2\pi kT}{h^2\kappa} \tag{7.6}$$

where h is a constant which makes $\mathcal{Z}$ dimensionless. The conformational entropy follows immediately from eq. (7.6):

$$S = -\frac{\partial\mathcal{F}}{\partial T} = \frac{k}{2} + \frac{k}{2}\log\frac{2\pi kT}{h^2\kappa} \tag{7.7}$$

Entropy allows us to define a process whose change in entropy, and hence, its realeased heat Q_x, is null. Acordingly, parameters must change as $T = \Lambda_{\mathrm{OD}}\kappa$. This is the protocole suggested in [66] as adiabatic. As Schmiedl points, this assumtion neglects the kinetic part, although they took it into account to calculate the efficiency of a cycle.

Although the OD approximation reproduces the trajectory of the system, the energetics needs the inertial term. Let us consider a system whose Hamiltonian does not neglect the kinetic part: $\mathcal{H}_{\mathrm{UD}}(x,p) = U(x,\kappa) + K(p,T) = \frac{1}{2}\kappa x^2 + \frac{p^2}{2m}$. Its entropy reads:

$$S = -\frac{\partial\mathcal{F}}{\partial T} = \frac{k}{2} + \frac{k}{2}\log\frac{4\pi^2k^2T^2m}{h^2\kappa} \tag{7.8}$$

In order to define a protocole where the entropy is fixed, we must change the temperature and the stiffness in a synchronous way. The temperature must change following $T^2 = \Lambda\kappa$, as it was pointed out in [64]. It is necessary to point how we cannot recover the overdamped limit even if $m \to 0$.

Fig. 7.1 gives a visual interpretation of the evolution of Γ through each process. We draw an elypse which rounds the joint probability $\rho(x,v)$, in the first instance we can consider its axes as $\langle x^2\rangle$ and $\langle v^2$ respectively. The area within the curve can interpretate as the most probable region of the phase space, being linked to the entropy of the system.

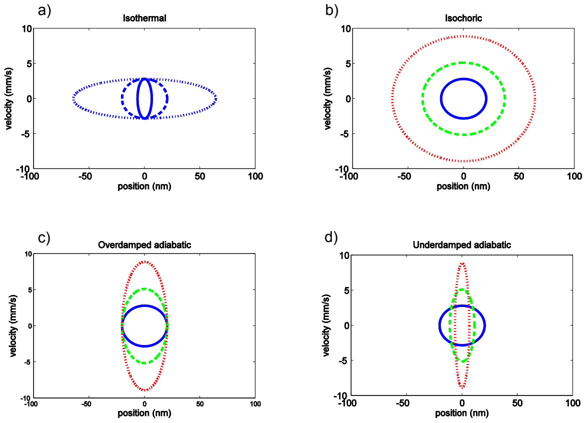

Figure 7.1: Contour plot of the joint probability $\rho(x,v)$ of a one dimensional system for the different processes. The area within the elypses represents the most probable values of the phase space. a) Isothermal. Temperature is fixed at 300K while κ=$\{1,10,100\}$ pN/μm (dotted, dashed and solid line respectively). $\Gamma(x,p)$ remains constant for momenta, while the particle can explore more space when stiffness is reduced. b) Isochoric. The value of κ is fixed at 10pN/μm, $T = \{300, 1000, 3000\}$ K for blue solid line, green dashed line and red dotted line respectively. Both components of $\Gamma(x,p)$ broads with the temperature, which represents an increment of the two contribution of the entropy, see eq.(7.8). c) Overdamped adiabatic. The process conserves the variance of the position under a protocole where $T = \Lambda^{\mathrm{OD}}\kappa$. Although the entropy associated to the position does not change, and therefore $\langle Q_x \rangle = 0$, the component in velocity changes. The picture shows that this process is analogous to the isothermal one but in the momenta space. The particular values of the parameters are κ=$\{3,10,30\}$ pN/μm and $T = \{300, 1000, 3000\}$ K for blue solid line, green dashed line and red dotted line respectively. d) Underdamped adiabatic. The area within the elypse is constant under the process, i.e., the total entropy remains constant. Therefore there is not a net flux of heat between the system and the environment, $\langle Q_x \rangle + \langle Q_v \rangle = 0$. κ=$\{3,33,300\}$ pN/μm and $T = \{300, 1000, 3000\}$ K for blue solid line, green dashed line and red dotted line, respectively.

7.2 Experimental methods

The experimental goal of this chapter is the synchronized control of the trap stiffness (κ) and the kinetic temperature (T_{kin}). The studied sample is a suspension of polystyrene beads (G. Kisker-Products for Biotechnology, http://www.kisker-biotech.com/, polystyrene microparticles PPs-1.0 with a diameter of $1.00 \pm 0.05\,\mu$m) in distilled de-ionized water. The solution is injected in a custom made chamber, see section 2.4.2, whose electrodes are fed by a voltage produced by a signal generator (TaborElectronics WW1071). The signal is amplified 1000 times by a voltage amplifier (Trek, Model 610E). The optical trap is generated by a 985 nm diode laser (Avanex, 1998PLM 3CN00472AG HIGH POWER 985nm, maximal power 300 mW). The position of the bead is tracked by the projection of the scattered light into a QPD, see section 2.3.3. Adquisition frequency is fixed at 5kHz for the study of the processes and varied up to 200kHz for the kinetic studies. The spheres were trapped above the bottom surface of the fluid chamber at the distance about $20\,\mu$m controlled by the piezoelectric stage. The value of the viscous friction coefficient γ was corrected due to the proximity of the chamber surface using the Faxen law as described in [73].

The optical power is managed by controlling the current through the laser. Optical power grows linearly with the current, what allows us have a linear relation between the input current and the stiffness $\kappa = CI_{\text{laser}} + \Delta\kappa$. Both parameters, κ and T_{kin}, are controlled by a custom made Labview program. Before each measurement, T_{kin} and κ are calibrated, as shown in Fig. 7.2.

Our aim is the study of non-isothermal processes in the quasistatic regime. Therefore, parameters must be changed as slow as possible. Unfortunately, we cannot generate synchronized protocoles with a continuous change in the parameters but as a combination of steps. Each step is fixed at 200 ms, one order of magnitude larger than the characteristic time γ/κ. All synchronized protocoles are generated in order to have a parameter change below the 10% of previous value.

7.3 Experimental results

The results are arranged in the following way. First, the two control protocoles are shown, the isothermal ($\mathrm{d}T = 0$) and the isochoric ($\mathrm{d}\kappa = 0$). As only one parameter is changed, it is easier to understand the energy exchanges. Afterwards, we study two different protocoles, one under the assumnption of overdamping and the other under the assumption of underdamping. Finally, we present a

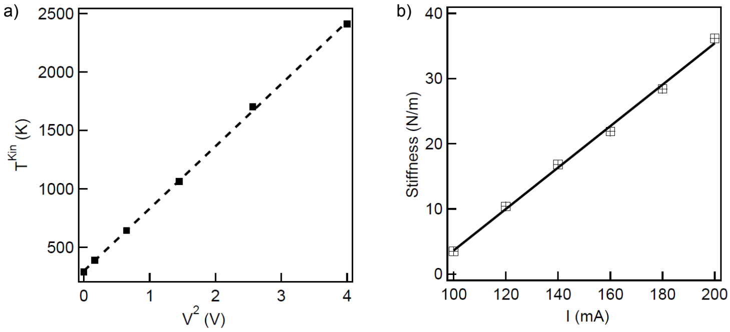

Figure 7.2: Experimental calibration of the free parameters. a) Kinetic temperature vs voltage. b) Trap stiffness vs laser current.

combination of different thermodynamic processes to build a Carnot cycle.

7.3.1 Isothermal process

There are several examples of isothermal processes with optical tweezers [85, 187]. In our case, the free parameter is the stiffness of the trap κ. The value of the stiffness starts at 4.9 pN/μm and finishes at 34.0 pN/μm, see the inset in Fig. 7.3. The cumulative sum of the released heat is shown in the main panel together with the analitical curve corresponding to the given parameters. The experimental value of the *potential heat* is $\langle Q_x^{\mathrm{exp}} \rangle = (-0.99 \pm 0.15)kT_c$. The theoretical value $\langle Q_x^{\mathrm{theo}} \rangle = -0.95kT_c$ lies within the error bar.

7.3.2 Isochoric process

The second control corresponds to an isochoric process. The stiffness remains fixed at 17.9 pN/μm while the kinetic temperature is varied between the temperature of the medium, 300 K, and 1300 K. The effective temperature is changed linearly with time, following $T(t) = T_{\mathrm{ini}} + Ct$, where $C = (T_{\mathrm{fin}} - T_{\mathrm{ini}})/\tau$. This protocole defines a heat flux to the system which is stored as internal energy. Fig. 7.4 shows the cumulative sum of the heat flux over the process. The value of exchange energy is $\langle Q_x^{\mathrm{exp}} \rangle = (1.4 \pm 0.4)kT_c$, being the analitical value is $\langle Q_x^{\mathrm{theo}} \rangle = 1.6kT_c$. As κ is fixed along the process, the exerted work in (by) the system is iddentically zero.

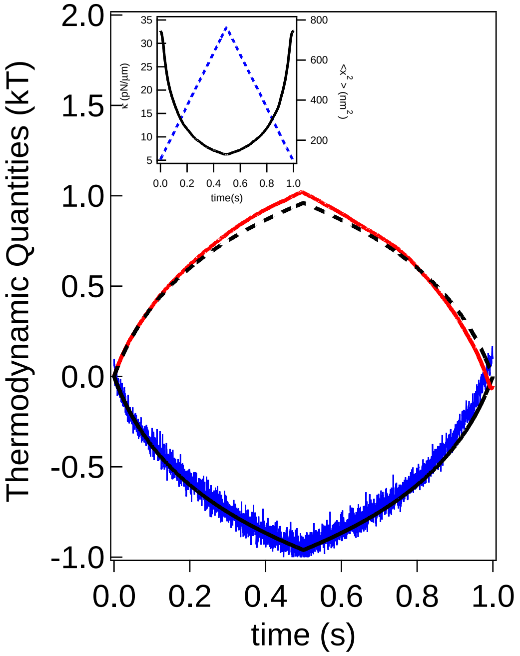

Figure 7.3: Isothermal process (forward and backward). System is in contact with a bath at constant temperature, T=300K, while κ evolves from 4.9 pN/μm to 34.0 pN/μm. Inset: stiffness (dashed blue line) and $\langle x^2\rangle$ (black solid line) evolution over the process. Variance is averaged over 200 cycles. The main panel shows the cumulative value of $\langle Q_x\rangle$ and $\langle W\rangle$ along the process, blue and red solid lines respectively. The values are average over 1000 cycles. Analitic value for the heat (work) is represented by the black solid (dashed) line.

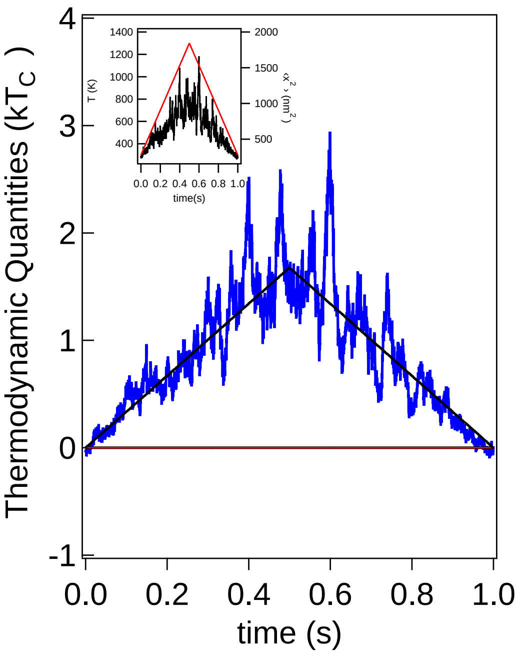

Figure 7.4: Isochoric process. The kinetic temperature is varied from 300K to 1300K while κ is fixed at 17.9 pN/μm (inset). Principal figure shows the average of the cumulative sum of potential heat, $\langle Q_x \rangle$, over the process. As the temperature increases with time, the average of the heat flux is directed to the system from the environment $Q_x > 0$, viceversa in backward protocole. The main panel shows the experimental cumulative value of $\langle Q_x \rangle$ and $\langle W \rangle$ along the process in comparison with the analitical values for the heat (work) is represented by the black solid (dashed) line., blue and red solid lines respectively. The values are average over 1000 cycles.

7.3.3 Adiabatic in the overdamped assumption

The inset in Fig. 7.5 shows the time-evolution of T and κ together with the measured value of $\langle x^2(t)\rangle$. The variance remains constant $\langle x^2\rangle_{\text{exp}} = (765 \pm 89)$ nm^2, in agreement with the expected value $\langle x^2\rangle_{\text{theo}}$=787 nm^2. The cumulative released potential heat as a function of time is shown in Fig. 7.5, together with the analitical curve associated to actual values. Experimental mean value of released heat is $\langle Q_x^{\text{exp}}\rangle = (-0.1 \pm 0.1)kT_c$. It agrees with the expected value$\langle Q_x^{\text{theo}}\rangle = 0$. We want to remark that these values refers only to the *potential heat* $\langle Q_x\rangle$. Although this heat is null on average, the increase of the kinetic temperature produces a net flux of heat to the system that increases the available total phase space in the momenta axis, see Fig. 7.1.

7.3.4 Adiabatic in the underdamped assumption

Inset of Fig.7.6 represents the studied protocole. The mean value of *potential heat* is $\langle Q_x^{\text{exp}}\rangle = (-0.3 \pm 0.1)kT_c$, what agrees with $\langle Q_x^{\text{theo}}\rangle = -0.3kT_c$. Fig 7.6 shows $\rho(Q)$ for the forward process. The decrease of $\langle x^2\rangle$ is understood as a compression of Γ_x. Indeed, this compression is compensated by the expansion of Γ_v, while the total entropy of the system does not change along the process. Therefore, no heat neither kinetic nor potential, is released to the environment if the protocole is slow enough.

7.4 Discussion

7.4.1 Distribution of potential heat

For any process carried out quasistatically, i.e., the system never goes out of an equilibrium state, we found the following expression:

$$\rho(Q_x) = \frac{\sqrt{\beta_1\beta_2}}{\pi} \exp\left\{\frac{\beta_1 - \beta_2}{2}\left(Q_x + \langle W\rangle\right)\right\} K_0\left(\frac{\beta_1 + \beta_2}{2}\left|Q_x + \langle W\rangle\right|\right) \quad (7.9)$$

where $\beta_i \equiv 1/kT_i$ and K_0 is the zeroth-order modified Bessel function of the second kind [1]. Eq. 7.9 is assymetric except for the isothermal case. Analytical expression is plotted for each distribution of heat, Fig. 7.7-7.8, theoretically, i.e., not a fit over the experimental points. The curves are particularized for each

---

[1] Eq. (7.9) is derived in Appendix D.1.

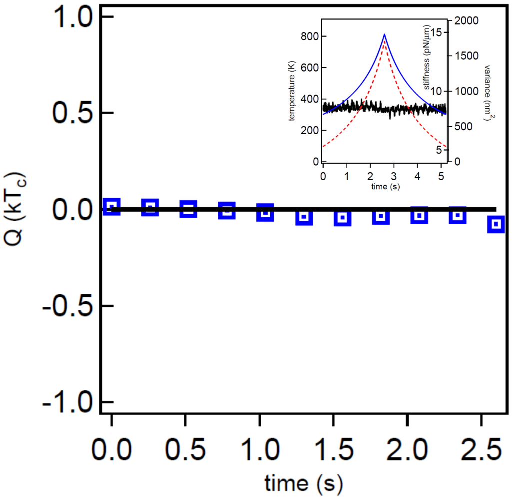

Figure 7.5: Adiabatic process assuming overdamped dynamics. Inset: Parameters evolution over time: temperature (solid blue line) and stiffness (dashed red line). Black solid line shows empirical value of $\langle x^2 \rangle$. Principal figure shows the cumulative value of $\langle Q_x \rangle$ over the process(squares). The value is average over 200 cycles. Analitic value for the given value is represented by the black solid line.

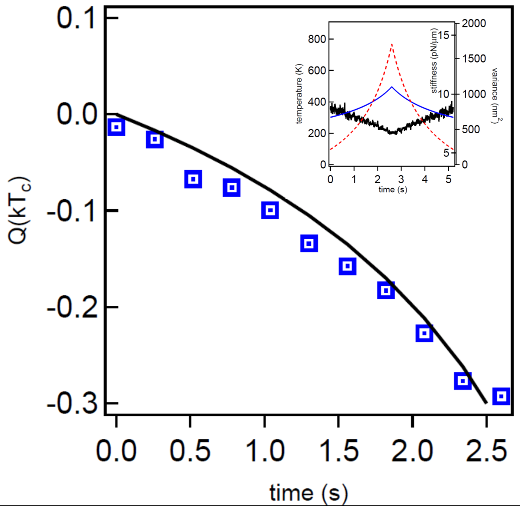

Figure 7.6: Adiabatic process assuming underdamped particle. Inset: Parameters evolution over time: temperature (solid blue line) and stiffness (dashed red line). Black solid line shows empirical value of $\langle x^2 \rangle$. Principal figure shows the cumulative value of $\langle Q_x \rangle$ over the process(squares). The value is average over 200 cycles. Analitic value for the given value is represented by the black solid line.

initial and final state of the process $\{T_i, \kappa_i\}$. We observe that the asymetry is shared by all the non-isothermal processes, the most accused asymmetry found in the case of the isochoric one, due to the larger change of T_{kin}. The asymmetry gives a huge importance to the *tails* of the distributions. In fact, the mode is always displaced to lower values than the mean. This fact agrees with the mean values of the thermodynamic quantities, see Table 7.1.

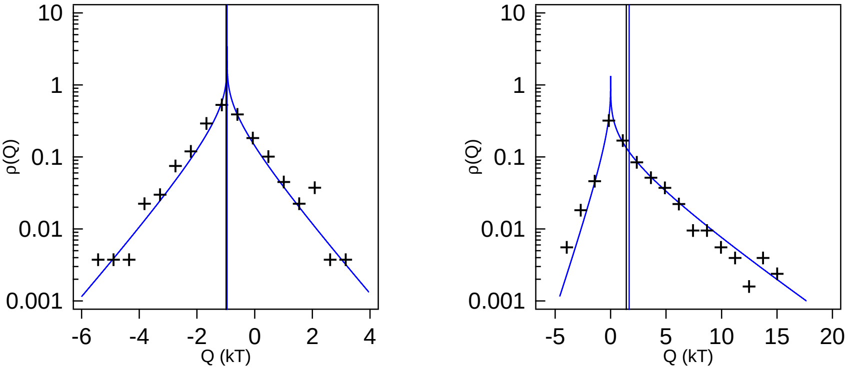

Figure 7.7: Potential heat distribution in the control processes. Left: Isothermal. $\rho(Q_x)$ is symmetric peaked at $-\langle W \rangle$. Right: Isochoric. The distribution is peaked at zero but the positive tail dominates the mean value of Q_x..

7.4.2 Kinetic study of a Brownian particle

Our experimental setup has a finite adquisition frequency (∼kHz) always below the inertial regime (∼MHz). The observation of the instantaneous velocity of a Brownian motion needs a higher frequency to measure it, the inertial time scales as $m/\gamma \sim \mu$s. Nevertheless, we can measure the mean value of the velocity along an interval ($\Delta t = 1/f_{\mathrm{acq}}$) as $\langle v(t) \rangle_{\Delta t} = \frac{1}{\Delta t}(x(t) - x(t - \Delta t))$. The histogram of velocities is shown in Fig. 7.9 for the two controls, isothermal and isochoric at different values of κ and T_{kin}. We observe that in the isothermal case, a change in the stiffness does not affect the velocity. On the other hand, when the kinetic temperature increases, the histogram of velocities broadens significantly. This fact must be taken into account in the definition of the phase space of the system Γ. Therefore, the overdamped approximation can fail in non-isothermal processes, as it is pointed in [64], and the underdamped motion

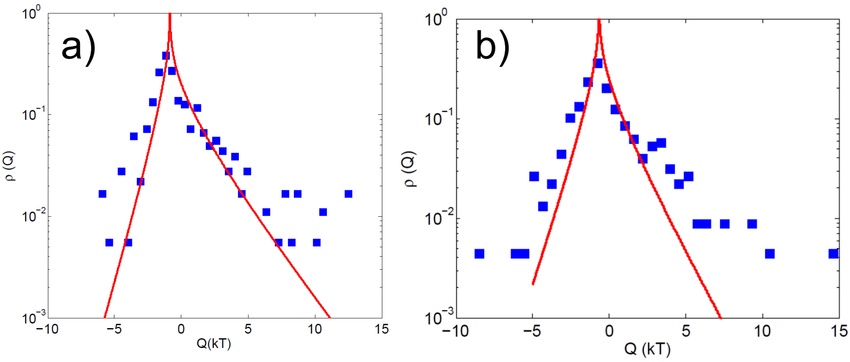

Figure 7.8: $\rho(Q_x)$ of adiabatic processes. a) Overdamped approximation. Mean value is at zero while the functional is peaked at a negative value. b) Underdamped approximation. The mean value of Q_x does not vanished, but its sum with $\langle Q_v \rangle$.

must be considered.

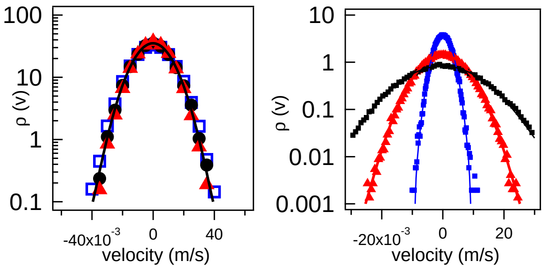

Figure 7.9: Velocity histograms. On the left, the stiffness is changed while temperature is fixed at 300K. The histogram remains constant. On the other hand, the stiffness is kept constant but kinetic temperature is changed (297, 3095 and 8581 K). $\rho(v)$ broadens when T_{kin} grows. Data is registered at 5kHz.

Moreover, we obtained an extrapolation that connects the observable velocity with the instantaneous one. In Fig. 7.10, we show the mean velocity in function of the adquisition time. The experiment is done in absence of external field, enviromental temperature, and for different intensities of the white noise. As we discuss in the previous chapter, the finite whiteness of our noise avoid the perfect analogy with a kinetic temperature. Under our point of view, the fail in the Crooks temperature is also deeply connected with the non-whiteness. Therefore, it is expectable that a better equipment will improve the results.

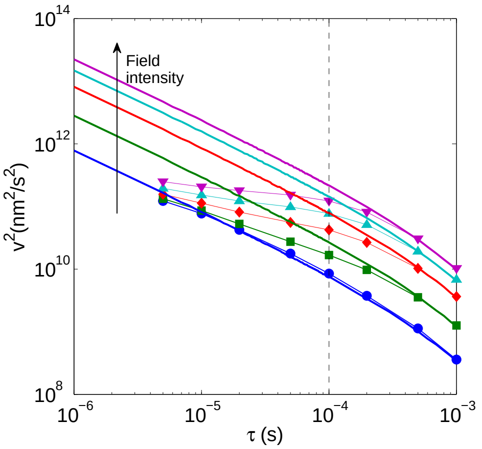

Figure 7.10: Experimental values of the mean velocity in function of the adquisition time. Each color corresponds to a different kinetic temperature, blue $T_{\rm kin}$ = 297K, green $T_{\rm kin}$ = 1064K, red $T_{\rm kin}$ = 3095K, cyan $T_{\rm kin}$ = 5684K and purple $T_{\rm kin}$ = 8581K. Solid lines represent the theoretical prediction, particularized to the corresponding kinetic temperature, while the solid points show the experimental values. Experiment evidences that the velocity collapse below adquisition times of 0.2 ms. Dashed line represents the amplificator limit.

The analytical prediction is also represented in the figure for each value of the external noise. The expression reads as follows:

$$\langle \overline{v}^2 \rangle = \frac{2kT}{m\Delta t^2}\left[\frac{1}{\omega_0^2} + \frac{1}{\omega_1}\left(\frac{e^{-\left(\frac{\gamma}{2m}+\omega_1\right)\Delta t}}{\frac{\gamma}{m}+2\omega_1} - \frac{e^{-\left(\frac{\gamma}{2m}-\omega_1\right)\Delta t}}{\frac{\gamma}{m}-2\omega_1}\right)\right] \tag{7.10}$$

where $\omega_0^2 = \kappa/m$ and $\omega_1 = \sqrt{\frac{\gamma^2}{4m^2} - \omega_0^2}$. Although we cannot measure the value of v directly, we can say that the overdamped approximation describes the dynamics of a Brownian particle but not its energetics along a non-isothermal process. The goal must be connect the measurable values of the velocity with the changes of the kinetic energy of the system.

7.5 Carnot Cycle

Classical engines extract useful work (W_{Cycle}) from a set of thermal baths at different temperatures[2]. Any engine is characterized by its efficiency (η) and power ($P = W_{\mathrm{Cycle}}/\tau$, being τ the cycle time). Carnot engine presents the highest efficiency $\eta_{\mathrm{C}} = 1 - T_h/T_c$, being considered a theoretical model due to its reduced power. Trying to avoid irreversibility, Sadi Carnot designed the cycle as a sequence of an isothermal compression at T_c, an adiabatic compression, an isothermal expansion at T_h and an adiabatic expansion of a piston filled with an ideal gas, see Fig. 7.11. There is an extensive theoretical bibliography about Carnot engine in the mesoscale, particulary, with a Brownian particle as working substance within an optical potential [66, 212, 213]. However, to the best of our knowledgement, there is not an experimental realization of the mesoscopic Carnot. The closest approximation is the Stirling engine developed by Blickle and Bechinger [33]. We combine the previously studied processes to build a mesoscopic Carnot engine. Unfortunately, experimental results are restricted to the overdamped energetics, the adiabatic process will not take into account the kinetic energy.

Fig. 7.11 a) draws an analogy between our mesoscopic cycle and a macroscopic Carnot engine. The cycle is composed by four processes. Starting at a given volume V_1, the piston is isothermally compressed up V_2 at temperature T_c, exherting a work to the piston $W_{1\rightarrow 2}$. The system never goes out of equilibrium,

---

[2] In this section, we define two baths. Hot bath is defined by the temperature T_h, cold bath by T_c

releasing an amount of heat $Q_{1\to 2} = -W_{1\to 2}$ to the environment through the diathermal walls. For process $2 \to 3$, the piston is surrounded by an adiabatic wall, what permits compressing it with a null release of heat. The temperature of the working substance has increased up to T_h. Step $3 \to 4$ allows to expand the piston to a volume V_4, isothermally at temperature T_h. The cycle is closed with an adiabatic process from V_4 to initial volume V_1.

Our propose is to build a Carnot cycle with an optical trapped microsphere as working substance. The role of the piston is played by the optical potential. Therefore, the stiffness of the parabolic potential will be consider analogous to the volume. As we discuss in the previous sections, the concept of adiabaticity is non-trivial. In this experiment, we will consider the overdamped expression, due to the imposiibility to measure the kinetic heat. Fig 7.11 b) shows the protocole carried out in this experiment. The adiabatic process consists in the synchronous variation of the temperature with the stiffness, $T = \Lambda\kappa$. Hence, the position variance is conserved.

Each process lasts the same interval of time, giving a total cycle time of τ_{Carnot}=9.6 s. In our particular case, κ_1=5.3 pN/μm, κ_2=23.2 pN/μm, κ_3=41.0 pN/μm, κ_4=9.4 pN/μm, T_c= 300K and T_h=533 K. Cumulative sum of work and heat over 100 cycles are represented in Fig. 7.12. Beyond the stochastic fluctuations, the behavior of the engine shows a negative value of the work, the system can extract work from the heat baths. The total work along a cycle is the sum of the work over each process. Considering quasistaticity, it reads:

$$\langle W_{\text{cycle}} \rangle = \sum_{i=0}^{4} \langle W_i \rangle = -\frac{k}{2}\left(T_h - T_c\right) \log \frac{\kappa_2}{\kappa_1} \tag{7.11}$$

The analitic value of the work per cycle assuming quasistaticity is -0.57kT_c per cycle, what agrees with the experimental value of $\langle W_{\text{cycle}} \rangle = (-0.6 \pm 0.1)kT_c$ [3]. Hence, the associate power is 6.3 10^{-2} kT_c/s. Efficiency of our engine is $\eta = 0.43 \pm 0.05$, really close to the Carnot efficiency, $\eta_c = 0.44$.

Another interesting thermodynamic quantity is the entropy. The representation of a Carnot cycle in a T- S diagram corresponds to a square. Fig.7.13 shows the experimental values averaged over the 100 cycles. From eq. (7.7), the difference of entropy between two given states is $\Delta S = \frac{k}{2} \log \frac{T_2/T_1}{\kappa_2/\kappa_1}$. By definition, along an adiabatic process, the entropy must be conserved $\Delta S_{\text{AD}} = 0$.

---

[3] The experimental average values of heat and work in each process are: $\langle W_{1\to 2} \rangle = (1.1 \pm 0.1)kT_c$, $\langle Q_{1\to 2} \rangle = (-1.1 \pm 0.2)kT_c$, $\langle W_{2\to 3} \rangle = (0.9 \pm 0.1)kT_c$, $\langle Q_{2\to 3} \rangle = (-0.3 \pm 0.3)kT_c$, $\langle W_{3\to 4} \rangle = (-2.0 \pm 0.1)kT_c$, $\langle Q_{3\to 4} \rangle = (1.4 \pm 0.5)kT_c$, $\langle W_{4\to 1} \rangle = (-0.6 \pm 0.1)kT_c$, $\langle Q_{4\to 1} \rangle = (0.6 \pm 0.3)kT_c$,

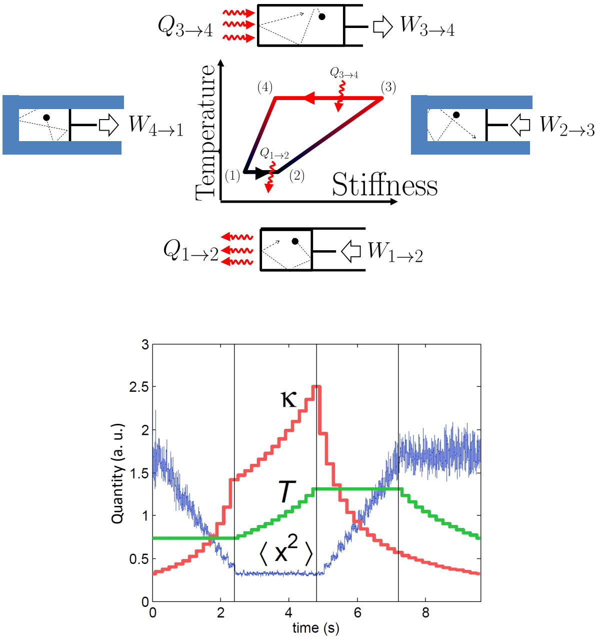

Figure 7.11: (a) Depiction of the cycle. Comparison with a gas in a piston. (b) Experimental protocole, $\kappa(t)$, $T(t)$ and $\langle x^2(t)\rangle$ in function of time in our experiment. Values are normalized with the mean value of each parameter.

On the other hand, along an isothermal process, the entropy will change an ammount $\Delta S_{\mathrm{IT}} = -\frac{k}{2}\log\frac{\kappa_2}{\kappa_1}$, eq. (7.7). Fig. 7.13 shows the T-S diagram of the cycle, where the time evolution is clockwise. Experimental points are obtained as an ensemble average over the 100 cycles, using a time window of 320ms each. Dashed line represents the analitic value of entropy for the given parameters. This experiment is a preview of the definitive experimental study of the Carnot cycle in the mesoscale. Future work will include a deeper study of the efficiency and the power as function of time cycle [66]. A study of the underdamped adiabatic must be also analysed, trying to connect $\langle v^2\rangle_\tau$ with the kinetic energy, so then, the kinetic heat.

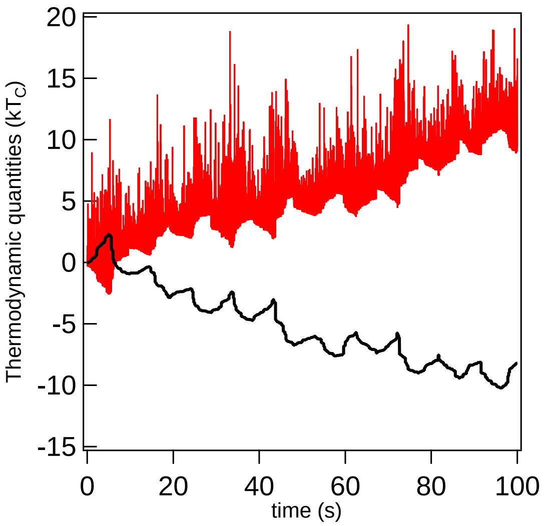

Figure 7.12: Cumulative work (blue) and heat (red) over 100 cycles.

7.6 Conclusions

In this chapter we have applied the technique developed in previous chapter to study non-isothermal processes. As the difference of temperature through a process can be of an order of magnitude, the thermal effects are powered, allowing to amplify the possible effects. We derived an analytical expression for $\rho(Q)$ which

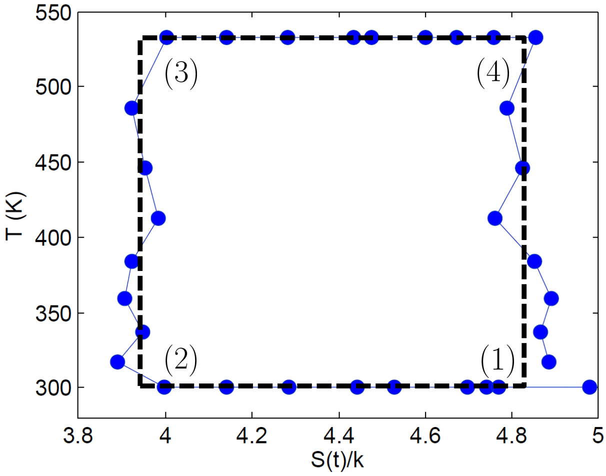

Figure 7.13: Experimental T-S diagram of the Carnot cycle. Black solid circles represents the empirical values, averaged within a 320ms time window. The dashed line shows the analitical values of the difference of entropy along the cycle..

agrees with our experimental results. We see how the changes of temperatures along a process are reflexed into an asymmetry of the pdf. On the other hand, we have studied the effects of the overdamping assumption when T changes. The kinetic energy must be taken into account to have a complete vision of the energy exchanges between the system and its environment. Unfortunately we cannot study the changes of kinetic energy through a direct observation of the instantaneous velocity but from the mean value of the velocity within our adquisition frequency. Different processes are combined to generate a Carnot cycle in the mesoscopic scale. We see how the cycle works at the prediced efficiency, remaining for future work a deeper study of the efficiency at maximum power [66, 213]. The comparison of the overdamped approximation assuming kinetic energy as dissipation with the underdamped asssumption must also be explored in future work.

7.7 Acknowdlegements

This chapter was developed under a colaboration with Prof. J. M. R. Parrondo group, Univ. Complutense de Madrid.

8

Universal features in the energetics of symmetry breaking

8.1 Introduction

The action of choosing between different options is present in several processes of nature. When we focus our attention in the mesoscopic world, the thermal noise allows the systems to take choices that are not the most energetically efficient. For example, consider the protein folding, one of the unsolved challenges in biochemistry. When the proteins folds, it elects a conformational state between different options, and therefore, the protein is storing an information [40].

Along the last decade, there have been published several experimental demostrations of the thermodynamics of the information. For example, Toyabe *et al* designed a microscopic Maxwell demon where the information is converted into energy [38]. In 2012, Berut *et al* tested experimentally the Landauer's limit [39]. In the same year, Alemany and co-workers used fluctuation theorems to obtain experimentally the difference of free energy of kinetic molecular stated [214]. A common point between these investigations is the posibility of the system to choose between different options, thus, breaking a symmetry within the system. A symmetry breaking (SB) involves an abrupt change in the set of microstates than the system can explore. Under the Boltzmann interpretation of entropy, the shrinkage of the phase space implies a reduction of the system's entropy, which must be compensated by a heat dissipation.

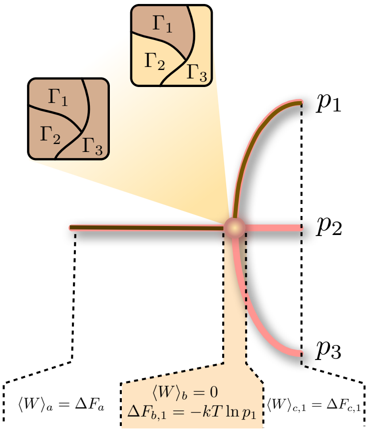

Figure 8.1: A sketch of the proof of Eq. (8.1) for a system that adopts instance 1 among three possibilities $i = 1, 2, 3$. Before and after the symmetry breaking, the reversible work is given by the increment of free energy: $\langle W\rangle = \Delta F$. At the symmetry breaking, a reduction of the phase space volume from Γ to Γ_1 occurs without the need of any external work: $\langle W\rangle_b = 0$. This reduction of phase space volume induces an increase of free energy $\Delta F_{b,1} = kT \log(Z_1/Z) = kT \log p_1$, where Z and Z_1 are partition functions calculated over Γ and Γ_1, respectively, and $p_1 = Z_1/Z$ is the probability the system to select region Γ_1 when the symmetry is broken. The total reversible work is $\langle W\rangle_1^{(\mathrm{SB})} = \langle W\rangle_a + \langle W\rangle_b + \langle W\rangle_{c,1} \geq kT \log p_1 + \Delta F_1$, where $\Delta F_1 = \Delta F_a + \Delta F_{b,1} + \Delta F_{c,1} = F_{\tau,1} - F_0$.

In this chapter, we derive an analytic formula which links the produced entropy along a choosing process with the event's probability to occur. The theoretical framework is tested in an optical trapping experiment.Afterwards, it is studied how the entropy is produced along the process. Finally, a Szilard engine is built. This engine shows the equivalence between information and energetics.

8.1.1 Symmetry breaking/restoring

Consider a system with Hamiltonian $\mathcal{H}(x;a)$ $(x \in \Gamma)$, depending on a control parameter a, and an isothermal process at temperature T involving a SB, where the parameter changes in time as a_t with $t \in [0,\tau]$. The average work required to complete the process, when the system adopts instance i, is bound by

$$\langle W \rangle_i^{(\mathrm{SB})} - \Delta F_i \geq kT \log p_i, \tag{8.1}$$

where k is the Boltzmann constant and $\Delta F_i = F_{\tau,i} - F_0$ is the change in free energy. The initial free energy is defined as usual, $F_0 = -kT \log Z(T, a_0)$ where $Z(T,a) = \int_\Gamma dx\, e^{-\beta \mathcal{H}(x;a)}$ is the partition function of the system. On the other hand, the final free energy $F_{\tau,i} = -kT \log Z_i(T, a_\tau)$ is a conformational free energy defined in terms of the partition function restricted to the region Γ_i, i.e., $Z_i(T, a_\tau) = \int_{\Gamma_i} dx\, e^{-\beta \mathcal{H}(x;a_\tau)}$. The bound in equation (8.1) is met with equality if the process is quasistatic. Recalling the relationship between the free energy, F, the internal energy E, and the entropy S of a system, $F = E - TS$, and the first law of thermodynamics $\Delta E = W + Q$, where Q is the heat or energy transfer from the thermal reservoir to the system, we easily derive a bound for the entropy production:

$$\langle S_{\mathrm{prod}} \rangle_i^{(\mathrm{SB})} \equiv \Delta S_i - \frac{\langle Q \rangle_i^{(\mathrm{SB})}}{T} \geq k \log p_i. \tag{8.2}$$

A rigorous proof of these bounds follows from fluctuation theorems (see Appendix E). However, the origin of the term $k \log p_i$ in Eqs. (8.1) and (8.2) can be easily understood. A SB comprises a contraction of the set of available states from Γ to Γ_i without the need of any extra work. This amounts to an increase of free energy $-kT \log(Z_i/Z)$ which is not compensated by work and heat dissipation. Assuming an instantaneous SB, $p_i = Z_i/Z$ yielding the extra term $kT \log p_i$ in Eqs. (8.1) and (8.2).

This work-free shrinkage of the available phase space is entirely due to the SB transition and is not in contradiction with the Second Law of Thermodynamics, because the final state $\rho_i(x)$ is not in complete equilibrium and the final entropy cannot be considered as a true thermodynamic entropy. In some contexts, S_i and F_i are called, respectively, conformational entropy and conformational free energy, but they are not true thermodynamic potentials (they are not state functions, for instance). However, both are useful tools to analyze the energetics of processes involving SB transitions [215]. An alternative interpretation of the compatibility between the Second Law and the decrease of entropy in Eq. (8.2) is that the latter is compensated by an increase of the meso- or macroscopic uncertainty, quantified by the Shannon entropy of the SB outcome, $H(p_i) = -\sum_i p_i \log p_i$. Notice that the average of Eq. (8.1) over p_i yields precisely $kT\,H(p_i)$.

Similar inequalities hold for a process where a symmetry is restored. To assess the energetics of a symmetry restoration (SR) we have to consider the time reversal of the restoration, which is a SB. Let us call $\tilde{p}_i$ the probability that the system adopts instance i in this SB resulting from the time reversal of the original process. Under time reversal, reversible work and free energy increment change sign. Therefore (see Appendix E):

$$\langle W\rangle_i^{(\mathrm{SR})} - \Delta F_i \geq -kT \log \tilde{p}_i, \tag{8.3}$$

where $\Delta F_i = F_\tau - F_{0,i}$ is the free energy change of the SR. Notice that now it is the initial free energy that depends on the instance i. For the entropy:

$$\langle S_{\mathrm{prod}}\rangle_i^{(\mathrm{SR})} \geq -k \log \tilde{p}_i. \tag{8.4}$$

Landauer's principle follows immediately from Eq. (8.3) applied to a one-bit memory consisting of a physical system with two stable states, 0 and 1, each one with the same free energy $F_0 = F_1$. The minimal cost of erasing a bit or, more precisely, to drive bit $i = 0$ or 1 to the state 0 (restore-to-zero operation) is $\langle W\rangle_i^{\mathrm{erasure}} \geq -kT \log \tilde{p}_i - \Delta F_i = -kT \log \tilde{p}_i$ for $i = 0$ or 1, since in both cases $\Delta F_i = F_i - F_0 = 0$. If the initial bit is unknown, the best we can do is $\tilde{p}_i = 1/2$ and $\langle W\rangle_i^{\mathrm{erasure}} \geq kT \log 2$.

The energetics of the Szilard engine [215, 216] can be as well easily reproduced from Eqs. (8.1) and (8.3). In the Szilard setup a system undergoes a SB and chooses between two instances 0 or 1 with probability p_0 and p_1, respectively. Then we measure the instance that has been chosen and restore the broken symmetry driving the system back to the original state through some protocol a_t^i. The time reversal of this protocol is a SB transition with possibly different probabilities $\tilde{p}_j^i$. The work necessary to implement the SB is bound by Eq. (8.1) and the work necessary to restore the symmetry is bound by Eq. (8.3). Therefore, the total average work that we have to perform to run the whole cycle obeys:

$$\begin{aligned}\langle W\rangle &= \sum_i p_i\left[\langle W\rangle_i^{(\mathrm{SB})}+\langle W\rangle_i^{(\mathrm{SR})}\right]\\ &\geq kT\sum_i p_i\log\frac{p_i}{\tilde{p}_i^i},\end{aligned}\tag{8.5}$$

and $\langle S_{\mathrm{prod}}\rangle = \langle W\rangle/T$. In the case of the original Szilard engine: $p_i = 1/2$ and $\tilde{p}_i^i = 1$, yielding $\langle W\rangle \geq -kT\log 2$, i.e., the extraction of an energy $kT\log 2$ in a cycle. If the demon does not use information from the measurement performing always the same protocol, i.e., $a_t^i = a_t$, then $\tilde{p}_j^i = \tilde{p}_j$ normalized to unity $\sum_i \tilde{p}_i = 1$ yielding $\langle W\rangle = kTD(p_i||\tilde{p}_i) \geq 0$ where $D(p||q)$ is the relative entropy between two probability distributions p and q [209, 217]. To build a Szilard engine, it is enough to find p_i and $\tilde{p}_i^i$ such that the average work $\langle W\rangle$ in Eq. (8.5) is negative; for instance by choosing protocols where $\tilde{p}_i^i > p_i$.

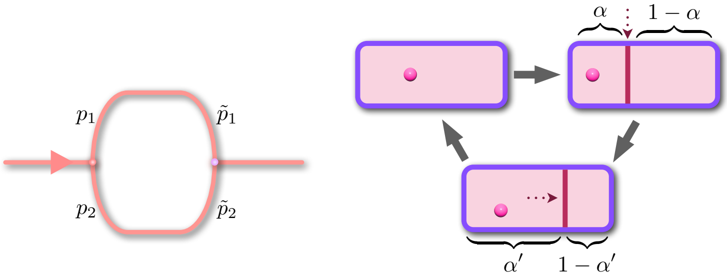

Figure 8.2: Breaking and restoring a symmetry: a piston is introduced at a distance α from the left wall of a box containing a single Brownian particle; the piston is shifted to position α' and then removed. In this case, the broken symmetry is the spatial homogeneity of the box. When the piston is inserted the system “makes a choice" between the left, $i = 1$, or right, $i = 2$, side of the box with probabilities $p_1 = \alpha$ and $p_2 = 1-\alpha$, respectively. The symmetry is restored when the piston is removed at position α'. The process of restoring the symmetry (piston removal) reversed in time is also a symmetry breaking with probabilities $\tilde{p}_1 = \alpha'$ and $\tilde{p}_2 = 1-\alpha'$. The work necessary to complete the cycle when the particle chooses the left side of the container is $\langle W\rangle \geq kT\log(p_1/\tilde{p}_1) = kT\log(\alpha/\alpha')$. The bound is met when the expansion (moving the piston from α to α') is carried out quasistatically, but the result is universal.

In Fig. 8.2 we show an example of symmetry breaking and restoration. We introduce a piston at position α in a box with a single particle. The particle gets trapped in the left or right part of the box with probability $p_1 = \alpha$ and $p_2 = 1 - \alpha$, respectively. The piston is shifted to position α' and then removed. The removal of the piston is the restoration of the initial symmetry: the spatial homogeneity. The time reversal of the piston removal is the insertion of the piston at position α'. In this reversal process the probability that the particle gets trapped in the left and right part of the box is, respectively, $\tilde{p}_1 = \alpha'$ and $\tilde{p}_2 = 1 - \alpha'$. For the total work of this process, our inequality yields:

$$\begin{aligned} \langle W\rangle_1 &= \langle W\rangle_1^{(\mathrm{SB})} + \langle W\rangle_1^{(\mathrm{SR})} && (8.6)\\ &= kT\log\frac{p_1}{\tilde{p}_1} = kT\log\frac{\alpha}{\alpha'}. && (8.7) \end{aligned}$$

and similarly when the particle gets trapped in the right part of the compartment: $\langle W\rangle_2 = kT\log\frac{1-\alpha}{1-\alpha'}$.

8.2 Methods

8.2.1 Experimental methods

The experimental goal of this experiment is to be able to manage an optical potential which evolves from a single position of equilibrium to a double well where no thermal transitions are allowed. The potential must be possible to bias in order to change the probability to choose each possibility. We implement two optical traps, fixing one at a desired position (from now, fixed trap **F**, whose position x_F^T is fixed at 0 nm) while we can displace the movable trap (**M**, whose position is denoted by x_M^T) between an initial position (i) to a final place (f). The total potential defined by the addition of both traps defines a single equilibrium position. The final configuration defines two posible equilibrium states. One of the conditions of the experiment is the quasistaticity, the free parameter, i.e., x_M, must change as slow as possible.

Roughly, the experimental setup consists in a 1060nm optical beam (Manlight, ML10-CW-P-OEM/TKS-OTS) which is steered by an AOD (ISOMET LS55 NIR). The beam is highly focused inside a custom-made chamber to create the trap by a high NA oil-immersed objective (Nikon, CFI PL FL 100× NA 1.30). The position of the bead is recorded by an aditional 532nm laser coaxial to the trapping laser. The scattered light is collected by the microscope objective (×10, NA=0.10) and projected to a QPD. A 532 band-pass filter is placed before the QPD to avoid the infrarred scattered light. More details as well as a scheme of the experimental setup can be found in section 2.4.3.

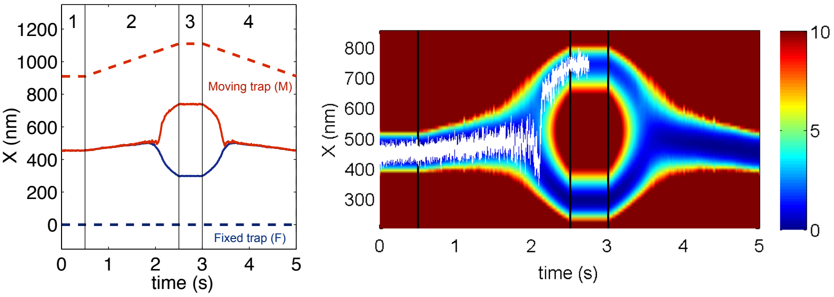

Figure 8.3: Experimental protocol of symmetry breaking and symmetry restore. Left) Positions of the F trap (blue dashed line) and M trap (red dashed line) as a function of time during the protocol. Ensemble average position of the trapped bead after implementing the protocol cyclically during $t = 2400\,\mathrm{s}$ over F trajectories (blue solid line) and M trajectories (red solid line). Right) Spatial-temporal mapping of the trapping potential $U(x,t)$ obtained from the statistics of trajectories of the bead during $t = 2400\,\mathrm{s}$ in the presence of an external force such that $p_F = 0.8$. Color bar in the right indicates the depth of the potential energy (in units of kT). A single trajectory of the bead when it choses the M trap is also plotted (white line). Notice that in this case, the bead ends in the M trap after performing Kramers transitions.

The dual trap is created by the *time-sharing regime* described in section 2.4.1. Here, we implement a voltage signal to the AOD controller which alternated between the two desired positions. In other words, we combine an square signal at 20kHz to build the two traps with an extra signal which defined the separation between the traps, in this case a forward-backward slope at a low frequency (in the present experiment, two different periods are studied, 5 seconds and 12 seconds). The total voltage signal is applied to the AOD controller, allowing us to control the protocole by a Labview program.

The detection of the Brownian particle is based in the detection of the scattered light of the extra 532nm laser. The system is calibrated by the PSD method before each measurement. The optical potential is biased by an electric force produced by a DC voltage applied in the custom made chamber electrodes[1]. The force is calibrated in function of the voltage and is changed in order to explore the different probabilities. We notice experimentally the low

---

[1] More details in section 2.4.2

forces which are necessary to bias it, always less than 2pN, what allow us to use small difference of voltage between the electrode, what prevent us to undesirable effects as Faradaic reactions in the metallic surface.

The **F** trap is held fixed while the **M** is moved along the $x-$axis following the four step protocol depicted in Fig.8.3a: 1) the two traps are initially at rest during a period of time $\tau_1 = 0.5\,\mathrm{s}$ with their centers separated by a distance $L_{\mathrm{ini}} = 910\,\mathrm{nm}$; 2) trap M is moved along the $x-$axis at constant velocity v_{trap} during a time τ_2; 3) the two traps are again kept fixed for a time $\tau_3 = 0.5\,\mathrm{s}$ with their centers separated by $L_{\mathrm{fin}} = 1,110\,\mathrm{nm}$; 4) trap M is moved back from L_{fin} to its initial position L_{ini} with velocity $-v_{\mathrm{trap}}$ in a time τ_2. The total duration of the cycle is $\tau = 2\tau_2 + 1\,\mathrm{s}$. By repeating this protocol cyclically, we can study both the SB (steps $1-2-3$) and the symmetry restoration (steps $3-4-1$). As it was mentioned, an uniform electrostatic field allows us to bias the motion of the bead towards the M or F trap. The protocol can be considered quasi-static for velocities around 100 nm/s or below, for which heat dissipation due to drag is of order $\gamma v_{\mathrm{trap}}^2 \approx 10^{-22}\,\mathrm{J/s} \approx 0.02\,kT/\mathrm{s}$, where $\gamma = 6\pi R\eta$ is the drag coefficient, $R = 0.5\,\mu\mathrm{m}$ being the radius of the bead and $\eta = 8.9 \times 10^{-4}\,\mathrm{Pa}\cdot\mathrm{s}$ the dynamic viscosity of water at 25°C. We have implemented two quasistatic protocols with $v_{\mathrm{trap}} = 100\,\mathrm{nm/s}$, $\tau_2 = 2\,\mathrm{s}$, and $v_{\mathrm{trap}} = 36.36\,\mathrm{nm/s}$, and $\tau_2 = 5.5\,\mathrm{s}$. In our experiments, the whole cycle is repeated under the same conditions (bead and electrostatic field) for 5000 s. At the end of the SB protocol (steps $1-2-3$), Kramers transitions are not observed and one can unambiguously distinguish two different final meso-states for the bead: F or M. We are able to track the position of the bead $x(t)$ with subnanometer precision with an acquisition frequency $f_{\mathrm{acq}} = 1\mathrm{kHz}$. In Fig.8.3b, we plot the average position of the bead of both F and M realizations as a function of time, $\langle x(t)\rangle_{F,M}$, which is calculated as an ensemble average over F and M trajectories, respectively. Next step is to calculate the thermodynamic quantities, in this case, heat and entropy, from the experimental observables.

8.2.2 Data analysis

One of the problems of measuring thermodynamic parameters is the necessity of knowing with high accuracy the value of the optical potential landscape at any moment of the protocole. We solved this challenge by the relation between the potential $U(x,t)$ and the position pdf $\rho(x,t)$, $U(x,t) = -kT\log(\rho(x,t)) + kT\log Z_t$, where Z_t is the partition function. This method is used in [39] modifying the free parameter step by step and calibrating the potential by taking data for a long time per each step. This methods lacks a huge time of observation when the barrier goes to higher values. We solved this problem by taking statistics of the trajectories itselves. As the protocole is slow enough, we can divide each cycle in small windows $[t - S/2, t + S/2]$, where S=50ms. By averaging over all the different cycles, and using the symmetrical time window of the backward process, as the protocole is symmetrical, the potential must be iddentical: $U(x,t) = U(x,\tau - t) \rightarrow \rho(x,t) = \rho(x,\tau - t)$. This averaging is crucial to avoid tautological consecuences of using the same data to calculate the potential and the thermodynamical parameters, having an independent data set to calculate the potential landscape. The histograms are developed using a fixed position window width of Δx =10nm. In order to calculate the heat dissipation in the different trajectories, the experimental potential landscape must be known for each possible value of the bead's position. Therefore, the experimental potential landscape estimation is fitted to a quartic polynomial: $U(x,t) = a_0(t) + a_1(t)x + a_2(t)x^2 + a_3(t)^3 + a_4(t)x^4$, where $a_i(t)$ are time-dependent parameters [39]. As the histograms are done using a sliding window, we have a final potential estimation for any position with a time resolution equal to the defined by the sample frequency (Δt =1ms). The fit is weighed as $w(x,t) = \exp \frac{-U(x,t)}{kT}$, so the data from the bottom of the potential are favored in the fit. All the data points that exceed $10kT$ are neglected from the fit due to their low statistics. We show in Fig. 8.5 how the double well is created from a state with a single minima Fig. 8.5a, to a double well with unavoidable thermal transitions Fig. 8.5f. The system makes the election when the potential barrier is small enough to be jumped with the thermal energy Fig. 8.5c-e.

The stochastic entropy has two contributions [188], the change in the state function, $\Delta S = S_{final} - S_{initial}$, corresponding to the reduction of the phase space, and the increase of the system entropy due to the heat dissipation, ΔS^{env}.

$$S_{prod} = \Delta S - Q/T \tag{8.8}$$

The first term can be calculated from the data interval associated to the equilibrium positions when the traps are close [0s, 0.5s], which corresponds to the initial value of the entropy, $S_{initial}$. In this situation the particle can access to the whole phase-space Γ, see Eq. (8.9). At the end of the SB process, there is another interval where the potential is static, and the particle is allowed to go completely to equilibrium, [2.5s, 3s], here, the value of the entropy can be evaluated as S_{final} taking into account that the particle can explore only a region of the phase space, Γ_i, see Eq. (8.10).

$$S_{initial} = -k \int_{\Gamma} dx \rho_{initial}(x,t) \log \rho_{initial}(x,t) \tag{8.9}$$

$$S_{final} = -k \int_{\Gamma_i} dx \rho_{final}(x,t) \log \rho_{final}(x,t) \tag{8.10}$$

The other term is evaluated by the calculation of the heat dissipation along each process. The heat is calculated as it is shown in Appendix E. The heat interchange between the system and the thermal bath can be considered Gaussian, as we show in Fig. 8.7. If we rewrite Eq. (8.8), we will find an upper bound to the heat along the process per each possibility:

$$\langle S_{prod} \rangle_i = \Delta S_i - \langle Q \rangle_i / T \geq \log p_i \Rightarrow \frac{\langle Q \rangle_i}{T} \leq \Delta S_i - \log p_i \tag{8.11}$$

This bound is respected by all the realizations, in particular for the presented in Fig. 8.7, where the mean value of the heat is represented by the solid vertical lines and the dotted lines represent $\Delta S_i - \log p_i$

8.3 Results

8.3.1 Linking probabilities with the energetics

The entropy production in the symmetry breaking (restoring) as function of the probability is shown in Fig. 8.6. We see that the entropy production is always larger (smaller in the case of the restoring) than the theoretical bound, and that we found negative values of the entropy productions, more negative the less probable is the option. This production of entropy is compensated by a heat absorption from the environment. In other words, the system takes energy from the thermal bath to choose between the different options. This result is a generalization of the Landauer's principle, relating information with energetics. Moreover, opposite to the erasement of a bit, what it is done here is the generation of a bit of information.

Recently, it have been published a study of how heat is released to the environment when the information is erased in function of time [218]. With the present data, we can study experimentally an analogous problem, how the heat is absorbed from the environment when information is generated. In our case, we have generated different probabilities to achieve the posible final states F,M, or equivalently, how the entropy is produced when the symmetry is broken.

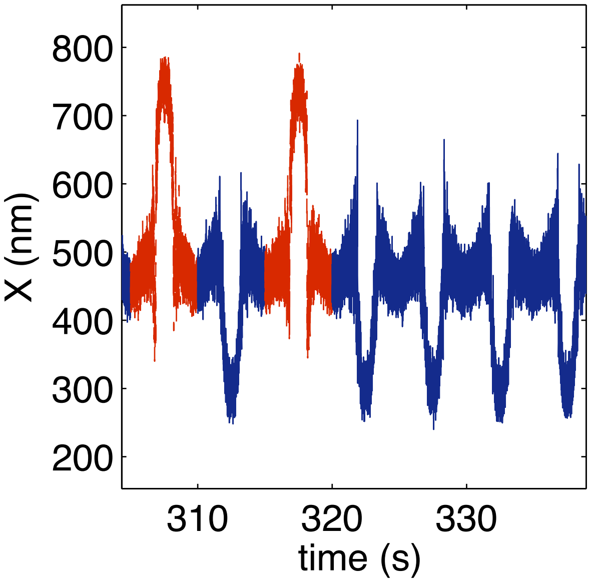

Figure 8.4: The F trajectories (blue) and M trajectories (red) obtained using the experimental protocol corresponding to Fig. 8.3.

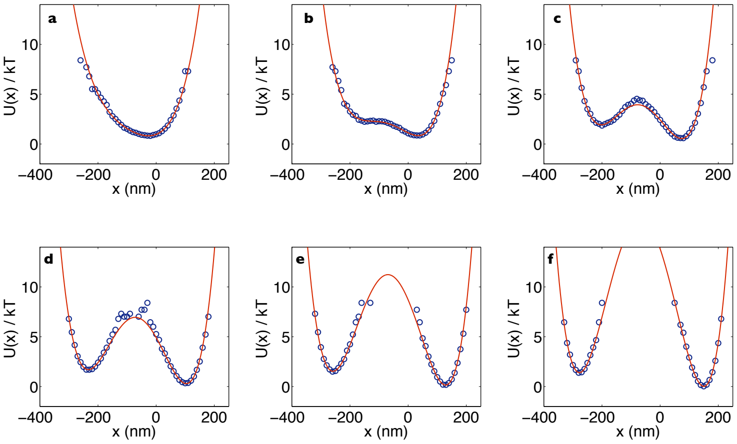

Figure 8.5: Experimental values of the trapping potential in units of kT (blue open circles) and its fit to a quartic potential (red curve) at different times t during the SB. a) $t = 1.7$ s. b) $t = 1.8$ s. c) $t = 1.9$ s. d) $t = 2$ s. e) $t = 2.1$ s. f) $t = 2.2$ s. The data are centered in such a way that the M trap moves from left to right (the origin in $x-$axis is set in the average position in the beginning of the cycle). The global minimum of the potential is set to zero.

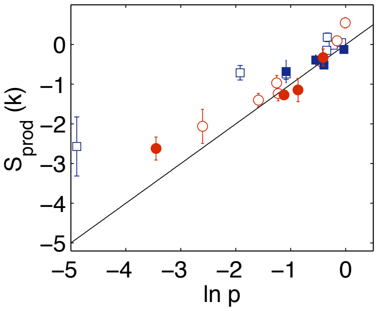

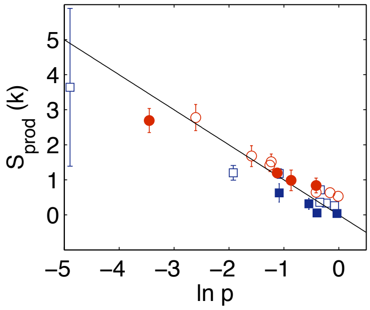

Figure 8.6: Ensemble average entropy production in the SB, $\langle S_{\rm prod}\rangle_i^{\rm (SB)}$ (top) and in the SR, $\langle S_{\rm prod}\rangle_i^{\rm (SR)}$ (down) as a function of the probability p_i $(\tilde{p}_i)$ of adopting instance $i = F, M$. Open symbols were obtained using the fast protocol ($\tau_2 = 2\,$s), and filled symbols were obtained using the slow protocol ($\tau_2 = 5.5\,$s). Blue squares represent the ensemble averages over F trajectories, whereas red circles represent the averages over M realizations. Error bars have only statistical sense and were obtained using a statistical significance of 90%.

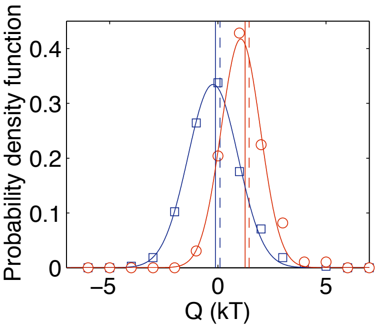

Figure 8.7: Probability density function of the heat (in units of kT) for the F trajectories (blue open squares) and M trajectories (red open circles). Solid curves are Gaussian fits, with $R^2 = 0.995$ for the F case and $R^2 = 0.990$ for the M case. Vertical lines are the empirical averages of the two ensembles and dashed vertical lines correspond to $\Delta S_i - \log p_i$.

In order to neglect the irreversible entropy due to the friction of the bead, we present the difference of entropy production ($\Delta S_{prod} \equiv \Delta S - Q/T$) between the events at certain probability (p_i) and its symmetric ($1-p_i$). Then, $\langle S^F_{prod}(p_i)\rangle - \langle S^M_{prod}(1-p_i)\rangle \geq k \log \frac{p_i}{1-p_i}$. As the protocole is completely symmetric, both values of the dissipated heat must be iddentical. Fig. 8.8 shows the difference of the cumulative production of entropy between the two posible choices in a processes. Each curve represents a different value of p_F.

The entropy production remained zero until the moment the double well was created. Then, the entropy started to be produced until the potential wall become too high to be jumped by thermal fluctuations. From this moment, the entropy production stopped. Our experimental data agrees qualitatively with the previous study [218]. Nevertheless, we have not carry out a quantitative study yet.

8.3.2 Building a Szilard engine

Using the techniques described above, we constructed a Szilard engine that extracts energy from a single thermal reservoir. The engine was implemented with a specific combination of SB and SR processes such that the lower bound

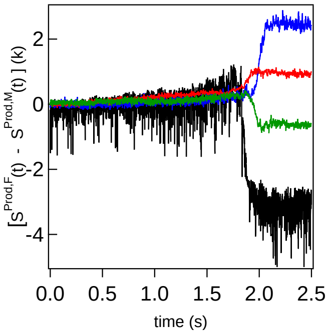

Figure 8.8: Entropy generation difference between the two posible choices in some representative cases as function of time: $p_F = 0.93$ (blue), $p_F = 0.71$ (red), $p_F = 0.15$ (green), $p_F = 0.01$ (black)

for the work $kT \sum_i p_i \log(p_i/\tilde{p}_i)$ is negative, see Eq. (8.5). The minimum work is attained for $p_i = 1/2$ and $\tilde{p}_i = 1$, for $i = F, M$, as in the original Szilard cycle. We performed multiple experiments at different conditions, and in three experiments we could achieve a combination of probabilities that gave us the negative average work: 1) $p_F = 0.35$, $p_M = 0.65$; 2) $\tilde{p}_M = 0.99$; and 3) $\tilde{p}_F = 0.93$. Then, our Szilard engine consists on the following feedback protocol. We start with the external voltage that gave us the first combination ($p_F = 0.35$, $p_M = 0.65$) and we measure continuously the bead position. If after the SB the bead is in the fixed trap (blue curves in Fig. 8.9), we change the external field to the value that gave us the combination ($\tilde{p}_F = 0.93$) and continue the protocol at this value of voltage until the SR is completed. If after the SB the bead is in the M trap (red curves in Fig. 8.9) we change the external field to the value that gave us the combination ($\tilde{p}_M = 0.99$) and continue the protocol at this value of voltage until the SR is completed. The cycle should be completed tuning quasistatically the external voltage back to its initial value for which $p_F = 0.35$ and $p_M = 0.65$. This last step has not been implemented in the experiment, but in principle it can be realized with arbitrary small entropy production.

Figure 8.9 shows the average heat (solid curves), the change of Shannon entropy of the probability distribution of the bead position (dashed curves) and the average entropy production (dotted curves) along the feedback cycle. The averages are taken over trajectories that end in the F trap (upper plot; blue curves), the M trap (middle plot; red curves), and over all trajectories

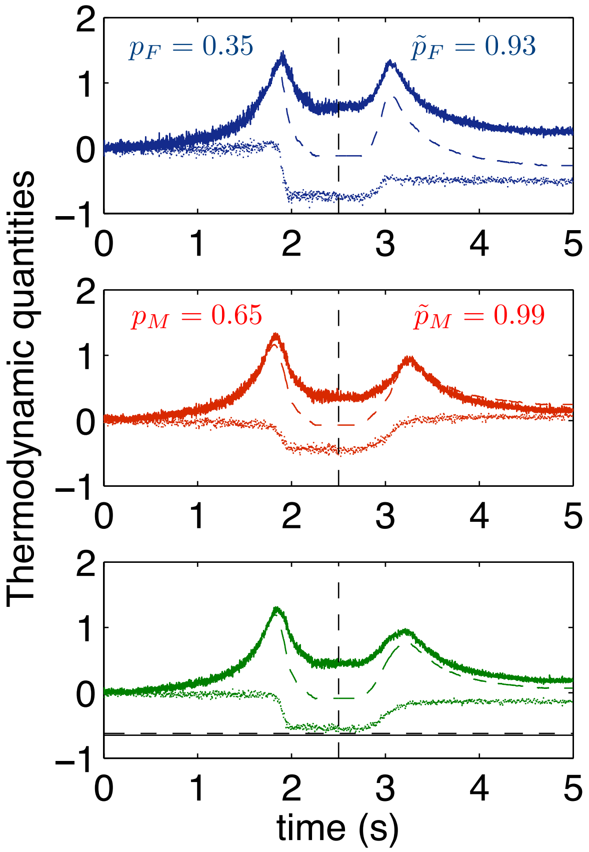

Figure 8.9: Average heat (solid lines, kT units), Shannon entropy of the trajectory distribution (dashed lines, k units), and average entropy production (dotted lines, k units) in the Szilard engine. The upper plot (blue curves) corresponds to the thermodynamic parameters averaged over the F trajectories. The middle plot (red curves) corresponds to the thermodynamic parameters averaged the M trajectories, and the lower plot shows the parameters averaged over all trajectories. The feedback protocol is explained in the text and indicated by the values of probabilities. The average values of the thermodynamic parameters shown on the bottom panel are obtained using the SB probabilities along the whole cycle. We also indicate in the bottom figure the values of information quantities for the combination of probabilities in the feedback cycle: $D(p_i||\tilde{p}_i) = \sum_i p_i \log(p_i/\tilde{p}_i)$ (black dashed line) and $-H(p_i) = \sum p_i \log p_i$ (black solid line).

(lower plot; green curves). Notice that the average of the thermodynamic parameters over all trajectories is done using the probabilities in the SB, that is, $\langle S_{\text{prod}}\rangle^{(\text{SB})} = \sum_i p_i \langle S_{\text{prod}}\rangle_i^{(\text{SB})}$ for the SB and $\langle S_{\text{prod}}\rangle^{(\text{SR})} = \sum_i p_i \langle S_{\text{prod}}\rangle_i^{(\text{SR})}$ for the SR. The entropy produced in the whole cycle averaged over all trajectories, $\langle S_{\text{prod}}\rangle = p_F \langle S_{\text{prod}}\rangle_F + p_M \langle S_{\text{prod}}\rangle_M$, is negative, as shown in the lower plot in Fig. 8.9. Notice that despite negative the average entropy production along the cycle is above $k\, D(p_i||\tilde{p}_i) = k \sum_i\, p_i\, (p_i/\tilde{p}_i)$ (and greater than the minimum entropy that can be produced $\langle S_{\text{prod}}\rangle/k > D(p_i||\tilde{p}_i) > -H(p_i)$ [215]) as predicted by our formulas [see Eq. (8.5)].

8.4 Conclusions

We derived an universal equivalence between the energetics of a process and the probability of a system to choose it among other options. This method can be used to obtain information about the distribution of the phase space (p_i) and the heat released to the environment. This expression can be considered a generalization of the Landauer's principle. We have tested our formulas in an optical tweezer experiment where a continuous transition from a single well to a double well optical potential produces a symmetry breaking affecting a Brownian particle (and the time reversal process to implement a symmetry restoration). Actually, we have a *bit generator machine* which is showing that the bit production is energetically more favorable the lower the probability to obtain the desired state of the bit. If we discart the non-desirable bits, under a feedback process, the result is inversal to the Landauer prediction. In this chapter we have shown how ***the energy to generate a bit of information can be extracted from the thermal bath energy, the less likely the event, most favorable being***. Nevertheless, in our research we are not taking into account the energy needed to measure, what obviously will compensate part of the obtained energy.

The experimental results agrees with the novel theoretical models for the recording or erasing information processes in a physical memory [218]. The final result of this research is the construction of an experimental Szilard engine where the average entropy production along a cycle is negative despite it is compensated by the information entropy. A potential application of our results might be the understanding of the energetics in folding and unfolding processes that appear in biochemistry. In fact, our results could be used to infer the probability of a protein to adopt a particular metastable conformation from energetic measurements. By measuring the average work done by a protein to change its conformation, we could estimate the probability of the protein to choose a particular conformation or the free energy change between metastable states. The advantage of our theoretical approach is that one does not need to realize the backward experiment to calculate the free energy changes as it is required to estimate free energy changes using extended fluctuation theorems.

8.5 Acknowdlegements

This chapter was developed in colaboration with Prof. J. M. R Parrondo group from Universidad Complutense de Madrid.

9

Conclusions

Since Robert Brown's observation of the motion of a grain of pollen in suspension, the study of the noise in nature has made possible to understand the behavior of small systems or collective systems. Along this thesis, we have studied the effect of noise in small systems, applying external sources of noise and studying the intrinsic noisy behaviour of biological systems.

First, we studied a single DNA molecule at different stretching. In this case, we have observed the dynamics of different stationary states of the biomolecule. We observed a power law in the PSD of the trajectory of dielectric bead used to anchor the DNA. Chapter 4 is related to the dynamics of single bacterium. We proposed a simple technique to study quantitatively the phenotype of individual cells, easily implentable in biological laboratories.

In the second part of the thesis, we have developed a technique to mimick temperature in OT experiments. Thanks to this technique, we could design non-isothermal processes permitting to check new theoretical models. Afterthat, we studied the energetics of the symmetry breaking, deriving an universal analytic expression. This equation was tested experimentally by an OT experiment.

- **New tools for optical tweezers technique**

  The detection of the trapped sample by the analysis of the scattered light has a small range if it is compared with other techniques as image tracking. We used the objective with lower NA to focused the detection laser. This allows to have a wider spot in the trapping plane, what increase the detection linear range up to several microns, ten times larger than in the traditional configuration. The interference pattern depends in the bead's radius, what is reflected in a relation between the size and the linear range. The technique is simple, but it has several shortcoming. The sensitivity is less than the obtained in the classical configuration. We noticed also that the instrumental noise of the optical setup affects stronger than un the conventional scheme. One of the shortcomings of the OT technique is the finiteness of its linear regime where $F = -\kappa\Delta x$ is valid. To have a good characterization of the OT force map is essential to compute forces with high accuracy. Here, we developed a technique to measure the force map with a single trapping laser, in setups where the beam is managed by an AOD.

Ignacio A. Martínez and Dmitri Petrov. *Back-focal-plane position detection with extended linear range for photonic force microscopy* **Applied Optics** 51 (25), 5973-5977 (2012)

Ignacio A. Martínez and Dmitri Petrov. *Force mapping of an optical trap using an acousto-optical deflector in a time-sharing regime* **Applied Optics**, 51 (22), 5522-5526 (2012)

- **Colored noise in the fluctuation of an extended single DNA molecule**

  Our experiments showed that the fluctuations of the DNA molecule extended up to 80% by a force of 3 pN include the additional colored noise with spectral dependence $1/f^{\alpha}$ with $\alpha \sim 0.75$. In our case, the difference with previous approaches is the comparable stiffness of the OT with the eleastic constant of the DNA [25]. For DNA in its natural conditions (in liquid), the Brownian noise stemming from fundamental thermal forces is the main contributor to the noise acting on the molecule. The Kramers transition theory is valid only when the thermal noise with white spectrum exists in the system. As we show here, the component with colored noise spectrum exists in the molecule and therefore these additional fluctuations may be added to the thermal noise, causing changes in the probability of noise-induced events. Recent experiments have shown that, for several proteins, the dependence of folding and unfolding rates on solvent viscosity does not obey Kramers theory [133]. A theoretical attempt to explain the violation of Kramers theory for the dependence of protein folding rates on viscosity showed that the presence of the correlated (colored) noise may be important [134].

Ignacio A. Martínez, Saurabh Raj and Dmitri Petrov. *Colored noise in the fluctuations of an extended DNA molecule detected by optical trapping* **European Biophysics Journal** 41 (1), 99-106 (2012)

- **Study of the dynamics of *S. enterica* by single *OT***

  By analyzing the statistical functions derived from following the trajectories $\{x(t), y(t)\}$ of a bacterium trapped by a single optical beam the different dynamic properties of different bacteria can be distinguished. The approach described herein is based on a model of the rotation of a solid optically trapped sphere. The optical trap technique can be easily implemented in a biological laboratory, since it requires only a small number of optical and electronic parts to convert a simple biological microscope into the required analyzer. In a demonstration of the utility of this method, we determined the motility profile of the *S.* Typhimurium *cheV* mutant derivative under anaerobic conditions, which case it exhibits tumbling behavior. This observation will contribute to elucidating the role of the CheV protein in the bacterial chemotaxis pathway.

  Ignacio A. Martínez, Susana Campoy, Meritxell Tort, Montserrat Llagostera and Dmitri Petrov. *A Simple Technique Based on a Single Optical Trap for the Determination of Bacterial Swimming Pattern* **PLOS ONE**, 8 (4),e61630 (2013)

- **Noise as temperature**

  We started from the following hypothesis: *a brownian particle can not distinguish the enforcement of an external Gaussian force with white spectra from an increase of the temperature of the media.* Using the intrisic charge of a polystyrene bead inmersed in water, we have presented an experimental technique that allows one to control the kinetic temperature of a Brownian particle over a wide range of values, from room temperature to several thousands Kelvin. We tested our technique in equilibrium, by the study of $\rho(x)$ and PSD, and out of equilibrium, by a protocole where the Crooks theorem is checked. We studied the associated temperature to each section, T_{hist}, T_{PSD} and T_{C}, doing an analitical analysis of the differences between them. The kinetic temperature is also applied to a double potential. The residence time in each metastable position is observed, studying the difference between different kinetic temperatures.

Ignacio A. Martínez, Édgar Roldan, Juan MR Parrondo and Dmitri Petrov. *Effective heating to several thousand kelvins of an optically trapped sphere in a liquid* **Physical Review E**, 87 (3), 032159 (2013)

- **Non-isothermal processes**

  Previous technique is implemented to generate different non-isothermal processes, such as *isochoric* or *adiabatic*, and to study the energetics of each process. Thanks to the large range of temperature, we can study the different theoretical frameworks. On the other hand, as the kinetic temperature is ellectronically managed, we can synchronize the changes of stiffness with the changes of temperature, allowing to study the different approach to *adiabatic processes* [64, 65, 188]. The different processes were developed in the quasistatic regime, therefore, the value of $\rho(W)$ is peaked in the average values, not showing a large deviation. On the other hand, the heat has an intrinsecal broadening, even when the protocole is done slowly. In our experiments we observe a non-Gaussian distribution of the $\rho(Q)$ in all the processes where T_{kin} is varied. We derived an analitic expresion which validied our experimental observation.

- **Universal features of symmetry breaking**

  We derived an analitic equivalence between the energetics of a process and the probability to choose it, in other words, a generalization of the Landauer's principle. This method can be used to obtain information about the distribution of the phase space (p_i) and the heat released to the environment. We tested experimentally the relation with an optical tweezers setup along symmetry breaking and restoring protocoles in the quasistatic limit. Actually, we have a *bit generator machine* which is showing that the bit production is energetically more favorable as lower is the probability to obtain the desired bit. The final result of this research is the construction of a Szilard engine where we can transform thermal energy into useful work.

  Édgar Roldan, Ignacio A. Martínez, Juan MR Parrondo and Dmitri Petrov. *Universal features in the energetics of symmetry breaking In preparation*

9.1 Open questions

Under our point of view, this thesis opens the door to several new experiments. For instance, the implement of the virtual temperature can be applied in the study of active transport, like Feymann ratchet, or in the study of micro-size engines' efficiency. Another example is the construction of the Büttiker-Landauer motor [219], the anisotropic feature of the kinetic temperature can be used to build to implement two different thermal baths to the system. A similar technique, but changing the applied noise to colored noise, can be used to study the thermodynamics of systems where the thermal bath is correlated, trying to realize experimentally the theory proposed by Takahiro Sagawa in the case of shot non-Gaussian noises [220]. Additionally, the experimental study of the stochastic resonance or the thermal activated transitions in the presence of colored noise like is proposed in [221], where an analitical study is presented. In the case of the features of SB, one of the possible applications is the study of the thermodynamics of the kinetic states in proteins, this field has recent contributions [214], and our work can be used to explain the dynamics of proteins [40]. The study of the differential case, analogous to [218], can be expanded to understand the reversibility of the process.

In the case of biomolecules, the study of the fluctuations at the overstretching regime can be done. Application of [222] in the study of synchronization effects and in different mutations, as SOS response, could also be developed.

9.2 Publications with main results of this thesis

1. Édgar Roldan, Ignacio A. Martínez, Juan MR Parrondo and Dmitri Petrov. *Universal features in the energetics of symmetry breaking*, *In preparation*

2. Ignacio A. Martínez, Susana Campoy, Meritxell Tort, Montserrat Llagostera and Dmitri Petrov. *A Simple Technique Based on a Single Optical Trap for the Determination of Bacterial Swimming Pattern* **PLOS ONE**, 8 (4),e61630 (2013)

3. Ignacio A. Martínez, Édgar Roldan, Juan MR Parrondo and Dmitri Petrov. *Effective heating to several thousand kelvins of an optically trapped sphere in a liquid* **Physical Review E**, 87 (3), 032159 (2013)

4. Ignacio A. Martínez and Dmitri Petrov. *Back-focal-plane position detection with extended linear range for photonic force microscopy* **Applied Optics** 51 (25), 5973-5977 (2012)

5. Ignacio A. Martínez and Dmitri Petrov. *Force mapping of an optical trap using an acousto-optical deflector in a time-sharing regime* **Applied Optics**, 51 (22), 5522-5526 (2012)

6. Ignacio A. Martínez, Saurabh Raj and Dmitri Petrov. *Colored noise in the fluctuations of an extended DNA molecule detected by optical trapping* **European Biophysics Journal** 41 (1), 99-106 (2012)

9.3 Other publications

Electrophoretic mobility of a growing cell studied by photonic force microscope Mario Tonin, Stefan Balint, Pau Mestres, Ignacio A. Martínez and Dmitri Petrov **Applied Physics Letters** 97 (20), 203704-203704-3 (2010)

A

Salmonella construction

A.1 Bacterial strains, media, and growth conditions

All bacterial strains and plasmids used in this work are listed in Table A.1. Except when indicated, the bacteria were grown at 37^{o}C in Luria–Bertani (LB) broth or plates. Ampicillin (100 mg/ml) or chloramphenicol (34 mg/ml) was added to the culture as necessary. Bacteria used in the optical trapping experiments were grown overnight in 2 ml of LB broth supplemented, when needed, with the appropriate antibiotic. Each culture was then diluted 1/10 into LB broth without antibiotic and incubated at 37^{o}C for 1 h. To reduce trap-mediated oxidative damage to the bacterial cells and ensure that a steady level of oxygen was reached during the optical measurements [59], an oxygen scavenging system, consisted of glucose oxidase and catalase at final concentrations of 100 μg/mL and 20 μg/ml, respectively, was added at least 2 h before the measurements [158]. The added glucose is a substrate for the oxygen scavenging system and provides the energy needed for swimming in anaerobic conditions [159]. For the optical traping measurements, the culture was further diluted 100-fold in trapping medium (1% Bacto Tryptone, 0.8% NaCl, 2% glucose, 100 mM Tris-

Cl, pH 7.5). The use of tryptone broth for the optical trapping experiements is appropriate to obtain reproducible cell motility assays [223]. Dead cells used as controls were prepared by addition of 2% formaldehyde to the culture, with subsequent dilution steps carried out following the same protocol used for the live bacterial cultures.

A.2 Construction of *S.* Typhimurium LT2 mutant derivatives

The *S.* Typhimurium LT2 mutant derivatives used in this work were knockout mutants constructed by the one-step PCR based gene replacement method [224]. All DNA techniques were performed as described elsewhere [225]. The chloramphenicol resistance cassette from the plasmid pKD3 was amplified using suitable 100-nucleotide (nt)- oligonucleotides containing 80-nt stretches homologous to each of the insertion sites, Table A.2 . The PCR product was DpnI digested and transformated into the *S.* Typhimurium LT2 electrocompetent cells containing the pKOBEGA plasmid [226]. Following selection of the transformant clones, the pKOBEGA plasmid was eliminated by taking advantage of its temperature sensitivity, growing the clones at 42°C. Gene substitution was confirmed by PCR and sequencing. In all cases, the resulting construct was transferred to a wild type *S.* Typhimurium LT2 strain by transduction, using the P22 HT bacteriophage [227]. The absence of the prophage in the selected transductant clones was determined by streaking them onto green plates as previously described [228]. The resulting strains were again verified by PCR and sequencing.

Table A.1: Bacterial strains and plasmids used in this work.

Strain or plasmid	Relevant characteristics	Source of reference
LT2	*S.* Typhimurium wild type strain	Generous gift of Prof. J. L. Ingraham
UA1902	As LT2 but $\Delta cheY$. Cm^R	This study
UA1903	As LT2 but $\Delta cheB$. Cm^R	This study
UA1905	As LT2 but $\Delta cheW$. Cm^R	This study
UA1906	As LT2 but $\Delta cheV$. Cm^R	This study
pKOBEGA	Plasmid Amp^R, ts	[226]
pKD3	Plasmid Amp^R, Cm^R	[227]

Table A.2: Oligonucleotides used in this work

Name	Sequence(5'→3')	Application
P1cheB	TGACCCTGGACGTTGAGATGCCGCGTATGGACGGCCTCGATTTTCTGGAAAACTGATGCGCCTGCGACCGATGCCGGTGgtgtaggctggagctgcttc	P1 primer used for S. Typhimurium cheB mutant construction
P2cheB	CCTTCACGCTGATTTGACAGAGTTTATTCAGACGCTCGGCAAACGAGCGGGTAAAGCCAGGCGGCATATGCTGCGTAATAatgggaattagccatggtcc	P2 primer used for S. Typhimurium cheB mutants construction
cheBeR	TGAAACAGCACATCCACGGA	Lower primer used for S. Typhimurium cheB mutants confirmation by PCR and sequencing
cheBeF	CAGTTGATGATTCCGCGCTA	Upper primer used for S. Typhimurium cheB mutants confirmation by PCR and sequencing
P1cheY	GCTTGGATTTAACAATGTGGAAGAGGCCGAAGACGGCGTCGATGCGCTGAACAAGCTCCAGGCGGGCGGCTTTGGTTTTagtgtaggctggagctgcttc	P1 primer used for S. Typhimurium cheY mutants construction
P2cheY	CATAACCGCTGGCGCCAGCCTGTGCGGCGGCGATAATATTCTCTTTTTTGGCTTCCGCCGTGACCATCAACACGGGTAAatgggaattagccatggtcc	P2 primer used for S. Typhimurium cheY mutants construction
cheYeR	CTCTGTTCCGGGATGTTTTCCA	Lower primer used for S. Typhimurium cheY mutants confirmation by PCR and sequencing
cheYeF	TCGTTTGCCGAGCGTCTG	Upper primer used for S. Typhimurium cheY mutants confirmation by PCR and sequencing
P1cheW	GGCGAGCCGTCAGGTCAGGAATTCCTGGTGTTTACACTGGGAAATGAAGAGTACGGCATCGATATCCTGAAAGTGCAGGAgtgtaggctggagctgcttc	P1 primer used for S. Typhimurium cheW mutants construction
P2cheW	TATCCAGCAGCGCCATCTCTTCGCTGTTAAGCAGTTTTTCGATATTCACCAGAATCAGCATACGCTCGCCGAGCGCGCCCatgggaattagccatggtcc	P2 primer used for S. Typhimurium cheW mutants construction
cheWeR	TCGCTGGCAATGGCGTCATA	Lower primer used for S. Typhimurium cheW mutants confirmation by PCR and sequencing
cheWeF	GTCACGTTGAGATCCAGTCA	Upper primer used for S. Typhimurium cheW mutants confirmation by PCR and sequencing
P1cheV	ATCAGGTCATTCCGGTGATTGATTTGCCAGCGGTAGCGGGCTGCAAGCCGGAAACCGGGCTGAATATTTTGCTGATCACCgtgtaggctggagctgcttc	P1 primer used for S. Typhimurium cheV mutants construction
P2cheV	CTTCCTGCGCCAGTTGCTGGATTCTCTCCCAGGCATCCTTGCCGGTCACATGCATCTGATGCGGAATTCCCATCGCGTTCatgggaattagccatggtcc	P2 primer used for S. Typhimurium cheV mutants construction
cheVeR	CGGCATCTCAAGATCTGTCAs	Lower primer used for S. Typhimurium cheV mutants confirmation by PCR and sequencing
cheVeF	GTCTTGGTACATCGCTGCAT	Upper primer used for S. Typhimurium cheV mutants confirmation by PCR and sequencing

B

Stochastic Calculus

B.1 Introduction: Where the classical calculus fails

The approximation to a perfect white noise of the Brownian force ($\xi(t)$) only has sense if the relevant time scale time is much larger than the correlation time of the force. In other words, the adquisition time of our experiment $1/f_{acq}$ is much higher than the inertial time of the sample $\tau_m = \gamma/m$. In this situation, we can replace the correlation function by a Dirac delta $\delta(t)$. Brownian force has the following properties:

$$\langle \xi(t) \rangle = 0 \tag{B.1}$$

$$\langle \xi(t)\xi(t+\tau) \rangle = 2kT\gamma\delta(t) \tag{B.2}$$

This idealization carries out some difficulties. The change of usual functions to functionals induces to the need to take care of all the calculus that we want to do. Otherwise, the obtained results will be qualitatively different to reality. To deal with this kind of calculus we must define systematic rules. In summary, we must known when the rules of ordinary calculus are valid, how the calculus rules change when we use this type of functions and where the new results appears to recognize them. The pioneer of the stochastic calculus was Kiyoshy Itô in the 50s of the last century [14]. He developed the first mathematical framework of the Langevin equation. Analogously to other branches of science, the study of this single problem, i.e, the Langevin equation, open the door of the development of a new field of analysis called *Stochastic Calculus*.

B.2 Wiener Processes

In order to study stochastic processes, Norbert Wiener introduced a stochastic process, named after him **Wiener Process** (WP), $\mathcal{W}_t$, as the basic object to interpret white Gaussian stochastic processes such as $\xi(t)$. The definition reads as follows:

$$\int_t^{t+dt} \xi(s)ds = \sqrt{2kT\gamma}d\mathcal{W}_t \tag{B.3}$$

where the differential of the Wiener process is $d\mathcal{W}_t = \mathcal{W}_{t+dt} - \mathcal{W}_t$. The time interval dt is an infinitesimal positive increment of time. If we link this definition with the LE we can probe that: $x(t) = x(0) + \sqrt{\frac{2kT}{\gamma}t}(\mathcal{W}_t - \mathcal{W}_0)$. On the other hand, from the properties of $\xi(t)$ (B.1) (B.2), it is possible to write: $\langle\left(\frac{d\mathcal{W}_t}{dt}\right)\left(\frac{d\mathcal{W}_t}{dt'}\right)\rangle = \delta(t-t')$. Another feature of $\mathcal{W}_t$ is that being $\xi(t)$ and $\frac{d\mathcal{W}_t}{dt}$ mathematically non-treatable as function of time, $\mathcal{W}_t$ does.

One possible question is why do not define $\mathcal{W}_t$ as $\xi(t)dt = \sqrt{2kT\gamma}d\mathcal{W}_t$. The reason is that $d\mathcal{W}_t$ should be different from $d\mathcal{W}_{t+\alpha dt} - d\mathcal{W}_{t-(1-\alpha)dt}$ with α different from 1. In addition, $d\mathcal{W}_t$ is $O(\sqrt{dt})$ and not $O(dt)$.

The Wiener processes have several useful properties:

- From (B.1), it follows that $\langle\mathcal{W}_t - \mathcal{W}_{t'}\rangle = 0$, for any t and t'. It implies that $\langle d\mathcal{W}_t\rangle$=0. Secondly, using the correlation property of $\xi(t)$ (B.2), it is possible to derive an analog property of the correlation in Wiener processes: $\langle d\mathcal{W}_t d\mathcal{W}_{t'}\rangle = 0$, where $t \neq t'$ implies there is no overlap between $[t, t+dt]$ and $[t', t'+dt']$.

- As $\xi(t)$ is ruled by a Gaussian distribution, $\mathcal{W}_{t'} - \mathcal{W}_t$ also does.

- Wiener process is not bounded variation. This property lies in the total variation of $\mathcal{W}_s$ inside $s \in [0, t]$ which is characterized by the $n \to \infty$ limit of $\sum_{j=1}^{n} \mid \mathcal{W}_{\frac{j}{n}t} - \mathcal{W}_{\frac{j-1}{n}t} \mid$. This limit is divergent with probability 1 for any Wiener process.

- The limit $\sum_{j=1}^{n\to\infty} \mid \mathcal{W}_{\frac{j}{n}t} - \mathcal{W}_{\frac{j-1}{n}t} \mid^2$ tends to t with probability 1. As each interval of time$(\frac{j}{n}t - \frac{j-1}{n}t)$ gives independent contribution, we can write $(d\mathcal{W}_t)^2 = dt$ with **no average** over the path.

B.3 Different kind of integrals

In order to have a consistent theory of stochastic calculus, we need to define how to do integrals in the form of $\int f(t) d\mathcal{W}_t$. These integrals are linked to the integrals which appear when we want to solve the LE. The problem appears due to the non-bounded variation property of the Wiener process, as it includes ambiguity in the definitions. To avoid this ambiguity, it is necessary to present strict definitions of the integrals. Let Δs be a positive interval of time, then it is possible to define two types of integrals, Itô calculus ((B.4), denoted by $\cdot$) and Stratonovich calculus ((B.5), denoted by $\circ$)

$$f(s)\left[\mathcal{W}_{s+\Delta s} - \mathcal{W}_s\right] \to f(s) \cdot d\mathcal{W}_s \tag{B.4}$$

$$\frac{f(s+\Delta s) + f(s)}{2}\left[\mathcal{W}_{s+\Delta s} - \mathcal{W}_s\right] \to f(s) \circ d\mathcal{W}_s \tag{B.5}$$

Notice that each kind of integral returns different results from the same integral. For example:
$\int_0^t (\mathcal{W}_s - \mathcal{W}_0) \cdot d\mathcal{W}_0 = \frac{(\mathcal{W}_t - \mathcal{W}_0)^2}{2} - \frac{t}{2}$
$\int_0^t (\mathcal{W}_s - \mathcal{W}_0) \circ d\mathcal{W}_0 = \frac{(\mathcal{W}_t - \mathcal{W}_0)^2}{2}$

One of the main differences of both type of calculus is the **non anticipating** property of the Itô type, i.e., $\langle f(t) \cdot d\mathcal{W}_t \rangle = 0$ if $f(t)$ does not depend on anything happening after t. This is equivalent to write:

$$\langle f(t) \cdot d\mathcal{W}_t \rangle = \langle f(t) \rangle \langle d\mathcal{W}_t \rangle = 0 \tag{B.6}$$

B.4 Stochastic Differential Equations (SDE): Itô lemma.

The Langevin equation can be rewritten in terms of the Wiener process as follows:

$$dx_t = a(x_t,t)dt + b(x_t,t)d\mathcal{W}_t \tag{B.7}$$

If we take the average of (B.7) along different trajectories inside a time interval $[t, t+dt]$, using the WP properties, we obtain:

$$\langle dx_t \rangle = a(x_t,t)dt \tag{B.8}$$

$$\langle (dx_t)^2 \rangle = b(x_t,t)^2 dt \tag{B.9}$$

Note that eq (B.9) is the Einstein's diffusion result ($\langle x^2(t)\rangle \propto t$). Next step needs the use of an arbitrary function ($f(x_t)$), where the differential in an infinitesimal interval of time (dt) can be defined as $df(x_t) \equiv f(x_{t+dt}) - f(x_t)$. From the differential of the function and eq.(B.7), it is defined the so-called **Itô lemma**:

$$df(x_t) = \left[a(x_t,t)f'(x_t) + \frac{b(x_t,t)^2}{2}f''(x_t)\right]dt + b(x_t,t)f'(x_t)d\mathcal{W}_t \tag{B.10}$$

where $f'(z) \equiv \frac{df(z)}{dz}$ and $f''(z) \equiv \frac{d^2f(z)}{dz^2}$. This is the analogous expression of the **chain rule** in the stochastic calculus.

The final question is: In physics, shall we use the Itô or Stratonovich convention? As we saw, there are qualitative differences between them, so this is not a trivial question. In physics, the use of the Stratonovich calculus is widely accepted. There are several reasons that support this choice. The first one is the non anticipating nature of Itô calculus, which is not in consonance with our expectancy to find $f(t)\xi(t)dt$ corresponding to a finite time resolution element. Secondly, Stratonovich calculus has inhereted the conventional calculus, that is closer to our intuition. Finally, the energetics of the stochastical processes will have similar expression to the classical ones just if we use the Stratonovich type to represent them [62].

B.5 Treatment of experimental data

An optical tweezers experiment will usually give as observables the position of the particle x, the stiffness of the trap κ and the equilibrium position of the trap

x_0. In order to calculate the energy exchanges W and Q along a given process described by a protocole λ, we use the Sekimoto approach. For instance, let $\kappa(t)$ changes in time, then defined as our control parameter $a(t)$. Sekimoto definition leads the following definition of heat and work:

$$W = \int_{\kappa_i}^{\kappa_f} \frac{\partial U}{\partial \kappa} \circ d\kappa = \int_{\kappa_i}^{\kappa_f} \frac{x^2}{2} \circ d\kappa \tag{B.11}$$

$$Q = \int_{x_i}^{x_f} \frac{\partial U}{\partial x} \circ dx = \int_{x_i}^{x_f} x\kappa \circ dx \tag{B.12}$$

Therefore, using Stratonovich calculus, the integrals are numerically obtained as:

$$W = \sum_{i=1}^{N} \frac{x[i+1]^2 + x[i]^2}{4} (\kappa[i+1] - \kappa[i]) \tag{B.13}$$

$$Q = \sum_{i=1}^{N} \frac{x[i+1]\kappa[i+1] + x[i]\kappa[i]}{2} (x[i+1] - x[i]) \tag{B.14}$$

where i denoted the index of the experimental array of observables. If $a(t)$ is another observable, an analogous treatment must be done.

C

Noise as temperature.

C.1 Calculation of $T_{\rm hist}$

We consider a Brownian particle whose motion is described by the Langevin equation (C.1),

$$\gamma\dot{x}(t) = -\kappa x(t) + \xi(t) + \zeta(t), \tag{C.1}$$

where $\xi(t)$ and $\zeta(t)$ are Gaussian noises with zero average $\langle\xi(t)\rangle = \langle\zeta(t)\rangle = 0$ and their correlation functions are

$$\begin{aligned} \langle\xi(t)\xi(t')\rangle &= 2kT\gamma\delta(t-t'), & \text{(C.2)} \\ \langle\zeta(t)\zeta(t')\rangle &= \sigma^2\Gamma(t-t'). & \text{(C.3)} \end{aligned}$$

The solution of Eq. (C.1) is:

$$x(t) = x(0)e^{-t/\tau_c} + \frac{e^{-t/\tau_c}}{\gamma}\int_0^t ds\; e^{s/\tau_c}[\xi(s) + \zeta(s)], \tag{C.4}$$

where $\tau_c = \gamma/\kappa$ is the relaxation time in the trap. If we multiply $x(t)$ by Eq. (C.1), and we do the average over different trajectories, we get

$$\frac{\gamma}{2}\frac{d\langle x^2\rangle}{dt} = -\kappa\langle x^2\rangle + \langle\xi x\rangle + \langle\zeta x\rangle, \tag{C.5}$$

where $\langle \xi x \rangle$ and $\langle \zeta x \rangle$ can be calculated using Novikov's theorem:

$$\langle \zeta(t) x(t) \rangle = \int_0^t ds \langle \zeta(t)\zeta(s) \rangle \left\langle \frac{\delta x(t)}{\delta \zeta(s)} \right\rangle. \tag{C.6}$$

Using Eq. (C.4), $\left\langle \frac{\delta x(t)}{\delta \zeta(s)} \right\rangle = \frac{1}{\gamma} e^{-(t-s)/\tau_c}$, therefore

$$\langle \zeta(t) x(t) \rangle = \frac{\sigma^2}{\gamma} \int_0^t ds\ \Gamma(t-s) e^{-(t-s)/\tau_c}, \tag{C.7}$$

whereas for the thermal noise

$$\langle \xi(t) x(t) \rangle = \int_0^t ds \langle \xi(t)\xi(s) \rangle \left\langle \frac{\delta x}{\delta \xi(s)} \right\rangle = kT. \tag{C.8}$$

Using Eqs. (C.7) and (C.8), Equation (C.5) can be rewritten as follows,

$$\frac{\gamma}{2} \frac{d\langle x^2 \rangle}{dt} = -\kappa \langle x^2 \rangle + kT + \frac{\sigma^2}{\gamma} \int_0^t dt'\ \Gamma(t') e^{-t'/\tau_c}. \tag{C.9}$$

In the steady state $t \to \infty$ and $d\langle x^2 \rangle / dt = 0$. In this limit, the above equation yields (6.7)

$$\kappa \langle x^2 \rangle_{\text{ss}} = kT + \frac{\sigma^2}{\gamma} \int_0^\infty dt'\ \Gamma(t') e^{-t'/\tau_c}. \tag{C.10}$$

By using equipartition theorem, we get T_{hist} as a function of the mean square displacement in the steady state,

$$T_{\text{hist}} = \frac{\kappa \langle x^2 \rangle_{\text{ss}}}{k} = T + \frac{\sigma^2}{\gamma k} \int_0^\infty dt'\ \Gamma(t') e^{-t'/\tau_c}, \tag{C.11}$$

which proves Eq. (6.8).

We notice that $\Gamma(t)$ has a characteristic timescale given by τ_Γ, so it can be expressed as a function of t/τ_Γ, say $\Gamma(t) = \Gamma(t/\tau_\Gamma)$. The correlation of the noise decays in this timescale, which makes that the integral in the above equation can be expressed, by using the change of variable $s = t/\tau_c$,

$$\int_0^\infty dt'\ \Gamma(t'/\tau_\Gamma) e^{-t'/\tau_c} = \tau_c \int_0^\infty ds\ \Gamma\left(\frac{\tau_c}{\tau_\Gamma} s \right) e^{-s}. \tag{C.12}$$

If $\tau_\Gamma \ll \tau_c$, the exponential decays much slower with s than the correlation of the noise in the units above, therefore it can be approximated by $e^{-s} \simeq 1 - s$,

$$\int_0^\infty dt'\ \Gamma(t'/\tau_\Gamma) e^{-t'/\tau_c} \simeq \tau_c \int_0^\infty ds\ \Gamma\left(\frac{\tau_c}{\tau_\Gamma} s \right) (1-s) = \frac{1}{2} - \frac{\tau_\Gamma}{\tau_c}. \tag{C.13}$$

For the last equality, we have used that $\Gamma(t)$ is normalized, $\int_{-\infty}^{\infty} dt\Gamma(t/\tau_\Gamma) = 1$, that it is symmetric around $t = 0$ and the definition of the correlation time of the noise $\tau_\Gamma = \int_0^\infty dt\ t\ \Gamma(t/\tau_\Gamma)$. By using Eq. (C.13) into Eq. (C.11), we prove Eq. (6.9)

$$T_{\text{hist}} \simeq \frac{\sigma^2}{2\gamma k}\left(1 - \frac{2\tau_\Gamma}{\tau_c}\right). \tag{C.14}$$

C.2 Calculation of $\langle W \rangle$

We now calculate the average of the work done when moving the trap centre at a constant velocity v for a period of time t. In this situation, the work done to move a trap that creates a moving quadratic potential $U(x(t), x_0(t)) = \frac{\kappa}{2}(x - x_0)^2$ is equal to

$$W = \int_0^t -\kappa(x - vt')v dt' = -\kappa v \int_0^t y(t')dt' \tag{C.15}$$

where we have used the definition of the work in Eq. (6.4) and $x_0(t) = v\ t$ as control parameter, and we have introduced the variable $y(t) = x(t) - vt$. $y(t)$ satisfies the following Langevin equation

$$\gamma\dot{y}(t) = -\kappa y(t) - \gamma v + \xi(t) + \zeta(t), \tag{C.16}$$

whose solution is

$$y(t) = y(0)e^{-t/\tau_c} + \frac{e^{-t/\tau_c}}{\gamma}\int_0^t ds\ e^{s/\tau_c}[-\gamma v + \xi(s) + \zeta(s)]. \tag{C.17}$$

The average over trajectories is given by

$$\langle y(t)\rangle = \langle y(0)\rangle e^{-t/\tau_c} - v\tau_c\left[1 - e^{-t/\tau_c}\right] = -v\tau_c\left[1 - e^{-t/\tau_c}\right], \tag{C.18}$$

where $\langle y(0)\rangle = \langle x(0)\rangle = 0$, since the bead is initially in equilibrium oscillating around the trap center located in $x = 0$. The average work reads

$$\langle W\rangle = -\kappa v \int_0^t \langle y(t')\rangle dt' = \gamma v^2 t + \frac{\gamma^2 v^2}{\kappa}\left[e^{-t/\tau_c} - 1\right], \tag{C.19}$$

which is the expression that we introduced in Eq. (6.11).

C.3 Calculation of T_{C}

For a process in which a physical system that starts in equilibrium it is driven out of equilibrium such that the probability distribution of the work is Gaussian, Crooks temperature is equal to Eq. (6.12)

$$T_C = \frac{\sigma_W^2}{2k\langle W\rangle}, \tag{C.20}$$

being $\langle W\rangle$ given by Eq. (6.11). We are now interested in calculating the variance of the work done in the nonequilibrium process consisting in moving the trap at a constant velocity v during a time t, which we call σ_W^2. We first notice that the work is defined in terms of the variable $y(t) = x(t) - vt$ as shown in Eq. (C.15). If we introduce the random variables

$$q_\xi(t') = \int_0^{t'} ds\, e^{-(t'-s)/\tau_c}\xi(s), \quad q_\zeta(t') = \int_0^{t'} ds\, e^{-(t'-s)/\tau_c}\zeta(s), \tag{C.21}$$

$y(t)$ can be rewritten as

$$y(t) = y(0)e^{-t/\tau_c} - v\tau_c\left[1 - e^{-t/\tau_c}\right] + \frac{1}{\gamma}\left[q_\xi(t) + q_\eta(t)\right]. \tag{C.22}$$

By replacing the above formula in Eq. (C.15), we get

$$W = -\gamma\ v\ y(0)\left[1 - e^{-t/\tau_c}\right] + \langle W\rangle - \frac{\kappa v}{\gamma}\int_0^t dt'[q_\xi(t') + q_\zeta(t')]. \tag{C.23}$$

Therefore, the work is a linear combination of random variables that are independent each other. This implies that the variance of the work can be expressed as the following sum

$$\sigma_W^2 = \gamma^2 v^2\left[1 - e^{-t/\tau_c}\right]^2\sigma_{x(0)}^2 + \frac{\kappa^2 v^2}{\gamma^2}\sigma_{q_\xi}^2 + \frac{\kappa^2 v^2}{\gamma^2}\sigma_{q_\zeta}^2. \tag{C.24}$$

The first term concerns the variance of the position at $t = 0$ in equilibrium, $\sigma_{x(0)}^2$, which is known (C.11).

$$\sigma_{x(0)}^2 = \frac{kT_{\mathrm{hist}}}{\kappa}, \tag{C.25}$$

The calculation of $\sigma_{q_\xi}^2$ and $\sigma_{q_\zeta}^2$ is not straightforward. The first can be calculated analytically whereas the second only for particular correlation functions of the external noise. We now show how a closed expression for the term concerning the thermal noise, $\sigma^2_{q_\xi}$, can be derived. This variance is defined as

$$\sigma^2_{q\xi} = \int_0^t dt_1 \int_0^t dt_2 \langle q_\xi(t_1) q_\xi(t_2)\rangle \tag{C.26}$$

where

$$\langle q_\xi(t_1) q_\xi(t_2)\rangle = \sigma^2 \int_0^{t_1} dt' \int_0^{t_2} dt'' e^{-(t_1-t')/\tau_c} e^{-(t_2-t'')/\tau_c} \Gamma(t'-t''). \tag{C.27}$$

For thermal Gaussian white noise, $\sigma^2 = 2\gamma kT$ and $\Gamma(t'-t'') = \delta(t'-t'')$, which yields

$$\langle q_\xi(t_1) q_\xi(t_2)\rangle = kT\frac{\gamma^2}{\kappa}\left[e^{-|t_1-t_2|/\tau_c} - e^{-(t_1+t_2)/\tau_c}\right]. \tag{C.28}$$

By replacing the above result into Eq. (C.26), and integrating, we obtain

$$\sigma^2_{q\xi} = 2kT\frac{\gamma^3}{\kappa^2}t + kT\frac{\gamma^4}{\kappa^3}\left[4e^{-t/\tau_c} - e^{-2t/\tau_c} - 3\right]. \tag{C.29}$$

After some algebra, T_C can be expressed as a function of $T_e = \sigma^2/2k\gamma$ for any correlation function $\Gamma(t)$ as follows:

$$T_c = T + \frac{\mathcal{L}\{\Gamma(t)\}(1/\tau_c) + \frac{1}{\tau_c^3}\int_0^t dt_1 \int_0^t dt_2 \int_0^{t_1} dt' \int_0^{t_2} dt'' e^{-(t_1-t')/\tau_c} e^{-(t_2-t'')/\tau_c}\Gamma(t'-t'')}{\frac{t}{\tau_c} + e^{-t/\tau_c} - 1} T_e, \tag{C.30}$$

where $\mathcal{L}\{\Gamma(t)\}(1/\tau_c)$ is the Laplace transform of $\Gamma(t)$ evaluated at $s = 1/\tau_c$,

$$\mathcal{L}\{\Gamma(t)\}(1/\tau_c) \equiv \int_0^\infty dt'\, \Gamma(t') e^{-t'/\tau_c}. \tag{C.31}$$

For the correlation function that fits the experimental data (6.10), Eq. (C.30) can only be calculated numerically. In the limit in which the external noise is white, *i.e.* $\sigma^2 = 2\gamma kT_e$ and $\Gamma(t) = \delta(t)$, we obtain an analogous result to (C.29) but replacing T by T_e. Only in this case $T_C = T_{\text{hist}} = T_{\text{PSD}} = T + T_e$ for any value of the driving time τ.

D

Non isothermal processes

D.1 Calculation of the heat distribution in a quasistatic process

We now calculate the heat distribution for a quasistatic process in which an overdamped Brownian particle whose position is labeled by x is trapped with a quadratic potential of stiffness κ, $U(x) = \frac{1}{2}\kappa x^2$. In the protocol, the temperature changes from T_1 to T_2 and the stiffness from κ_1 to κ_2. We assume that the process is quasistatic and therefore the distribution of the position at any time t during the process is the equilibrium (Gaussian) distribution

$$\rho(x,t) = \rho_{\text{eq}}(x, \beta(t), \kappa(t)) = \frac{e^{-\beta(t)\kappa(t)x^2/2}}{\mathcal{Z}(t)}, \tag{D.1}$$

where $\beta(t) = 1/kT(t)$ and $\mathcal{Z}(t) = \sqrt{2\pi/\beta(t)\kappa(t)}$.

In a quasistatic process, the work distribution is peaked at its mean value [62]

$$\rho_W(W) = \delta(W - \langle W \rangle). \tag{D.2}$$

Taking into account the First Law of Thermodynamics, $Q = \Delta U - W$, the heat distribution is equal to the distribution of the internal energy change centered in $\Delta U = -\langle W\rangle$

$$\rho_Q(Q) = \rho_{\Delta U}(\Delta U + \langle W\rangle). \tag{D.3}$$

If the initial position of the particle is $x(0) = x_1$ and the final position is $x(\tau) = x_2$, the shane in internal energy is

$$\Delta U = \frac{1}{2}(\kappa_2 x_2^2 - \kappa_1 x_1^2). \tag{D.4}$$

We now calculate the distribution of ΔU for a quasistatic process where the temperature and stiffness change from (T_1, κ_1) to (T_2, κ_2). The probability distribution of ΔU being equal to u is

$$\rho_{\Delta U}(u) = \iint \delta\left(u - \frac{1}{2}(\kappa_2 x_2^2 - \kappa_1 x_1^2)\right) \rho_{\mathrm{eq}}(x_1, \beta_1, \kappa_1)\rho_{\mathrm{eq}}(x_2, \beta_2, \kappa_2)\, dx_1\, dx_2, \tag{D.5}$$

where the integration is done from $-\infty$ to ∞ unless we specify different integration limits.

We now make the change of variables

$$y_i = \frac{1}{2}\kappa_i x_i^2, \tag{D.6}$$

with $i = 1, 2$. The distribution of the random variable y_i is

$$\rho(y_i, \beta_i, \kappa_i) = \int \delta\left(y_i - \frac{1}{2}\kappa x_i^2\right) \rho(x_i, \beta_i, \kappa_i)\, dx_i, \tag{D.7}$$

where the $\delta-$ function in the integrand can be rewritten as

$$\delta\left(y_i - \frac{1}{2}\kappa x_i^2\right) = \frac{1}{\sqrt{2\kappa_i y_i}}\left(\delta(y_i - \sqrt{2y_i/\kappa_i}) + \delta(y_i + \sqrt{2y_i/\kappa_i})\right). \tag{D.8}$$

By replacing (D.8) and (D.1) in (D.7), and taking into account that y_i takes only positive values, we obtain

$$\rho(y_i) = \sqrt{\frac{2}{\kappa_i y_i}}\frac{1}{\mathcal{Z}_i}\, e^{-\beta_i y_i}\theta(y_i), \tag{D.9}$$

where $\theta(y_i)$ is the step function evaluated at y_i, and $\mathcal{Z}_i = \sqrt{2\pi/\beta_i\kappa_i}$.

The distribution of the internal energy change can be expressed in terms of the new variables

$$\rho_{\Delta U}(u) = \iint \delta\left(u - y_2 + y_1\right) \rho(y_1, \beta_1, \kappa_1)\rho(y_2, \beta_2, \kappa_2)\, dy_1\, dy_2. \tag{D.10}$$

Integrating over y_2,

$$\rho_{\Delta U}(u) = \int \rho(y_1, \beta_1, \kappa_1)\rho(u + y_1, \beta_2, \kappa_2)\, dy_1. \tag{D.11}$$

Using the expression for the distribution $\rho(y_i)$ (D.9), we obtain

$$\begin{aligned} \rho_{\Delta U}(u) &= \frac{2}{\sqrt{\kappa_1\kappa_2}}\frac{1}{Z_1 Z_2}\int \frac{e^{-\beta_1 y_1}}{\sqrt{y_1}}\frac{e^{-\beta_2(u+y_1)}}{\sqrt{u+y_1}}\theta(y_1)\theta(u+y_1)\, dy_1 && \text{(D.12)} \\ &= \frac{\sqrt{\beta_1\beta_2}}{\pi}e^{-\beta_2 u}\int \frac{e^{-(\beta_1+\beta_2)y_1}}{\sqrt{y_1(u+y_1)}}\theta(y_1)\theta(u+y_1)\, dy_1. && \text{(D.13)} \end{aligned}$$

For $u > 0$, the integral in (D.13) is equal to

$$\int_0^\infty \frac{e^{-(\beta_1+\beta_2)y_1}}{\sqrt{y_1(u+y_1)}}\, dy_1 = e^{\frac{\beta_1+\beta_2}{2}u} K_0\left(\frac{\beta_1+\beta_2}{2}u\right), \tag{D.14}$$

where K_0 is the zeroth-order modified Bessel function of the second kind. For $u < 0$,

$$\int_{-u}^\infty \frac{e^{-(\beta_1+\beta_2)y_1}}{\sqrt{y_1(u+y_1)}}\, dy_1 = e^{\frac{\beta_1+\beta_2}{2}u} K_0\left(-\frac{\beta_1+\beta_2}{2}u\right). \tag{D.15}$$

Then, for any value of u, we obtain

$$\rho_{\Delta U}(u) = \frac{\sqrt{\beta_1\beta_2}}{\pi}e^{\frac{\beta_1-\beta_2}{2}u} K_0\left(\frac{\beta_1+\beta_2}{2}|u|\right) \tag{D.16}$$

Given Eq. (D.16), the heat distribution (D.3) equals to

$$\rho_Q(Q) = \frac{\sqrt{\beta_1\beta_2}}{\pi}e^{\frac{\beta_1-\beta_2}{2}(Q+\langle W\rangle)} K_0\left(\frac{\beta_1+\beta_2}{2}|Q+\langle W\rangle|\right), \tag{D.17}$$

which depends on the initial and final values of the temperature but not on the initial and final values of the stiffness. The distribution is asymmetric with respect to $Q = -\langle W\rangle$ except for the isothermal case ($\beta_1 = \beta_2$).

D.2 Derivation of the mean value of the velocity at finite sampling rate

Let us consider a Brownian particle of mass m trapped with a harmonic potential of stiffness κ in a fluid at temperature T and with friction coefficient

γ. The particle moves in one dimension and its dynamics is described by the underdamped Langevin equation. The PSD of the velocity in the underdamped limit is

$$S_v(\omega) = \frac{2\gamma kT}{m^2} \frac{\omega^2}{\left[(\omega_0^2 - \omega^2)^2 + \frac{\gamma^2}{m^2}\omega^2\right]}, \tag{D.18}$$

where $\omega_0^2 = \frac{\kappa}{m}$. The mean square velocity can be calculated from the PSD

$$\langle v^2 \rangle = \frac{1}{2\pi} \int_{-\infty}^{\infty} d\omega\, S_v(\omega) = \frac{\gamma kT}{\pi m^2} \int_{-\infty}^{\infty} d\omega\, \frac{\omega^2}{\left[(\omega_0^2 - \omega^2)^2 + \frac{\gamma^2}{m^2}\omega^2\right]}. \tag{D.19}$$

The integral in the right hand side, which we denote by I_1, can be evaluated using complex integration techniques. Let us consider the following function of a complex variable z

$$f(z) = \frac{z^2}{\left[(\omega_0^2 - z^2)^2 + \frac{\gamma^2}{m^2}z^2\right]}. \tag{D.20}$$

The function $f(z)$ vanishes when the imaginary part of z tends to $\pm\infty$. Therefore, I_1 coincides with the integration of $f(z)$ over a contour C that goes along the real line from $-\infty$ to ∞ and then counterclockwise along a semicircle centered at 0 from ∞ to $-\infty$ as shown in Fig.D.1.

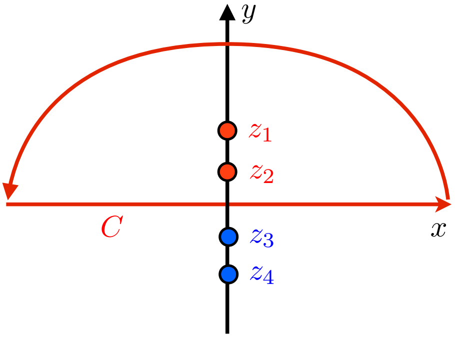

Figure D.1: Location of the poles of $f(z) = \frac{z^2}{\left[(\omega_0^2 - z^2)^2 + \frac{\gamma^2}{m^2}z^2\right]}$ in the complex plane and sketch of the integration contour.

The latter integral can be calculated using the residue theorem,

$$I_1 = \int_C dz\, f(z) = 2\pi i \sum_k \mathrm{Res}(f(z), z_k), \tag{D.21}$$

where the sum is done over the poles of $f(z)$ that lie within the contour C. $f(z)$ has four simple poles

$$z = i\left(\pm\frac{\gamma}{2m} \pm \omega_1\right), \tag{D.22}$$

where $\omega_1 = \sqrt{\frac{\gamma^2}{4m^2} - \omega_0^2} > 0$. There are two poles that lie within C, $z_1 = i(\gamma/2m + \omega_1)$ and $z_2 = i(\gamma/2m - \omega_1)$. We also define $z_3 = i(-\gamma/2m + \omega_1)$ and $z_4 = i(-\gamma/2m - \omega_1)$. The residual of $f(z)$ at $z = z_1$ is

$$\mathrm{Res}(f(z), z_1) = \frac{z_1^2}{(z_1 - z_2)(z_1 - z_3)(z_1 - z_4)} = -i\frac{\frac{\gamma}{2m} + \omega_1}{4(\gamma/m)\omega_1}, \tag{D.23}$$

and

$$\mathrm{Res}(f(z), z_2) = \frac{z_2^2}{(z_2 - z_1)(z_2 - z_3)(z_2 - z_4)} = i\frac{\frac{\gamma}{2m} - \omega_1}{4(\gamma/m)\omega_1}, \tag{D.24}$$

yielding

$$I_1 = \pi\frac{m}{\gamma}. \tag{D.25}$$

If we replace the value of I_1 in (D.19), we obtain the expected result from the equipartition theorem,

$$\langle v^2 \rangle = \frac{kT}{m}. \tag{D.26}$$

Experimentally, the instantaneous velocity cannot be measured accurately unless the sampling frequency is of the order of $m/\gamma \sim$ MHz. For smaller sampling frequencies (e.g. of the order of kHz) one can only measure an average velocity

$$\overline{v}(t) = \frac{1}{\Delta t}\int_t^{t+\Delta t} v(s)ds, \tag{D.27}$$

where Δt is the inverse of the sampling frequency. We now study the relationship between the correlation of the time-averaged velocity $\langle \overline{v}^2 \rangle$ and that of the instantaneous velocity, $\langle v^2 \rangle$, as a function of the sampling time Δt. The Fourier transform of the averaged velocity is

$$\begin{aligned}
\tilde{\overline{v}}(\omega) &= \frac{1}{\sqrt{2\pi}\Delta t}\int_{-\infty}^{\infty} dt \int_{t}^{t+\Delta t} ds\, v(s) e^{-i\omega t} \\
&= \frac{1}{\sqrt{2\pi}\Delta t}\int_{-\infty}^{\infty} dt \int_{-\infty}^{\infty} ds\, v(s) \mathrm{rect}\left[\frac{1}{\Delta t}(t+\Delta t/2 - s)\right] e^{-i\omega t} \\
&= \frac{1}{\Delta t}\int_{-\infty}^{\infty} ds\, v(s) e^{-i\omega s} e^{i\omega\Delta t/2} \frac{1}{\sqrt{2\pi}}\int_{-\infty}^{\infty} dt\, \mathrm{rect}\left[\frac{1}{\Delta t}(t+\Delta t/2 - s)\right] e^{-i\omega(t+\Delta t/2-s)} \\
&= \frac{1}{\Delta t}\int_{-\infty}^{\infty} ds\, v(s) e^{-i\omega s} e^{i\omega\Delta t/2} \frac{\Delta t}{\sqrt{2\pi}} \mathrm{sinc}\left(\frac{\omega \Delta t}{2\pi}\right) \\
&= e^{i\omega\Delta t/2} \mathrm{sinc}\left(\frac{\omega \Delta t}{2\pi}\right) \frac{1}{\sqrt{2\pi}}\int_{-\infty}^{\infty} ds\, v(s) e^{-i\omega s} \\
&= e^{i\omega\Delta t/2} \mathrm{sinc}\left(\frac{\omega \Delta t}{2\pi}\right) \tilde{v}(\omega), \qquad \text{(D.28)}
\end{aligned}$$

where rect is the rectangular function and $\mathrm{sinc}(x) = \frac{\sin(\pi x)}{\pi x}$. The PSD of the averaged velocity can be expressed in terms of the PSD of the instantaneous velocity,

$$S_{\overline{v}}(\omega) = \mathrm{sinc}^2\left(\frac{\omega \Delta t}{2\pi}\right) S_v(\omega). \qquad \text{(D.29)}$$

Therefore, the correlation of the averaged velocity is [cf. Eq. (D.19)]

$$\langle \overline{v}^2 \rangle = \frac{1}{2\pi}\int_{-\infty}^{\infty} d\omega\, \mathrm{sinc}^2\left(\frac{\omega \Delta t}{2\pi}\right) S_v(\omega) = \frac{4\gamma k T}{\pi m^2 \Delta t^2}\int_{-\infty}^{\infty} d\omega\, \frac{\sin^2\left(\frac{\omega\Delta t}{2}\right)}{\left[(\omega_0^2-\omega^2)^2 + \frac{\gamma^2}{m^2}\omega^2\right]}. \qquad \text{(D.30)}$$

Using the property $\sin^2\left(\frac{\omega\Delta t}{2}\right) = \frac{1-\cos(\omega\Delta t)}{2}$, $\langle \overline{v}^2 \rangle$ can be expressed as a sum of two integrals,

$$\begin{aligned}
\langle \overline{v}^2 \rangle &= I_2 + I_3 && \text{(D.31)} \\
I_2 &= \frac{2\gamma k T}{\pi m^2 \Delta t^2}\int_{-\infty}^{\infty} d\omega\, \frac{1}{\left[(\omega_0^2-\omega^2)^2 + \frac{\gamma^2}{m^2}\omega^2\right]} = \frac{2kT}{m\omega_0^2\Delta t^2} && \text{(D.32)} \\
I_3 &= -\frac{2\gamma k T}{\pi m^2 \Delta t^2}\int_{-\infty}^{\infty} d\omega\, \frac{\cos(\omega\Delta t)}{\left[(\omega_0^2-\omega^2)^2 + \frac{\gamma^2}{m^2}\omega^2\right]}, && \text{(D.33)}
\end{aligned}$$

where

$$\begin{aligned}
&\int_{-\infty}^{\infty} d\omega \, \frac{\cos(\omega\Delta t)}{\left[(\omega_0^2 - \omega^2)^2 + \frac{\gamma^2}{m^2}\omega^2\right]} \\
&\qquad = \mathrm{Re}\left[\int_{-\infty}^{\infty} dz \, \frac{e^{iz\Delta t}}{\left[(\omega_0^2 - z^2)^2 + \frac{\gamma^2}{m^2}z^2\right]}\right] \\
&\qquad = \frac{\pi m}{\omega_1\gamma}\left[\frac{e^{-\left(\frac{\gamma}{2m}-\omega_1\right)\Delta t}}{\frac{\gamma}{m} - 2\omega_1} - \frac{e^{-\left(\frac{\gamma}{2m}+\omega_1\right)\Delta t}}{\frac{\gamma}{m} + 2\omega_1}\right],
\end{aligned} \tag{D.34}$$

yielding

$$I_3 = \frac{2kT}{m\Delta t^2\omega_1}\left[\frac{e^{-\left(\frac{\gamma}{2m}+\omega_1\right)\Delta t}}{\frac{\gamma}{m} + 2\omega_1} - \frac{e^{-\left(\frac{\gamma}{2m}-\omega_1\right)\Delta t}}{\frac{\gamma}{m} - 2\omega_1}\right]. \tag{D.35}$$

Using Eqs. (D.31), (D.32) and (D.35) we obtain the following analytical expression for the correlation of the averaged velocity

$$\langle \overline{v}^2 \rangle = \frac{2kT}{m\Delta t^2}\left[\frac{1}{\omega_0^2} + \frac{1}{\omega_1}\left(\frac{e^{-\left(\frac{\gamma}{2m}+\omega_1\right)\Delta t}}{\frac{\gamma}{m} + 2\omega_1} - \frac{e^{-\left(\frac{\gamma}{2m}-\omega_1\right)\Delta t}}{\frac{\gamma}{m} - 2\omega_1}\right)\right]. \tag{D.36}$$

The above expression reproduces the result for the correlation of the instantaneous velocity (D.26). When $\Delta t \to 0$, $\langle \overline{v}^2 \rangle \to kT/m = \langle v^2 \rangle$. When $\Delta t \to \infty$, $\langle \overline{v}^2 \rangle \to 0$. For intermediate values of Δt, the variance of the averaged velocity lies below kT/m, $\langle \overline{v}^2 \rangle < kT/m$, as shown in the experiment.

E

Universal features of symmetry breaking

E.1 Derivation of equations (8.3) and (8.4)

First, we give a simplified derivation of Eq. (8.1) that illustrates the origin of the entropy decrease given by Eq. (8.2) in the main text. Suppose that the symmetry breaking occurs at some stage of a process, when the system crosses a critical point during a localized and short time interval. Fig. E.1 shows a sketch of the whole process, for a system that adopts instance 1 among three possibilities $i = 1, 2, 3$. Before and after the symmetry breaking we can apply standard thermodynamics: the minimal work required to drive the system is the one performed under quasistatic, reversible conditions, and is equal to the increment of free energy. For instance, the work necessary to drive the system from the initial state to the equilibrium state right before the critical point is bound by:

$$\langle W \rangle_a \geq F_{\text{crit}} - F_0, \tag{E.1}$$

where $F = -kT \log \mathcal{Z}$, and $\mathcal{Z}$ is the partition function $\mathcal{Z} = \int_\Gamma dqdp\, e^{-\beta\mathcal{H}}$ calculated by integrating the exponential of the Hamiltonian $\mathcal{H}(q,p)$ over the whole phase space Γ, with $\beta = 1/(kT)$. The same argument can be used for the work done after the symmetry has been broken, when the dynamics is confined within a region Γ_i of the phase space:

$$\langle W\rangle_{c,i} \geq F_{\tau,i} - F_{\text{crit},i}, \tag{E.2}$$

where $F_i = -kT\log\mathcal{Z}_i$, but now $\mathcal{Z}_i = \int_{\Gamma_i} dqdp\, e^{-\beta\mathcal{H}}$ is the partition function *restricted* to region Γ_i. The crucial step in our argument is what happens *at* the critical point. The symmetry breaking induces a shrinkage of the available phase space volume, from Γ to Γ_i. The dynamical details of this shrinkage can be rather involved, but we can consider the following rough and simplified picture: the system fills the entire phase space Γ with probability $e^{-\beta\mathcal{H}(q,p)}/\mathcal{Z}$; suddenly, the phase space is partitioned in compartments Γ_i, $i = 1, 2, \ldots, m$, and the system gets confined in one of those compartments. The work necessary to implement this partition and confinement is zero (or arbitrary small) and the probability that the system becomes confined in compartment i is $p_i = \mathcal{Z}_i/\mathcal{Z}$ or, equivalently:

$$F_{\text{crit}} - F_{\text{crit},i} = kT\log p_i. \tag{E.3}$$

Collecting Eqs. (E.1)-(E.3), we immediately get the bound (8.1) for the total work $\langle W\rangle_i^{(\text{SB})} = \langle W\rangle_a + \langle W\rangle_{c,i}$.

A more rigorous proof follows from the extended fluctuation relation (EFR) derived in [229, 230] for processes starting at an equilibrium state restricted to regions of the phase space. In one of its forms (Eq. (17) in [229] or, equivalently, Eq. (2) in [230]) the EFR can be written as:

$$\rho_F(W|A\to B)P_F(B|A)\, e^{-\beta W} = \rho_R(-W|B\to A)P_R(A|B)\, e^{-\beta\Delta F_{A\to B}}, \tag{E.4}$$

where A and B denote regions of the phase space and the subscripts F and R refer, respectively, to a process and its time reverse. $P_F(B|A)$ is the probability that the system ends in region B starting at restricted equilibrium in region A, whereas $P_R(A|B)$ is the probability to end in region A in the reverse process starting in equilibrium in region B. $\rho_F(W|A\to B)$ $[\rho_R(W|B\to A)]$ is the probability distribution of the work in the forward (reverse) process, conditioned to trajectories starting at A (B) and ending at B (A). Finally, $\Delta F_{A\to B} \equiv F_B - F_A$ is the difference of conformational free energies between states B and A.

In a symmetry breaking, the system starts in equilibrium all over the whole phase space, i.e., $A = \Gamma$ is the phase space. Hence $P_R(A|B) = 1$ and F_A is

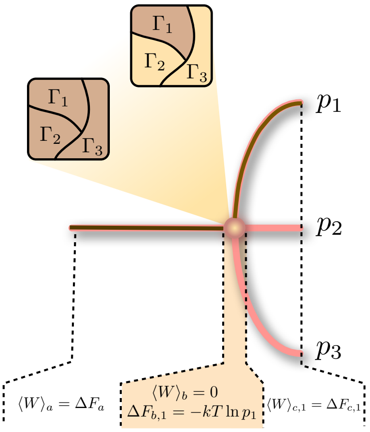

Figure E.1: A sketch of the proof of Eq. (1) for a system that adopts instance 1 among three possibilities $i = 1, 2, 3$. Before and after the symmetry breaking, the reversible work is given by the increment of free energy: $\langle W\rangle = \Delta F$. At the symmetry breaking, a reduction of the phase space volume from Γ to Γ_1 occurs without the need of any external work: $\langle W\rangle_b = 0$. This reduction of phase space volume induces an increase of free energy $\Delta F_{b,1} = kT \log(Z_1/Z) = kT \log p_1$, where Z and Z_1 are partition functions calculated over Γ and Γ_1, respectively, and $p_1 = Z_1/Z$ is the probability that the system ends within region Γ_1 when the symmetry is broken. The total reversible work is $\langle W\rangle_1^{(\mathrm{SB})} = \langle W\rangle_a + \langle W\rangle_b + \langle W\rangle_{c,1} \geq kT \log p_1 + \Delta F_1$, where $\Delta F_1 = \Delta F_a + \Delta F_{b,1} + \Delta F_{c,1} = F_{\tau,1} - F_0$.

equal to the initial equilibrium free energy. On the other hand, we set the final region as the one corresponding to instance i, $B = \Gamma_i$. With the notation used in the main text: $P_F(B|A) = p_i$, $\Delta F_{A\to B} = \Delta F_i$, $\rho_F(W|A \to B) = \rho_i(W)$ is the distribution of the work performed on the system when the instance i is chosen in the SB, and $\rho_R(W|B \to A) = \tilde{\rho}_i(W)$ is the distribution of the work in the reverse process when the initial state is the one given by instance i. Then the EFR (E.4) applied to the SB reduces to

$$\rho_i(W) p_i\, e^{-\beta(W-\Delta F_i)} = \tilde{\rho}_i(-W). \tag{E.5}$$

Taking logarithms and averaging over $P_i(W)$ one finds

$$\langle W\rangle_i^{(\mathrm{SB})}-\Delta F_i \equiv \int dw\, \rho_i(W)(W-\Delta F_i) = kT\log p_i+kT\int dW\, \rho_i(W)\log\frac{\rho_i(W)}{\tilde{\rho}_i(-W)}. \tag{E.6}$$

The last term is proportional to the relative entropy between the work distribution in the forward and reverse processes $D[\rho_i(W)||\tilde{\rho}_i(-W)]$ which is always positive [217, 231] and zero in the quasistatic limit (see below). Therefore,

$$\langle W\rangle_i^{(\mathrm{SB})} - \Delta F_i \geq kT\log p_i, \tag{E.7}$$

which is Eq. (8.1).

The above inequality applied to quasistatic processes can be explored using the original Crooks work theorem [189] which applies to processes starting at equilibrium. In those cases, the work is almost a deterministic quantity, except for the uncertainty associated with the SB. Consequently, the probability density for the work is peaked around a finite set of values $\langle W\rangle_i$ (in our case, $i = F, M$). Assuming Gaussian fluctuations around these values with variances σ_i, the work distribution in the SB is

$$\rho^{(\mathrm{SB})}(W) = \sum_i \frac{p_i}{\sqrt{2\pi\sigma_i}}\exp\left(-\frac{(W-\langle W\rangle_i)^2}{2\sigma_i^2}\right), \tag{E.8}$$

p_i being the probability that the system chooses the path i in the SB process. Crooks' theorem expresses the following symmetry relation between the work distribution in a process and its time reversal (SB and SR processes in this case, respectively),

$$\frac{\rho^{(\mathrm{SB})}(W)}{\rho^{(\mathrm{SR})}(-W)} = \exp\left(\frac{W-\Delta F}{kT}\right), \tag{E.9}$$

where $\rho^{(\mathrm{SR})}(W)$ is the probability density for the work performed in the SR (backward) experiment and ΔF is the free energy difference between the initial and the final states of the SB (foward) process. Combining (E.8) and (E.9), one obtains for the work distribution for the SR:

$$\rho^{(\mathrm{SR})}(W) = \sum_i \frac{\tilde{p}_i}{\sqrt{2\pi\sigma_i}}\exp\left(-\frac{(W+\langle W\rangle_i-\frac{\sigma_i^2}{kT})^2}{2\sigma_i^2}\right). \tag{E.10}$$

where the probability $\tilde{p}_i$ in the corresponding time reversal SB satisfies:

$$\tilde{p}_i = p_i \exp\left(-\frac{\langle W\rangle_i - \Delta F - \frac{\sigma_i^2}{2kT}}{kT}\right). \tag{E.11}$$

Hence,

$$\langle W\rangle_i - \Delta F = kT \log \frac{p_i}{\tilde{p}_i} + \frac{\sigma_i^2}{2kT}. \tag{E.12}$$

The variance σ_i has no lower bound, and can be even smaller than kT for slow driving ($\sigma_i = 0$ in the quasistatic limit). Since $\sigma_i > 0$, by replacing $\tilde{p}_i = Z_i/Z$ we recover the bound given by Eq. (8.1). Equation (E.12) can also be reproduced by evaluating the relative entropy between Gaussian work distributions in the equality obtained from the EFR (E.6).

Derivation of Eqs. (8.3) and (8.4)

A similar inequality holds for a process where a symmetry is restored. A SR can be considered as the time reversal of a symmetry breaking. Let us call $\tilde{p}_i$ the probability that the system adopts instance i in the reverse process , i.e., if we run in reverse the protocol that restores the symmetry, each instance i would occur with probability $\tilde{p}_i$ (see Fig. 8.2 for an example). Under a time reversal, reversible work and free energy increment change their sign. Therefore, we can apply Eq. (8.1) to obtain

$$\langle W\rangle_i^{(\mathrm{SR})} \geq -kT \log \tilde{p}_i + \Delta F_i, \tag{E.13}$$

$\Delta F_i = F_{\mathrm{fin}} - F_{\mathrm{init},i}$ is the free energy change of the SR. The above equation can be expressed as an inequality for the average entropy production in the symmetry restoring process:

$$\langle S_{\mathrm{prod}}\rangle_i^{(\mathrm{SR})} \geq -k \log \tilde{p}_i. \tag{E.14}$$

E.2 Explicit calculation of the average entropy production in a specific symmetry breaking

Consider a Brownian particle at thermal bath at temperature T in a time-dependent potential $U(x,t)$. The position of the particle at time t is x_t. Then, the change of potential energy in an interval of time $[t, t+\Delta t]$ is:

$$\Delta U(t) = U(x_{t+\Delta t}, t+\Delta t) - U(x_t, t), \tag{E.15}$$

which can be written as:

$$\Delta U(t) = \delta W(t) + \delta Q(t), \tag{E.16}$$

where the work done in the interval of time $[t, t+\Delta t]$ is given by:

$$\delta W(t) = U(x_t, t+\Delta t) - U(x_t, t), \tag{E.17}$$

and the heat transferred to the particle in $[t, t+\Delta t]$:

$$\delta Q(t) = U(x_{t+\Delta t}, t+\Delta t) - U(x_t, t+\Delta t). \tag{E.18}$$

These expressions are exact if the potential changes in discrete steps. Suppose that the potential is constant and equal to $U(x,t)$ between $t-\Delta t$ and t. At time t the potential changes abruptly to $U(x, t+\Delta t)$ and remains constant up to $t+\Delta t$ and so on. The change introduces an energy $\delta W(t) = U(x_t, t+\Delta t) - U(x_t, t)$. Then the particle moves from x_t to $x_{t+\Delta t}$ in the constant potential $U(x, t+\Delta t)$. The change in energy $\delta Q(t) = U(x_{t+\Delta t}, t+\Delta t) - U(x_t, t+\Delta t)$ is therefore due to the thermal bath.

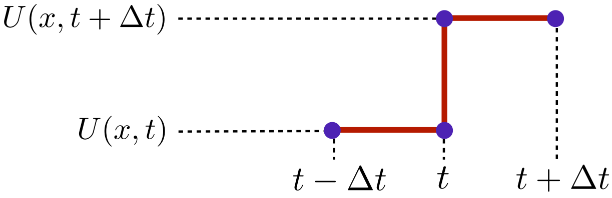

Figure E.2: The time dependent potential.

If the potential changes smoothly, the expressions above are still a good approximation for the work and heat. In fact, they can be reduced to expressions for $\Delta t \to 0$ [176]:

$$\begin{aligned} \delta W(t) &= \frac{\partial U(x_t, t)}{\partial t}\Delta t, && \text{(E.19)} \\ \delta Q(t) &= \left.\frac{\partial U(x,t)}{\partial x}\right|_{x=x_t} \circ \Delta x_t. && \text{(E.20)} \end{aligned}$$

If $\rho(x,t)$ is the probability density of x_t, the average heat and work up to time t are given by:

$$\begin{aligned}\langle \delta W(t)\rangle &= \int dx\,\rho(x,t)\,[U(x,t+\Delta t)-U(x,t)]\\ &\simeq \int dx\,\rho(x,t)\frac{\partial U(x,t)}{\partial t}\Delta t, \qquad \text{(E.21)}\\ \langle \delta Q(t)\rangle &= \int dx\,\rho(x,t+\Delta t)U(x,t+\Delta t)-\int dx\,\rho(x,t)U(x,t+\Delta t)\\ &\simeq \int dx\,\frac{\partial \rho(x,t)}{\partial t}U(x,t)\Delta t. \qquad \text{(E.22)}\end{aligned}$$

We notice that the integral is done from $t'=0$ to $t'=t$ unless different integration limits are indicated. The sum of both terms yields the change of internal energy:

$$\langle \delta W(t)\rangle + \langle \delta Q(t)\rangle = \int dx\,\frac{\partial[\rho(x,t)U(x,t)]}{\partial t}\Delta t. \qquad \text{(E.23)}$$

The average entropy production up to time t is:

$$\begin{aligned}\langle S_{\text{prod}}(t)\rangle &= -\frac{\langle \delta Q(t)\rangle}{T} - k\int dx\,\frac{\partial[\rho(x,t)\log\rho(x,t)]}{\partial t}\Delta t\\ &= -\frac{1}{T}\int dx\,\frac{\partial\rho(x,t)}{\partial t}U(x,t)\Delta t - k\int dx\,\frac{\partial\rho(x,t)}{\partial t}\log\rho(x,t)\Delta t - k\int dx\,\frac{\partial\rho(x,t)}{\partial t}\Delta t\\ &= -k\int dx\,\frac{\partial\rho(x,t)}{\partial t}\left[\frac{U(x,t)}{kT}+\log\rho(x,t)\right]\Delta t. \qquad \text{(E.24)}\end{aligned}$$

If we replace $U(x,t)$ by $-kT\log\rho(x,t)-kT\log\mathcal{Z}_t$, $\mathcal{Z}_t$ being the partition function at time t, then

$$\langle S_{\text{prod}}(t)\rangle = k\int dx\,\frac{\partial\rho(x,t)}{\partial t}\mathcal{Z}_t\Delta t = 0, \qquad \text{(E.25)}$$

which is identically zero because $\rho(x,t)$ is normalized at any time t. Notice that, with the replacement $U(x,t)\to -kT\log\rho(x,t)-kT\log Z_t$, the total entropy production is zero even far from the quasistatic limit.

We analyze how the previous relations change when a SB occurs along the process. At the end of the SB, the bead follows the F or the M trap. The total probability distribution can be written as:

$$\rho(x,t) = \sum_{i=F,M} p_i\,\rho_i(x,t), \tag{E.26}$$

where p_i is the probability to be in trap $i = M, F$ and $\rho_i(x,t)$ is the probability distribution of x_t conditioned to be at the end of the process in the trap $i = M, F$. The expression for the total entropy production conditioned to the final trap can be obtained by repeating the previous arguments:

$$\langle S_{\rm prod}(t)\rangle_i = -k \int dx\, \frac{\partial \rho_i(x,t)}{\partial t} \left[\frac{U(x,t)}{kT} + \log \rho_i(x,t) \right] \Delta t. \tag{E.27}$$

With the replacement $U(x,t) \to -kT \log \rho(x,t) - kT \log Z_t$, the total entropy production reads

$$\langle S_{\rm prod}(t)\rangle_i = -k \int dx\, \frac{\partial \rho_i(x,t)}{\partial t} \log \frac{\rho_i(x,t)}{\rho(x,t)} \Delta t. \tag{E.28}$$

We will assume the following scenario for the SB:

$$\text{For } t \le t_1: \qquad \rho_M(x,t) = \rho_F(x,t) = \rho(x,t) \tag{E.29}$$

$$\text{For } t \ge t_2: \qquad \text{supp}\,\rho_M(x,t) \cap \text{supp}\,\rho_F(x,t) = \emptyset, \tag{E.30}$$

i.e., the SB is occurs in a time interval $[t_1, t_2]$, before which the two probability distributions ρ_M and ρ_F are identical. After t_2 the two probability distributions have non overlapping supports. The total entropy production along the whole process $t \in [0, \tau]$ is obtained by integrating (E.28) over time. From $t = 0$ to $t = t_1$, $\rho_i = \rho$ and therefore the integrand is zero. From $t = t_2$ to τ the integral over x is limited to the support of $\rho_i(x,t)$, where $\rho(x,t)/\rho_i(x,t) = p_i$, and therefore:

$$-k \int dx\, \frac{\partial \rho_i(x,t)}{\partial t} \log \frac{\rho_i(x,t)}{\rho(x,t)} = k \log p_i \int dx\, \frac{\partial \rho_i(x,t)}{\partial t} = 0. \tag{E.31}$$

In the interval $[t_1, t_2]$ after integration by parts:

$$\begin{aligned} \langle S_{\rm prod}\rangle_i &= -k \int_{t_1}^{t_2} dt \int dx\, \frac{\partial \rho_i(x,t)}{\partial t} \log \frac{\rho_i(x,t)}{\rho(x,t)} \\ &= k \log p_i + k \int_{t_1}^{t_2} dt \int dx\, \rho_i(x,t) \frac{\partial}{\partial t} \log \frac{\rho_i(x,t)}{\rho(x,t)} \\ &= k \log p_i - k \int_{t_1}^{t_2} dt \int dx\, \rho_i(x,t) \frac{\partial}{\partial t} \log \rho(x,t) \end{aligned} \tag{E.32}$$

where we have used $\log[\rho_i(x,t_2)/\rho(x,t_2)] = -\log p_i$ and $\log[\rho_i(x,t_1)/\rho(x,t_1)] = 0$ and the fact that $\int dx\, \rho_i(x,t)\frac{\partial}{\partial t}\log\rho_i(x,t) = 0$ for all t due to the normalization of $\rho_i(x,t)$.

If the SB occurs in an interval $[t_1,t_2]$ where $\rho(x,t)$ does not change, then $\langle S_{\rm prod}\rangle_i = k\log p_i$. Notice that the replacement $U(x,t) \to -kT\log\rho(x,t) - kT\log Z_t$ does not ensure now that the total entropy production vanishes.

Bibliography

[1] S. M Kay. *Fundamentals of Statistical signal processing, Volume 2: Detection theory.* Prentice Hall PTR, 1998.

[2] R. M. Henkelman. Measurement of signal intensities in the presence of noise in mr images. *Med. Phys.*, 12:232, 1985.

[3] J. R Parker. *Algorithms for image processing and computer vision.* Wiley. com, 2010.

[4] M. Takayasu and H. Takayasu. 1/f noise in a traffic model. *Fractals*, 1(4):860–866, 1993.

[5] M. Levy, S. Solomon, and G. Ram. Dynamical explanation for the emergence of power law in a stock market model. *Int. J. Mod. Phys. C*, 7(01):65–72, 1996.

[6] G. Baselli, S. Cerutti, S. Civardi, F. Lombardi, A. Malliani, M. Merri, M. Pagani, and G. Rizzo. Heart rate variability signal processing: a quantitative approach as an aid to diagnosis in cardiovascular pathologies. *Int. J. Biomed. Comput.*, 20(1):51–70, 1987.

[7] A. Ashkin, JM Dziedzic, JE Bjorkholm, and S. Chu. Observation of a single-beam gradient force optical trap for dielectric particles. *Opt. Lett.*, 11(5):288–290, 1986.

[8] A. R. Bausch, W. Möller, and E. Sackmann. Measurement of local viscoelasticity and forces in living cells by magnetic tweezers. *Biophys. J.*, 76(1):573–579, 1999.

[9] G. Binnig, C. F. Quate, and C. Gerber. Atomic force microscope. *Phys. Rev. Lett.*, 56(9):930–933, 1986.

[10] D. J. Evans, E. G. D. Cohen, and G. P. Morriss. Probability of second law violations in shearing steady states. *Phys. Rev. Lett.*, 71(15):2401–2404, 1993.

[11] C. Bustamante, J. Liphardt, and F. Ritort. The nonequilibrium thermodynamics of small systems. *Physics Today*, 58, 2005.

[12] F. L. Curzon and B. Ahlborn. Efficiency of a carnot engine at maximum power output. *Am. J. Phys.*, 43:22, 1975.

[13] R. D. Astumian, P. B. Chock, T. Y. Tsong, Y. D. Chen, and H. V. Westerhoff. Can free energy be transduced from electric noise? *Proc. Natl. Acad. Sci. U. S. A.*, 84(2):434–438, 1987.

[14] C. W. Gardiner et al. *Handbook of stochastic methods*, volume 3. Springer Berlin, 1985.

[15] D. Nozaki, D. J. Mar, P. Grigg, and J. J. Collins. Effects of colored noise on stochastic resonance in sensory neurons. *Phys. Rev. Lett.*, 82(11):2402, 1999.

[16] S. M. Bezrukov and I. Vodyanoy. Noise-induced enhancement of signal transduction across voltage-dependent ion channels. *Nature*, 378(6555):362–364, 1995.

[17] A. Manwani and C. Koch. Detecting and estimating signals in noisy cable structures, i: Neuronal noise sources. *Neural Comput.*, 11(8):1797–1829, 1999.

[18] S. Leibler. Moving forward noisily. *Nature: International weekly journal of science*, 370(6489):412–413, 1994.

[19] R. D. Astumian and M. Bier. Fluctuation driven ratchets: molecular motors. *Phys. Rev. Lett.*, 72(11):1766, 1994.

[20] C. Bustamante, Z. Bryant, and S. B. Smith. Ten years of tension: single-molecule dna mechanics. *Nature*, 421(6921):423–427, 2003.

[21] S. R. Quake, H. Babcock, and S. Chu. The dynamics of partially extended single molecules of dna. *Nature*, 388:151–154, 1997.

[22] Z. Gueroui, E. Freyssingeas, C. Place, and B. Berge. Transverse fluctuation analysis of single extended DNA molecules. *Eur. Phys. J. E*, 11:105–108, 2003.

[23] P. G. De Gennes. Coil-stretch transition of dilute flexible polymers under ultrahigh velocity gradients. *J. Chys. Chem.*, 60:5030–5042, 1974.

[24] P. Pincus. Excluded volume effects and stretched polymer chains. *Macromolecules*, 9:386–388, 1976.

[25] J-Ch. Meiners and S. R. Quake. Femtonewton force spectroscopy of single extended DNA molecules. *Phys. Rev. Lett.*, 84:5014–5017, 2000.

[26] J. Pleiss. The promise of synthetic biology. *Appl. Microbiol. Biotechnol.*, 73(4):735–739, 2006.

[27] P. Hänggi and F. Marchesoni. Artificial brownian motors: Controlling transport on the nanoscale. *Rev. Mod. Physics*, 81(1):387, 2009.

[28] H. C. Berg. Cell motility: Turning failure into function. *Nat. Phys.*, 2013.

[29] D. M. Carberry, J. C. Reid, G. M. Wang, E. M. Sevick, D. J. Searles, and D. J. Evans. Fluctuations and irreversibility: An experimental demonstration of a second-law-like theorem using a colloidal particle held in an optical trap. *Phys. Rev. Lett.*, 92(14):140601, 2004.

[30] D. Collin, F. Ritort, C. Jarzynski, S. B. Smith, I. Tinoco, and C. Bustamante. Verification of the crooks fluctuation theorem and recovery of rna folding free energies. *Nature*, 437(7056):231–234, 2005.

[31] H. Mao, J. R. Arias-Gonzalez, S. B. Smith, I. Tinoco Jr, and C. Bustamante. Temperature control methods in a laser tweezers system. *Biophys. J.*, 89:1308–1316, 2005.

[32] G. E. Crooks and C. Jarzynski. Work distribution for the adiabatic compression of a dilute and interacting classical gas. *Physical Review E*, 75(2):021116, 2007.

[33] V. Blickle and C. Bechinger. Realization of a micrometre-sized stochastic heat engine. *Nat. Phys.*, 2011.

[34] R. Landauer. Irreversibility and heat generation in the computing process. *IBM J. Res. Dev.*, 5(3):183–191, 1961.

[35] T. Sagawa. *Thermodynamics of information processing in small systems.* Springer Verlag, 2012.

[36] L. Szilard. On the decrease of entropy in a thermodynamic system by the intervention of intelligent beings. *Behav. Sci.*, 9(4):301–310, 1964.

[37] C. H. Bennett. Demons, engines and the second law. *Sci. Amer.*, 257(5):108–116, 1987.

[38] S. Toyabe, T. Sagawa, M. Ueda, E. Muneyuki, and M. Sano. Experimental demonstration of information-to-energy conversion and validation of the generalized jarzynski equality. *Nat. Phys.*, 6(12):988–992, 2010.

[39] A. Bérut, A. Arakelyan, A. Petrosyan, S. Ciliberto, R. Dillenschneider, and E. Lutz. Experimental verification of landauer/'s principle linking information and thermodynamics. *Nature*, 483(7388):187–189, 2012.

[40] C. Cecconi, E. A. Shank, C. Bustamante, and S. Marqusee. Direct observation of the three-state folding of a single protein molecule. *Science*, 309(5743):2057–2060, 2005.

[41] C. Gosse and V. Croquette. Magnetic tweezers- micromanipulation and force measurement at the molecular level. *Biophys. J.*, 82:3314 – 3329, 2002.

[42] A. Ashkin. Acceleration and trapping of particles by radiation pressure. *Phys. Rev. Lett.*, 24(4):156–159, 1970.

[43] D. G. Grier. A revolution in optical manipulation. *Nature*, 424(6950):810–816, 2003.

[44] K. C. Neuman and S. M. Block. Optical trapping. *Rev. Sci. Instrum.*, 75(9):2787–2809, 2004.

[45] K. Dholakia and P. Reece. Optical micromanipulation takes hold. *Nano today*, 1(1):18–27, 2006.

[46] K. Visscher and S. M. Block. Versatile optical traps with feedback control. In Richard B. Valee, editor, *Molecular Motors and the Cytoskeleton Part B*, volume 298 of *Methods in Enzymology*, pages 460 – 489. Academic Press, 1998.

[47] F. Beunis, F. Strubbe, K. Neyts, and D. Petrov. Beyond millikan: The dynamics of charging events on individual colloidal particles. *Phys. Rev. Lett.*, 108:016101, 2012.

[48] Y. Z. Yoon, J. Kotar, A. T. Brown, and P. Cicuta. Red blood cell dynamics: from spontaneous fluctuations to non-linear response. *Soft Matter*, 7(5):2042–2051, 2011.

[49] P. Hanggi and P. Jung. Colored noise in dynamical systems. *Adv. Chem. Phys.*, 89:239–326, 1995.

[50] C. Bustamante, Y. R. Chemla, N. R. Forde, and D. Izhaky. Mechanical processes in biochemistry. *Annu. Rev. Biochem.*, 73:705, 2004.

[51] W. J. Greenleaf, M. T. Woodside, and S. M. Block. High-resolution, single-molecule measurements of biomolecular motion. *Annu. Rev. Biophys. Biomol. Struct.*, 36:171, 2007.

[52] F. Ritort. Single-molecule experiments in biological physics: methods and applications. *J. Phys.: Condens. Matter*, 18:R531ÐR583, 2006.

[53] R. M. Berry and H. C. Berg. Absence of a barrier to backwards rotation of the bacterial flagellar motor demonstrated with optical tweezers. *Proc. Natl. Acad. Sci. U. S. A.*, 94(26):14433–14437, 1997.

[54] M. Koch and A. Rohrbach. Object-adapted optical trapping and shape-tracking of energy-switching helical bacteria. *Nat. Photonics*, 6(10):680 – 686, 2012.

[55] J. M. Dziedzic A. Ashkin and T. Yamane. Optical trapping and manipulation of single cells using infrared laser beams. *Nature*, 330(6150):769–771, 1987.

[56] A. Ashkin and Dziedzic. Optical trapping and manipulation of viruses and bacteria. *Science*, 235(4795):1517–1520, 1987.

[57] S. M. Block, D. F. Blair, and H. C. Berg. Compliance of bacterial flagella measured with optical tweezers. *Nature*, 338(6215):514–518, 1987.

[58] W. S. Ryu, R. M. Berry, and H. C. Berg. Torque-generating units of the flagellar motor of escherichia coli have a high duty ratio. *Nature*, 403(6768):444–447, 2000.

[59] T. L. Min, P. J. Mears, L. M. Chubi, C. V. Rao, I. Golding, and Y. R. Chemla. High-resolution, long-term characterization of bacterial motility using optical tweezers. *Nat. Methods*, 6(11):831–835, 2009.

[60] T. Altindal, S. Chattopadhyay, and X. Wu. Bacterial chemotaxis in an optical trap. *PloS ONE*, 6(4), 2011.

[61] G. Volpe and D. Petrov. Torque detection using brownian fluctuations. *Phys. Rev. Lett.*, 97(21):210603, 2006.

[62] K. Sekimoto. *Stochastic Energetics.* Lecture Notes in Physics. Springer, Berlin, Heidelberg, 2010.

[63] R. K. Pathria. *Statistical Mechanics.* Butterworth Heinemann, London, 2nd edition, 1996.

[64] A. Celani, S. Bo, R. Eichhorn, and E. Aurell. Anomalous thermodynamics at the microscale. *Phys. Rev. Lett.*, 109:260603, 2012.

[65] S. Bo and A. Celani. Entropic anomaly and maximal efficiency of microscopic heat engines. *Phys. Rev. E.*, 87(5):050102, 2013.

[66] T. Schmiedl and U. Seifert. Efficiency at maximum power: An analytically solvable model for stochastic heat engines. *Europhys. Lett.*, 81(2):20003, 2008.

[67] T. H. Maiman. Stimulated optical radiation in ruby. *Nature*, 187:493–494, 1960.

[68] S. Chu, JE Bjorkholm, A. Ashkin, and A. Cable. Experimental observation of optically trapped atoms. *Phys. Rev. Lett.*, 57(3):314–317, 1986.

[69] S. B. Smith, Y. Cui, and C. Bustamante. Overstretching B-DNA: the elastic response of individual double-stranded and single-stranded DNA molecules. *Science*, 271:795 –799, 1996.

[70] M. D. Wang, H. Yin, R. Landick, J. Gelles, S. M. Block, M.D. Wang, H. Yin, R. Landick, J. Gelles, and S.M. Block. Stretching dna with optical tweezers. *Biophys. J.*, 72(3):1335 – 1346, 1997.

[71] J. D. Jackson and R. F. Fox. Classical electrodynamics. *Am. J. Phys.*, 67:841, 1999.

[72] A. Mazolli, M. Neto, and HM Nussenzveig. Theory of trapping forces in optical tweezers. *P. Roy. Soc A - Math. Phys.*, 459(2040):3021–3041, 2003.

[73] K. Svoboda and S. M. Block. Biological applications of optical forces. *Annu. Rev. Biophys. Biomol. Struct.*, 23(1):247–285, 1994.

[74] A. Ashkin. Forces of a single-beam gradient laser trap on a dielectric sphere in the ray optics regime. *Biophys. J.*, 61(2):569 – 582, 1992.

[75] A. Pralle, M. Prummer, E. L. Florin, E. H. K. Stelzer, J. K. H. Hörber, et al. Three-dimensional high-resolution particle tracking for optical tweezers by forward scattered light. *Microsc. Res. Tech.*, 44(5):378–386, 1999.

[76] F. Gittes and C. F. Schmidt. Interference model for back-focal-plane displacement detection in optical tweezers. *Opt. Lett.*, 23:7–9, 1998.

[77] G. M. Gibson, J. Leach, S. Keen, A. J. Wright, and M. J. Padgett. Measuring the accuracy of particle position and force in optical tweezers using high-speed video microscopy. *Opt. express*, 16(19):14561–14570, 2008.

[78] A. Rohrbach, E. L. Florin, and E. H. Stelzer. Photonic force microscopy: Simulation of principles and applications. In *European Conference on Biomedical Optics*, pages 75–86. International Society for Optics and Photonics, 2001.

[79] D. G. Grier and Y. Roichman. Holographic optical trapping. *Appl. Opt.*, 45(5):880–887, 2006.

[80] K. Visscher, S. P. Gross, and S. M. Block. Construction of mutiple-beam optical traps with nanometric-resolution position sensing. *IEEE J. of Sel. Topics in Quantum Electronics*, 2:1066 – 1076, 1996.

[81] J. E. Molloy. Optical chopsticks: digital synthesis of multiple optical traps. *Methods Cell Biol.*, 55:205 – 216, 1998.

[82] O. Otto, C. Gutsche, F. Kremer, and U.F. Keyser. Optical tweezers with 2.5 khz bandwidth video detection for single-colloid electrophoresis. *Rev. Sci. Instrum.*, 79:023710, 2008.

[83] J. Dong, C. E. Castro, M. C. Boyce, M. J. Lang, and S. Lindquist. Optical trapping with high forces reveals unexpected behaviors of prion fibrils. *Nat. Str. and Mol. Biology*, 17:1422 – 1430, 2010.

[84] L. P. Faucheux, G. Stolovitzky, and A. Libchaber. Periodic forcing of a brownian particle. *Phys. Rev. E*, 51:5239 — 5250, 1995.

[85] G. Wang, E. Sevick, E. Mittag, D. Searles, and D. Evans. Experimental demonstration of violations of the second law of thermodynamics for small systems and short time scales. *Phys. Rev. Lett.*, 89:050601, 2002.

[86] A. Imparato, L. Peliti, G. Pesce, G. Rusciano, and A. Sasso. Work and heat probability distribution of an optically driven brownian particle: Theory and experiments. *Phys. Rev. E*, 76:050101–1 – 050101–4, 2007.

[87] A. Simon and A. Libchaber. Escape and synchronization of a brownian particle. *Phys. Rev. Lett.*, 68:3375 — 3378, 1992.

[88] L. I. McCann, M. Dykman, and B. Golding. Thermally activated transitions in a bistable three-dimensional optical trap. *Nature*, 402:785–787, 1999.

[89] C. Schmidt, B. Dybiec, P. Hänggi, and C. Bechinger. Stochastic resonance vs. resonant activation. *Europhys. Lett.*, 74:937 – 943, 2006.

[90] K. Dholakia and P. Zemanek. Colloquium: Gripped by light: optical binding. *Rev. Mod. Physics*, 82:1767 – 1791, 2010.

[91] J. Gomez-Solano, A. Petrosyan, S. Ciliberto, R. Chetrite, and K. Gawedzki. Experimental verification of a modified fluctuation-dissipation relation for a micron-sized particle in a nonequilibrium steady state. *Phys. Rev. Lett.*, 103:040601–1 – 040601–4, 2009.

[92] J. Crocker and D. G. Grier. Methods of digital video microscopy for colloidal studies. *J. Colloid Interface Sci.*, 179:298 – 310, 1996.

[93] M. J. Lang, C. L. Asbury, J. W. Shaevitz, and S. V. Block. An automated two-dimensional optical force clamp for single molecule studies. *Biophys. J.*, 83:491–501, 2002.

[94] A. Rohrbach, C. Tischer, D. Neumayer, E. L. Florin, and E. H. K. Stelzer. Trapping and tracking a local probe with a photonic force microscope. *Rev. Sci. Instrum.*, 75:2197 – 2210, 2004.

[95] A. Rohrbach, H. Kress, and E. H. K. Stelzer. Three-dimensional tracking of small spheres in focused laser beams: influence of the detection angular aperture. *Opt. Lett.*, 28:411 – 413, 2003.

[96] G. Volpe, G. Kozyreff, and D. Petrov. Backscattering position detection for photonic force microscopy. *J. Appl. Phys.*, 102:0847011–08470111, 2007.

[97] B. Richards and E. Wolf. Electromagnetic diffraction in optical systems ii. *P. Roy. Soc A - Math. Phys.*, 253:358 – 379, 1959.

[98] F. Gittes and C. F. Schmidt. Signals and noise in micromechanical measurements. *Methods Cell Biol.*, 55:129 – 156, 1998.

[99] S. Perrone, G. Volpe, and D. Petrov. 10-fold detection range increase in quadrant-photodiode position sensing for photonic force microscope. *Rev. Sci. Instrum.*, 79:106101–1 – 106101–3, 2008.

[100] N. B. Viana, M. S. Rocha, O. N. Mesquita, A. Mazolli, P. A. Maia Neto, and H. M. Nussenzveig. Towards absolute calibration of optical tweezers. *Phys. Rev. E*, 75:021914–1 – 021914–14, 2007.

[101] Yih-Fan Chen, G. A. Blab, and J-Ch. Meiners. Stretching submicron biomolecules with constant-force axial optical tweezers. *Biophys. J.*, 96:4701–4708, 2009.

[102] R. M. Simmons, J. T. Finer, S. Chu, and J. A. Spudich. Quantitative measurements of force and displacement using an optical trap. *Biophys. J.*, 70:1813 — 1822, 1996.

[103] W. Singer, S. Barnet, N. Hecker, and M. Ritsch Marte. Three- dimensional force calibration of optical tweezers. *J. Mod. Optic.*, 47:2921 – 2931, 2000.

[104] M. Capitanio, G. Romano, R. Ballerini, M. Giuntini, F. S. Pavone, D. Dunlap, and L. Finzi. Calibration of optical tweezers with differential interference contrast signals. *Rev. Sci. Instrum.*, 73:1687 – 1696, 2002.

[105] A. Balijepalli, T. W. LeBrun, J. J. Gorman, and S. K. Gupta. Methods to directly measure the trapping potential in optical tweezers. *Proc. SPIE*, 7038:70380V, 2008.

[106] A. C. Richardson, S. N. S. Reihani, and L. B. Oddershede. Non-harmonic potential of a single beam optical trap. *Opt. Express*, 16:15709 — 15717, 2008.

[107] Y. Zhao, G. Milne, J. C. Edgar, G. D. M. Jeffries, D. McGloin, and D. T. Chiu. Quantitative force mapping of an optical vortex trap. *Appl. Phys. Lett.*, 92:161111–1 – 161111–3, 2008.

[108] T. Godazgar, R. Shokri, and S. N. S. Reihani. Potential mapping of optical tweezers. *Opt. Lett.*, 36:3284 — 3286, 2011.

[109] A. A. R. Neves, A. Fontes, L. de Y. Pozzo, A. A. de Thomaz, E. Chillce, E. Rodrigez, L. C. Barbosa, and C. L. Cesar. Electromagnetic forces for an arbitrary optical trapping of a spherical dielectric. *Optics Express*, 14:13101 – 13106, 2006.

[110] M. Jahnel, B. Behrndt, A. Jannasch, E. Schaffer, and S. W. Grill. Measuring the complete force field of an optical trap. *Opt. Lett.*, 36:1260 — 1262, 2011.

[111] A. Rohrbach and E. H. K. Stelzer. Trapping forces, force constants, and potential depths for dielectric spheres in the presence of spherical aberrations. *Appl. Opt.*, 41:2494 — 2507, 2002.

[112] N. G. van Kampen. *Stochastic Processes in Physics and Chemistry.* North-Holland, Amsterdam, 1992.

[113] S. B. Smith, L. Finzi, and C. Bustamante. Direct mechanical measurements of the elasticity of single dna molecules by using magnetic beads. *Science*, 258(5085):1122–1126, 1992.

[114] P. Cluzel, A. Lebrun, C. Heller, R. Lavery, J-L. Viovy, D. Chatenay, and F. Caron. Dna: an extensible molecule. *Science*, 271:792–794, 1996.

[115] T. T. Perkins. Optical traps for single molecule biophysics: a primer. *Laser and Photon. Rev.*, 3:203–220, 2009.

[116] S. Rao, S. Raj, S. Balint, C. Bardina Fons, S. Campoy, M. Llagostera, and D. Petrov. Single DNA molecule detection in an optical trap using surface-enhanced Raman scattering. *Appl. Phys. Lett.*, 96:21370–213703, 2010.

[117] J. F. Marko and E. D. Siggia. Stretching DNA. *Macromolecules*, 28:8759–8770, 1995.

[118] S. F Tolić-Norrelykke, E. Schäffer, J. Howard, F. S Pavone, F. Jülicher, and H. Flyvbjerg. *Rev. Sci. Instrum.*, 77(10):103101, 2006.

[119] R. S. Dutra, N. B. Viana, P. A. MaiaNeto, and H. M. Nussenzveig. Polarization effects in optical tweezers. *J. Opt. A: Pure Appl. Opt.*, 9:S221ÐS227, 2007.

[120] A. R. Carter, Y. Seol, and T. T. Perkins. An automated two-dimensional optical force clamp for single molecule studies. *Biophys. J.*, 96:2926–2934, 2009.

[121] E. A. Abbondanzieri, W. J. Greenleaf, J. W. Shaevitz, R. Landick, and S. M. Block. Direct observation of base-pair stepping by RNA polymerase. *Nature*, 438:460, 2005.

[122] C-H. Lien, M-T. Wei, T-Y. Tseng, C-D. Lee, C. Wang, T-F. Wang, H. D. Ou-Yang, and A. Chiou. Probing of dynamic differential stiffness of dsDNA interacting with RecA in the enthalpic regime. *Opt. Express*, 17:20376–20385, 2009.

[123] J. R. Moffitt, Y. R. Chemla, D. Izhaky, and C. Bustamante. Differential detection of dual traps improves the spatial resolution of optical tweezers. *Proc. Natl. Acad. Sci. U. S. A.*, 103:9006–9011, 2006.

[124] J. R. Moffitt, Y. R. Chemla, S. B. Smith, and C. Bustamante. Recent advances in optical tweezers. *Annu. Rev. Biochem.*, 77:205, 2008.

[125] M. S. Keshner. 1/f noise. *IEEE Proc.*, 79:212, 1982.

[126] F. N. Hooge. 1/f noise. *Physica B*, 83:14–23, 2002.

[127] C. A. Merchant, K. H., M. Wanunu, V. Ray, N. Peterman, J. Bartel, M. D. Fischbein, K. Venta, Z. Luo, A. T. C. Johnson, and M. Drndić. Dna translocation through graphene nanopores. *Nano Lett.*, 10(8):2915–2921, 2010.

[128] R. F. Voss. Evolution of long-range fractal correlations and 1/f noise in DNA base sequences. *Phys. Rev. Lett.*, 68:3805–3808, 1992.

[129] W. Li and D. Holste. Universal 1/f noise, crossovers of scaling exponents, and chromosome-specific patterns of guanine-cytosine content in DNA sequences of the human genome. *Phys Rev E*, 71:041910, 2005.

[130] K. S. Nagapriya, A. K. Raychaudhuri, and D. Chatterji. Direct observation of large temperature fluctuations during DNA thermal denaturation. *Phys. Rev. Lett.*, 96:038102, 2006.

[131] P. Hänggi, P. Talkner, and M. Borkovec. Reaction-rate theory: fifty years after kramers. *Rev. Mod. Physics*, 62(2):251, 1990.

[132] P. Hanggi. Escape over fluctuating barriers driven by colored noise. *Chem. Physics*, 180:157–166, 1994.

[133] K. W. Planxco and D. Baker. Limited internal friction in the rate-limiting step of a two-state protein folding reaction. *Proc. Natl. Acad. Sci. U. S. A.*, 95:13591–13596, 1998.

[134] B. C. Bag, Chin-Kun Hubc, and M. S. Li. Colored noise, folding rates and departure from KramersÕ behavior. *Phys. Chem. Chem. Phys.*, 12:11753–11762, 2010.

[135] A. R. Carter, G. M. King, and T. T. Perkins. Back-scattering detection provides atomic-scale localization precision, stability, and registration in 3D. *Optics Express*, 15:13434–13445, 2007.

[136] J. W. Shaevitz, E. A. Abbondanzieri, R. Landick, and S. M. Block. Backtracking by single RNA polymerase molecules observed at near-base-pair resolution. *Nature*, 426:864, 2003.

[137] H. C. Berg and R. A. Anderson. Bacteria swim by rotating their flagellar filaments. *Nature*, 245:380–382, 1973.

[138] M. Silverman and M. Simon. Flagellar rotation and the mechanism of bacterial motility. *Nature*, 249:73–74, 1974.

[139] H. Terashima, S. Kojima, and M. Homma. Flagellar motility in bacteria structure and function of flagellar motor. *Int. Rev. Cell. Mol. Biol.*, 270:39–85, 2008.

[140] K. F. Jarrell and M. J. McBride. The surprisingly diverse ways that prokaryotes move. *Nat Rev Microbiol*, 6:466–476, 2008.

[141] S. I. Aizawa. Flagellar assembly in salmonella typhimurium. *Mol. Microbiol.*, 19:1–5, 1996.

[142] R. M. Macnab. How bacteria assemble flagella. *Annu. Rev. Microbiol.*, 57:77–100, 2003.

[143] D. R. Thomas, N. R. Francis C. Xu, and D. J. DeRosier. The three-dimensional structure of the flagellar rotor from a clockwise-locked mutant of salmonella enterica serovar typhimurium. *J. Bacteriol.*, 188:7039Ð7048, 2006.

[144] R. M. Macnab. Bacterial flagella rotating in bundles: a study in helical geometry. *Proc. Natl. Acad. Sci. U. S. A.*, 74:221–225, 1977.

[145] L. Turner, W. S. Ryu, and C. Berg H. Real-time imaging of fluorescent flagellar filaments. *J. Bacteriol.*, 182(10):2793–2801, 2000.

[146] J. B. Stock and M.G. Surette. *Chemotaxis.:Escherichia coli and Salmonella typhimurium: Cellular and Molecular Biology.* ASM Press, Washington, DC, 1996.

[147] J. S. Parkinson, P. Ames, and C. A. Studdert. Collaborative signaling by bacterial chemoreceptors. *Curr. Opin. Microbiol.*, 8:116–121, 2005.

[148] M. S. Jurica and B. L. Stoddard. Mind your b's and r's: bacterial chemotaxis, signal transduction and protein recognition. *Structure*, 6:809–813, 1998.

[149] R. M. Macnab and D. E. Koshland. The gradient-sensing mechanism in bacterial chemotaxis. *Proc. Natl. Acad. Sci. U. S. A.*, 69:2509–2512, 1998.

[150] J. A. Ibarra and O. Steele-Mortimer. Salmonella–the ultimate insider. salmonella virulence factors that modulate intracellular survival. *Cell. Microbiol.*, 11:1579–1586, 2009.

[151] G. Sano, Y. Takada, S. Goto, K. Maruyama, Y. Shindo, K. Oka K, and et al. Flagella facilitate escape of salmonella from oncotic macrophages. *J. Bacteriol.*, 189:8224Ð8232, 2007.

[152] B. D. Jones, C. A. Lee, and S. Falkow. Invasion by salmonella typhimurium is affected by the direction of flagellar rotation. *Infect. Immun.*, 60:2475–2480, 1992.

[153] R. M. Macnab. Examination of bacterial flagellation by dark- field microscopy. *J. Clin. Micro-biol.*, 4:258–265, 1976.

[154] U. Alon, L. Camarena, M. G. Surette, B. Aguera y Arcas, Y. Liu, S. Leibler, and J. B. Stock. Response regulator output in bacterial chemotaxis. *EMBO J.*, 17:4238–4248, 1998.

[155] J. F. Staropoli and U. Alon. Computerized analysis of chemotaxis at different stages of bacterial growth. *Biophys. J.*, 75:513Ð519, 2000.

[156] G. M. Whitesides, E. Ostuni, S. Takayama, X. Jian, and D. E. Ingber. Soft lithography in biology and biochemistry. *Annu. Rev. Biomed. Eng.*, 3:335–373, 2001.

[157] T. Ahmed and T. S. Shimizu R. Stocker. Microfluidics for bacterial chemotaxis. *Integr Biol (Camb)*, 2:604–629, 2010.

[158] M. P. Landry, P. M. McCall, Z. Qi, and Y. R. Chemla. Characterization of photoactivated singlet oxygen damage in single-molecule optical trap experiments. *Biophys. J.*, 97:2128Ð2136, 2009.

[159] J. Adler and B. Templeton. The effect of environmental conditions on the motility of escherichia coli. *Microbiology*, 46:175–184, 1967.

[160] A. L. DeFranco, J. S. Parkinson, and D. E. Koshland DE Jr. Chemotactic mechanism of salmonella typhimurium: preliminary mapping and characterization of mutants. *J. Bacteriol.*, 139:107–114, 1979.

[161] H. M. Warrick, B. L. Taylor, and D. E. Koshland Jr. Chemotactic mechanism of salmonella typhimurium: preliminary mapping and characterization of mutants. *J. Bacteriol.*, 130:223–231, 1977.

[162] H. C. Berg. *E coli in motion.* Springer, New York, 2004.

[163] A. L. Collins and B. A. Stocker. Salmonella typhimurium mutants generally defective in chemotaxis. *J. Bacteriol.*, 128:754–765, 1976.

[164] H. C. Berg and D. A. Brown. Chemotaxis in escherichia coli analysed by three-dimensional tracking. *Nature*, 239(5374):500–504, 1972.

[165] R. P. Alexander, A. C. Lowenthal, R. M. Harshey, and K. M. Ottemann. Chev: Chew-like coupling proteins at the core of the chemotaxis signaling network. *Trends Microbiol.*, 18:494–503, 2010.

[166] G. E. Dean, S. I. Aizawa, and R. M. Macnab. flaaii (motc, chev) of salmonella typhimurium is a structural gene involved in energization and switching of the flagellar motor. *J. Bacteriol.*, 154:84–91, 1983.

[167] K. C. Neuman, E. H. Chadd, G. F. Liou, K. Bergman, and S. M. Block. Characterization of photodamage to escherichia coli in optical traps. *Biophys. J.*, 77:2856–2863, 1999.

[168] H. C. Berg and L. Turner. Cells of e. coli swim either and forward. *Proc. Natl. Acad. Sci. U. S. A.*, 92(2):477–479, 1995.

[169] H. Szurmant and G. W. Ordal. Diversity in chemotaxis mechanisms among the bacteria and archaea. *Microbiol. Mol. Biol. Rev.*, 68:301–319, 2004.

[170] S. L. Porter, G. H. Wadhams, and J. P. Armitage. Signal processing in complex chemotaxis pathways. *Nat Rev Microbiol.*, 9:153–165, 2011.

[171] J. Frye, J. E. Karlinsey, H. R. Felise, B. Marzolf, N. Dowidar, M. McClelland, and K. T. Hughes. Identification of new flagellar genes of salmonella enterica serovar typhimurium. *J. Bacteriol.*, 188:2233–2243, 2006.

[172] R. C. Fink, M. R. Evans, S. Porwollik, A. Vazquez-Torres, J. Jones-Carson, B. Troxell, S. J. Libby, M. McClelland, and H. M. Hassan. Fnr is a global regulator of virulence and anaerobic metabolism in salmonella enterica serovar typhimurium (atcc 14028s). *J. Bacteriol.*, 189:2262–2273, 2007.

[173] M. R. Evans, R. C. Fink, A. Vazquez-Torres, S. Porwollik, J. Jones-Carson, M. McClelland, and H. M. Hassan. Analysis of the arca regulon in anaerobically grown salmonella enterica sv. typhimurium. *BMC Microbiol.*, 11:58, 2011.

[174] C. L. Asbury, A. N. Fehr, and S. M. Block. Kinesin moves by an asymmetric hand-over-hand mechanism. *Science*, 302(5653):2130–2134, 2003.

[175] H. B. Callen. Thermodynamics and an introduction to thermostatistics. Technical report, ISBN 0-471-86256-8. Wiley-VCH, 1985.

[176] K. Sekimoto. Langevin equation and thermodynamics. *Prog. Theor. Phys.*, 130:17–27, 1998.

[177] U. Seifert. Stochastic thermodynamics: principles and perspectives. *Eur. Phys. J. B*, 64(3-4):423–431, 2008.

[178] S. Carnot. *Réflexions sur la puissance motrice du feu*, volume 26. Librairie Philosophique Vrin, 1824.

[179] J. P. Sethna. *Statistical mechanics: entropy, order parameters, and complexity.* Oxford University Press New York, 2006.

[180] L. Brillouin. Maxwell's demon cannot operate: Information and entropy. i. *J. Appl. Phys.*, 22(3):334–337, 1951.

[181] Claude Elwood Shannon and Warren Weaver. A mathematical theory of communication, 1948.

[182] C. H. Bennett and R. Landauer. The fundamental physical limits of computation. *Scientific American*, 253(1):48–56, 1985.

[183] P. Langevin. Sur la théorie du mouvement brownien. *CR Acad. Sci. Paris*, 146(530-533), 1908.

[184] A. Einstein. The theory of the brownian movement. *Ann. der Physik*, 17:549, 1905.

[185] Anita Jannasch, Mohammed Mahamdeh, and Erik Schäffer. Inertial effects of a small brownian particle cause a colored power spectral density of thermal noise. *Phys. Rev. Lett.*, 107(22):228301, 2011.

[186] H. A. Kramers. Brownian motion in a field of force and the diffusion model of chemical reactions. *Physica*, 7(4):284–304, 1940.

[187] J. R. Gomez-Solano, L. Bellon, A. Petrosyan, and S. Ciliberto. Steady-state fluctuation relations for systems driven by an external random force. *Europhys. Lett.*, 89(6):60003, 2010.

[188] U. Seifert. Entropy production along a stochastic trajectory and an integral fluctuation theorem. *Phys. Rev. Lett.*, 95(4):040602, 2005.

[189] G. E. Crooks. Entropy production fluctuation theorem and the nonequilibrium work relation for free energy differences. *Phys. Rev. E*, 60:2721–2726, 1999.

[190] . Loschmidt. *Akad. d. W. Math. Naturw. II*, 73(128), 1876.

[191] D. J. Evans and D. J. Searles. Equilibrium microstates which generate second law violating steady states. *Phys. Rev. E*, 50:1645–1648, 1994.

[192] U. Seifert. Stochastic thermodynamics, fluctuation theorems and molecular machines. *Rep. Prog. Phys.*, 75(12):126001, 2012.

[193] C. Jarzynski. Equalities and inequalities: irreversibility and the second law of thermodynamics at the nanoscale. In *Time*, pages 145–172. Springer, 2013.

[194] N. Merhav and Y. Kafri. Statistical properties of entropy production derived from fluctuation theorems. *J. Stat. Mech.-Theory E*, 2010(12):P12022, 2010.

[195] C. Jarzynski. Nonequilibrium equality for free energy differences. *Phys. Rev. Lett.*, 78:2690–2693, Apr 1997.

[196] V. Blickle, T. Speck, L. Helden, U. Seifert, and C. Bechinger. Thermodynamics of a colloidal particle in a time-dependent nonharmonic potential. *Phys. Rev. Lett.*, 96(7):070603, 2006.

[197] R. Radunz, D. Rings, K. Kroy, and F. Cichos. Hot brownian particles and photothermal correlation spectroscopy. *J. Phys. Chem. A*, 113:1674–1677, 2009.

[198] P. V. Ruijgrok, N. R. Verhart, P. Zijlstra, A. L. Tchebotareva, and M. Orrit. Brownian fluctuations and heating of an optically aligned gold nanorod. *Phys. Rev. Lett.*, 107:037401–1–037401–4, 2011.

[199] M. Schaechter, O. Maaløe, and N. O. Kjeldgaard. Dependency on medium and temperature of cell size and chemical composition during balanced growth of salmonella typhimurium. *J. Gen. Microbiol.*, 19(3):592–606, 1958.

[200] M. C. Williams, J. R. Wenner, I. Rouzina, and V. A. Bloomfield. Entropy and heat capacity of dna melting from temperature dependence of single molecule stretching. *Biophys. J.*, 80(4):1932–1939, 2001.

[201] A. Ashkin and J. Dziedzic. Feedback stabilization of optically levitated particles. *Appl. Phys. Lett.*, 30:202 –204, 1977.

[202] T. Li, S. Kheifets, and M. G. Raizen. Millikelvin cooling of an optically trapped microsphere in vacuum. *Nat. Phys.*, 7:527–530, 2011.

[203] J. Gieseler, B. Deutsch, R. Quidant, and L. Novotny. Subkelvin parametric feedback cooling of a laser-trapped nanoparticle,. *Phys. Rev. Lett.*, 109:103603, 2012.

[204] G. Box, G. M. Jenkins, and G. Reinsel. *Time Series Analysis: Forecasting & Control (3rd Edition).* Prentice Hall, 3rd edition, 1994.

[205] O. Mazonka and C. Jarzynski. Exactly solvable model illustrating far-from-equilibrium predictions. *e-print cond-mat/9912121*, 1999.

[206] JR Gomez-Solano, A Petrosyan, and S Ciliberto. Heat fluctuations in a nonequilibrium bath. *Physical Review Letters*, 106(20):200602, 2011.

[207] PG Steeneken, K Le Phan, MJ Goossens, GEJ Koops, GJAM Brom, C Van der Avoort, and JTM Van Beek. Piezoresistive heat engine and refrigerator. *Nature Physics*, 7(4):354–359, 2011.

[208] R Van Zon and EGD Cohen. Extension of the fluctuation theorem. *Phys. Rev. Lett.*, 91(11):110601, 2003.

[209] J. M. R. Parrondo, C. Van den Broeck, and R. Kawai. Entropy production and the arrow of time. *New J. Phys.*, 11(7):073008, 2009.

[210] Félix Ritort. Work fluctuations, transient violations of the second law and free-energy recovery methods: Perspectives in theory and experiments. In *Poincaré Seminar 2003*, pages 193–226. Springer, 2004.

[211] I. A. Martínez, E. Roldan, J. M. R. Parrondo, and D. Petrov. Effective heating to several thousand kelvin of an optically trapped sphere in a liquid. *Phys. Rev. E*, 87:032159, 2013.

[212] Ken Sekimoto, Fumiko Takagi, and Tsuyoshi Hondou. Carnot's cycle for small systems: Irreversibility and cost of operations. *Physical Review E*, 62(6):7759, 2000.

[213] Massimiliano Esposito, Ryoichi Kawai, Katja Lindenberg, and Christian Van den Broeck. Efficiency at maximum power of low-dissipation carnot engines. *Physical review letters*, 105(15):150603, 2010.

[214] A. Alemany, A. Mossa, I. Junier, and F. Ritort. Experimental free-energy measurements of kinetic molecular states using fluctuation theorems. *Nat. Phys.*, 2012.

[215] T. Sagawa and M. Ueda. Minimal energy cost for thermodynamic information processing: measurement and information erasure. *Phys. Rev. Lett.*, 102(25):250602, 2009.

[216] H. S. Leff and A. F. Rex. Maxwell's demon. entropy, information, computing. *Bristol: Adam Hilger, 1990, edited by Leff, Harvey S.; Rex, Andrew F.*, 1, 1990.

[217] R. Kawai, J. M. R. Parrondo, and C. Van den Broeck. Dissipation: The phase-space perspective. *Phys. Rev. Lett.*, 98(8):080602, 2007.

[218] Léo Granger and Holger Kantz. Differential landauer's principle. *Europhys. Lett.*, 101(5):50004, 2013.

[219] R. Benjamin and R. Kawai. Inertial effects in büttiker-landauer motor and refrigerator at the overdamped limit. *Phys. Rev. E*, 77:051132, May 2008.

[220] K. Kanazawa, T. Sagawa, and H. Hayakawa. Stochastic energetics for non-gaussian processes. *arXiv preprint arXiv:1111.5906*, 2011.

[221] A. Baura, M. K. Sen, G. Goswami, and B. C. Bag. Colored non-gaussian noise driven open systems: Generalization of kramers' theory with a unified approach. *J. Chem. Phys.*, 134:044126, 2011.

[222] I. A. Martínez, S. Campoy, M. Tort, M. Llagostera, and D. Petrov. A simple technique based on a single optical trap for the determination of bacterial swimming pattern. *PloS one*, 8(4):e61630, 2013.

[223] J. Adler and B. Templeton. A method for measuring chemotaxis and use of method to determine optimum conditions for chemotaxis by escherichia coli. *J. Gen. Microbiol.*, 74:77–91, 1973.

[224] K. A. Datsenko and B. L. Wanner. One-step inactivation of chromosomal genes in escherichia coli k-12 using pcr products. *Proc. Natl. Acad. Sci. U. S. A.*, 97(12):6640–6645, 2000.

[225] J. Sambrook and D. Russell. *Molecular cloning: a laboratory manual.* Cold Spring Harbor Laboratory Press, Cold Spring Harbor, NY, 2001.

[226] M. K. Chaveroche, J. M. Ghigo, and C. dŐEnfert. A rapid method for efficient gene replacement in the filamentous fungus aspergillus nidulans. *Nucleic Acids Res.*, 28:E67, 2000.

[227] S. Campoy, M. Jara, N. Busquets, A. M. Perez De Rozas, I. Badiola, and J. Barbe. Role of the high-affinity zinc uptake znuabc system in salmonella enterica serovar typhimurium virulence. *Infect. Immun.*, 70:4721Ð4725, 2002.

[228] R. W. Davis, D.R. Botstein, and J. R. Roth. *Advanced bacterial genetics. A manual for genetic engineering.* Cold Spring Harbor Laboratory Press, Cold Spring Harbor, NY, 1980.

[229] P. Maragakis, M. Spichty, and M. Karplus. A differential fluctuation theorem. *J. Phys. Chem. B*, 112(19):6168–6174, 2008.

[230] I. Junier, A. Mossa, M. Manosas, and F. Ritort. Recovery of free energy branches in single molecule experiments. *Physical review letters*, 102(7):070602, 2009.

[231] T. M. Cover and J. A. Thomas. *Elements of information theory.* John Wiley & Sons, 2012.